Cranfield University

School of Aerospace, Transport and Manufacturing

PhD Thesis

Academic years 2011-2015

Tassos Mesogitis

Stochastic simulation of the cure of advanced composites

Supervisor: Dr Alex Skordos, Professor Andrew Long

February 2015

Cranfield University

School of Aerospace, Transport and Manufacturing

PhD Thesis

Academic years 2011-2015

Tassos Mesogitis

Stochastic simulation of the cure of advanced composites

Supervisor: Dr Alex Skordos, Professor Andrew Long

February 2015

Abstract

This study focuses on the development of a stochastic simulation methodology to study the effects of cure kinetics uncertainty, in plane fibre misalignment and boundary conditions uncertainty on the cure process of composite materials. Differential Scanning Calorimetry was used to characterise cure kinetics variability of a commercial epoxy resin used in aerospace applications. It was found that cure kinetics uncertainty is associated with variations in the initial degree of cure, activation energy and reaction order. Image analysis was employed to characterise in plane fibre misalignment in a carbon fibre ±45º non-crimp fabric. The experimental results showed that variability in tow orientation was significant with a standard deviation of about 1.2º. A set of experiments using an infusion set-up was carried out to quantify boundary conditions uncertainty related to tool temperature, ambient temperature and surface heat transfer coefficient using thermocouples (tool/ambient temperature) and heat flux sensors (surface heat transfer coefficient). It was concluded that boundary conditions uncertainty can show considerable short term and long term variability. Conventional Monte Carlo and Probabilistic Collocation Method were integrated with a thermo-mechanical cure simulation model in order to investigate the effect of cure kinetics, fibre misalignment and boundary conditions variability on process outcome. The cure model was developed and implemented using a finite element model incorporating appropriate material sub-models of cure kinetics, specific heat capacity, thermal conductivity, moduli, thermal expansion and cure shrinkage. The effect of cure kinetics uncertainty on the temperature overshoot of a thick carbon fibre epoxy flat panel was investigated using the two stochastic simulation schemes. The stochastic simulation results showed that variability in cure kinetics can introduce a significant scatter in temperature overshoot, presenting a coefficient of variation of about 30%. Furthermore, it was shown that the collocation method can offer an efficient solution with significantly lower computational cost compared to Monte Carlo at comparable accuracy. Stochastic simulation of the cure of an angle shaped carbon fibre-epoxy component within the Monte Carlo scheme showed that fibre misalignment can cause considerable variability in the process outcome. The coefficient of variation of maximum residual stress can reach up to approximately 2% (standard deviation of 1 MPa) whilst qualitative and quantitative variations in final distortion of the cured part occur with the standard deviation in twist and corner angle reaching values of 0.4 º and 0.05º respectively. Simulation of the cure of a thin carbon fibre-epoxy panel within the Monte Carlo scheme indicated that surface heat transfer and tool temperature variability dominate variability in cure time, resulting in a coefficient of variation of about 22%. In addition to Monte Carlo, the effect of surface heat transfer coefficient and tool temperature variations on cure time was addressed using the collocation method. It was found that probabilistic collocation is capable of capturing variability propagation with good accuracy while offering tremendous benefits in terms of computational costs.

Keywords: Stochastic Simulation, Cure simulation, Uncertainty, Monte Carlo, Probabilistic Collocation Method, Statistics.

Acknowledgements

I am very grateful to my supervisors Dr Alex Skordos and Professor Andrew Long for their technical and moral support, guidance, patience and continuous effort to improve this piece of work. I would like to thank Mr Jim Harley for the technical assistance that made part of the experimental work possible. I would also like to thank Assistant Professor Anestis Kalfas for giving me the opportunity to study at Cranfield University.

Special thanks to my father Spyros and my mother Anastasia for their continuous moral support, encouragement and financial backing.

I would especially like to thank my very good friends and housemates Konstantinos Tzanidakis and Michael Frank. I would also like to thank my very good friends Marios Stamatis, Michalis Papanikolaou, Emmanouil Dagdilelis, Stavros Vavias and Fanis Arampatzis for their constant encouragement and moral support.

Thanks to my fellow mates Giacomo, Diego, Vincenco, Paul and Tom.

Contents

List of Tables i

List of Figures ii

Notation vii

1. Introduction 1
   - 1.1 Motivation and contribution 1
   - 1.2 Aim and objectives 3
   - 1.3 Project setting 4
   - 1.4 Thesis road map 4
2. Uncertainty in the manufacturing of fibrous thermosetting composites 6
   - 2.1 Introduction 6
   - 2.2 Stochastic simulation methods 7
   - 2.3 Variability of dry textiles and pre-pregs 9
   - 2.4 Uncertainty in forming/draping 10
   - 2.5 Uncertainty during impregnation/consolidation 11
     - *2.5.1 Fabric heterogeneity effects* 12
     - *2.5.2 Nesting effects* 14
     - *2.5.3 Edge effects* 15
     - *2.5.4 Void formation* 16
   - 2.6 Uncertainty in composites cure 18
     - *2.6.1 Material properties and boundary conditions variation effects on cure* 18
     - *2.6.2 Residual stresses-shape distortion* 19
   - 2.7 Property measurement and model uncertainties 20
   - 2.8 Overview 22
3. Materials and experimental methods 25
   - 3.1 Introduction 25
   - 3.2 Materials 25
   - 3.3 Differential Scanning Calorimetry 25
   - 3.4 Image acquisition/analysis 28
   - 3.5 Heat flux sensors/ thermocouples 30
   - 3.6 Overview 33
4. Cure simulation model 35
   - 4.1 Introduction 35

4.2 Thermo-mechanical problem ... 35

4.2 Constitutive models ... 37

4.2.1 Glass transition temperature ... 38

4.2.2 Cure kinetics ... 39

4.2.3 Specific heat capacity ... 41

4.2.4 Thermal conductivity ... 44

4.2.5 Mechanical properties ... 45

4.2.6 Cure shrinkage ... 49

4.2.7 Thermal expansion coefficients ... 49

4.2.8 Implementation of constitutive models ... 52

4.3 Overview ... 56

5. Stochastic simulation methodology ... 57

5.1 Introduction ... 57

5.2 Representation of input parameters uncertainty ... 57

5.2.1 Random series of observations ... 57

5.2.2 One dimensional mean-reverting Ornstein-Uhlenbeck process ... 57

5.2.3 Two-dimensional Ornstein-Uhlenbeck field ... 59

5.2.4 Cholesky factorisation ... 60

5.2.5 Spectral decomposition ... 61

5.2.6 Karhunen- Loève expansion ... 64

5.3 Monte Carlo Scheme ... 66

5.4 Probabilistic Collocation Method ... 67

5.5 Implementation of stochastic simulation methodology ... 70

5.5.1 Cure kinetics uncertainty/ boundary conditions uncertainty ... 70

5.5.2 Fibre misalignment ... 73

5.6 Overview ... 74

6. Stochastic simulation of the influence of cure kinetics uncertainty on temperature overshoot in composites cure ... 76

6.1 Introduction ... 76

6.2 Analysis of cure kinetics uncertainty ... 77

6.2.1 Experimental results ... 77

6.2.2 Quantification of cure kinetics uncertainty ... 78

6.2.3 Statistical properties of cure kinetics ... 83

6.3 Stochastic cure simulation: cure kinetics only ... 85

6.4 Stochastic cure simulation: thick carbon fibre-epoxy laminate 90

6.5 Overview 99

7. Stochastic simulation of the influence of fibre path variability on residual stress and distortion generated during composites cure 100

7.1 Introduction 100

7.2 Analysis of fibre misalignment of non-crimp fabrics 101

7.2.1 Statistical properties and spatial autocorrelation 102

7.2.2 Stochastic textile simulation 104

7.3 Stochastic cure simulation.. 106

7.3.1 Incorporation of fibre misalignment 108

7.3.2 Stochastic cure simulation results 110

7.4 Overview 125

8. Stochastic simulation of the influence of boundary conditions and cure kinetics uncertainty on cure time in composites cure 126

8.1 Introduction 126

8.2 Stochastic process development.. 126

8.3 Boundary conditions uncertainty 127

8.3.1 Experimental results 127

8.3.2 Stochastic processes... 130

8.4 Stochastic cure simulation... 136

8.4.1 Short term variability 138

8.4.2 Effect of level variability across different runs 143

8.5 Overview 152

9. Overall discussion.. 153

10. Conclusions... 158

11. Suggestions for further investigations 161

References.. 163

Appendices 180

Appendix A Cure simulation model user subroutines... 180

Appendix B Interfaces between stochastic model and FEA solver 184

Appendix B.1 cure kinetics uncertainty/ boundary conditions uncertainty........ 184

Appendix B.2 Fibre misalignment 187

Appendix C List of publications 189

List of Tables

Table 2-1 Permeability measurements for two plain weave glass fibre fabrics; plain weave glass 1 [17], plain weave glass fabric 2 [33]. 12

Table 4-1 Di Benedetto equation parameters for RTM6. 39

Table 4-2 Nominal cure kinetics parameters for RTM6. 41

Table 4-3 Specific heat capacity parameters. 43

Table 4-4 Thermal conductivity coefficients. 45

Table 4-5 Mechanical properties. 47

Table 4-6 Thermal expansion coefficients parameters. 51

Table 5-1 I/O for interface between stochastic simulation model and FEA solver; cure kinetics uncertainty, boundary conditions uncertainty. 72

Table 5-2 I/O for interface between stochastic simulation model and FEA solver; fibre misalignment. 74

Table 6-1 Estimated kinetics parameters, standard deviation of kinetics parameters, coefficient of variation of kinetics parameters, sensitivity analysis results. 80

Table 6-2 statistical properties of uncertain parameters. 83

Table 6-3 Correlation matrix of kinetics parameters. 84

Table 6-4 Maximum absolute difference between the observed and expected cumulative distribution; Kolmogorov-Smirnov goodness of fit. 84

Table 6-5 Stochastic cure simulation results; maximum cure reaction rate. 90

Table 6-6 stochastic cure simulation results; temperature overshoot, time of temperature overshoot. 98

Table 7-1 Statistical properties of tow orientation of carbon fibre ± 45º NCF. 102

Table 7-2 Correlation matrix of tow orientation of carbon fibre ± 45º NCF. 102

Table 7-3 Deterministic model and stochastic simulation results: maximum longitudinal residual stress, corner angle and twist angle of the upper flange 119

Table 7-4 Sensitivity analysis case scenarios. 120

Table 7-5 Sensitivity analysis results. 125

Table 8-1 Statistical properties of boundary conditions uncertainty across different experimental runs. 136

Table 8-2 Stochastic simulation results; effect of variability over time on cure time. 142
Table 8-3 Stochastic cure simulation results; effect of level variability on cure time. 144
Table 8-4 Values of stochastic parameters for two realisations of stochastic model. 148
Table 8-5 Third order response surface of cure time.. 149

List of Figures

Fig. 1-1 Manufacturing of fuselage panels for the A350 XWB (© Premium AEROTEC GmbH.) [3].. 2
Fig. 2-1 Schematic representation of stochastic simulation....................................... 7
Fig. 2-2 Tow waviness.. 9
Fig. 2-3 Schematic representation of interdependencies in composite manufacturing. 24
Fig. 3-1 TA-instruments DSC Q200 apparatus... 27
Fig. 3-2 Evolution of heat flow of during dynamic DSC of RTM6............................ 28
Fig. 4-1 Response of the resin specific heat capacity model.................................. 43
Fig. 4-2 Response of the resin modulus model. 48
Fig. 4-3 Response of the resin Poisson’s ratio model. 48
Fig. 4-4 Response of the resin coefficient of thermal expansion model. 52
Fig. 4-5 Schematic representation of the interface between the main solver and the user defined subroutines. 53
Fig. 5-1 Collocation points selection at high probability regions. 69
Fig. 5-2 Schematic representation of Probabilistic Collocation Method................... 70
Fig. 5-3 Interface between stochastic simulation model and FEA solver: cure kinetics uncertainty/ boundary conditions uncertainty. 72
Fig. 5-4 Interface between stochastic simulation model and FEA solver: fibre misalignment. 74
Fig. 6-1 Evolution of reaction rate as a function of temperature during dynamic cure at 1ºC/min. Letters denote the different batches of resin and numbers different samples within the same batch. 78

Fig. 6-2 Schematic representation of methodology for quantification of cure kinetics uncertainty. 80
Fig. 6-3 Sensitivity analysis results; reaction energy $E2$. 81
Fig. 6-4 Sensitivity analysis results; reaction order m. 81
Fig. 6-5 Sensitivity analysis results; initial degree of cure ao. 82
Fig. 6-6 Sensitivity analysis results; reaction energy $E1$. 82
Fig. 6-7 Sensitivity analysis results; reaction order $n2$. 83
Fig. 6-8 Prescribed temperature boundary condition. 87
Fig. 6-9 Cure reaction rate vs time. 87
Fig. 6-10 Evolution of mean of cure reaction rate vs time. 88
Fig. 6-11 Evolution of standard deviation of cure reaction rate vs time. 88
Fig. 6-12 Convergence of statistics of mean of maximum cure reaction rate. 89
Fig. 6-13 Convergence of statistics of standard deviation of maximum cure reaction rate. 89
Fig. 6-14 Probability distribution of maximum cure reaction rate. 90
Fig. 6-15 Colour map of laminate temperature; point A prescribed temperature boundary condition, point B centre of the laminate, point C natural air convection boundary condition. Deterministic model results. 92
Fig. 6-16 Evolution of laminate temperature; point A prescribed temperature boundary condition, point B centre of the laminate, point C natural air convection boundary condition. Deterministic model results. 93
Fig. 6-17 Evolution of cure reaction rate; point A prescribed temperature boundary condition, point B centre of the laminate, point C natural air convection boundary condition. Deterministic model results. 93
Fig. 6-18 Evolution of laminate degree of cure; point A prescribed temperature boundary condition, point B centre of the laminate, point C natural air convection boundary condition. Deterministic model results. 94
Fig. 6-19 Convergence of statistics of mean of temperature overshoot. 95
Fig. 6-20 Convergence of statistics of standard deviation of temperature overshoot. 96
Fig. 6-21 Probability distribution of temperature overshoot. 96
Fig. 6-22 Convergence of statistics of mean of time of temperature overshoot. 97
Fig. 6-23 Convergence of standard deviation of time of temperature overshoot. 97

Fig. 6-24 Probability distribution of time of temperature overshoot. 98

Fig. 7-1 Image analysis of ± 45º NCF. 101

Fig. 7-2 Probability distributions of fibre orientation of carbon fibre ± 45º NCF; upper side 103

Fig. 7-3 Probability distributions of fibre orientation of carbon fibre ± 45º NCF; lower side 103

Fig. 7-4 Directional autocorrelation of fibre orientation of carbon fibre ± 45º NCF.. 104

Fig. 7-5 Directional autocorrelation of simulated tows; 0º. 105

Fig. 7-6 Directional autocorrelation of simulated tows ±25 º. 106

Figure 7-7 Angle shape carbon fibre- epoxy subcomponent. 107

Fig. 7-8 prescribed temperature boundary condition, degree of cure at boundary. 108

Fig. 7-9 Residual stress of the outer layers in the fibre direction at the end of the process after release from the tool and final distortion multiplied by a factor of 50: (a) cross ply-deterministic model; (b) cross ply-stochastic model; (c) bias ply-deterministic model; (d) bias ply-stochastic model; (e) quasi-isotropic-deterministic model; (f) quasi-isotropic-stochastic model. 112

Fig. 7-10 Convergence of Monte Carlo simulation: mean of maximum longitudinal residual stress. 113

Fig. 7-11 Convergence of Monte Carlo simulation: standard deviation of maximum longitudinal residual stress. 114

Fig. 7-12 Probability distribution of maximum longitudinal residual stress. 114

Fig. 7-13 Convergence of Monte Carlo simulation: mean of corner angle of the lower flange. 116

Fig. 7-14 Convergence of Monte Carlo simulation: standard deviation of corner angle of the lower flange. 117

Fig. 7-15 Probability distribution of corner angle. 117

Fig. 7-16 Convergence of Monte Carlo simulation: mean of twist angle of the upper flange. 118

Fig. 7-17 Convergence of Monte Carlo simulation: standard deviation of twist angle of the upper flange. 118

Fig. 7-18 Probability distribution of twist angle of upper flange. 119

Figure 7-19 Sensitivity analysis results, standard deviation: (a) maximum longitudinal stress; (b) shape distortion. 122

Figure 7-20 Sensitivity analysis results, autocorrelation: (a) maximum longitudinal stress; (b) shape distortion. 124

Fig. 8-1 Schematic representation of methodology for modelling of boundary conditions uncertainty. 127

Fig. 8-2 Tool temperature as a function of time. 128

Fig. 8-3 Ambient temperature as a function of time. 129

Fig. 8-4 Surface heat transfer coefficient as a function of time. 129

Fig. 8-5 Autocorrelation as a function of time lag- Run 1; tool temperature. 131

Fig. 8-6 Autocorrelation as a function of time lag- Run 1; ambient temperature. 131

Fig. 8-7 Autocorrelation as a function of time lag- Run 1; surface heat transfer coefficient. 131

Fig. 8-8 Procedure of modelling of tool temperature uncertainty (a) cosinusoidal fit, (b) linear fit, (c) modelling of stationary process, (d) autocorrelation of simulated residuals over time. 134

Fig. 8-9 Procedure of modelling of ambient temperature uncertainty (a) linear fit, (b) modelling of stationary process, (c) autocorrelation of simulated residuals over time. 135

Fig. 8-10 Evolution of laminate degree of cure and temperature through the thickness of the laminate. Deterministic model results. 138

Fig. 8-11 Surface heat transfer coefficient variability over time; evolution of laminate degree of cure and temperature through the thickness of the laminate. Inset: detail during the first dwell. 140

Fig. 8-12 Tool temperature variability over time; evolution of laminate degree of cure and temperature through the thickness of the laminate. Inset: detail during the first dwell. 141

Fig. 8-13 Ambient temperature variability over time; evolution of laminate degree of cure and temperature through the thickness of the laminate. Inset: detail during the first dwell. 142

8-14 Probability distribution of cure time for boundary conditions and cure kinetics uncertainty. 144

8-15 Probability distribution of cure time for cure kinetics uncertainty only. 145

8-16 Probability distribution of cure time for ambient temperature uncertainty only. 145

8-17 Probability distribution of cure time for tool temperature uncertainty only. 146

8-18 Probability distribution of cure time for heat transfer coefficient uncertainty only. 146

8-19 Evolution of cure reaction rate as a function of time through the thickness of the laminate.. 147

Fig. 8-20 Probability distribution for cure time; surface heat transfer coefficient and tool temperature uncertainty.. 150

Fig. 8-21 Convergence of mean of cure time; surface heat transfer coefficient and tool temperature uncertainty.. 151

Fig. 8-22 Convergence of standard deviaiton of cure time; surface heat transfer coefficient and tool temperature uncertainty... 151

Notation

A) Symbols (in order of appearance)

v_f	Fibre volume fraction
N_{exp}	Number of experiments
K_1	Permeability in the longitudinal direction
K_2	Permeability in the transverse direction
H_T	Total heat of reaction
H_{exp}	Heat of reaction during dynamic cure
a_o	Initial degree of cure
H	Heat of reaction
t_1	Time the reaction starts
t_2	Time the reaction is completed
a	Degree of cure
$f(x, y)$	Pixel array of digital image
$F(u, v)$	Fourier spectrum
$r_\theta(x, y)$	Reference region array

$k_\theta(x, y)$	Kernel of reference region array
M	Size of reference region array
K	Size of pixel array
$\rho(\theta)$	Correlation
$\overline{r_\theta}$	Average of reference region array
$\bar{f}$	Average of pixel array
$E(\theta)$	Radial energy in polar coordinates
$\dot{Q}$	Heat flux
HF	Heat flux sensor output
CM	Heat flux sensor calibration multiplier
TCF	Heat flux sensor temperature compensation factor
h	Surface heat transfer coefficient
T_s	Surface temperature
c_p	Specific heat capacity
r	Spatial coordinate
t	Time

$\boldsymbol{K}$	Thermal conductivity tensor
ρ	Density
$\boldsymbol{\sigma}$	Stress tensor
$\boldsymbol{Q}$	Stiffness matrix
$\boldsymbol{\varepsilon}$	Strain tensor
C^S	Cure shrinkage coefficient tensor
a^{th}	Thermal expansion coefficient tensor
n	Vector normal to the surface
T_∞	Fluid temperature
u_x	Displacement in x direction
u_y	Displacement in y direction
u_y	Displacement in z direction
T_g	Glass transition temperature
T_{go}	Glass transition temperature for uncured material
$T_{g\infty}$	Glass transition temperature for fully cure material
λ	Glass transition temperature model fitting constant

k_1	Reaction rate constant
k_2	Reaction rate constant
n_1	Reaction order
n_2	Reaction order
m	Reaction order
$k_{1,c}$	Chemical reaction rate constant
$k_{2,c}$	Chemical reaction rate constant
k_d	Diffusion reaction rate constant
A_D	Pre-exponential factor of diffusion
A_1	Pre-exponential factor
A_2	Pre-exponential factor
E_D	Activation energy of diffusion
R	Universal gas constant
b	Cure kinetics constant
f	Equilibrium free volume
E_1	Activation energy

E_2	Activation energy
w	Cure kinetics constant
g	Cure kinetics constant
w_f	Weight fraction
c_{pf}	Fibre specific heat capacity
c_{pr}	Resin specific heat capacity
A_{rcp}	Resin specific heat capacity model constant
B_{rcp}	Resin specific heat capacity model constant
Δ_{rcp}	Resin specific heat capacity model constant
si	Resin specific heat capacity model constant
C_{rcp}	Resin specific heat capacity model constant
K_{11}	Thermal conductivity in the longitudinal direction
K_{22}	Thermal conductivity in the transverse direction
K_{33}	Thermal conductivity in the transverse direction
K_{lf}	Fibre thermal conductivity in the transverse direction

K_r	Resin thermal conductivity
K_{tf}	Fibre thermal conductivity in the longitudinal direction
A_{lf}	Fibre thermal conductivity model constant
B_{lf}	Fibre thermal conductivity model constant
B_{tf}	Fibre thermal conductivity model constant
a_{kr}	Resin thermal conductivity model coefficient
b_{kr}	Resin thermal conductivity model coefficient
c_{kr}	Resin thermal conductivity model coefficient
d_{kr}	Resin thermal conductivity model coefficient
e_{kr}	Resin thermal conductivity model coefficient
E_{11}	Young modulus in the longitudinal direction
E_r	Resin Young modulus
E_{lf}	Fibre Young modulus in the longitudinal direction
E_{22}	Young modulus in the transverse direction
E_{33}	Young modulus in the transverse direction
E_{t_f}	Fibre Young modulus in the transverse direction

G_{12}	Shear modulus
G_r	Resin shear modulus
G_{13}	Shear modulus
G_{12f}	Fibre shear modulus
G_{23}	Shear modulus
G_{23f}	Fibre shear modulus
ν_{12}	Poisson’s ratio
ν_{12f}	Fibre Poisson’s ratio
ν_r	Resin Poisson’s ratio
ν_{13}	Poisson’s ratio
ν_{23}	Poisson’s ratio
E_{r_L}	Resin Young modulus in liquid/rubber state
E_{r_G}	Resin Young modulus in glassy state
ν_{r_L}	Resin Poisson’s ratio in liquid/rubber state
ν_{r_G}	Resin Poisson’s ratio in glassy state

ν_r	Resin Poisson’s ratio
G_r	Resin shear modulus
C_{11}^{S}	Cure shrinkage coefficient in the longitudinal direction
C_{22}^{S}	Cure shrinkage coefficient in the transverse direction
C_{33}^{S}	Cure shrinkage coefficient in the transverse direction
V_r^{S}	Resin volumetric shrinkage
$V_r^{S\infty}$	Maximum resin volumetric shrinkage
ε_{ij}^{S}	Cure shrinkage strain components
ε_r^{S}	Resin incremental cure shrinkage strain
a_{11}^{th}	Thermal expansion coefficient in the longitudinal direction
a_r	Resin thermal expansion coefficient
a_{lf}	Longitudinal fibre thermal expansion coefficient
a_{22}^{th}	Thermal expansion coefficient in the transverse direction
a_{33}^{th}	Thermal expansion coefficient in the transverse direction
a_{tf}	Transverse fibre thermal expansion coefficient

a_r	Resin thermal expansion coefficient
a_{r_G}	Resin thermal expansion coefficient in the glassy state
a_{r_L}	Resin thermal expansion coefficient in the liquid/rubber state
$A^i_{a_{lf}}$	Longitudinal fibre thermal expansion coefficient parameter
$A^i_{a_{tf}}$	Transverse fibre thermal expansion coefficient parameter
a^{th}_{ij}	Thermal expansion coefficient components
ε^{th}_{ij}	Thermal strain
T_{inc}	Temperature increment
X	Random series of observations
μ_r	Mean value of random series of observations
σ_r	Standard deviation of random series of observations
y	Set of standard normal variables
S	One-dimensional mean reverting stochastic process
λ	Speed of reversion of mean reverting stochastic process
σ	Volatility of mean reverting stochastic process

W_t	Brownian motion
$C(x,y)$	Autocovariance function of two-dimensional stochastic field
σ_c	Standard deviation of two-dimensional stochastic field
b_x	Correlation length in x direction
b_y	Correlation length in y direction
Σ	Covariance matrix
L	Cholesky root
V	Cholesky factorisation realisations
Y	Vector of standard normal variables
$V(x,y)$	Two-dimensional random field
$S(k_x,k_y)$	Spectral density function of two-dimensional random field
k_x	Wave numbers over the frequency domain
k_y	Wave numbers over the frequency domain
$G(k_x,k_y)$	Bi-quadrant power spectral density function
$u(k_x,k_y)$	Gaussian two- dimensional stochastic field
$v(k_x,k_y)$	Gaussian two- dimensional stochastic field

N_x	Interval over the frequency domain
N_y	Interval over the frequency domain
k_{xu}	Cut-off wave frequency
k_{yu}	Cut-off wave frequency
$\phi^{(i)}_{n_x n_y}$	Set of uniformly distributed random phase angles
λ_i	Eigenvalues
$f_i(x,y)$	Eigenfunctions
δ_{ij}	Kronecker- delta function
N_{MC}	Number of Monte Carlo realisations
Γ_p	Polynomial chaos of order p
$\left\{\xi_{i_k}\right\}_{k=1}^{M}$	Set of standard normal variables
$H_i(\xi)$	Hermite polynomial of order i
Ψ	Stochastic variable
$\Phi^*(\psi)$	Cumulative distribution of stochastic variable Ψ
$\Phi(\psi)$	Cumulative function of stochastic variable Ψ

$D_N(\psi)$	Difference between observed and expected cumulative distribution
$D(\psi)$	Kolmogorov- Smirnov critical value
$\frac{\widehat{da}}{dt}_{max}$	Surrogate model for maximum cure reaction rate
$\hat{T}_{ex}$	Surrogate model for temperature overshoot
$\hat{t}_{ex}$	Surrogate model for time of temperature overshoot
A_h	Level of surface heat transfer coefficient
B_h	Volatility of surface heat transfer coefficient
T_T	Tool temperature
A_T	Level of tool temperature
B_T	Slope of linear fit of tool temperature
C_T	Amplitude of cosinusoidal fit of tool temperature
ω_T	Frequency of cosinusoidal fit of tool temperature
S_T	Mean reverting stochastic process of tool temperature residuals
T_A	Ambient temperature
A_A	Level of ambient temperature

B_A	Slope of linear fit of ambient temperature
S_A	Mean reverting stochastic process of ambient temperature residuals
T_1	Temperature of the first dwell of standard cure profile for RTM6
T_2	Temperature of the first dwell of standard cure profile for RTM6

B) Abbreviations (in order of appearance)

MC	Monte Carlo scheme
SSFEM	Spectral stochastic finite element method
K-L	Karhunen–Loève expansion
PCM	Probabilistic Collocation Method
RTM	Resin transfer moulding
DSC	Differential Scanning Calorimetry
DMA	Dynamic Mechanical Analysis
NCF	Non- crimp fabric
FFT	Fast Fourier Transform
OU	Ornstein-Uhlenbeck process

1. Introduction

1.1 Motivation and contribution

The basis for the improved performance of composite materials is the high specific strength (strength to density ratio) and specific stiffness (modulus to density ratio) [1]. A composite component is significantly lighter than its metallic counterpart for a given stiffness and strength. Apart from favouring weight savings, composites provide higher corrosion/wear and fatigue resistance. However, the application of composite materials is often limited by cost implications due to their complex manufacturing. Modern composite materials were first introduced in the late 1950's and received attention by the aerospace industry, especially the military sector, due to their high specific properties and the relative inelasticity of this sector to costs in this period. In the late 1960's, the F-4 (General Dynamics) used boron epoxy rudders. Some years later, the F-14 (US Navy) and F-15 (US Air Force) used boron-epoxy empennages [2]. In the 1980's composites replaced aluminium alloys in the manufacturing of low cost lightweight airframes. In addition, several nacelle and engine components were manufactured using composite materials. As time passed, composites broadened gradually their application playing a significant role in many crucial industry sectors such as: commercial/military aviation, automotive, construction, marine, and sports. Nowadays, several large aircrafts use composite materials, consuming significantly lower amounts of fuel. For instance, the Boeing 787 Dreamliner uses approximately 50 % composites by weight [3], consuming 20% less fuel than its predecessor 767. Airbus A350 is the company's first airliner with both the wings and fuselage made primarily from composite materials (53% of its total weight is manufactured by composites) [3]. The A350 first flew in 2013 and it is expected to consume less fuel than the Dreamliner, reducing the operating costs by about 8%. (Figure 1-1). However, the use of composites in the aerospace sector is still maturing and further improvements are required in process design related to manufacturing costs and sustainability, for the market to reach its full potential in the future.

Fig. 1-1 Manufacturing of fuselage panels for the A350 XWB (© Premium AEROTEC GmbH.) [3].

Fabrication of thermosetting composites is a complex procedure, involving sub-processes of different physics such as forming, consolidation/impregnation and curing. Each of the manufacturing steps influences subsequent manufacturing sub-processes, creating strong interdependencies between process parameters and properties of the product. Process monitoring, automation and process optimisation have become crucial objectives of research as a result of the adoption of advanced composites as the main material of choice for large aero-structures. To this end, process simulation models have received a great deal of attention in the last decades. Most of these models are deterministic, treating all process parameters as constants or prescribed. However, in reality the manufacturing processes of composites involve many uncertainties. Some research on the effects of uncertainties in composite manufacturing has been carried out; however, in its great majority has focused on fabric geometrical variability and its effects on the impregnation process. On the contrary, very limited data and results exist concerning variability during the cure step, whilst the parameters introducing uncertainty into the cure step have not been explicitly characterised and evaluated. In particular, several input parameters that introduce variability to the process have not been investigated explicitly, whilst a limited part of the overall problem has been considered based on hypothetical scenarios for the extend and type of variability rather than experimental data. Overall, stochastic simulation of the cure has received limited attention. Consequently, a significant gap exists between real phenomena and cure simulation models.

Cure is a global step, i.e. it is a mandatory step in all fibre reinforced thermosetting composites manufacturing routes. During the cure process external heat is supplied initiating cross – linking chemical reactions in the matrix leading to the solidification of the material. The cure is of crucial importance affecting the mechanical and physical properties of the product, including part quality, and governing a range of potential process defects such as under-curing, residual stresses, shape distortion and large exotherms. Thus, a fundamental understanding of the real phenomena is critical for the design of the manufacturing process. The development and implementation of an integrated stochastic simulation scheme would allow incorporation of variability in process design/optimisation to address robustness – performance trade-offs to contribute to the development of more efficient process cycles in terms of cost and time.

1.2 Aim and objectives

The aim of this project is to develop a stochastic cure simulation methodology capable of predicting the influence of material property and process parameter uncertainty on the variability of the outcome of high performance application cure processes. To achieve this, the following objectives have to be met:

- Development and implementation of an efficient cure simulation model.
- Quantification of input variable uncertainty as follows:
  - Cure kinetics uncertainty.
  - Fibre misalignment in Non-Crimp Fabrics (NCF).
  - Boundary conditions uncertainty including prescribed temperature, ambient temperature and surface heat transfer coefficient.
- Identification of stochastic parameters that induce significant process variability using sensitivity analysis.
- Statistical characterisation of the stochastic parameters and development of the associated models.
- Development and implementation of a stochastic cure simulation model.
- Quantification of process outcome variability with respect to:
  - Temperature overshoot.
  - Cure time.
  - Residual stresses formation.

    - Shape distortion.
  - Evaluation of stochastic simulation methodology efficiency.

1.3 Project setting

The present study is part of a multi-institution research project supported by the EPSRC Centre for Innovative Manufacturing in Composites (CIMComp). This Centre involves four academic institutions including Cranfield University, eight industrial partners, an Industrial Doctoral Centre (IDC) and four Technology Centres and aims at the creation of an innovative research base for fundamental understanding and development of composites manufacturing by focusing on the development of novel composites manufacturing processes based on efficiency, sustainability, short cycle times and low operational cost. The activity is currently divided in the following core projects:

- Multi-scale Modelling to Predict Defect Formation During Resin Infusion.
- Novel approaches to the manufacture of complex geometrics from broad goods.
- Structural Joints using Novel Embedded Inserts.
- Innovative Multi-material and Multi-architecture Preforms.
- Compression Moulding of Multi-Architecture Composites (CMMC).
- Defect Generation Mechanisms in Thick and Variable Thickness Composite Parts (DefGen).

The present study is part of the first core project. The partners of this project are Nottingham University, University of Bristol and Cranfield University, Rolls-Royce, ESI, LMAT, Vestas and Airbus. It focuses on the development and validation of a multi-scale approach to predict defect formation and variability in manufacturing using resin infusion.

1.4 Thesis road map

The main body of this study is divided as follows:

- Chapter 2 reviews the state of the art of uncertainty in composite manufacturing. This chapter summarises experimental and simulation results regarding the quantification and influence of material properties and process parameters uncertainty on the process outcome and on process-induced defects.

- Chapter 3 reports the experimental methodology and details of materials used in this study.
- Chapter 4 describes the cure simulation model methodology applied and reports the constitutive material models.
- Chapter 5 presents the stochastic simulation methodology adopted for modelling of input parameters variability.
- Chapter 6 presents results on the influence of cure kinetics uncertainty on composites cure. Two case studies are demonstrated; stochastic cure simulation of neat epoxy resin (cure kinetics only), and stochastic cure simulation of a thick carbon fibre-epoxy flat panel where heat transfer effects are considered.
- Chapter 7 focuses on the effect of fibre misalignment on residual stresses formation and shape distortion occurring during the cure process. In particular, the cure of an angle shape carbon fibre-epoxy laminate subcomponent with three different lay-up sequences is considered.
- Chapter 8 presents the influence of boundary conditions uncertainty on the heat transfer phenomena occurring during the cure. The contributions of the all potential stochastic parameters are considered and the most significant factors are identified. The development is applied to the simulation of the cure of a thin carbon fibre-epoxy flat panel.

Chapters 9-11 present an overall discussion on the outcomes of this work, conclusions and suggestions for areas of further development and investigation on variability in composites manufacturing.

2. Uncertainty in the manufacturing of fibrous thermosetting composites

2.1 Introduction

In this chapter, experimental and numerical results concerning the statistical characterisation and the influence of inputs variability on the main steps of composites manufacturing including process-induced defects are presented and analysed. The manufacturing process of composite materials involves many uncertainties which can result in a considerable amount of scrap associated with significant cost and environmental implications. Furthermore, the existence of defects generated due to variability can compromise the performance of composite components, leading to the use of more conservative designs that do not fully exploit the performance and environmental opportunities offered by composites. These uncertainties can be summarised as follows [4,5]:

(i) Fibre architecture variations which are usually generated during production, handling or storage of pre-pregs, dry textiles and preforms.

(ii) Matrix material uncertainties caused by variations in storage conditions or uncertainties in resin composition and formulation.

(iii) Variations in environmental parameters and process conditions.

Fibre heterogeneity can significantly affect the forming/draping step [6], as well as introduce permeability and thermal property variability affecting the filling and curing steps of processing. Furthermore, fibre architecture governs the structural performance of components, with local variability playing a critical role in non-linear phenomena such as failure and damage. Matrix material uncertainties influence the filling and curing stages which in turn influence the quality of the final product. Variations in process parameters may affect all manufacturing steps and consequently the quality of the component. A design approach that would take these effects into account explicitly would need to be based on stochastic simulations of composites manufacturing to allow quantification of process outcome variability as a function of material selection and process parameter definition decisions made at an early stage.

Stochastic simulation involves four main steps (Fig. 2-1): a) quantification of the input variable uncertainties (uncertainty quantification); b) development of a stochastic model representing the variability of uncertain parameters and their cross correlation (stochastic model); c) implementation of a model that propagates uncertainty through a deterministic process model (propagator), d) quantification of the output parameters uncertainty [7,8]. The input variables are considered to be either time independent random parameters, which can be described by multivariate probability distributions or random fields, or time dependent stochastic processes described by stochastic differential equations. The random fields or stochastic processes are uncovered by carrying out relevant experiments.

The aim of the present chapter is to summarise the state of the art on experimental and stochastic simulation methodologies and results focusing on statistical characterisation and the influence of input variability on the main steps of composites manufacturing including process-induced defects, as well as to highlight the interdependencies between the process parameters. Uncertainty introduced by experimental methods and modelling practices is also included.

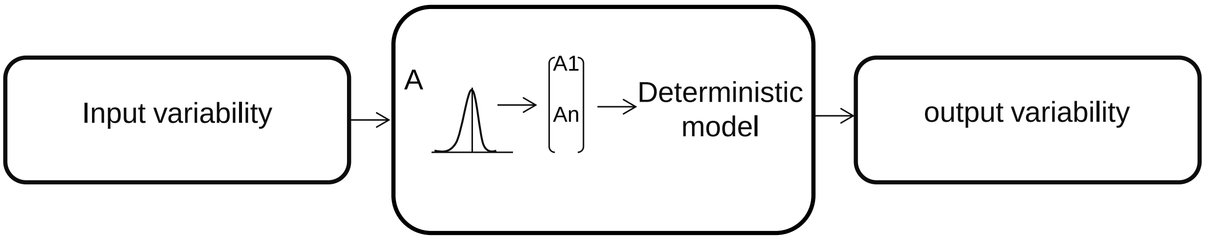

Fig. 2-1 Schematic representation of stochastic simulation.

2.2 Stochastic simulation methods

Stochastic simulation methods can be divided into two categories; intrusive and non-intrusive. Intrusive techniques involve reformulation of the main model equations while non-intrusive techniques treat the main model as an independent model. The most common non-intrusive method is the Monte Carlo scheme (MC), which is a sampling technique used to generate random samples of input variables values from their respective statistical distributions [7]. Since random sampling is used, a quite large number of the deterministic main model runs is usually required to ensure convergence and accuracy, leading to high computational cost, especially in the case of complex and multi-dimensional stochastic problems [9]. The Spectral Stochastic Finite Element (SSFEM) method is the most common intrusive technique [10]. It uses the Karhunen–Loève (K–L) expansion to discretise the input random field and the polynomial chaos expansion to represent the output variables using a set of orthogonal functions [10]. The coefficients of the polynomial chaos expansion are calculated using the probabilistic Galerkin approach. The domain of the solution incorporates the probability space resulting in a system of equations significantly larger than that of the deterministic problem, with the associated increase in computational costs [9]. The Probabilistic Collocation method (PCM) offers an intermediate solution between Monte Carlo and stochastic finite elements. This method is similar to the SSFEM using both the K–L expansion and the polynomial chaos expansion to represent the input and output random fields, respectively. However, the unknown polynomial chaos coefficients are calculated by the probabilistic collocation approach, which is a weighting technique for minimising residuals. The collocation points are the roots of the next higher order orthogonal polynomial for each stochastic parameter and are chosen so that the residuals between the polynomial chaos expansions and model outputs approach zero, implying that the collocation points are selected from regions of higher probability. Consequently, a system of linear equations is obtained for every output parameter. Using this sampling method, no reformulation of the deterministic model is required, which is solved several times for each collocation point. This of course has significant benefits in terms of computational efficiency when the number of stochastic components is relatively low [9].

The capabilities of the collocation method have been demonstrated in the context of composite manufacturing in the case of simulation of RTM filling. The results indicated the capability of the technique and its significant benefits compared to Monte Carlo [11]. More details concerning the SSFEM and the probabilistic collocation method can be found in [9,10].

2.3 Variability of dry textiles and pre-pregs

Variability is present in all forms of textile reinforcements including pre-pregs and dry textiles [12]. Variability in as supplied-dry reinforcements and pre-pregs is associated with tow waviness (Fig. 2-2), tow size and shape variations, distribution of fibres inside the tows, resin content variations and is generated during production, handling or storage [12-16]. For instance, the alignment and stiffness characteristics of the rollers used during the production of pre-pregs, can sometimes cause resin content variations, or the way pre-pregs are wrapped on to a drum for storage can cause wrinkles which in turn may result in considerable tow misalignment [12,15]. Geometrical variability of tows spreads to adjacent locations due to friction forces at tow crossovers (woven textiles) and fibre continuity [13] resulting in spatially correlated random fields of the uncertain variables. Fibre orientation variability can be described by a normal distribution [13,17-20] combined with strong spatial autocorrelation spread over several unit cells of the textile [13,21,22]. An experimental investigation of the internal geometry of 3D woven textiles using micro-computed tomography underlined the importance of variability in dry reinforcements [23]. The coefficient of variation of the dimensions of the tows and the inter-tow spacing reaches values of 16 and 6%, respectively. Experimental results on the internal geometry of non-crimp woven fabrics showed variability in the range of 4-8% for the tows dimensions, of 3-4% for tow spacing [24]. These sources of variation exist in the reinforcement in its as received state, setting the minimum level of uncertainty in all subsequent steps of composite manufacturing.

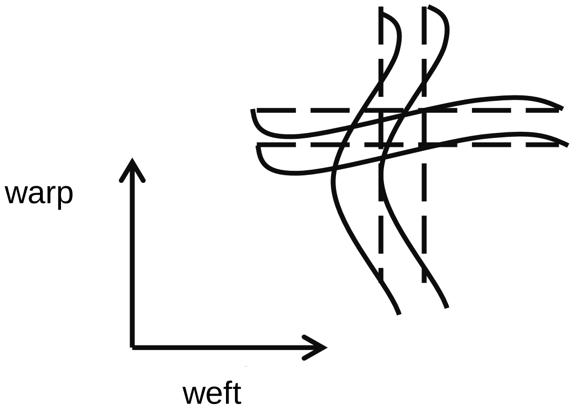

Fig. 2-2 Tow waviness.

2.4 Uncertainty in forming/draping

The forming/draping stage of the manufacturing process causes significant shear deformation in the case of doubly curved components [25]. There are two main mechanisms of shear deformation during the forming/draping step; scissoring i.e. the change in the inter-fibre angle, and inter-fibre sliding which occurs in processes involving extremely high deformations [26,27]. These phenomena can lead to wrinkles and can be eliminated using localised stitching [28]. Shear deformation has significant impact on local fibre volume fraction and thickness; regions of higher deformation present an increase in fibre volume fraction or thickness depending on whether the tooling used is rigid or not [27]. Pre-pregs and dry textiles are not perfectly aligned therefore additional localised buckling and wrinkling may occur affecting the forming behaviour of the material [29]. Stochastic simulation shows that tow orientation uncertainties can cause significant variations in the outcome of the forming of woven composites, with coefficients of variation of minimum and average wrinkling strain in the range of 10-20% [13]. Initial tow waviness of as-received unidirectional pre-pregs may have beneficial effects during draping, since additional waviness can be introduced instead of tow misalignment, which may eliminate the formation of wrinkles [15]. Apart from the initial fibre angle variations, boundary conditions uncertainty, such as variations in the blank holder force may also influence the forming step [30]. Furthermore, the fact that there is a large number of ways to drape over a complex geometry implies additional uncertainty of the process [12,15]. In general the manifestation of variability is more pronounced when manual work is involved. Mechanical conditioning is considered to be a way to increase repeatability and to reduce variability since the tow tensions due to weaving can be balanced [25]. However, it is very difficult to apply mechanical conditioning in industrial applications unless handling is adapted for this purpose.

Therefore, the shear behaviour of reinforcements can show significant variations from part to part. These effects can influence a wide variety of parameters such as the permeability, the development of residual stresses during the curing stage, dimensional accuracy, and the mechanical properties of the final part indicating the presence of strong interdependencies of various sources of variability in composite manufacturing [12,26-28].

2.5 Uncertainty during impregnation/consolidation

Permeability of dry reinforcement is the key parameter controlling the impregnation step in liquid composite moulding processes. Significant amount of research has been carried out concerning permeability evaluation to allow consideration of process issues such as formation of dry spots and voids; extended impregnation cycles, uneven impregnation and resin rich pockets [31]. Preform architecture variability due to different handling and storage conditions or shear deformations during the forming/draping stage, nesting effects during lay-up, low resistance channels along the preform causing macroscopic and microscopic voids, and random experimental errors result in considerable permeability variations [14,32-34]. Other sources of uncertainty in the impregnation stage can be resin viscosity variations, foreign material inclusion during impregnation, preform volume fraction variations, as well as accidental misplacement of the preform in the mould [8,35]. Experimental and simulation results using non –crimp fabrics have shown that there is a linear relationship between the coefficient of variation of permeability and the coefficient of variation of fibre volume fraction [17,36]. Several experimental and simulation studies have outlined the stochastic nature of permeability. Relative standard deviations up to 20% were observed during permeability measurements [18,32,33,37-42], while according to other results permeability relative standard deviation can reach values up to 30% [17] (Table 2-1). The high scatter observed in [17] is probably due to the small number of experiments compared to the other studies. Nesting is one of the primary reasons for this large scatter in permeability [33]. In addition, experimental results have indicated that the anisotropy ratio of in-plane permeability, which dictates the filling pattern and thus is of crucial importance for mould design, can also show strong variability following a lognormal distribution [33]. Different anisotropy distributions among different textiles are observed, even when the distribution of the principal permeability values is similar [43]. For instance, a plain weave fabric shows the largest scatter in anisotropy, whereas a twill weave shows the smallest. This implies that the principal permeability values may show strong correlation in some preforms, whereas in other materials little or no correlation may be observed [43]. Preforms with strong correlation and small anisotropy scatter, are expected to be manufactured more consistently. The flow pattern can considerably vary even for configurations of the same porosity, implying that the latter alone cannot be used to predict permeability [44]. Furthermore, for porosities in the range of 0.45-0.7, transverse permeability decreases as fibre heterogeneity increases [44]. This phenomenon is attributed to the formation of narrow gaps between the fibres which lead to permeability reduction. Permeability can show considerable variations at the micro-scale; inside the fibre bundles [45,46]. Transverse fibre bundles permeability tends to be lower in the case of non-uniformly distributed filaments than for fibre bundles with uniform filament arrangements, whilst fibre bundle permeability in the axial direction tends to be higher [46]. These findings indicate that permeability should be described as a stochastic variable and thus a large number of experiments are required to measure it properly [43]. According to Hoes et al. [33], at least 20 experiments are required to have a proper estimate of the mean value, whereas at least 30 experiments are required to have a proper estimate of the standard deviation. Similarly with tow orientation, it has been shown that global permeability values can be described by a normal distribution [17-20]. However, simulation results indicated that permeability at the mesoscale (unit cell size) cannot be represented by a normal distribution [36]. This was also observed in the case of a random mat [47].

Table 2-1 Permeability measurements for two plain weave glass fibre fabrics; plain weave glass 1 [17], plain weave glass fabric 2 [33].

Material	Dimensions	v_f	N_{exp}	K_1 (10^{-10} m^2)	K_2 (10^{-10} m^2)
Plain weave glass fibre 1	200mm (circular)	53%	19	1.24±0.36 (±29.2%)	0.65±0.167 (±25.7%)
Plain weave glass fibre 2	300x300mm	41.7%	85	1.79±0.4 (±22.3%)	1.44±0.29 (±20%)

2.5.1 Fabric heterogeneity effects

As mentioned in section 2.4, during the draping step the fabric is subjected to significant shear deformation intensifying the already existing geometrical heterogeneities. As a result, the draping step affects significantly the local permeability values and thus the flow rate and the injection pressure by altering the permeability anisotropy ratio, fibre volume fraction and porosity distribution in the textile [27,48,49]. The permeability decreases in a non-linear manner with increasing fibre volume fraction [27,32]. Consequently, one would expect that shear deformation caused during draping would always reduce the local permeability values in the regions of high shear. However, flow visualisation results indicate that in some cases high volume fraction regions caused by shear deformation during draping, may result in higher permeability values. The effect of draping on permeability is characterised by three competing effects; the reduction of local permeability due to higher fibre volume fraction in the regions of high shear, reorientation of fibres due to shear leading to reorientation of the permeability principal axes, and the fact that a smaller amount of resin is required to saturate the textile in the regions of high volume fraction. Therefore, although fibre volume fraction is higher at these regions, the flow front can be faster [27]. Similar results are found in radial injection experiments, in which the permeability in the fibre direction was found to increase slightly with increasing shear up to a maximum, followed by a reduction, whereas transverse permeability was found to decrease continuously as the shear angle increases [48]. Consequently, when fibre volume fraction effects dominate, the permeability is locally reduced due to shear deformation, whilst the opposite effect occurs when the influence of the reorientation of the permeability principal axes is more pronounced.

While preform permeability is dependent on fibre distribution at microscopic level, i.e. within fibre tows and bundles, [45] as well as at macroscopic level, i.e. fibre angle uncertainties, the flow front shape is locally determined by the size of the unit cell [4,5,17]. Fibre architecture variability at macroscopic level can be described by the fibre angle variation, and the fibre-void distribution [5,17]. Since geometrical uncertainties are spread to adjacent locations in the material, the in plane fibre spacing can be modelled by continuous random fields based on a spectral expansion [4]. Stochastic simulation based on this approach as well as experimental results, showed that although the global permeability distribution is governed by local permeability variations [50] (global permeability is the spatial harmonic mean of the local permeability), global and local permeability uncertainties should be differentiated [4,17]. Fibre-void distribution heterogeneities imply high angle variations, which consequently result in higher local permeability variations. The global permeability variations in turn increase rapidly with fibre angle variations, until they reach a maximum. Thus, there is a critical point beyond which global permeability variations start to decrease. Nonetheless the local variations are high, at the global scale; the textile appears to be more uniform leading to lower global variances [17]. In the case of smaller moulds the effect of fibre misalignment at the mesoscale, whether large or small is dominant. On the other hand, as the mould dimensions increase, these local inhomogeneities tend to cancel each other out and the textile appears to be more uniform leading to lower global permeability variations [17,36]. This suggests that the global permeability distribution is governed by the mould dimensions; larger moulds lead to lower global permeability variations [36].

2.5.2 Nesting effects

Nesting during the lay-up process is governed by both mechanical and geometric phenomena, and it is of crucial importance as it affects the permeability, the thermal conductivity and the mechanical behaviour of the composite. In general, nesting affects the laminate thickness, the fibre volume fraction and the pore pattern. Therefore, nesting can introduce significant spatial scatter in laminate properties at different locations over a composite part, as well as considerable batch to batch variability [51-55]. Compressibility studies have clearly indicated that irrespective of fabric type, for a given pressure, the thickness per layer decreases due to nesting [51-56]. However, in the results presented in [57], the thickness per layer increased with increasing number of lamina layers, as a result of friction between the layers which prevents the occurrence of nesting.

Several experimental and computational studies have identified the importance of nesting on permeability variation, implying that nesting variability is the main reason for permeability scatter. Simulations investigating the effect of nesting on the permeability of plain weave fabrics showed that permeability values can vary by an order of magnitude between maximum and zero nesting conditions [58,59]. Experimental results using a large number of samples demonstrate a high permeability variation; the highest measured value can be three times the lowest one [19]. The same order of scatter can be identified in local permeability calculations using the pore network technique [60].

Nesting can show considerable scatter associated with several parameters. It has been shown that shear deformation has a great impact on nesting. In particular, a textile is less prone to nesting if it is subjected to shear deformation [61]. Consequently, at higher shear angles the scatter in thickness per layer is reduced.

Furthermore, nesting can be confined by increasing the tightness of the textile. When the fibre tows are placed tighter, the “hills and valleys” of fibre tows are steeper and nesting is more difficult to occur. Inter-tow spacing also affects nesting. The textile tightness decreases as the inter-tow spacing increases, and hence nesting is less pronounced leading to lower thickness variation. Therefore, tow angle variations influence indirectly nesting, as they are associated with inter-tow spacing. In the case of non-crimp fabrics the stitching pattern dictates nesting [61]. Nesting is also influenced by the tool properties, such as mould stiffness and surface condition, as well as the compression force during consolidation. These effects have not been investigated so far.

Another phenomenon associated with compressibility and nesting effects is the formation of resin rich zones. Resin rich zones are usually formed in the gaps between the internal mould surface and the textile preform, as well as in the fabric, around stiches [62]. Shifting of the preform during consolidation may also result in resin rich pockets [12]. In the case of curved parts, resin rich zones may be formed due to the fact that the preform tends to fit tightly around the corner regions [62]. Furthermore, nesting of individual fibre tows may cause local resin rich zones in the regions between the tows. As a result, resin rich zones can lead to additional out of plane tow misalignment having detrimental effects on the mechanical properties of the final part [12]. The formation of resin rich pockets is difficult to predict, and consequently introduces considerable variability in the process. The magnitude of the gap between the mould inner surface and the preform is a function of the friction between the mould and the preform as well as of the compressibility of the preform [62]. This implies that uncertainties on tooling properties such as friction coefficient due to repetitive usage or variations on the properties and the amount of release agent may influence the formation of resin rich pockets.

2.5.3 Edge effects

Race tracking is a source of preform permeability uncertainty during liquid moulding processes [63]. Race tracking is inevitable in industrial applications and refers to edge effects caused by imperfect fit between the preform and the edges of the mould

[64-66]. As a result, low flow resistance channels are formed along the edges, where the resin flow front moves faster and the local permeability is considerably higher [64,65]. This phenomenon introduces significant variability since it is only dependent on how the textile is cut and placed into the mould cavity [65]. A statistical study showed that the permeability values caused by race-tracking can be described by a Weibull distribution [64]. Therefore, in the case of one-dimensional permeability experiments where race tracking is likely, the Weibull distribution can be used to characterise permeability instead of the conventional normal distribution [67].

2.5.4 Void formation

Liquid composite moulding processes often suffer from flow-induced voids leading to poor part quality. Entrapped voids can influence the stress distribution in the part and lead to stress concentrations, which can eventually result in local failure. Experimental studies have shown that for a 1% increase in void content, the flexural strength, flexural modulus, and inter-laminar shear strength can decrease more than 5% [68-70]. Void formation also reduces the fatigue strength and durability of the material and makes it more susceptible to environmental conditioning and moisture absorption. Due to these detrimental effects, the void content should be minimised as much as possible. The mechanisms leading to entrapped voids are associated with preferential flow channels arising from preform heterogeneities which in turn lead to permeability variations [71]. Thus, void formation can be considered to be a directional phenomenon [72]. However, in some cases void formation is not related to resin flow, and can be attributed to initial resin air content, release agent evaporation and volatiles formed by the reaction products during cure [71]. These mechanisms are more pronounced in autoclave processes [73].

Two distinct flow patterns occur during resin impregnation due to fibre architecture heterogeneities: viscous flow, which is pressure driven and dominates in macro-pores and capillary flow which is dominant in micro-pores due to capillary forces [73,74]. The flow front is usually uneven between these two mechanisms, leading to the formation of voids. The viscous flow leads the capillary flow at high injection rates, resulting in microscopic intra-tow voids caused by fingering, whereas, at low injection rates, the capillary flow is dominant causing macroscopic inter-tow voids [74]. These phenomena are usually described by the capillary number expressed as the ratio between viscous and capillary forces [71]. The size and shape of intra-tow micro-voids are strongly affected by geometric heterogeneities inside the fibre tows as well as non-structural stitches [64]. Race-tracking can sometimes lead to macro-voids generated when flow patterns reach the vent locations prior to full saturation [65].

Image analysis of glass/epoxy composites with different volume fractions highlighted the importance of fibre volume fraction on void formation in resin transfer moulding processes [74]. Higher fibre volume fractions result in lower void content and void areal density. This behaviour is attributed to higher injection pressures, more uniform fibre architecture as well as lower matrix volume fraction. Three distinct types of voids can be identified; voids in resin rich areas, intra-tow voids, and inter-tow voids. Increasing the fibre volume fraction decreases the contribution of resin voids to total void content and total void areal density. On the contrary, the contribution of intra-tow voids to total void areal density increases by increasing fibre volume fraction, while the contribution to total void content is reduced, implying that the size of intra-tow voids decreases at higher volume fractions. The contribution of voids located next to fibre bundles does not show any clear dependence on fibre volume fraction. Fibre volume fraction also affects the distribution of voids along the radius of curved parts of components [74].

The size and location of voids can vary significantly. In general, voids can be classified to spherical and bigger random-shaped voids [74]. Randomly shaped voids have more severe effects on mechanical performance since they can cause premature crack initiation. The content and the aerial density of random voids decrease at higher volume fractions [74]. Consequently, the probability of premature crack initiation is reduced by increasing the fibre volume fraction. The spatial void distribution is also an important parameter since it dictates the overall performance of the final part [71]. An uneven void content distribution can arise from inter-layer space variations or space variations between the preform and the mould [71]. Moreover, the fibre content also influences spatial void distribution. At higher fibre volume fractions, formation mechanisms can be affected since the elevated injection pressure can cause considerable void shrinkage and void transportation may be facilitated towards the exit vent locations [74]. Thus, at high fibre volume fractions both preform heterogeneity and void mobility mechanisms affect spatial void distribution.

Nesting effects play an important role on void formation [20,75]. Both the magnitude and variability of dry spot content are strongly influenced by nesting and the distribution layer permeability in the case of vacuum assisted resin transfer moulding processes. Increasing the preform thickness enhances dry spot formation and its variability within the textile [75]. High scatter in by-pass paths permeability and high values of distribution layer permeability result in high scatter in dry spot content. This high scatter can be reduced by lowering the distribution layer permeability. High dry spot content variation implies that the formation of dry spots depends on the spatial distribution of the by-pass paths permeability.

2.6 Uncertainty in composites cure

The cure process is a complex thermo-mechanical phenomenon involving several sources of uncertainty such as material and tooling characteristics variation as well as environmental/boundary condition uncertainties. These uncertainties can affect the formation of residual stresses and can result in under-curing, over-curing, cure-induced voids and severe temperature overshoots which may cause thermal degradation [7,12,76].

2.6.1 Material properties and boundary conditions variation effects on cure

The resin cure kinetics is of crucial importance having a great impact on the curing process. The parameters of cure kinetics models are usually estimated using Differential Scanning Calorimetry (DSC), and can vary due to different handling and storage conditions of the resin or the presence of fibre sizing [77]. Particularly, handling and shelf life history uncertainties can cause variability in resin state and the initial degree of cure [8,12,77,78]. The thermal, mechanical, and thermo-mechanical properties of the material can show significant uncertainties affecting the cure process. These uncertainties are generated by the inherent uncertainties of the constituents as well as the previous steps of the manufacturing process. Thermal conductivity variations are caused by variations in fibre orientation and fibre volume fraction [79]. Variations in heat capacity can be caused by scatter in the heat capacity of the constituents and fibre volume fraction [79]. Thermal expansion coefficients are affected by uncertainty in the moduli and thermal expansion coefficients of the constituents, volume fraction variations and ply misalignment [79,80]. Fibre volume fraction variations also affect the total heat of reaction, whereas mechanical properties uncertainty is a function of material properties and fibre volume fraction variations [79].

Environmental/boundary condition uncertainties including ambient temperature, moisture, convective heat, prescribed pressure and temperature can show variations introducing additional variability to the process [79,81]. Apart from environmental conditions, the convective heat is affected by the geometric characteristics of the tools [76] and by other random factors such as wrinkles in vacuum bags. Variability in convective heat can result in uneven curing and temperature distribution, which can potentially lead to severe temperature overshoots, or even incomplete cure. The occurrence of temperature overshoots is also influenced by tool properties [76,82], implying that in the case of composite tooling, additional variability may be added.

Cure temperature and resin kinetics variations have a great impact on cure time distribution [7]. In particular, cure temperature variations dominate over resin kinetics uncertainties having the greatest influence on cure time variability, while faster reacting resins show higher cure time variability than systems with higher activation energy [7]. Unlike fibre orientation uncertainties, the variation of cure process parameters has been not explicitly quantified.

2.6.2 Residual stresses-shape distortion

The cure of composites always results in residual stresses which can lead to delamination, crack initiations, and shape distortions such as spring-in or warpage [83,84]. The formation of residual stresses is mainly dependent on the mechanical and thermo-mechanical properties of the constituents [62,85]. As mentioned in section 2.6.1, these properties are strongly influenced by the fibre volume fraction, implying that fibre volume fraction variations can introduce considerable scatter to the formation of residual stresses [62,86]. Regions with locally lower fibre volume fraction are more prone to geometrical distortions and defects due to process-induced stresses [12,86]. A variation in the order of 6% in fibre volume fraction can lead to 5% variation in the spring-in angle [86]. Such deviations can cause serious assembly issues. The development of residual stresses is also affected by cure kinetics variations, with variability in activation energy having the greatest impact [85]. Tooling properties affect the development of residual stresses as well [87]. Numerical simulations [87] have indicated that different mould materials have different effects on the development of process-induced residual stresses and strains, implying that in the case of composite tools further uncertainties may be added.

2.7 Property measurement and model uncertainties

There are several techniques and modelling practices to characterise the behaviour of composites during the different stages of manufacturing. The shear behaviour of preforms can be characterised using optical methods, picture frame experiments or bias-extension experiments. Sample size is of crucial importance; a larger shearing force is required with increasing sample area. Considerable discrepancies can be observed between the three methods, especially at angles above 30^o [25]. A round-robin study involving picture frame experiments and bias-extension experiments for different textiles, indicated deviations between the different laboratories. In both cases, the scatter increased with shear angle [25].

In plane permeability can be measured by two principal ways: the radial flow technique and the linear flow technique. Both of these methods have several variants, such as permeability measurements during saturated or unsaturated flow as well as constant pressure or constant flow rate measurements. Since there are no standard guidelines established to date, it is debatable which technique is the most accurate [88]. It has been shown that unsaturated linear flow experiments show the highest reproducibility [37,89,90]. According to [88,91,92], linear flow experiments are consistent with radial flow experiments, with the latter showing higher variations, whilst in [93] differences were found between the unsaturated linear technique and the wetting radial technique. In the case of linear flow experiments, errors can be introduced if the flow channel axis does not coincide with the principal axis of the fabric [88]. In addition, linear experiments can be significantly influenced by race tracking [94]. As Wang et al. [95] recommended execution of both radial and linear flow experiments should be carried out in order to obtain accurate experimental results. Significant deviations can be observed between the saturated and unsaturated flow technique due to transient capillary effects during wetting flow experiments [37,90,91,96]. In general, saturated flow experiments lead to higher permeability values than those obtained from unsaturated flow experiments [88]. The different types of fluids used to measure permeability can also contribute to variability [97]. The shape of the mould can also introduce scatter in permeability measurements, implying that measurement performed using conventional geometries may not be appropriate for designing complex parts [18]. Although the question of sample size is still open [47], as discussed in section 2.5.1, in general, larger moulds lead to lower global permeability variations [36]. A scatter of the same order as the experimental error was observed during a round-robin exercise between three different laboratories. The observed scatter was related to variation in specimen preparation [37]. However, round-robin results involving 16 different experimental procedures indicated a scatter of up to one order of magnitude in principal permeability values, whereas the ratio of principal permeability varied by a factor of up to 2. The main source of uncertainty between the different procedures was attributed to human factors including misconceptions about the experimental process, the use of unsuitable data treatment, different permeability definitions, inconsistent use of units and different specimen preparation conditions [88]. In a second international permeability round-robin test, nine institutions carried out in-plane unsaturated permeability measurements of a carbon-fibre fabric using common guidelines [98]. It was indicated that the scatter between the different institutions was similar to the scatter from each institution, implying that the use of benchmark guidelines can assist in obtaining reproducibility in permeability measurements. Furthermore, it was shown that the main source of uncertainty lies on the different experimental procedures rather than human errors as it was suggested by [88].

There are several cure monitoring techniques such as DSC, dielectrometry, infrared spectroscopy, and dynamic mechanical analysis (DMA). In general cure state measurements using DSC and dielectrics agree well [99], whereas significant differences are observed in the measurement of glass transition temperature between different techniques such as DSC and DMA [100]. Although DSC is the most common method to characterise cure kinetics, considerable discrepancies can be observed due to variability in baseline decision, different range of measured data, measurement quality variation, and variation in data reduction decisions. [97]. In addition, significant scatter can be observed between different cure kinetics models due to different modelling practices and the aforementioned characterisation uncertainties [97].

2.8 Overview

The fabrication of thermosetting composites is a very complex procedure, involving processes of different physics and scales. Each of the steps of composite manufacturing (forming, consolidation/impregnation and curing) introduces variability to the subsequent manufacturing processes, creating strong interdependencies between the process parameters and their variability and the properties of the product. Therefore, deterministic process simulation models are not able to capture fully the real phenomena, rendering the development and implementation of stochastic simulation tools for composite manufacturing imperative.

Fibre volume fraction seems to play the dominant role in composites manufacturing. Fibre volume fraction variations due to geometrical heterogeneities caused during the production of pre-pregs/dry textiles and forming /draping step along with nesting and edge effects can introduce significant scatter in permeability during the impregnation/consolidation step. This can result in flow-induced voids and resin rich zones further affecting the fibre volume fraction distribution. Fibre volume fraction also affects the thermal, mechanical and thermo-mechanical properties of the constituents introducing variability to the cure of composites. Furthermore, the cure process is significantly influenced by environmental/boundary condition uncertainties as well as resin property uncertainties due to different handling and storage conditions. These effects can introduce variability in residual stresses/shape distortion and can lead to serious cure induced defects. A schematic representation of these interdependencies is depicted in Fig. 2-3.

Unlike permeability variations, limited data exist regarding uncertainty in forming/draping. In addition, variability in composites cure has not been explicitly characterised; the results presented in the literature were obtained using conceptual values for the input variable uncertainties rather than experimental data. Therefore further investigation should be carried out towards the statistical characterisation and incorporation of all the sources of uncertainty during the forming/draping and cure step.

The findings presented in this chapter highlight the importance of variability in composites manufacturing and thus the need for future development and incorporation of stochastic simulation schemes into the existing commercial simulation tools. This implies that stochastic simulation should play a major role in process design; adopting stochastic simulation tools will have tremendous benefits in terms of costs. Benchmark guidelines should be developed regarding characterisation techniques and modelling practices in all manufacturing steps, to minimise property measurement and model uncertainties.

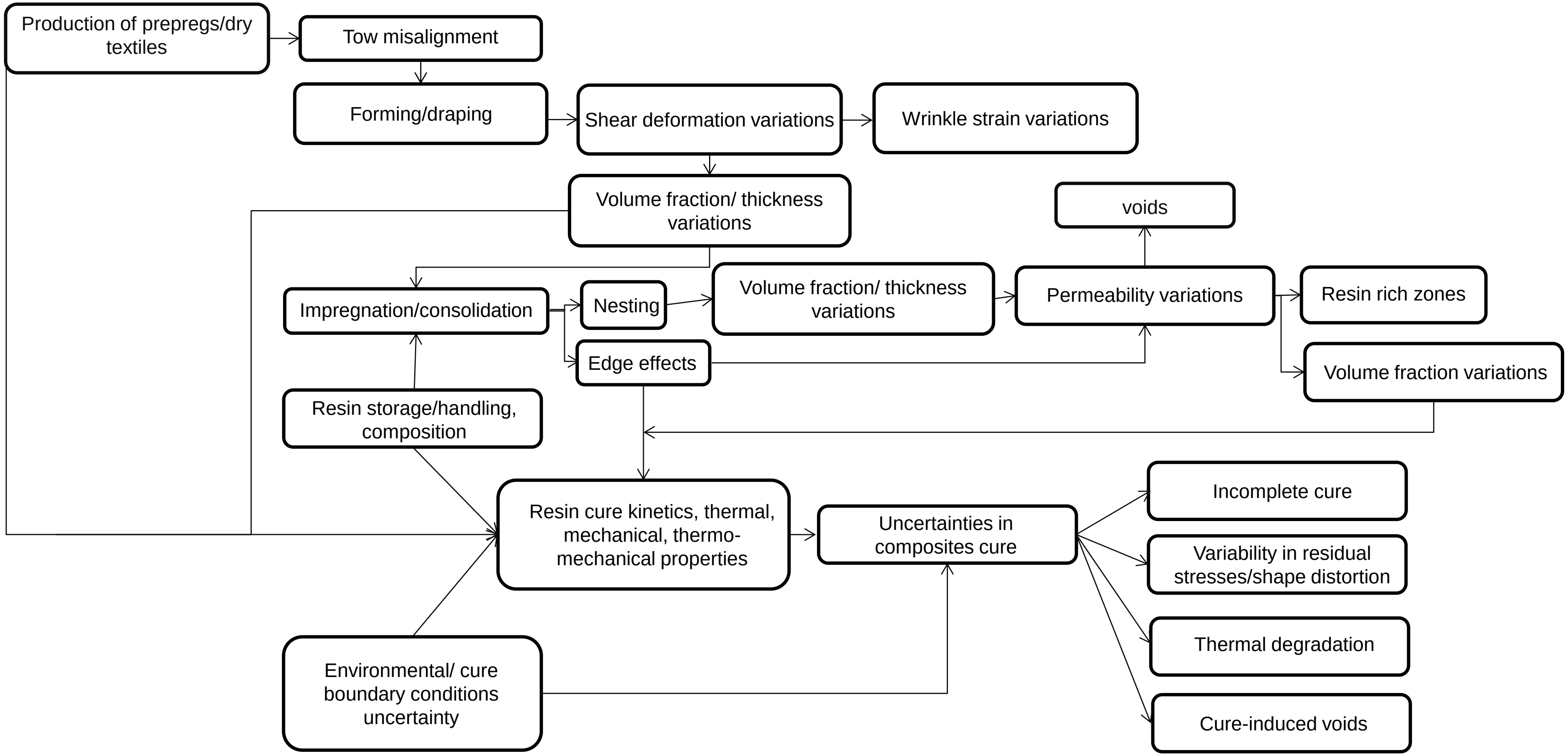

Fig. 2-3 Schematic representation of interdependencies in composite manufacturing.

3. Materials and experimental methods

3.1 Introduction

Quantification of input parameters uncertainty required a series of experiments. This chapter reports the experimental methods and details the materials used to quantify and characterise cure kinetics uncertainty, fibre misalignment and boundary conditions uncertainty.

3.2 Materials

The resin system used was the commercial epoxy resin Hexcel RTM6 [101]. Hexcel RTM6 is a premixed mono-component epoxy system, developed to fulfil the requirements of the aerospace and space industries in advanced RTM processes. The service temperature of RTM6 ranges from -60°C up to 180°C. In addition, at room temperature it is a highly viscous translucent paste and its viscosity decreases abruptly by increasing the temperature [101]. The textile considered was a 6k HTS carbon fibre ±45º NCF by Hexcel [102] with a chain knit stitch pattern. The areal density of the fabric is 534 g/m^2. A 4.5 mm thick carbon fibre-epoxy flat panel fabricated by infusion was used to quantify boundary conditions uncertainty. The matrix system of the panel was Hexcel RTM6, whilst the reinforcement was Hexcel AS7 12k carbon fibre [103] with an areal density is 268 g/m^2.

3.3 Differential Scanning Calorimetry

Differential scanning calorimetry (DSC) was used in order to quantify cure kinetics uncertainty. In this technique the difference between the heat flow of the sample and a reference at the same temperature is recorded. DSC scans can be carried out either under isothermal or dynamic conditions at prescribed heating rates. In the case of a thermoset, the result of a DSC scan is a curve of heat flux with a peak due to the exothermic reactions as a function of time or temperature. DSC curves are commonly used to characterise cure kinetics of a sample including the cure reaction rate and degree of cure. The cure behaviour of the epoxy system of this study was investigated using the TA-instruments DSC Q200 apparatus shown in Figure 3-1. A nitrogen purge gas with a flow rate of 50 ml/min was employed to avoid oxidation of samples during the experiments. In addition, a Tzero^{TM} sample press and the corresponding pans and lids were used.

Resin samples of 4-10 mg were encapsulated and placed at the instrument furnace under ambient conditions. All tests were equilibrated at 80 ºC and then a heating rate of 1ºC/min was applied up to 240 ºC. Samples from four different batches as well as different samples from every batch were tested. All batches were within their lifetime.

The total heat of reaction, H_T, can be calculated as follows:

$$H_T = \frac{H_{exp}}{(1 - a_o)} \tag{3-1}$$

where H_{exp} is the total heat of reaction released during the dynamic cure and a_o is the initial degree of cure of the resin.

During dynamic cure the resin emits or absorbs heat, at a rate depending on heat capacity evolution. Consequently, an appropriate baseline should be chosen reflecting this phenomenon in order to carry out the integration shown in Eq. (3-2). As shown in Figure 3-2, a dynamic DSC curve typically has a bell shape starting and ending at a plateau, which corresponds to the start and the end of conversion, respectively. The main functionality of the baseline is to connect the two plateaus which are normally not at the same level. In common practice a linear or sigmoidal baseline is used, however, there is no theoretical justification for the implementation of such a baseline, given the fact that the heat capacity of the resin is not expected to change in a linear or sigmoidal fashion. Therefore, an iterative baseline was used [104,105] to perform integration of heat flow versus time as follows:

$$H_{exp} = \int_{t_1}^{t_2} \frac{H}{dt} dt \tag{3-2}$$

Here, t_1 and t_2 is the time the reaction started and was completed, respectively. The degree of cure a, at any time t, can be evaluated using the following expression [106]:

$$a = a_o + \frac{\int_{t_1}^{t} \frac{H}{dt} dt}{H_T} \tag{3-3}$$

The heat capacity of the resin is changing gradually from the onset until the end of the reaction and its value at any intermediate point is considered as a linear function of the progress of the reaction. Thus, at the start of the conversion this method yields the initial heat capacity value, whilst at maximum conversion it yields the final heat capacity value [104].

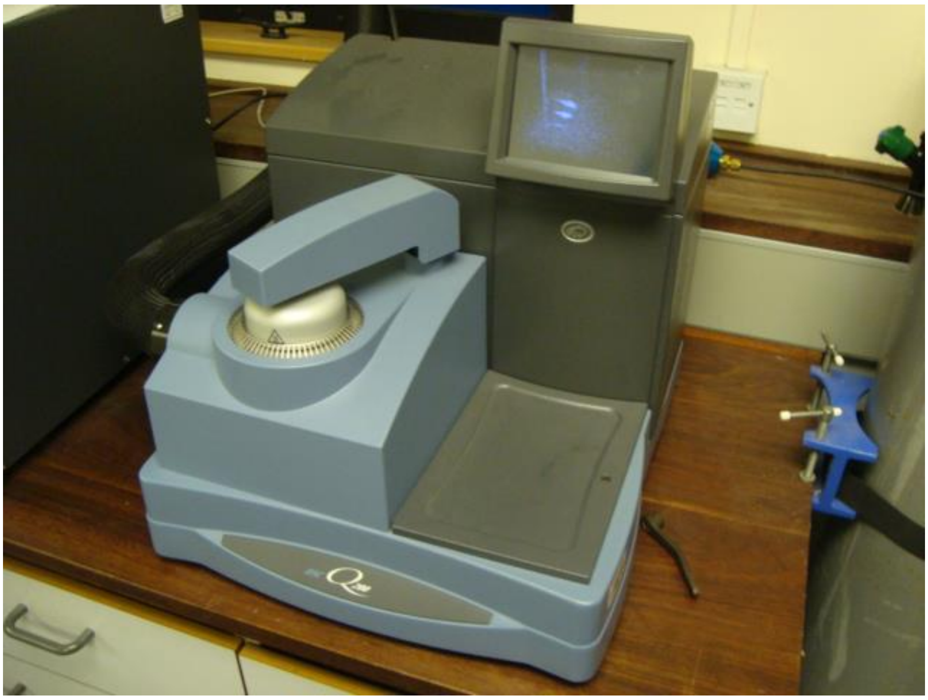

Fig. 3-1 TA-instruments DSC Q200 apparatus.

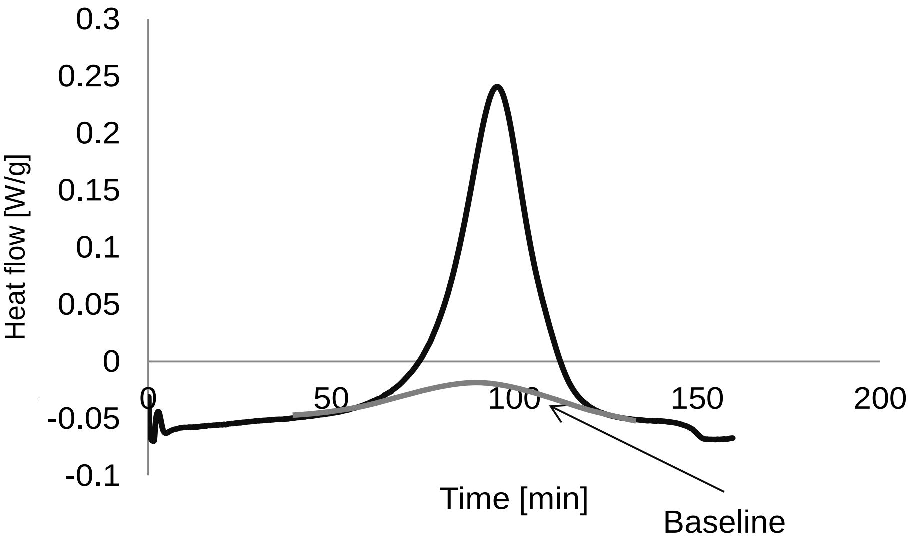

Fig. 3-2 Evolution of heat flow of during dynamic DSC of RTM6.

3.4 Image acquisition/analysis

A set of digital images of the textile of this study were acquired using a Sony camera to investigate fibre misalignment. The camera was mounted on a KSL KL150 tufting head mounted on a 6-axis robot arm in order to control and record the exact position of each image, as shown in Figure 3-3. The position of the robot was controlled using KCWIN; an interface appropriate for robot control.

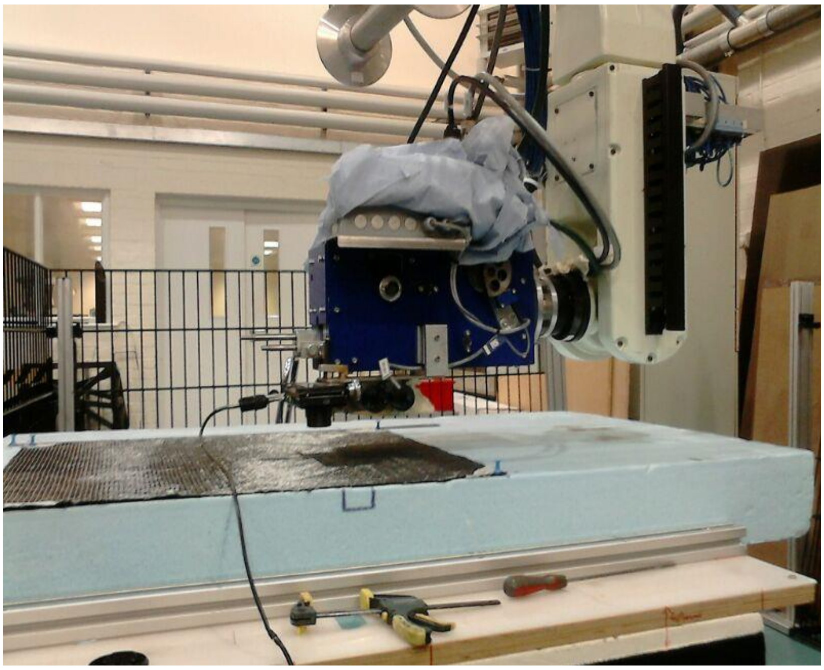

Fig. 3-3 Image acquisition set-up.

Investigation of tow orientation variability of a textile requires the development and implementation of an image analysis procedure employed at a local level. An in-house image analysis code [13] developed to characterise fibre misalignment in woven textiles has been enhanced in order to characterise fibre misalignment in unidirectional materials such as NCF. The image analysis code is based on Fast Fourier Transform (FFT) and correlation analysis. The approach adopted involves calculation of local fibre direction relative to the fibre orientation of a reference image, so that the spatial random field is explicitly quantified.

A grey-scale image of the unidirectional textile can be represented by a pixel array $f(x,y)$ expressing the distribution of brightness with its $F(u,v)$ Fourier spectrum. Fourier transform of a linear periodic image yields a two-dimensional spectrum with maxima in the direction normal to the orientation of the image [107]. Integration of $|F(u,v)|$ along radial directions allows estimation of the tows and non-structural stitch of the NCF as the directions of maximum accumulated radial energies [107]. Here, Fast Fourier Transform is employed to obtain a prior estimation of the fibre orientation. The correlation analysis is then used for accurate calculation of local fibre orientation using a reference region $r_\theta(x,y)$, which is carried out by rotating a kernel $k_\theta(x,y)$ of size $M \times M$ obtained from a reference image. The reference region is:

$$r_\theta(x,y) = k_\theta(xcos\theta + ysin\theta, -xsin\theta + ycos\theta) \tag{3-4}$$

The correlation of a reference region $r_\theta(x,y)$ of size $M \times M$ with the image $f(x,y)$ of size $K \times K$ is calculated as follows [13]:

$$\rho(\theta) = \frac{\sum_{i=1,j=1}^{M,M}(r_\theta(x_i,y_i) - \overline{r_\theta})(f(x_i,y_i) - \bar{f})}{\sqrt{\sum_{i=1,j=1}^{M,M}(r_\theta(x_i,y_i) - \overline{r_\theta})^2 \sum_{i=1,j=1}^{M,M}(f(x_i,y_i) - \bar{f})^2}} \tag{3-5}$$

where $\overline{r_\theta}$ and $\bar{f}$ are the average of the $r_\theta(x,y)$ and $f(x,y)$ arrays, respectively.

The image analysis procedure is as follows:

- Image acquisition into a discrete pixel array $f(x,y)$.
- Determination of a reference image.
- Application of Fast Fourier Transform to compute $F(u,v)$ and the modulus $|F(u,v)|$.
- Calculation of radial energy $E(\theta)$ in polar coordinates, $E(\theta) = \int_0^{+\infty} |F(r,\theta)|\, dr$.
- Estimation of approximate fibre orientation that maximizes $E(\theta)$.
- Calculation of difference between fibre orientation of reference and current image.
- Calculation of correlation of the current image with the reference image by rotating the reference image using directional cosines.
- Estimation of the angle that maximises correlation.

The last three steps constitute the modifications made to the original code [13] in order measure fibre misalignment in NCF.

Seven hundred and forty-eight images of size of 640x480 pixels were acquired from each side (upper/lower) of the fabric of this study on a 34×22 grid with 5 mm spacing. Application of the Fast Fourier Transform was carried out on a 256×256 region. Implementation of Eq. 3-5 is computationally intensive; therefore the size of the reference region $r(x,\theta)$ was 60×60. Additional datasheets on a coarser (10 x 10 mm) and finer (2.5 x 2.5 mm) grid were produced to investigate the dependence of the results on the grid size. The accuracy of the image acquisition and analysis procedure was studied by acquiring and analysing 50 images at the same location.

3.5 Heat flux sensors/ thermocouples

In order to quantify boundary conditions uncertainty ten tests were carried out using the experimental set-up illustrated in Figure 3-4. It comprises an ELKOM 8.4 KW electrical heating platen, a 10 mm thick aluminium tooling plate, a nylon N64PS-x VAC INNOVATION peel ply fabric, a nylon VAClease xR1.2 VAC INNOVATION vacuum bag, two K-type thermocouples and two RdF micro-foil heat flux sensors [108]. A composite panel was placed on the tooling plate, covered with the peel ply and the vacuum bag and sealed before testing. Two heat flux sensors were mounted on the vacuum bag (Figure 3-4) to measure natural air convection variability as well as its spatial dependence. A K-type thermocouple was placed on the tool to quantify tool temperature uncertainty and a second one away from the apparatus to measure ambient temperature variability. The temperature was equilibrated at 160 ^{0}C in all tests. A National Instruments LabVIEW in house code was used for data acquisition and the data were acquired with a frequency of 0.8 Hz.

The micro-foil heat flux sensor consists of a thin layer as shown in Figure 3-6, and is a differential thermocouple type sensor using a T-type thermocouple. Given that the same heat flux should flow through the sensor and the surface where the sensor is mounted, the sensor is directly measuring the heat loss or gain through the thin layer by measuring the temperature difference between opposite sides of the thin layer.

This sensor produces a voltage output which is proportional to heat flux. In particular, the heat-flux $\dot{Q}$ is given by the following relation:

$$\dot{Q} = (HF)/(CM\,TCF) \tag{3-6}$$

where HF is the sensor output, CM a calibration multiplier and TCF a temperature compensation factor. The calibration multiplier (unique to each sensor) is measured at 21^{o}C and is not linear with temperature. The sensors used in this study had a calibration multiplier of 0.15 µV per W/m^2. The temperature compensation factor is a function of temperature and can be found in Figure 3-7 [108]. In the case of the two K-type thermocouples as well as the T-type thermocouples incorporated in the sensors an output in ^{o}C is produced, whilst in the case of the sensors a voltage output is produced and therefore Eq. (3-6) was utilised to calculate the heat flux. Subsequently, the heat transfer coefficient h was computed using the measurements of bag and air temperature T_A.

$$h = \frac{\dot{Q}}{T_s - T_A} \tag{3-7}$$

where T_s is the temperature at the surface of the bag.

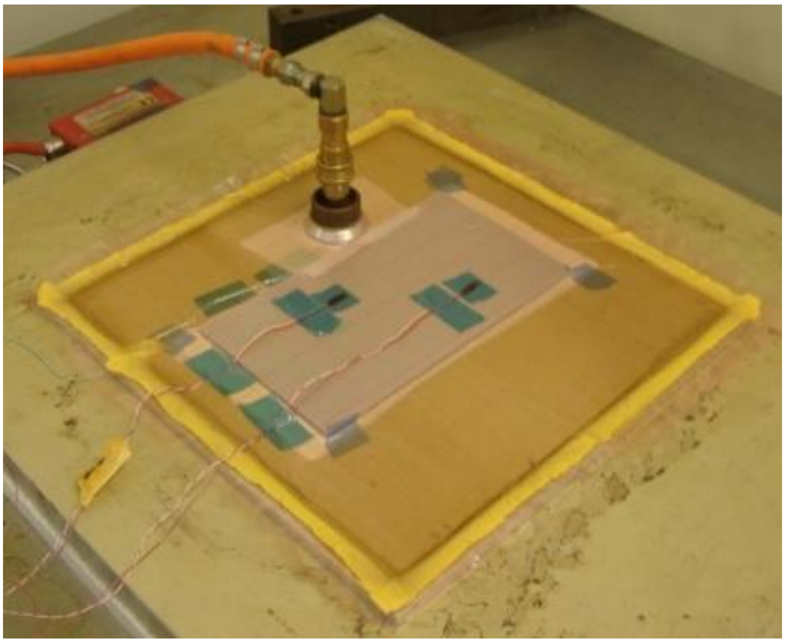

Fig. 3-4 Experimental set-up for quantification of boundary condition uncertainty.

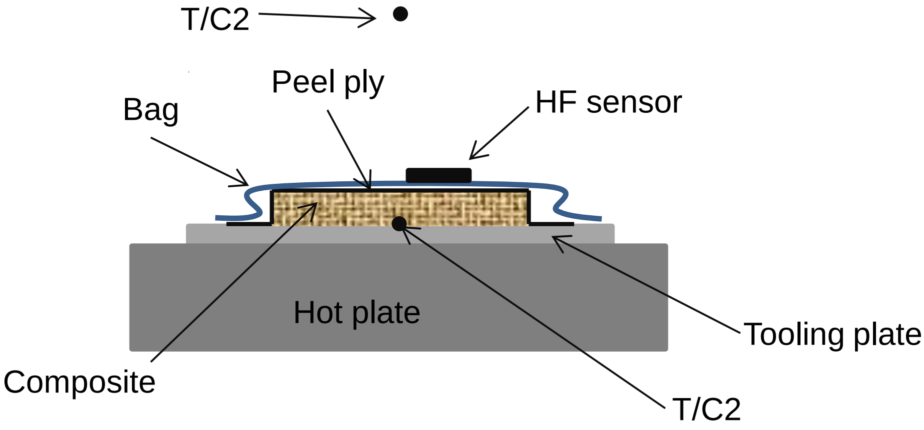

Figure 3-5 Schematic representation of cross-section of experimental set-up used for quantification of boundary condition uncertainty.

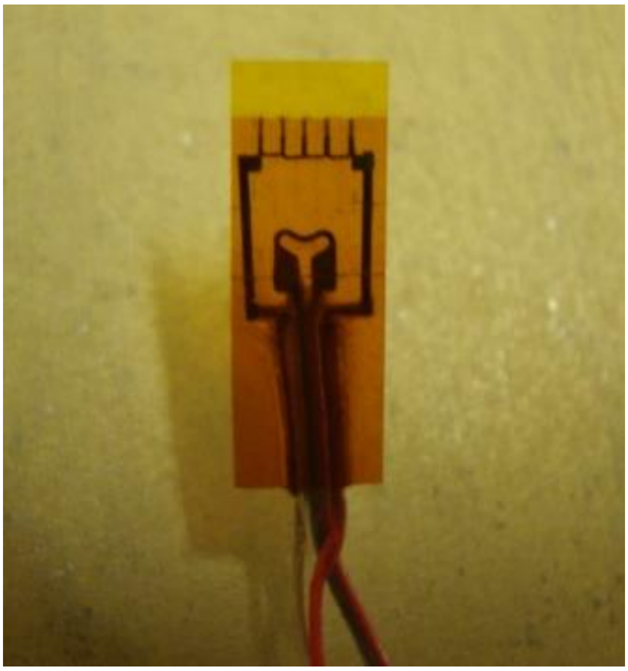

Fig. 3-6 Micro-Foil Heat flux sensor [108]**.**

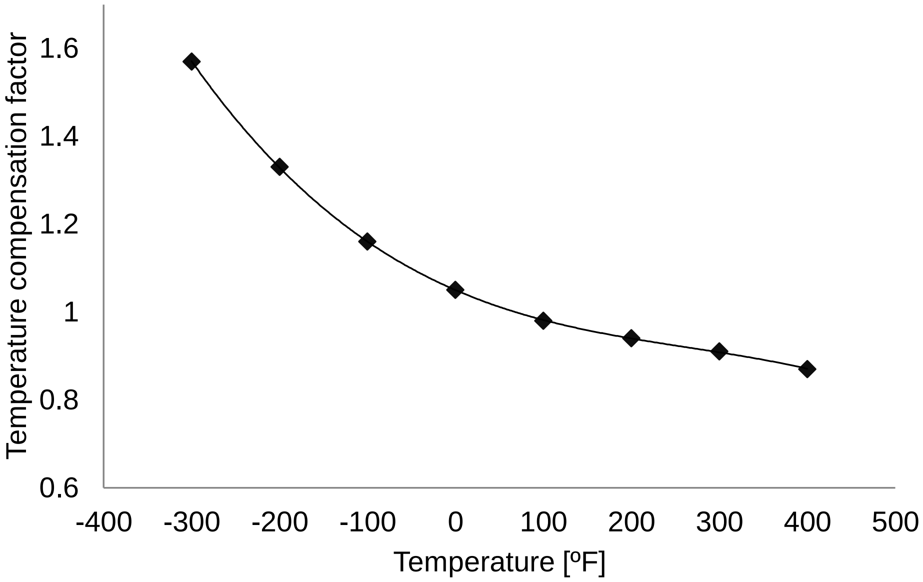

Fig. 3-7 Micro-foil heat flux sensor output compensation factor as a function of surface temperature [108].

3.6 Overview

The experimental methods and materials used to quantify cure kinetics uncertainty, local tow orientation variability and boundary conditions uncertainty have been presented. A series of Differential Scanning Calorimetry (DSC) tests were carried out to investigate cure kinetics uncertainty of a commercial epoxy resin used in aerospace applications, whilst an in-house image analysis code was enhanced to characterise fibre misalignment of a ±45º NCF. An infusion set-up was used to quantify tool temperature, ambient temperature and surface heat transfer coefficient using thermocouples (tool/ambient temperature) and heat flux sensors (heat transfer coefficient).

4. Cure simulation model

4.1 Introduction

The cure simulation model was developed using the commercial Finite Element Analysis (FEA) solver MSC.Marc [109]. The modelling approach used in this study was based on 3D iso-parametric 8-node composite brick elements; 149 MSC.Marc element type for thermo-mechanical analysis and 175 MSC.Marc element type for thermal analysis [110]. These elements allow modelling of layered materials; different material properties, fibre orientation and thickness can be assigned to different layers within the same element. Each layer contains four integration points and a numerical integration scheme based on Gaussian quadrature is employed [110]. A set of material property user-subroutines were used for the incorporation of cure kinetics and the dependence of material properties on the state of material and temperature. Initial conditions on the degree of cure and temperature were implemented using the USINC user subroutine. Prescribed time-dependent temperature boundary conditions were applied using the FORCDT user subroutine, whereas natural air convection was implemented via the UFILM user subroutine [111]. Mechanical boundary conditions were applied by means of table driven input. Post processing of elements and nodal variables was carried out using the PLOTV and UPSTNO user subroutines [111]. The mechanical behaviour is considered to be quasi static rendering the problem transient/quasi static comprising of a series of heat transfer passes and mechanical passes for each increment of the solution.

4.2 Thermo-mechanical problem

The full thermo-mechanical problem is described here; the heat transfer problem can be considered as a subcase of the coupled solution. A staggered solution approach is adopted in the solver [109] to carry out the cure thermo-mechanical analysis. The cure kinetics analysis is carried out first, then the heat transfer analysis is performed followed by the mechanical analysis. In particular, the cure reaction rate is first calculated based on the estimated temperatures at the beginning and end of each increment. The heat generation due to the cure reaction is then calculated and added into the heat transfer system of equations (see Eq. 4-1) at the beginning of each cycle of the heat transfer pass. The cure shrinkage and the thermal strain is then considered in the mechanical pass of the coupled analysis.

The heat transfer problem applicable during the cure process can be expressed by a three-dimensional energy balance combined with Fourier's heat conduction law and incorporating the exothermic heat generated due to the chemical reaction of the resin as follows [112]:

$$\rho c_p \frac{\partial T(\boldsymbol{r},t)}{\partial t} = \nabla \cdot \boldsymbol{K} \nabla T(\boldsymbol{r},t) + \left(1 - v_f\right) \rho_r H_T \frac{da}{dt} \tag{4-1}$$

Here ρ and c_p are the density and the specific heat capacity of the composite, respectively, $\boldsymbol{K}$ is the thermal conductivity tensor, T the temperature, t and $\boldsymbol{r}$ the time and spatial coordinate and a the degree of cure. The rate of heat generation due to cure is the product of $\left(1 - v_f\right)$ where v_f is the volume fraction of the fibres, density of the resin ρ_r, total heat of reaction H_T and cure reaction rate da/dt.

The mechanical problem is based on the momentum conservation combined with a constitutive law incorporating contributions for the elastic response of the material, resin shrinkage and thermal expansion/contraction as follows:

$$\boldsymbol{\sigma} = \boldsymbol{Q}\left(\boldsymbol{\varepsilon} + \boldsymbol{C^s} \Delta a - \boldsymbol{a^{th}} \Delta T\right) \tag{4-2}$$

here $\boldsymbol{\sigma}$ denotes the stress tensor and $\boldsymbol{Q}$ is the stiffness matrix. The cure shrinkage strain is a function of the cure shrinkage coefficient matrix $\boldsymbol{C^s}$ and degree of cure increment Δa, whereas the thermal expansion strain is a function of the thermal expansion coefficient matrix $\boldsymbol{a^{th}}$, and the corresponding temperature increment ΔT.

The initial conditions during the cure simulation include initial degree of cure and initial temperature as follows:

$$\alpha(\boldsymbol{r},0) = a_i \tag{4-3}$$

$$T(\boldsymbol{r}, 0) = T_i \tag{4-4}$$

The time-dependent temperature boundary condition on the prescribed temperature side is given by:

$$T(\boldsymbol{r}, t) f(t), \boldsymbol{r} \epsilon S_1 \tag{4-5}$$

whilst the natural air convection is defined as:

$$n \cdot K \nabla T(\boldsymbol{r}, t) = h(T_s - T_\infty), \boldsymbol{r} \epsilon S_2 \tag{4-6}$$

where $f(t)$ is the thermal profile followed by the tool during the cure, h is the surface heat transfer coefficient, T_s is the surface temperature, T_∞ the fluid temperature, n the vector normal to the surface and S_1 and S_2 the parts of the boundary where the prescribed temperature and natural air convection boundary conditions apply respectively. The mechanical boundary conditions comprise displacement constraints in different directions as follows:

$$u_x(\boldsymbol{r}) = 0, \boldsymbol{r} \in S_3 \tag{4-7}$$

$$u_y(\boldsymbol{r}) = 0, \boldsymbol{r} \in S_4 \tag{4-8}$$

$$u_z(\boldsymbol{r}) = 0, \boldsymbol{r} \in S_5 \tag{4-9}$$

where S_3 , S_4 and S_5 denote the parts of the boundary where the x, y and z displacement constraints are applied respectively.

4.2 Constitutive models

The cure of a thermosetting resin causes complex chemical and physical changes as the material is transformed from a viscous liquid to a highly cross-linked solid [106]. The cross-linking reaction kinetics is affected by the applied temperature. In addition, exothermic heat is generated as the resin cures [113]. Therefore, material properties are strongly dependent on material state and thus the corresponding constitutive material models need to represent this behaviour accurately. To this end, the approach adopted in this study is based on the development of cure kinetics models accompanied by a model of the development of the glass transition temperature. The model of the development of the glass transition temperature is used to compute the instantaneous glass transition temperature as a function of the current degree of cure. Consequently, most of the properties are expressed as a function of material state, i.e. whether the temperature is below or over the glass transition temperature using an exponential step function, with adjustable height and breadth. The materials used to develop the cure simulation model are the commercial epoxy resin Hexcel RTM6 [101], and the Hexcel G1157 [114] pseudo unidirectional carbon fibre reinforcement.

A cure simulation model incorporates several sub-models which represent the dependence of material properties on current material state. The material sub-models comprise thermal, mechanical and thermo-mechanical properties and can be summarised as follows:

- Thermal properties
    - Cure kinetics
    - Specific heat capacity
    - Thermal conductivity tensor

- Mechanical properties
    - Elastic tensor
    - Poisson’s ratio

- Thermo-mechanical properties
    - Thermal expansion coefficients
    - Cure shrinkage

4.2.1 Glass transition temperature

The Di Benedetto equation has been widely used to describe the behaviour of several epoxy resin systems, including Hexcel RTM6. The Di Benedetto equation is as follows [115]:

$$T_g = T_{go} + \frac{\left(T_{g\infty} - T_{go}\right)\lambda\alpha}{1-(1-\lambda)\alpha} \tag{4-10}$$

where T_{go} and $T_{g\infty}$ are the glass transition temperatures of the uncured and fully cured material, respectively, while λ is a fitting constant controlling the convexity of this non-linear dependence. The values of these parameters regarding the RTM6 epoxy resin are presented in Table 4-1 [116].

Table 4-1 Di Benedetto equation parameters for RTM6.

$T_{go}\ \ (^0C)$	-11
$T_{g\infty}\ \ (^0C)$	206
λ	0.435

4.2.2 Cure kinetics

The cure kinetics model of Hexcel RTM6 is a combination of an n^{th} order model and an autocatalytic model and can be described by the following equation [106,117]:

$$\frac{da}{dt} = k_1(1-a)^{n_1} + k_2(1-a)^{n_2}a^m \tag{4-11}$$

where da/dt is the reaction rate, a the current degree of cure, and n_1, n_2, m reaction orders. The reaction rate constants incorporate diffusion rate limitation terms [116]:

$$\frac{1}{k_i} = \frac{1}{k_{i,c}} + \frac{1}{k_d} \quad i = 1,2 \tag{4-12}$$

where $k_{i,c}$ are chemical rate constants following an Arrhenius temperature dependence:

$$k_{iC} = A_i e^{\left(\frac{-E_i}{RT}\right)}\ i = 1,2 \tag{4-13}$$

and k_d is a diffusion rate constant defined as [116]:

$$k_D = A_D e^{\left(\frac{-E_D}{RT}\right)} e^{\left(\frac{-b}{f}\right)} \tag{4-14}$$

where T is the instantaneous temperature, E_i activation energies, A_i pre-exponential factors, A_D and E_D the pre-exponential factor and activation energy of the diffusion process, respectively, R the universal gas constant, b a constant, and f the equilibrium free volume expressed as [118]:

$$f = w\left(T - T_g\right) + g \tag{4-15}$$

where w and g are constants.

The nominal cure kinetics parameters for RTM6 are listed in Table 4-2. Note that a_o is the initial degree of cure which is used in the kinetics model as the initial condition of the integration of Eq. (4-4) and its nominal value is 0.02. The total heat of reaction of RTM6 is 465 J/g [106], whilst its density is 1110 kg/m^3 [101].

Table 4-2 Nominal cure kinetics parameters for RTM6.

$A_1(1/s)$	17580 [106]
$A_2(1/s)$	21525 [106]
$A_D(1/s)$	6.48E+18 [116]
$E_1(J/mol)$	70500 [106]
$E_2(J/mol)$	59050 [106]
$E_D(J/mol)$	136800 [116]
n_1	1.80 [106]
n_2	1.32 [106]
m	1.16 [106]
b	0.467 [116]
w [1/K]	0.00048 [116]
g	0.025 [116]
a_o	0.02 [106]

4.2.3 Specific heat capacity

The composite specific heat capacity is influenced by both constituents. Using the rule of mixtures the specific heat capacity of the composite is:

$$c_p = w_f c_{pf} + \left(1 - w_f\right) c_{pr} \tag{4-16}$$

where w_f is the weight fraction of the fibre, c_{pf} the fibre specific heat capacity and c_{pr} the specific heat capacity of the resin. The weight fraction of the fibre is defined as:

$$w_f = \frac{v_f \rho_f}{\rho} \tag{4-17}$$

Here ρ_f is the density of the fibre whereas ρ is the density of the composite. The density of Hexcel G1157 is 1760 kg/m^3 [114]. The density of the composite is computed using the rule of mixtures:

$$\rho = v_f \rho_f + (1 - v_f)\rho_r \tag{4-18}$$

The fibre specific heat capacity is a linear function of temperature and can be expressed as follows [119]:

$$c_{pf} = 0.0023T + 0.765 \tag{4-19}$$

The specific heat capacity of the resin depends on both temperature and degree of cure. The dependence on degree of cure is expressed using a dependence on the instantaneous glass transition temperature of the resin as follows:

$$c_{pr} = A_{rc_p}T + B_{rc_p} + \frac{\Delta_{rc_p}}{1 + e^{C_{rc_p}(T - T_g - si)}} \tag{4-20}$$

Eq.(4-20) results in a linear dependence of specific heat capacity on temperature for material in the same state and a step transition around the glass transition temperature. Here A_{rc_p} and B_{rc_p} are constants expressing the linear relation of the resin specific heat capacity with temperature, while $\varDelta_{rc_p}$, C_{rc_p} and si are constants referring to the strength, breadth and temperature shift of the transition around T_g. The values of the coefficients used in Eq. (4-20) were estimated by fitting to experimental data produced by modulated scanning calorimetry (MDSC) [119] using a Genetic Algorithm and are reported in Table 4-3.

Table 4-3 Specific heat capacity parameters.

Constants	RTM6
$A_{rc_p}(Jg^{-1}{}^{\circ}\mathrm{C}^{-2})$	0.0025
$B_{rc_p}(Jg^{-1}{}^{\circ}\mathrm{C}^{-1})$	1.80
$\Delta_{rc_p}(Jg^{-1}{}^{\circ}\mathrm{C}^{-1})$	-0.25
$C_{rc_p}(1/{}^{\circ}\mathrm{C})$	1.10
$si({}^{\circ}\mathrm{C})$	16.5

Figure 4-1 illustrates the response of the resin specific heat capacity model. A step change is observed at the glass transition of the material. At the transition from a viscous liquid or rubber to a solid glass the vibrational and configurational behaviour of the system becomes subject to additional constraints leading to reduced heat absorption and lower heat capacity.

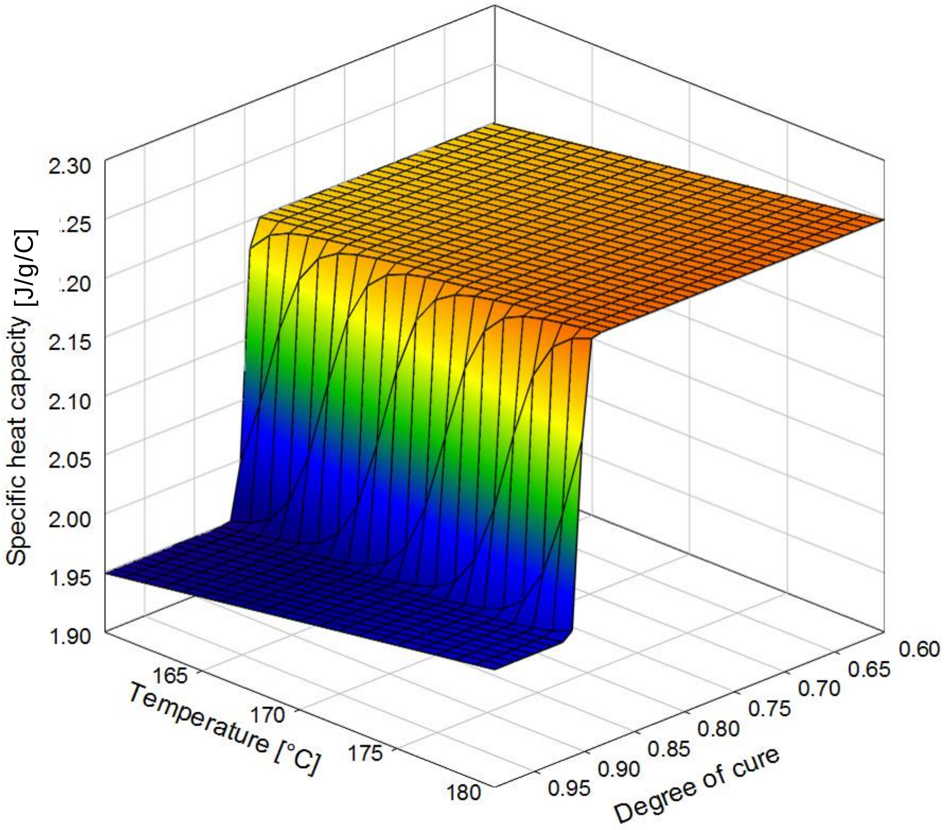

Fig. 4-1 Response of the resin specific heat capacity model.

4.2.4 Thermal conductivity

Each composite lamina is considered a transversely isotropic material. The thermal conductivity in the longitudinal direction can be calculated as follows [120]:

$$K_{11} = v_f K_{lf} + (1 - v_f)K_r \tag{4-21}$$

K_{lf} and K_r are the thermal conductivity of the fibre in this direction and of the resin. In the transverse direction the thermal conductivity can be computed as follows [120]:

$$\begin{aligned} K_{22} = K_{33} &= v_f K_r \left(\frac{K_{tf}}{K_r} - 1\right) + K_r \left(\frac{1}{2} - \frac{K_{tf}}{2K_r}\right) \\ &+ K_r \left(\frac{K_{tf}}{K_r} - 1\right) \sqrt{v_f^2 - v_f + \frac{\left(\frac{K_{tf}}{K_r} + 1\right)^2}{\left(\frac{2K_{tf}}{K_r} - 2\right)^2}} \end{aligned} \tag{4-22}$$

where K_{tf} is the fibre conductivity in the transverse direction. The fibre conductivity in the longitudinal and transverse direction is defined as follows:

$$K_{lf} = A_{lf}T + B_{lf} \tag{4-23}$$

$$K_{tf} = B_{tf} \tag{4-24}$$

The thermal conductivity of the resin can be expressed as [119]:

$$K_r = a_{K_r}Ta^2 + b_{K_r}Ta + c_{K_r}T + d_{K_r}a^2 + e_{K_r}a + f_{K_r} \tag{4-25}$$

The coefficients of equations (4-21)-(4-25) are presented in Table 4-4.

Table 4-4 Thermal conductivity coefficients.

Coefficients	RTM6	G1157
$A_{lf}(Wm^{-1}°\text{C}^{-2})$	-	0.0074 [121]
$B_{lf}(Wm^{-1}°\text{C}^{-1})$	-	9.7 [121]
$B_{tf}(Wm^{-1}°\text{C}^{-1})$	-	0.84 [121]
$a_{Kr}(Wm^{-1}°\text{C}^{-2})$	0.0008 [119]	-
$b_{Kr}(Wm^{-1}°\text{C}^{-2})$	-0.0011 [119]	-
$c_{Kr}(Wm^{-1}°\text{C}^{-2})$	-0.0002 [119]	-
d_{Kr}	-0.0937 [119]	-
e_{Kr}	0.22 [119]	-
f_{Kr}	0.12 [119]	-

4.2.5 Mechanical properties

A widely used micro-mechanics model was chosen [122] to model the composite mechanical properties. The longitudinal and the transverse moduli are calculated as follows:

$$E_{11} = (1 - v_f)E_r + v_f E_{lf} \tag{4-26}$$

$$E_{22} = \frac{E_r}{1 - \sqrt{v_f}\left(1 - {E_r}/{E_{tf}}\right)} = E_{33} \tag{4-27}$$

where E_r is the isotropic moduli of the resin and E_{lf} , E_{tf} the fibre moduli in the longitudinal and transverse fibre directions respectively. The composite shear modulus and Poison’s ratio can be modelled as follows [122]:

$$G_{12} = \frac{G_r}{1 - \sqrt{v_f}\left(1 - {G_r}/{G_{12f}}\right)} = G_{13} \tag{4-28}$$

$$G_{23} = \frac{G_r}{1 - \sqrt{v_f}\left(1 - {G_r}/{G_{23f}}\right)} \tag{4-29}$$

$$\nu_{12} = v_f \nu_{12f} + \left(1 - v_f\right)\nu_r = \nu_{13} \tag{4-30}$$

$$\nu_{23} = \frac{E_{22}}{2G_{23}} - 1 \tag{4-31}$$

The mechanical properties of the resin system of this study were modelled using a relation that allows a step transition around the instantaneous glass transition temperature as follows:

$$E_r = E_{r_L} + \frac{E_{r_G} - E_{r_L}}{1 + e^{C_{rcp}\left(T - T_g - si\right)}} \tag{4-32}$$

$$\nu_r = \nu_{r_L} + \frac{\nu_{r_G} - \nu_{r_L}}{1 + e^{C_{rcp}\left(T - T_g - si\right)}} \tag{4-33}$$

$$G_r = \frac{E_r}{2(1 + \nu_r)} \tag{4-34}$$

The values of C_{rc_p} and si are identical to those reported in relation to the specific heat capacity constitutive model for the same epoxy system. The subscripts r_G and r_L indicate the material properties in the glass and rubber/liquid state respectively. The mechanical properties of both the resin and the fibre are presented in Table 4-5. Figures 4-2 and 4-3 illustrate the response of the resin mechanical properties model. A step change is observed in the modulus of the resin at the glass transition of the material. The modulus of the resin increases abruptly during the transition from the viscous liquid or rubber state of low stiffness to the glassy solid state of high stiffness. In addition, the Poisson's ratio decreases significantly presenting a step change, as illustrated in Figure 4-3. These phenomena are attributed to the fact that the mobility of the polymer system becomes gradually limited as the polymer network becomes fixed allowing the material to be capable to sustain higher stresses.

Table 4-5 Mechanical properties.

Mechanical properties	RTM6	G1157
$E_{lf}\ (GPa)$	-	238 [123]
$E_{tf}\ (GPa)$	-	28 [123]
$G_{12f}\ (GPa)$	-	24 [123]
$G_{23f}\ (GPa)$	-	7.2 [123]
ν_{12f}	-	0.23 [123]
ν_{23f}	-	0.33 [123]
ν_{31f}	-	0.03 [123]
$E_{r_G}\ (GPa)$	3.07 [124]	-
$E_{r_L}\ (GPa)$	0.033 [125]	-
ν_{r_G}	0.38 [125]	-
ν_{r_L}	0.495 [125]	-

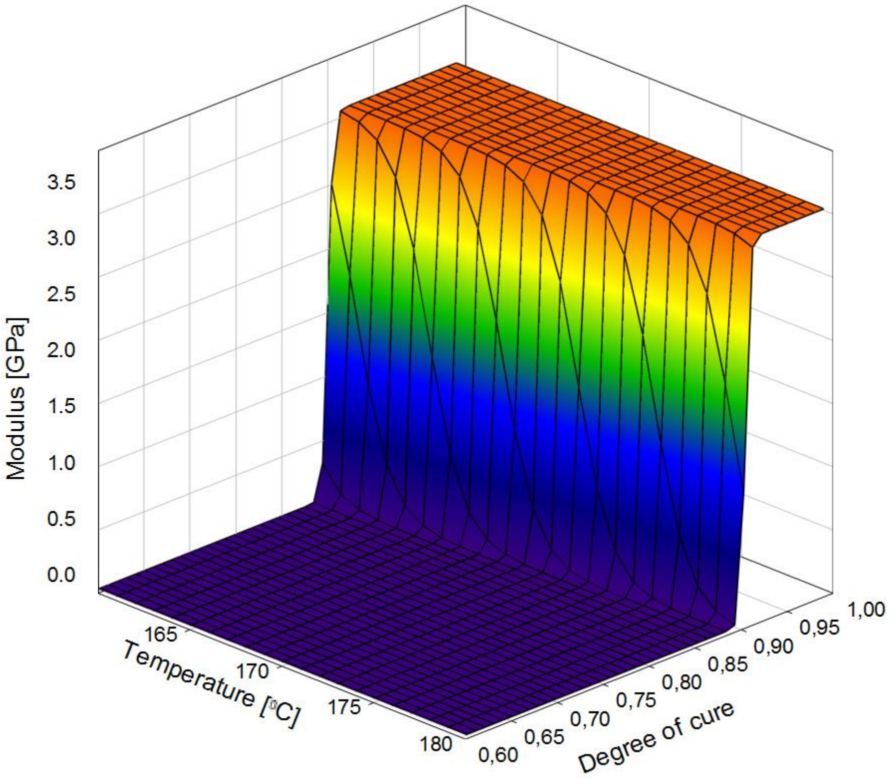

Fig. 4-2 Response of the resin modulus model.

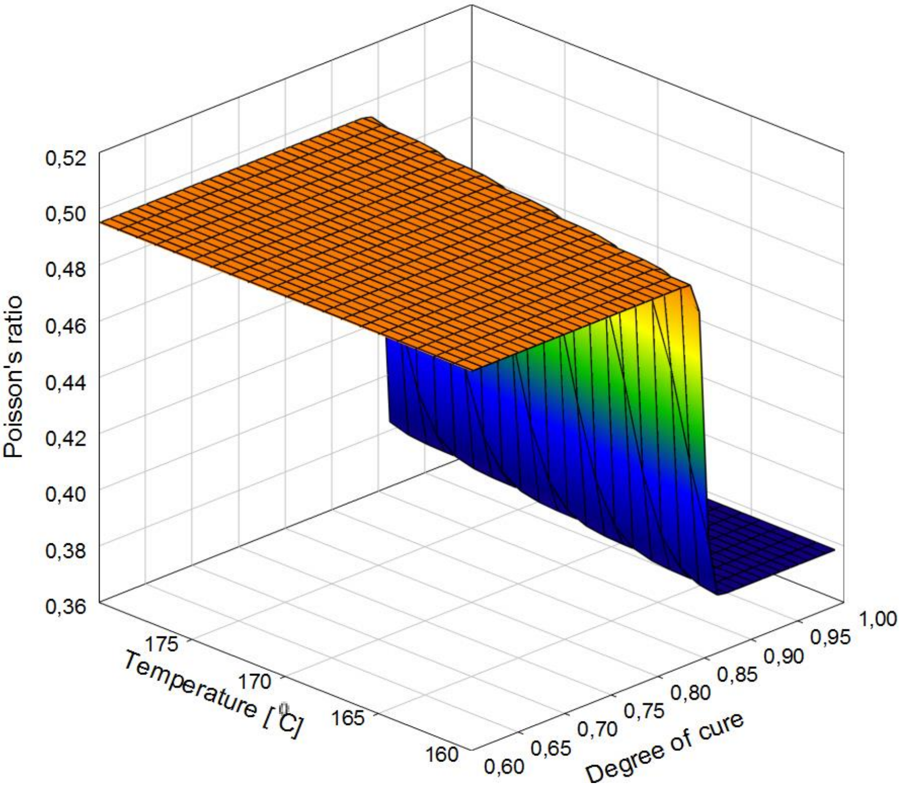

Fig. 4-3 Response of the resin Poisson's ratio model.

4.2.6 Cure shrinkage

The composite presents a direction-dependent shrinkage strain due to its transversely isotropic nature. The anisotropic cure shrinkage coefficients are computed as follows [126]:

$$C_{11}^{S} = \frac{\left(1 - v_f\right)E_r}{\left(1 - v_f\right)E_r + v_f E_{lf}} \tag{4-35}$$

$$C_{22}^{S} = (\nu_r + 1)\left(1 - v_f\right) - \nu_{12} C_{11}^{S} = C_{33}^{S} \tag{4-36}$$

where C_{11}^{S} is the cure shrinkage coefficient in the longitudinal direction and C_{22}^{S} is the cure shrinkage coefficient in the transverse direction. The fibre is not active in terms of chemical shrinkage, whereas the resin can be assumed to follow a linear dependence on the degree of cure a given by:

$$V_r^{S} = V_r^{S\infty} a \tag{4-37}$$

Here V_r^{s} is the volumetric cure shrinkage and $V_r^{S\infty}$ is the maximum volumetric shrinkage. The maximum volumetric shrinkage $V_r^{S\infty}$ is 0.018 [125]. The incremental cure shrinkage strain of the resin is then calculated as follows [126]:

$$\varepsilon_r^{s} = (1 + V_r^{s})^{1/3} - 1 \tag{4-38}$$

The shrinkage strain components of the composite are calculated by using the directional cure shrinkage coefficient matrix:

$$\varepsilon_{ij}^{S} = C_{ij}^{S} \varepsilon_r^{s} \tag{4-39}$$

4.2.7 Thermal expansion coefficients

The composite thermal expansion coefficients can be modelled using micromechanics as follows:

$$a_{11}^{th} = \frac{(1 - v_f)E_r a_r + v_f E_{lf} a_{lf}}{(1 - v_f)E_r + v_f E_{lf}} \tag{4-40}$$

$$\begin{aligned} a_{22}^{th} = (1 - v_f)a_r + v_f a_{tf} + (1 - v_f)a_r + v_f v_{12f} a_{lf} \\ - v_{12} a_{11}^{th} = a_{33}^{th} \end{aligned} \tag{4-41}$$

where a_{11}^{th} and a_{22}^{th} are the longitudinal and transverse coefficients, respectively. a_r is the resin isotropic thermal expansion coefficient and a_{lf} and a_{tf} are the longitudinal and transverse coefficients of the fibre, respectively. The coefficient of thermal expansion of the resin follows a step transition around the glass transition which is represented similarly to the specific heat capacity and mechanical properties models as follows:

$$a_r = a_{r_L} + \frac{a_{r_G} - a_{r_L}}{1 + e^{C_{rcp}(T - T_g - si)}} \tag{4-42}$$

As Eqs. (4-43)-(4-44) indicate, the fibre thermal expansion coefficients are a polynomial function of temperature [127].

$$a_{lf} = \sum_{i=0,4} A_{a_{lf}}^{i} T^{i} \tag{4-43}$$

$$a_{tf} = \sum_{i=0,3} A_{a_{tf}}^{i} T^{i} \tag{4-44}$$

All parameters required for computation of the thermal expansion coefficients are listed in Table 4-6 [127]. The response of the resin thermal expansion coefficient model is presented in Figure 4-4. The coefficient of thermal expansion of the resin drops significantly at the glass transition, due to the significant decrease in intermolecular motion caused by the transition of the resin from the viscous liquid or rubber state to the solid glassy state.

Table 4-6 Thermal expansion coefficients parameters.

Parameters	RTM6	G1157
$A_{a_{lf}}^{3}\ (K^{-3})$	-	4.92E-15
$A_{a_{lf}}^{2}\ (K^{-2})$	-	-1.57E-11
$A_{a_{lf}}^{1}\ (K^{-1})$	-	1.70E-08
$A_{a_{lf}}^{0}$	-	-4.75E-06
$A_{a_{tf}}^{2}\ (K^{-2})$	-	-6.95E-12
$A_{a_{tf}}^{1}\ (K^{-1})$	-	1.55E-08
$A_{a_{lf}}^{0}$	-	-6.19E-07
$A_{a_{lf}}^{3}\ (K^{-3})$	-	-
a_{r_L}	1.36E-4	-
a_{r_G}	6.90E-5	-

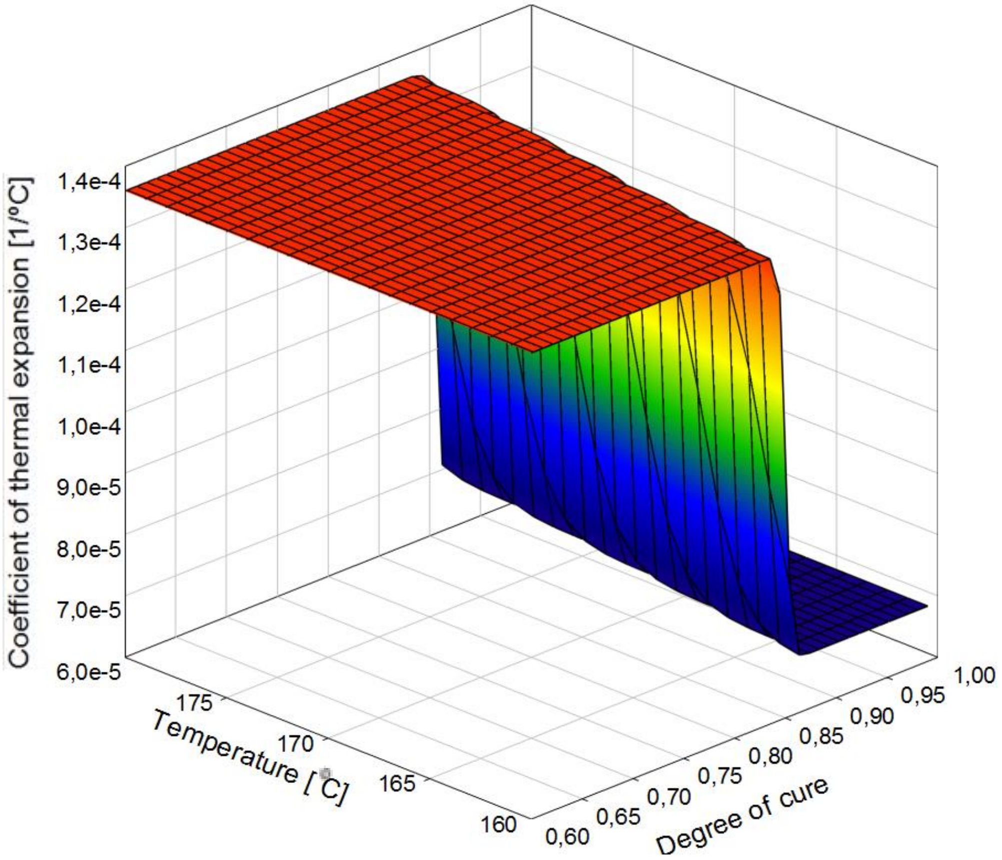

Fig. 4-4 Response of the resin coefficient of thermal expansion model.

4.2.8 Implementation of constitutive models

A set of user subroutines were used to implement the relations described in section 4.2; each sub-model was incorporated to the main code using the respective user subroutine. All user subroutines are called at each increment for every integration point per element in the mesh as shown in Figure 4-5. Examples of the UCURE, ANKOND, HOOKLW and ANEXP user subroutines can be found in Appendix A.

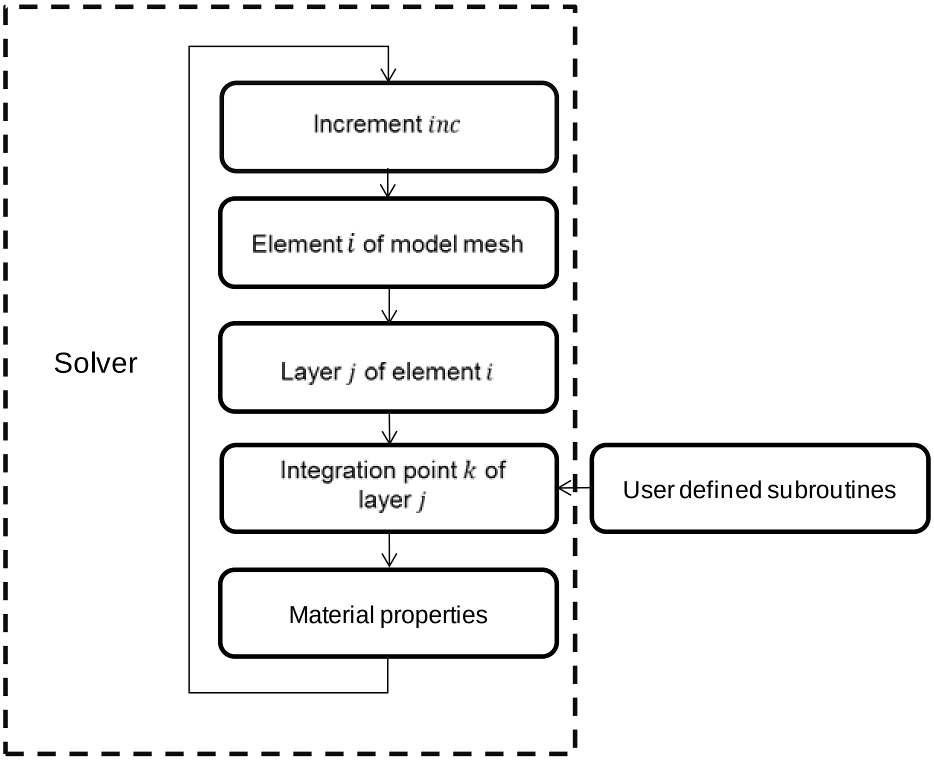

Fig. 4-5 Schematic representation of the interface between the main solver and the user defined subroutines.

- UCURE

This user subroutine is used to compute the cure kinetics, degree of cure and total heat of reaction using the equations described in section 4.2.1 and 4.2.2. The degree of cure is calculated at each increment for every element using explicit numerical integration. In addition, if the degree of cure reaches values above 0.999 the cure rate is forced to be zero, implying fully cured material.

- USPCHT

As discussed in the previous section the specific heat capacity depends on both the cure temperature and degree of cure. Therefore, the ELMVAR subroutine is used to extract the degree of cure at each integration point of the mesh as the degree of cure cannot be specified in the USPCHT subroutine. The specific heat is computed at each increment for every integration point per element in the mesh using Eqs. (4-16)- (4-20).

- ANKOND

This subroutine is used to compute the anisotropic thermal conductivity matrix of the composite. As the composite laminate is considered to be a transversely isotropic material, the diagonal elements i.e. the thermal conductivity in the three main directions are calculated according to the equations presented in section 4.2.4, whilst the remaining elements of the matrix are set to zero. The ELMVAR subroutine is also incorporated to extract the degree of cure at each integration point of the mesh. The thermal conductivity matrix is:

$$K = \begin{bmatrix} K_{11} & K_{12} & 0 \\ K_{21} & K_{22} & 0 \\ 0 & 0 & K_{33} \end{bmatrix} \tag{4-45}$$

- HOOKLW

The HOOKLW subroutine is used to define the stress-strain law. The compliance matrix $[B]^{-1}$ is first defined and the INVERT subroutine is then called to return $[B]$ so that:

$$\begin{bmatrix} \sigma_{11} \\ \sigma_{22} \\ \sigma_{33} \\ \sigma_{23} \\ \sigma_{13} \\ \sigma_{12} \end{bmatrix} = \begin{bmatrix} B_{11} & B_{12} & B_{13} & B_{14} & B_{15} & B_{16} \\ B_{21} & B_{22} & B_{23} & B_{24} & B_{25} & B_{26} \\ B_{31} & B_{32} & B_{33} & B_{34} & B_{35} & B_{36} \\ B_{41} & B_{42} & B_{43} & B_{44} & B_{45} & B_{46} \\ B_{51} & B_{52} & B_{53} & B_{54} & B_{55} & B_{56} \\ B_{61} & B_{62} & B_{63} & B_{64} & B_{65} & B_{66} \end{bmatrix} \begin{bmatrix} \varepsilon_{11} \\ \varepsilon_{22} \\ \varepsilon_{33} \\ \gamma_{12} \\ \gamma_{23} \\ \gamma_{31} \end{bmatrix} \tag{4-46}$$

The compliance matrix $[B]^{-1}$ is defined according to the transversely isotropic material properties as follows [122]:

$$\begin{bmatrix}\varepsilon_{11}\\ \varepsilon_{22}\\ \varepsilon_{33}\\ \gamma_{12}\\ \gamma_{23}\\ \gamma_{31}\end{bmatrix}=\begin{bmatrix}\frac{1}{E_{11}} & \frac{-\nu_{21}}{E_{22}} & \frac{-\nu_{31}}{E_{33}} & 0 & 0 & 0\\ \frac{-\nu_{12}}{E_{11}} & \frac{1}{E_{22}} & \frac{-\nu_{32}}{E_{33}} & 0 & 0 & 0\\ \frac{-\nu_{13}}{E_{11}} & \frac{-\nu_{23}}{E_{22}} & \frac{1}{E_{33}} & 0 & 0 & 0\\ 0 & 0 & 0 & \frac{1}{G_{12}} & 0 & 0\\ 0 & 0 & 0 & 0 & \frac{1}{G_{23}} & 0\\ 0 & 0 & 0 & 0 & 0 & \frac{1}{G_{13}}\end{bmatrix}\begin{bmatrix}\sigma_{11}\\ \sigma_{22}\\ \sigma_{33}\\ \sigma_{12}\\ \sigma_{23}\\ \sigma_{13}\end{bmatrix} \tag{4-47}$$

The elements of $[B]^{-1}$ are calculated using the equations presented in section 4.2.5. The ELMVAR subroutine is called to incorporate the dependence of the composite mechanical properties on the degree of cure.

- USHRINKAGE

The degree of cure shrinkage, the volumetric shrinkage strain as well as the directional cure shrinkage coefficient matrix is computed using the USHRINKAGE subroutine. The direction cure shrinkage strain is computed at each increment for every integration point per element in the mesh using Eqs. (4-35)- (4-39).

- ANEXP

This user subroutine is used to define the strain increments of the composite due to thermal expansion. The coefficients of thermal expansion are calculated using the respective equations. Then, the incremental thermal strain in the three main directions is calculated as follows:

$$\Delta\varepsilon_{ij}^{th}=a_{ij}^{th}T_{inc} \tag{4-48}$$

where a_{ij}^{th} is the thermal expansion coefficient and T_{inc} is the temperature increment. The thermal strain at each time increment is given by the following relation:

$$\varepsilon_{ij}^{th}=\sum_{k=1}^{inc}\Delta\varepsilon_{ij}^{th} \tag{4-49}$$

4.3 Overview

A coupled thermo-mechanical cure simulation model using the finite element analysis solver MSC.Marc has been developed. The model is three dimensional and transient. The materials considered were Hexcel G1157 pseudo unidirectional carbon fibre reinforcement and Hexcel RTM6 epoxy resin. The material properties depend on both temperature and degree of cure and the material sub-models of cure kinetics, specific heat capacity, thermal conductivity, moduli, cure shrinkage and thermal expansion were implemented in user defined subroutines UCURE, USPCHT, ANKOND, HOOKLW, USHRINKAGE and ANEXP.

5. Stochastic simulation methodology

5.1 Introduction

The stochastic simulation methodology developed and implemented in this study is presented and analysed in this chapter. The methodology presented here is used to model input parameters uncertainty and to investigate its propagation through the curing process. The stochastic processes used to model input parameters uncertainty were chosen based on the experimental results of this study. The presentation corresponds to non-intrusive stochastic simulation techniques and second order stationary Gaussian stochastic processes, i.e. processes with mean and variance independent of time or space.

5.2 Representation of input parameters uncertainty

5.2.1 Random series of observations

Surface heat transfer coefficient was modelled using random series of observations. A random series is a sequence of observations which are ordered randomly in time and thus are independent of one another presenting no serial correlation over time. The stochastic equation of a random series of observations X is the following:

$$X = \mu_r + \sigma_r y \tag{5-1}$$

where μ_r is the mean value, σ_r the standard deviation and y a set of independent identically distributed normal variables equal to the number of time steps.

5.2.2 One dimensional mean-reverting Ornstein-Uhlenbeck process

A mean-reverting stochastic process variable in time was employed to simulate tool and ambient temperature. The Ornstein-Uhlenbeck process (OU) is an autoregressive second order stationary Gaussian random process, which is widely used for modelling of mean reverting processes. These are processes that tend to return to a long term mean with speed that is proportional to the distance from it. The stochastic differential equation of an OU process S is as follows [128]:

$$dS = \lambda(\mu - S)dt + \sigma dW_t \tag{5-2}$$

Here W_t is a Brownian motion so that $W_t \sim N(0,1)$ and $dW_t \sim N(0, \sqrt{dt})$, λ controls the speed of reversion around the mean of the process, μ is the long term mean of the stochastic process and σ the process volatility. The analytical solution of Eq. (5-1) is [128]:

$$S_t = e^{-\lambda\Delta t} S_{t-1} + \left(1 - e^{-\lambda\Delta t}\right)\mu + \sigma\sqrt{\frac{\left(1 - e^{-2\lambda\Delta t}\right)}{2\lambda}} W_t \tag{5-3}$$

where Δt is the time increment. Estimation of the parameters of Eq. (5-2) using the experimental data obtained for the tool and ambient temperature was based on the maximisation of the likelihood function [128]. Maximisation of the log-likelihood function yields the following equations for the mean μ and the rate of the reversion λ respectively:

$$\mu = \frac{S_y S_{xx} - S_x S_{xy}}{N\left(S_{xx} - S_{xy}\right) + \left(S_x^2 - S_x S_y\right)} \tag{5-4}$$

$$\lambda = -\frac{1}{\Delta t} ln \frac{S_{xy} - \mu S_x - \mu S_y + N\mu^2}{S_{xx} - 2\mu S_x + N\mu^2} \tag{5-5}$$

where N is the number of samples and

$$S_x = \sum_{i=1}^{N} S_{i-1} \tag{5-6}$$

$$S_y = \sum_{i=1}^{N} S_i \tag{5-7}$$

$$S_{xx} = \sum_{i=1}^{N} S_{i-1}^2 \tag{5-8}$$

$$S_{xy} = \sum_{i=1}^{N} S_{i-1}S_i \tag{5-9}$$

$$S_{yy} = \sum_{i=1}^{N} S_i^2 \tag{5-10}$$

The volatility σ is given by:

$$\sigma = \sqrt{\frac{2\lambda\left[S_{yy} - 2aS_{xy} + a^2S_{xx} - 2\mu(1-a)\left(S_y - aS_x\right) + N\mu^2(1-a)^2\right]}{(1-a^2)N}} \tag{5-11}$$

where

$$a = e^{-\lambda\Delta t} \tag{5-12}$$

5.2.3 Two-dimensional Ornstein-Uhlenbeck field

Local tow orientation was treated as a spatial random field variable in space and its auto-covariance function was modelled using the two-dimensional Ornstein-Uhlenbeck sheet (OU) which is a variant of the stochastic process presented in section 5.2.2 appropriate for modelling spatial random fields with mean reverting features. The auto-covariance function of the two-dimensional Ornstein- Uhlenbeck sheet is defined as [129,130]:

$$C(x,y) = {\sigma_c}^2 e^{-|x_1-x_2|/b_x - |x_1-x_2|/b_y} \tag{5-13}$$

Here σ_c is the standard deviation, b_x and b_y are the correlation lengths in the x and y directions, respectively, which determine the decay rate of autocorrelation between two points of the process. Eq. (5-13) was used as the basis to discretise the resulting random field using the Cholesky factorisation, spectral decomposition and Karhunen-Loève expansion.

5.2.4 Cholesky factorisation

The covariance matrix Σ and the vector of mean values μ_c include all the information on the statistical properties of the stochastic variables and their cross-correlation. By definition, the covariance matrix Σ is symmetric and positive definite and can be expressed as:

$$\Sigma = LL^T \tag{5-14}$$

where L is a lower triangular matrix and is the Cholesky root. The product of the Cholesky root with the vector Y of independent identically distributed normal variables is a vector V that has the statistical properties of the stochastic field, and is defined as follows:

$$V = LY \tag{5-15}$$

The methodology described by Eqs. (5-14) and (5-15) is employed in two steps. First, the Cholesky root is evaluated as defined in Eq. (5-14). This step has relatively high computational cost depending on the number of stochastic variables; however, it needs to be executed only once. Realisations of the random vector Y are then generated and transformed to realisations of the vector V using Eq. (5-15). This step is of low computational cost and is executed a number of times equal to the number of required realisations of the stochastic variables.

In addition to local tow orientation, the Cholesky factorisation was used to model cure kinetics uncertainty. In this case the covariance matrix is generated using the experimental data by calculating the variance and covariance of the stochastic parameters; variance values appear along the diagonal and covariance values appear in the off-diagonal elements.

5.2.5 Spectral decomposition

The spectral decomposition method expands the random field $V(x,y)$ as a series of trigonometric functions with random phase angles as a function of its spectral density function $S(k_x,k_y)$. According to the Wiener-Khintchine theorem, the autocorrelation function of a second order stationary random process has a spectral decomposition defined by the power density function of that process. Therefore, given a two-dimensional second order stationary random field $V(x,y)$ with zero mean, autocorrelation function $C(x,y)$ and power spectral density function $S(k_x,k_y)$, the following relationships hold (Wiener-Khintchine transform) [131]:

$$S(k_x,k_y) = \frac{\int_{-\infty}^{\infty}\int_{-\infty}^{\infty} C(x,y)e^{-i(k_x x+k_y y)}\,\mathrm{d}x\mathrm{d}y}{(2\pi)^2} \tag{5-16}$$

$$C(x,y) = \frac{\int_{-\infty}^{\infty}\int_{-\infty}^{\infty} S(k_x,k_y)e^{i(k_x x+k_y y)}\,\mathrm{d}k_x\mathrm{d}k_y}{(2\pi)^2} \tag{5-17}$$

where $x,\ y$ are coordinates over the space domain and k_x and k_y the corresponding wave numbers over the frequency domain. The power spectral density $S(k_x,k_y)$ is a real symmetric non-negative function. Therefore, the bi-quadrant power spectral density $G(k_x,k_y)$ can be defined as follows [131]:

$$G(k_x,k_y) = 2S(k_x,k_y) \tag{5-18}$$

The spectral representation of the random field $V(x,y)$ is given by the following relation [132-134]:

$$\begin{aligned} V(x,y) = \int_{-\infty}^{\infty}\int_{-\infty}^{\infty} & \left[cos(k_x x + k_y y)du(k_x,k_y) \right. \\ & \left. + sin(k_x x + k_y y)dv(k_x,k_y)\right] \end{aligned} \tag{5-19}$$

where $u(k_x, k_y)$ and $v(k_x, k_y)$ are real independent Gaussian stochastic fields with zero mean and orthogonal increments $du(k_x, k_y)$ and $dv\,(k_x, k_y)$ that satisfy the following expression:

$$E\left[du^2(k_x, k_y)\right] = E\left[dv^2(k_x, k_y)\right] = 2S(k_x, k_y)dk_x dk_y \tag{5-20}$$

Algebraic manipulations of Eq. (5-19) presented in detail in [134], lead to

$$\begin{aligned}\hat{V}(x, y) = \sqrt{2}\sum_{n_x=0}^{N_x-1}\sum_{n_y=0}^{N_y-1}\Big[&A_{n_x n_y} cos\left(k_{xn_x}x + k_{yn_y}y + \phi^{(1)}_{n_x n_y}\right)\\ &+ \tilde{A}_{n_x n_y} cos\left(k_{xn_x}x - k_{yn_y}y + \phi^{(2)}_{n_x n_y}\right)\Big]\end{aligned} \tag{5-21}$$

where:

$$A_{n_x n_y} = \sqrt{2S\left(k_{xn_x}, k_{yn_y}\right)\Delta k_x \Delta k_y} \tag{5-22}$$

$$\tilde{A}_{n_x n_y} = \sqrt{2S\left(k_{xn_x}, -k_{yn_y}\right)\Delta k_x \Delta k_y} \tag{5-23}$$

$$k_{xn_x} = n_x \Delta k_x \quad ; \quad k_{yn_y} = n_y \Delta k_y \tag{5-24}$$

$$\Delta k_x = \frac{k_{xu}}{N_x} \quad ; \quad \Delta k_y = \frac{k_{yu}}{N_y} \tag{5-25}$$

and:

$$A_{0n_y} = A_{n_x0} = 0 \quad \text{for} \quad n_x = 0,1,\dots N_x - 1$$
$$\text{and} \quad n_y = 0,1,\dots N_y - 1 \qquad (5\text{-}26)$$

$$\tilde{A}_{0n_y} = \tilde{A}_{n_x0} = 0 \quad \text{for} \quad n_x = 0,1,\dots N_x - 1$$
$$\text{and} \quad n_y = 0,1,\dots N_y - 1 \qquad (5\text{-}27)$$

Eqs. (5-25) and (5-26) are equivalent to:

$$S(0,k_y) = S(k_x,0) = 0 \qquad (5\text{-}28)$$

Thus, the power spectral density function is discretised in N_x × N_y intervals. Here k_{xu} and k_{yu} denote the upper cut-off wave numbers in the frequency domain, implying that the power spectral density function is considered to be zero outside the following region:

$$-k_{xu} \leq k_x \leq k_{xu} \text{ and } -k_{yu} \leq k_y \leq k_{yu} \qquad (5\text{-}29)$$

Here $\phi_{n_xn_y}^{(1)}$ and $\phi_{n_xn_y}^{(2)}$ are different sets of random phase angles distributed uniformly over the interval $[0,2\pi]$. The conditions set in Eqs. (5-26) and (5-27) are necessary to ensure that the mean value and the autocorrelation function of a sample function are identical to the respective targets as N_X, $N_y \rightarrow \infty$.

In the case of the Ornstein-Uhlenbeck sheet, described by Eq. (5-13), the spectral density function is:

$$S(k_x,k_y) = \frac{\sigma^2}{\pi^2}\frac{b_xb_y}{(1+b_x^2k_x^2)(1+b_y^2k_y^2)} \qquad (5\text{-}30)$$

5.2.6 Karhunen- Loève expansion

The Karhunen- Loève expansion (K-L) is a series representation utilising eigenfunctions as the orthogonal basis [98-99]. For a second order stationary random field $V(x,y)$ defined on a probability space (Ω, A, P) and indexed on a bounded domain D the random process can be expanded as follows [10,134-136]:

$$V(x,y) = \mu + \sum_{i=1}^{M} \sqrt{\lambda_i} f_i(x,y) \xi_i \tag{5-31}$$

in which λ_i and $f_i(x,y)$ are the M larger eigenvalues and the corresponding eigenfunctions of the covariance function $C(x,y)$, whereas ξ_i is a set of independent identically distributed normal variables. Given that the covariance function is bounded, symmetric and positive definite, it has the following eigen-expansion [137]:

$$C(x_1,y_1;x_2,y_2) = \sum_{i=1}^{\infty} \lambda_i\, f_i(x_1,y_1) f_i(x_2,y_2) \tag{5-32}$$

The eigenvalues and the corresponding eigenfunctions are the solution of the Fredholm integral equation defined as [10]:

$$\int_D V(x_1,y_1;x_2,y_2)\, f_i(x_2,y_2) dx_2 dy_2 = \lambda_i f_i(x_1,y_1) \tag{5-33}$$

Eq. (5-33) arises from the fact that the eigenfunctions form a complete orthogonal set satisfying the relation [135,136]:

$$\int_D f_i(x,y)\, f_j(x,y) dx dy = \delta_{ij} \tag{5-34}$$

where δ_{ij} is the Kronecker delta function.

Implementation of this discretisation technique is often hindered by the difficulty to solve the Frefholm integral equation shown in Eq. (5-33). Analytical solutions are available only for a limited number of covariance functions [136]. In the general case, numerical techniques are used to approximate the eigenvalues and the eigenfunctions such as the wavelet- Galerkin scheme [136]. The efficiency and the accuracy of the technique is hence dictated by the accuracy of the eigen-pairs as well as the value of M. It has been shown that the performance of K-L is high only in the case of highly correlated stochastic fields, where only a few terms, corresponding to the M larger eigenvalues are required to capture accurately variability propagation of the random field [134,135].

In the case of a stochastic process defined over the interval $[-\alpha,\alpha]$ and $[-\beta,\beta]$ over the x and y direction, with a covariance function as defined by Eq.(5-13), the eigenvalues and the eigenfunctions are obtained by solving the integral equation (Eq. (5-33)) analytically [9]:

for odd i:

$$\lambda_i = \sigma^2\left(\frac{2b_x}{\omega_{xi}^2+b_x^2}\frac{2b_y}{\omega_{yi}^2+b_y^2}\right) \tag{5-35}$$

$$f_i(x,y) = \frac{\cos(\omega_{xi}x)}{\sqrt{a+\frac{\sin(2\omega_{xi}a)}{2\omega_{xi}}}}\frac{\cos(\omega_{yi}y)}{\sqrt{\beta+\frac{\sin(2\omega_{yi}a)}{2\omega_{yi}}}} \tag{5-36}$$

for even i:

$$\lambda_i{}^* = \sigma^2\left(\frac{2b_x}{\omega_{xi}^{*2}+b_x^2}\frac{2b_y}{\omega_{yi}^{*2}+b_y^2}\right) \tag{5-37}$$

$$f_i{}^*(x,y) = \frac{\cos(\omega_{xi}^*x)}{\sqrt{a+\frac{\sin(2\omega_{xi}^*a)}{2\omega_{xi}^*}}}\frac{\cos(\omega_{yi}^*y)}{\sqrt{\beta+\frac{\sin(2\omega_{yi}^*a)}{2\omega_{yi}^*}}} \tag{5-38}$$

where ω_{ij} and ω_{ij}^* are computed by the following transcendental equations:

$$b_j - \omega_{ij} \tan(\omega_{ij} a) = 0 \tag{5-39}$$

$$\omega_{ij}^* + b_j \tan(\omega_{ij}^* \beta) = 0 \tag{5-40}$$

for $j = x, y$.

5.3 Monte Carlo Scheme

Monte Carlo (MC) is the most common stochastic simulation method used in the context of composite manufacturing, due to its simplicity [4,5,13,17]. In this method N_{MC} random samples of the input stochastic parameters are generated using a random number generator and appropriate treatment to produce variables with the correct statistical behaviour. These are subsequently utilised to execute the direct model leading to a population of the response vector. Thus, the deterministic model runs N_{MC} times. The process outcome uncertainty is then characterised by the distribution of output parameters and its moments. For instance, if x_i is the temperature overshoot of a thick laminate during its cure cycle, then the unbiased estimates of the mean value μ_{MC} and standard deviation σ_{MC} of the sample are defined as follows:

$$\mu_{MC} = \frac{\sum_{i=1}^{N_{MC}} x_i}{N_{MC}} \tag{5-41}$$

$$\sigma_{MC} = \sqrt{\frac{\sum_{i=1}^{N_{MC}} (x_i^2 - \mu^2 N_{MC})}{N_{MC} - 1}} \tag{5-42}$$

The accuracy of the method depends on the number of samples generated. Given that the mean value of a parameter converges faster than its standard deviation, the number of samples is determined by the convergence of the standard deviation. In particular, the estimate of standard deviation is inversely proportional to $\sqrt{N_{MC}}$. A respectively large number of the deterministic model runs are required to ensure convergence and accuracy, implying high computational cost, especially in the case of large-scale stochastic problems [134]. Given that MC is providing unbiased estimates of the statistical properties of the response vector, it is often used as a benchmark technique for validating other stochastic simulation methods.

The Monte Carlo scheme was employed in this work to investigate the effect of all three input parameters (cure kinetics uncertainty, fibre misalignment, boundary conditions uncertainty) on the outcome of the manufacturing process.

5.4 Probabilistic Collocation Method

The Probabilistic Collocation Method (PCM) [138] has been developed to reduce the cost of computationally expensive stochastic problems. In general, the collocation method is a typical technique in mathematics for reducing a complex problem to a simpler form [139]. The main concept of PCM is to construct a response surface for every output parameter, as a function of uncertain parameters in the form of orthogonal polynomials, called the polynomial chaos. The polynomial chaos is a function of uncorrelated Gaussian variables and is defined as [9,10]:

$$\begin{aligned} u = a_0\Gamma_0 + \sum_{i_1=1}^{\infty} a_{i_1}\Gamma_1\left(\xi_{i_1}\right) \\ + \sum_{i_1=1}^{\infty}\sum_{i_2=1}^{i_1} a_{i_1 i_2}\Gamma_2\left(\xi_{i_1},\xi_{i_2}\right) \\ + \sum_{i_1=1}^{\infty}\sum_{i_2=1}^{i_1}\sum_{i_3=1}^{i_2} a_{i_1 i_2 i_3}\Gamma_3\left(\xi_{i_1},\xi_{i_2},\xi_{i_3}\right) + \cdots, \end{aligned} \tag{5-43}$$

where $\Gamma_p\left(\xi_{i_1},\ldots.,\xi_{i_p}\right)$ is the polynomial chaos of order p and $\left\{\xi_{i_k}\right\}_{k=1}^{M}$ a set of independent identically distributed normal variables. The polynomials given in Eq. (5-43) are orthogonal with respect to the Gaussian probability measure $e^{-\frac{1}{2}\xi^T\xi}d\xi$, which implies that in the case of Gaussian variables the polynomial chaos is defined as a set of Hermite polynomials. Therefore, the polynomial chaos of order p can be expressed as [10]:

$$\Gamma_p\left(\xi_{i_1},\ldots.,\xi_{i_p}\right) = (-1)^p \frac{\partial^p}{\partial\xi_{i_1},\ldots.,\partial\xi_{i_p}} e^{-\frac{1}{2}\xi^T\xi} \tag{5-44}$$

Details concerning the construction of the polynomial chaos can be found in [10].

The probabilistic collocation method is used to compute the unknown coefficients in the polynomial chaos expansion. The residuals between the actual model outputs and the corresponding response surfaces are required to be zero at a set of collocation points. Thus, the unknown coefficients are estimated by equating the model outputs to the corresponding polynomial chaos expansions at a set of collocation points in the sample space [9]. The number of collocation points is at least equal to the number of unknown coefficients. Therefore, for each output parameter a set of linear equations results with the respective polynomial chaos coefficients as the unknowns. Linear solvers can be used to solve these equations. Having constructed a response surface for each output parameter, statistical analysis is carried out to quantify output parameters uncertainty. Following this strategy, the size of the stochastic problem is significantly reduced, since execution of the deterministic model is required only a few times, at the set of collocation points.

The collocation points are combinations of the roots of the next higher order Hermite polynomial than the order of the response surface. This selection methodology is identical to Gaussian quadrature for integral estimation [9,139]. For instance, the first to third order Hermite polynomials are:

$$H_1(\xi) = \xi \tag{5-45}$$

$$H_2(\xi) = \xi^2 - 1 \tag{5-46}$$

$$H_3(\xi) = \xi^3 - 3\xi \tag{5-47}$$

The collocation points for a second order response surface are combinations of the roots of the third order Hermite polynomial (-$\sqrt{3}$, 0, +$\sqrt{3}$).

Special care must be taken so that the collocation points are selected from regions of high probability. In general, it is advised that the collocation points should be close to the origin (0,0) and be symmetric with respect to the origin [140]. In addition, it is important to include the origin, since in the case of Gaussian variables it corresponds to the region of highest probability [9]. Therefore, in the case of a fourth order response surface it is desirable to include the origin, even if it is not a root of the fifth order Hermite polynomial. This methodology is illustrated in Fig. 5-1. The largest discrepancy between the response surface and the actual model occurs at regions of low probability, thus only a small error is produced. The collocation method can be sometimes unstable; therefore, a modified regression based collocation approach is usually employed to improve accuracy. Given that several combinations of collocation points can be chosen, the number of collocation points used is higher than the number of the unknown coefficients, implying that the effect of each collocation point is reduced [9]. The steps in performing a stochastic analysis using PCM, are presented in Fig. 5-2.

The Probabilistic Collocation method was applied to quantify the effect of cure kinetics uncertainty on temperature overshoot variability. Furthermore, PCM was implemented to study the influence of surface heat transfer coefficient and tool temperature variability on cure time. In both cases, PCM was compared to MC in terms of accuracy and efficiency.

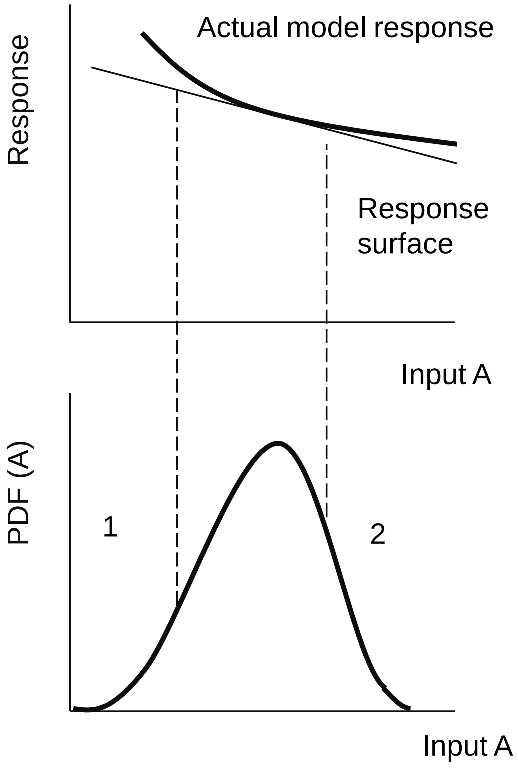

Fig. 5-1 Collocation points selection at high probability regions.

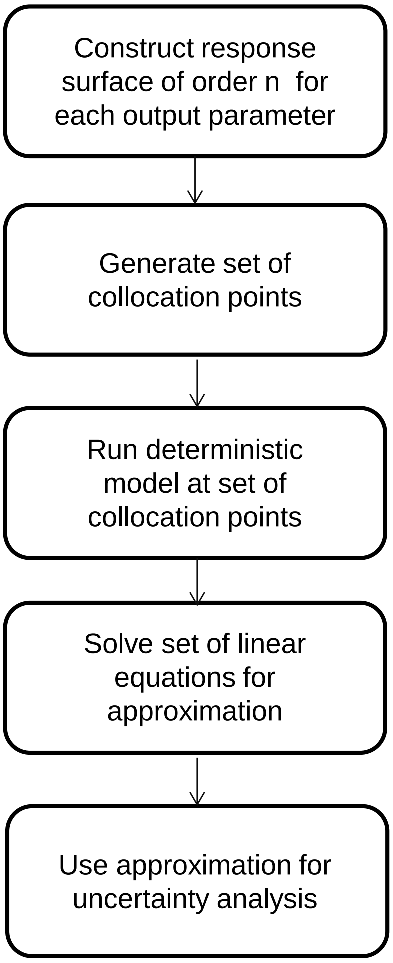

Fig. 5-2 Schematic representation of Probabilistic Collocation Method.

5.5 Implementation of stochastic simulation methodology

In this section the framework developed to couple the stochastic simulation methodology with the FEA solver for the investigated input parameters is described. Examples of the developed interfaces between the stochastic simulation models and the FEA solver can be found in Appendix B.

5.5.1 Cure kinetics uncertainty/ boundary conditions uncertainty

Investigation of the effect of cure kinetics uncertainty and boundary conditions uncertainty on the process outcome was carried out using both MC and PCM. Consequently, an interface was developed to integrate the FE cure model described in Chapter 4 with the two stochastic simulation models. The interface was implemented in FORTRAN and its functionality is shown schematically in Figure 5-3.

The stochastic simulation model generates realisations of the stochastic parameters. The interface reads the MSC.MARC input file and user defined subroutines developed to carry out the stochastic cure simulation and identifies the location of the stochastic variables. A new input file and set of user subroutines are written using the generated realisations of the stochastic parameters. The solver is then called and a cure simulation is executed using the new input file and user subroutine. At the end of each simulation the parameters of interest are saved in a matrix. In the case of MC realisations of the input parameters are generated randomly and the process is iterated a number of times until the mean and standard deviation of the output parameters converge. In the case of PCM realisations of the stochastic variables are generated at a set of collocation points and the process is iterated a number of times equal to the number of collocation points. The values of the output parameters calculated at the set of collocation points are then used to construct the corresponding surrogate models. A statistical analysis is then performed using the developed surrogate models as described in section 5.4. Table 5-1 summarises the input and output parameters and the corresponding stochastic simulation method used for investigation of the influence of cure kinetics uncertainty and boundary conditions uncertainty on the process outcome using the interface illustrated in Figure 5-3.

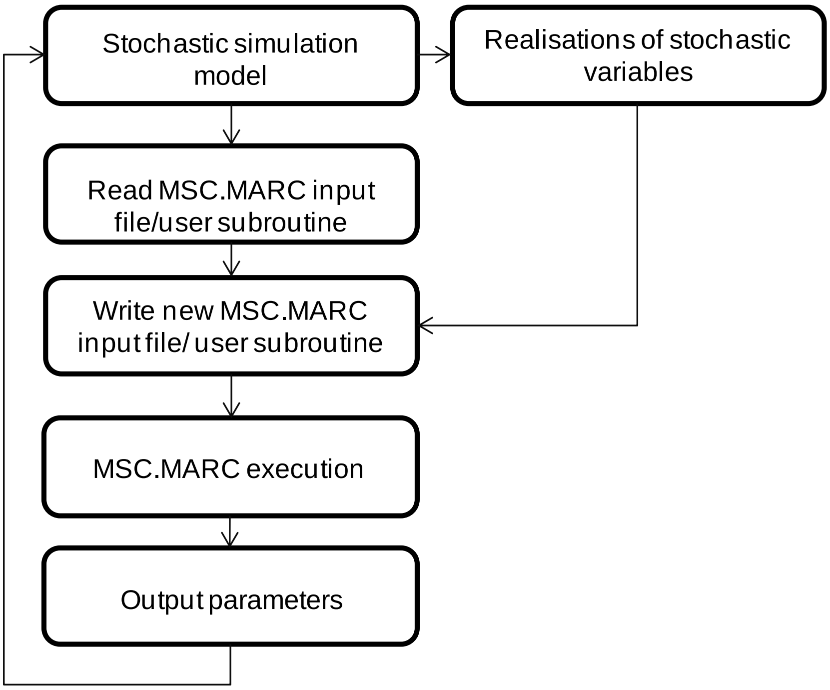

Fig. 5-3 Interface between stochastic simulation model and FEA solver: cure kinetics uncertainty/ boundary conditions uncertainty.

Table 5-1 I/O for interface between stochastic simulation model and FEA solver; cure kinetics uncertainty, boundary conditions uncertainty.

Case study	Stochastic variables	Output parameters	Stochastic simulation method
Cure kinetics uncertainty	Activation energy, E_2	Temperature overshoot	Monte Carlo/ Collocation
	Reaction order, m		
	Initial degree of cure, a_o		
Cure kinetics uncertainty	Activation energy, E_2	Cure time	Monte Carlo
	Reaction order, m		
	Initial degree of cure, a_o		
Boundary conditions uncertainty	Tool temperature	Cure time	Monte Carlo
	Ambient temperature		
	Surface heat transfer coefficient		
Boundary conditions uncertainty	Surface heat transfer coefficient	Cure time	Collocation
	Tool temperature		

5.5.2 Fibre misalignment

An interface between the Monte Carlo scheme and the thermo-mechanical finite element based cure simulation model was developed to allow quantification of the effect of fibre misalignment on residual stresses generation and shape distortion. The interface was developed in FORTRAN and its functionality is illustrated in Figure 5-4. The stochastic simulation model generates realisations of local tow orientation for each layer of the fabric incorporating spatial autocorrelation. Realisations of tow orientation between each layer are generated independently implying that no nesting effects are considered. These realisations are then saved in a number of text files equal to the number of the layers of the fabric. Subsequently, the FEA solver is called and a cure simulation is executed. During the execution of the process simulation, the user defined subroutine developed to incorporate the constitutive material models is reading the generated realisations in order to incorporate fibre misalignment in the cure simulation model. Incorporation of fibre misalignment is carried out by modifying the thermal conductivity matrix, compliance tensor, cure shrinkage coefficient matrix and thermal expansion coefficient matrix (section 7.3.1.). At the end of each simulation the output parameters are saved in a matrix. This procedure is iterated until the mean and the standard deviation of the investigated output parameters converge. Table 5-2 summarises the input and output parameters used for investigation of the effect of fibre misalignment on the process outcome using the interface illustrated in Figure 5-4.

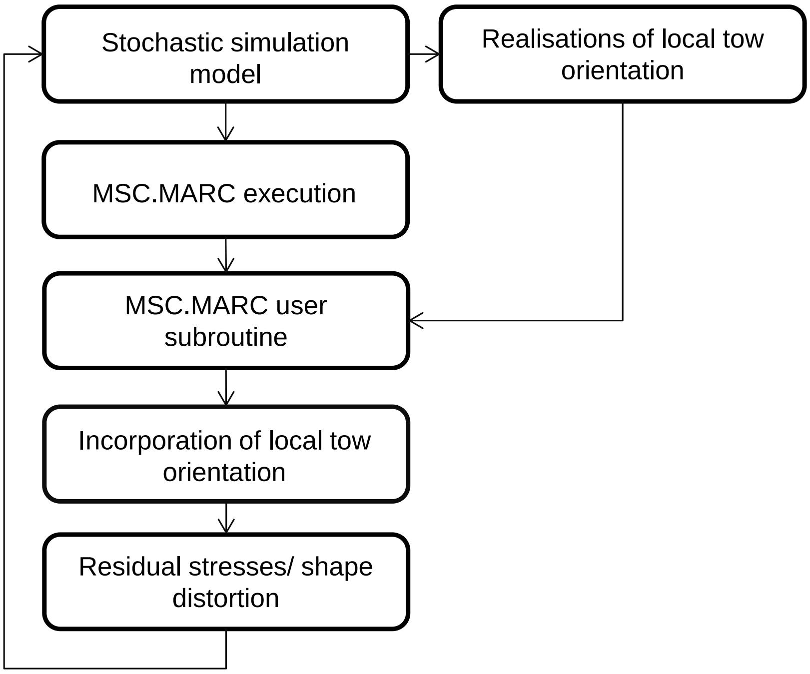

Fig. 5-4 Interface between stochastic simulation model and FEA solver: fibre misalignment.

Table 5-2 I/O for interface between stochastic simulation model and FEA solver; fibre misalignment.

Stochastic variables	Output parameters	Stochastic simulation method
Local tow orientation	Maximum longitudinal residual stress	Monte Carlo
	Corner angle	
	Twist angle	

5.6 Overview

The stochastic simulation methodology presented here was implemented to carry out the stochastic cure simulation for the different case studies. K-L has the potential to represent a stochastic field with a considerably smaller number of independent normal variables compared to Cholesky factorisation and spectral decomposition. However, K-L can perform accurately only in the case of highly correlated random fields, unlike the other two techniques which are not limited by the correlation lengths of the random field. Two stochastic simulation schemes were developed; the traditional Monte Carlo scheme and the Probabilistic Collocation Method. Monte

Carlo is the simplest stochastic simulation scheme and is not limited by the dimension of the problem but due to its random nature is computationally expensive. On the contrary, the collocation method has the potential to offer a solution with considerably lower computational cost; however, if the dimension of the problem is large, the collocation method is limited by the large number of polynomial chaos coefficients. For instance, a four-dimensional third order polynomial is consisted of thirty four terms. Due to its unbiased estimates, Monte Carlo is used as a benchmark method to assess the collocation method in terms of accuracy.

Two interfaces were developed to link the cure simulation model with the corresponding stochastic simulation models for the different case studies. The first interface allows quantification of the effect of cure kinetics and boundary conditions uncertainty on the process outcome and was used to couple the FEA cure model with both MC and PCM. The second interface allows investigation of the influence of fibre misalignment on residual stress formation and shape distortion and was used to integrate the FEA cure simulation model with MC.

6. Stochastic simulation of the influence of cure kinetics uncertainty on temperature overshoot in composites cure

6.1 Introduction

The cure process can be potentially influenced by resin behaviour variability due to variations in handling and storage conditions. Naturally these effects can play a role in cure process defects such as severe temperature overshoots or under-cure and also introduce variability in residual stresses/shape distortion. The effect of cure temperature variations and cure kinetics uncertainty on cure time has been investigated in a pure simulation study by coupling a cure kinetics model with a Latin Hypercube sampling scheme showing that cure temperature variations tend to dominate cure time variability [7]. Furthermore, taking into account uncertainty in the optimisation of the cure process, has shown that optimal cure time increases with increasing variability [141]. These results, which are based on simulation and hypothesised levels of uncertainty, gain significant practical importance when their conclusions are combined with experimental studies of uncertainty in cure kinetics. In addition to material behaviour and process parameters uncertainty, cure kinetics can show significant variations due to experimental characterisation and data reduction discrepancies [97].

In this chapter, results from the quantification of cure kinetics uncertainty due to variable resin handling/storage conditions and investigation of its propagation through the manufacturing process are presented, with a focus on the influence on temperature overshoot. A series of experiments was carried out using Differential Scanning Calorimetry (DSC) to characterise cure kinetics uncertainty of Hexcel RTM6 epoxy resin. The variability in experimental behaviour is attributed to certain parameters of cure kinetics as expressed by a phenomenological model and the corresponding stochastic object is developed. The resulting stochastic simulation problem is addressed by coupling the cure simulation model presented in Chapter 4 with conventional Monte Carlo (MC) and an implementation of the Probabilistic Collocation Method (PCM) (Chapter 5). The Cholesky factorisation described in detail in section 5.2.4 is employed to model input parameters uncertainty. Two case studies are investigated; cure simulation of neat resin and the cure process of a thick carbon fibre-epoxy laminate. In both cases, the two stochastic simulation approaches are compared in terms of accuracy and efficiency.

6.2 Analysis of cure kinetics uncertainty

Investigation of cure kinetics uncertainty required a series of experiments using Differential Scanning Calorimetry (DSC). The aim was to quantify cure kinetics uncertainty by fitting the experimental data with the cure kinetics model described in Chapter 4. The variability in experimental behaviour was attributed to certain parameters of cure kinetics as expressed by a phenomenological model and the corresponding stochastic object was developed.

6.2.1 Experimental results

A series of DSC experiments was carried out using a TA-instruments DSC Q200 apparatus (section 3.3). Dynamic heating runs were conducted at a constant heating rate in order to determine the total heat of reaction released during the dynamic cure and the evolution of the degree of cure as well as of the reaction rate for all tests carried out. Samples from four different batches were tested. Tests were duplicated within each batch. All samples were within their lifetime. All DSC tests were carried out at a heating rate of 1ºC/min from 80 ºC to 240 ºC after equilibration at the initial temperature. The degree of cure and the corresponding cure reaction rate were computed by integrating the heat flow versus time data using an iterative baseline [104] as described in section 3.3.

Fig. 6-1 illustrates the results expressed as reaction rate versus temperature for the eight tests carried out. All curves had the same qualitative characteristics with a peak at intermediate temperatures and a shoulder towards the end of the reaction. The main peak of the reaction is slightly asymmetric and ends with a plateau at a low reaction rate. This is followed by a drop to negligible reaction at very high temperatures. The repeatability is very high within the same batch with curves being almost identical. In particular, the absolute differences between curves of the same batch for values of degree of cure of 20%, 40%, 60% and 80% varied from 8×10^{-6} to 2×10^{-5} s^{-1}, which was more than one order lower than the values of cure reaction rate obtained in the experiments. This shows that the experimental and signal analysis method induced negligible variations to the results. In contrast, significant variability can be observed in the comparison between batches. This variability is manifested in the maximum reaction rate, the position of the maximum, the temperature at which the reaction starts and the temperature of the high temperature shoulder.

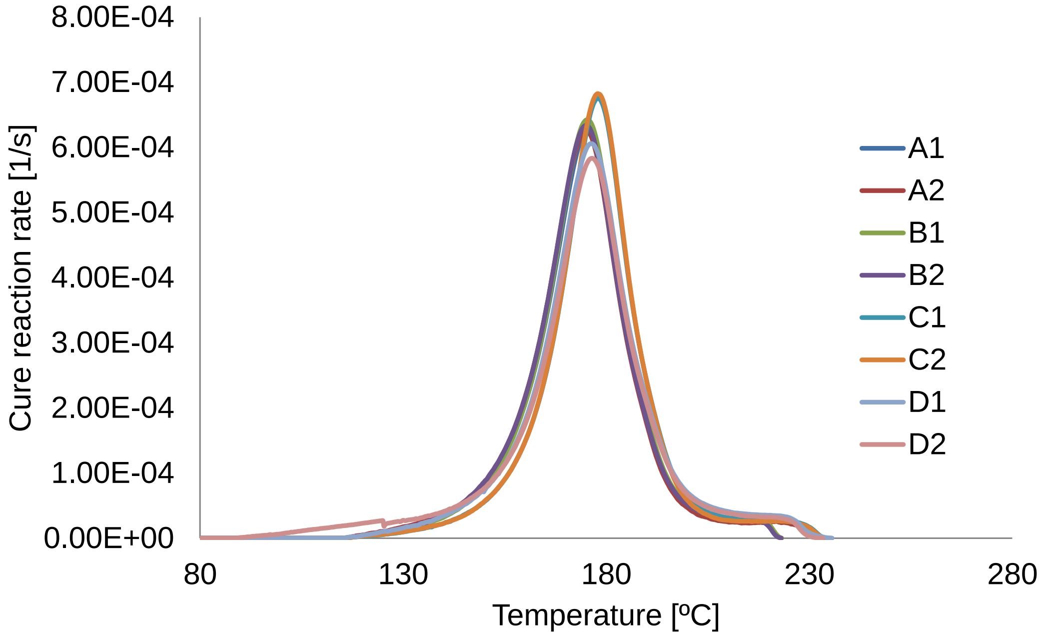

Fig. 6-1 Evolution of reaction rate as a function of temperature during dynamic cure at 1ºC/min. Letters denote the different batches of resin and numbers different samples within the same batch.

6.2.2 Quantification of cure kinetics uncertainty

The procedure for the estimation of the cure kinetics model parameters for the different DSC tests is shown schematically in Fig. 6-2. The parameters in Eqs. (4.11)- (4.15) were estimated using the hybrid Genetic Algorithm implemented in the Solver Add-in of Microsoft Excel [142]. In addition to these parameters the procedure was utilised to estimate the initial degree of cure, which is involved in the kinetics model as the initial condition of the integration. The overall model for the kinetics parameters was obtained by carrying out an overall fitting based on the published values for the resin system presented in section 4.2.2 (Tables 4-1 and 4-2), in order to define relatively narrow ranges for the search. The mean value of the total heats of reaction computed after integration of each experimental curve was used to obtain an initial guess for the initial degree of cure. The determination of the cure model parameters and initial degree of cure for each sample was then followed by fitting each experimental curve to the cure kinetics model. This procedure provided estimation of the mean value μ and standard deviation σ of each parameter. Table 6-1 reports the values of the kinetics parameters estimated following this procedure. A sensitivity analysis was carried out by using the cure kinetics model described in section 4.2.2 to determine which of the parameters should be considered as stochastic. Each parameter was varied by one positive (+σ) and one negative (-σ) standard deviation and the average relative absolute differences of predicted reaction rates from the cure kinetics model using the estimated parameter value were computed. The mean between these two values was used as an indication of the model sensitivity to the level of variability of each of the model parameters (Table 6-1). It should be noted that this relative difference corresponds to increments equal to one standard deviation around the mean, i.e. a 68% probability assuming a normal distribution of the variables.

The activation energy E_2, the reaction order m and the initial degree of cure a_o introduced the highest discrepancies, presenting a relative difference of 11%, 10% and 4%, respectively, whilst the rest of parameters induced discrepancies lower than 3%. Consequently, the main sources of uncertainty in the experimental results are the variability in the initial degree of cure a_o, activation energy E_2 and reaction order m.

Figures 6-3, 6-4 and 6-5 illustrate the sensitivity analysis results for the three variables. The initial degree of cure influences the temperature of reaction onset introducing a shift to the cure reaction rate - temperature curve. The reaction order m and the activation energy E_2 mainly affect the height and the position of the main reaction rate peak. Figures 6-6 and 6-7 present the sensitivity analysis results for the n^{th} order term parameters in Eq. (4.11). As it can be observed, the reaction order n_2 affects the height of the main cure reaction rate peak, whilst the reaction energy E_1 influences the height and the position of the main reaction rate peak as well. However, given the observed spread of values, they introduce relatively lower discrepancies compared to E_2 , m and a_o (Table 6-1), and therefore can be considered as deterministic.

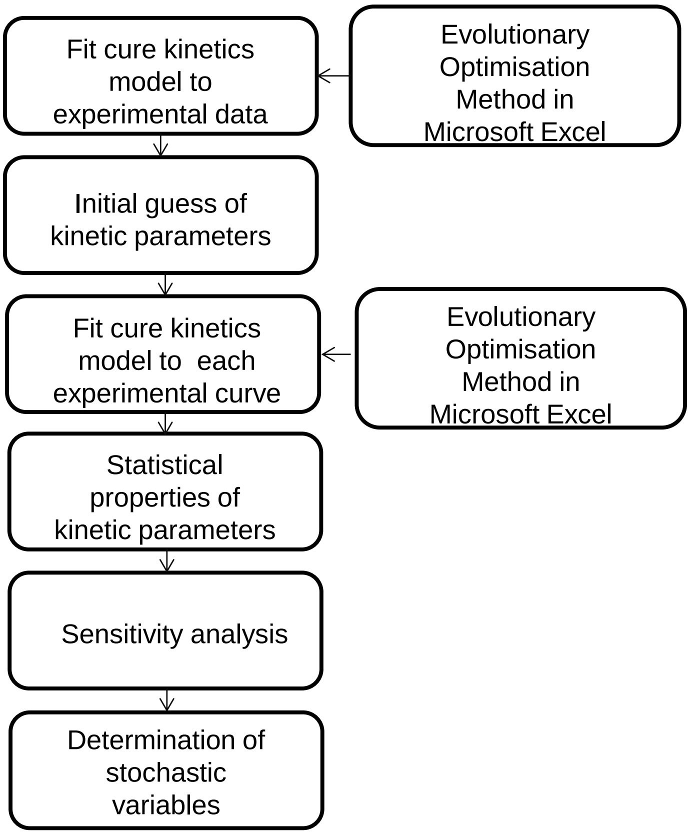

Fig. 6-2 Schematic representation of methodology for quantification of cure kinetics uncertainty.

Table 6-1 Estimated kinetics parameters, standard deviation of kinetics parameters, coefficient of variation of kinetics parameters, sensitivity analysis results.

Parameter	value	σ	σ/μ [%]	relative difference [%]
E_2 [J/mol]	57820	600	1	11
m	1.29	0.094	7	10
a_o	0.033	0.006	19	4
A_1 [1/s]	19000	677	3.5	0.4
A_2 [1/s]	22080	583	2.6	1.7
A_D [1/s]	6.76E+18	2.75E+17	4	0.02
E_1 [J/mol]	72900	897	1	2.5
E_D [J/mol]	138000	3155	2	0.5
n_1	1.97	0.18	9	0.2
n_2	1.53	0.09	6	2
b	0.4524	0.05	11	0.7
w [1/K]	0.00047	8.3E-5	9	0.5
g	0.029	0.006	19	0.4

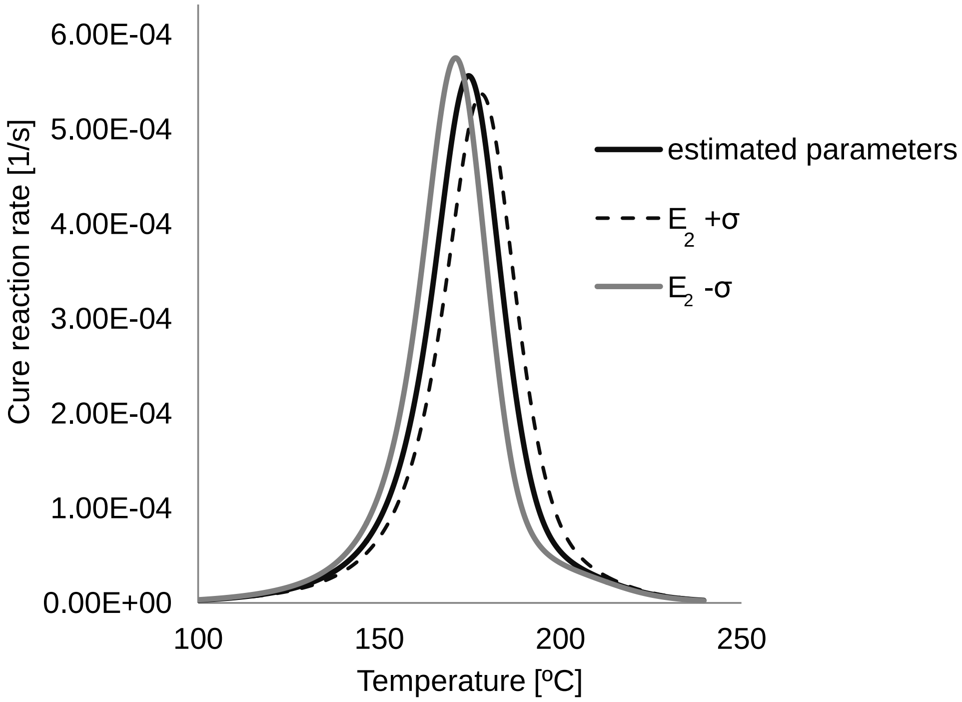

Fig. 6-3 Sensitivity analysis results; reaction energy E_2.

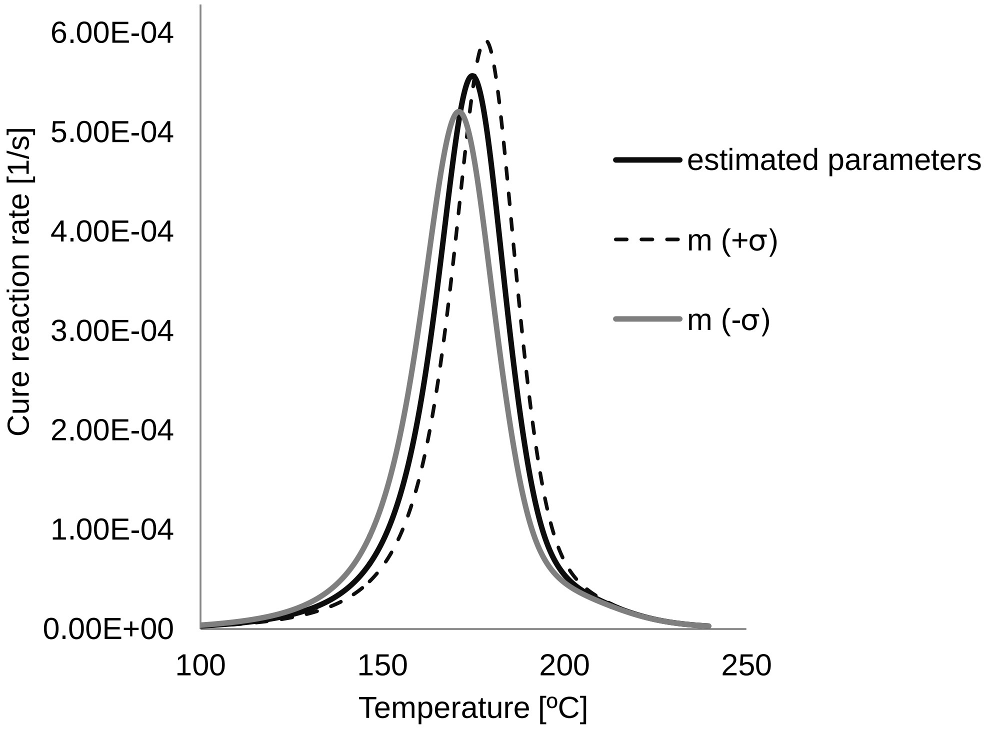

Fig. 6-4 Sensitivity analysis results; reaction order m.

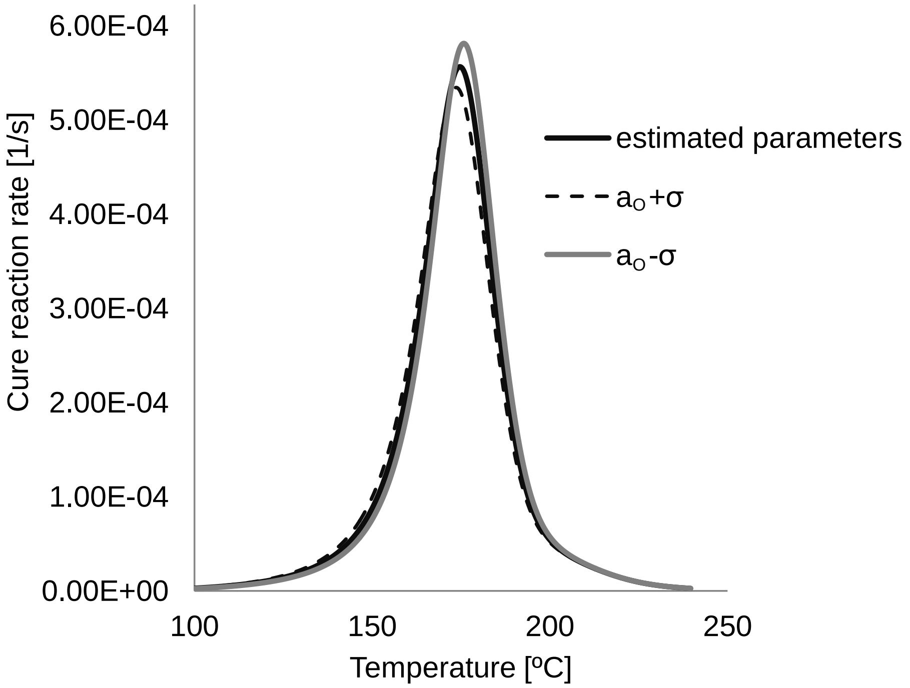

Fig. 6-5 Sensitivity analysis results; initial degree of cure a_o.

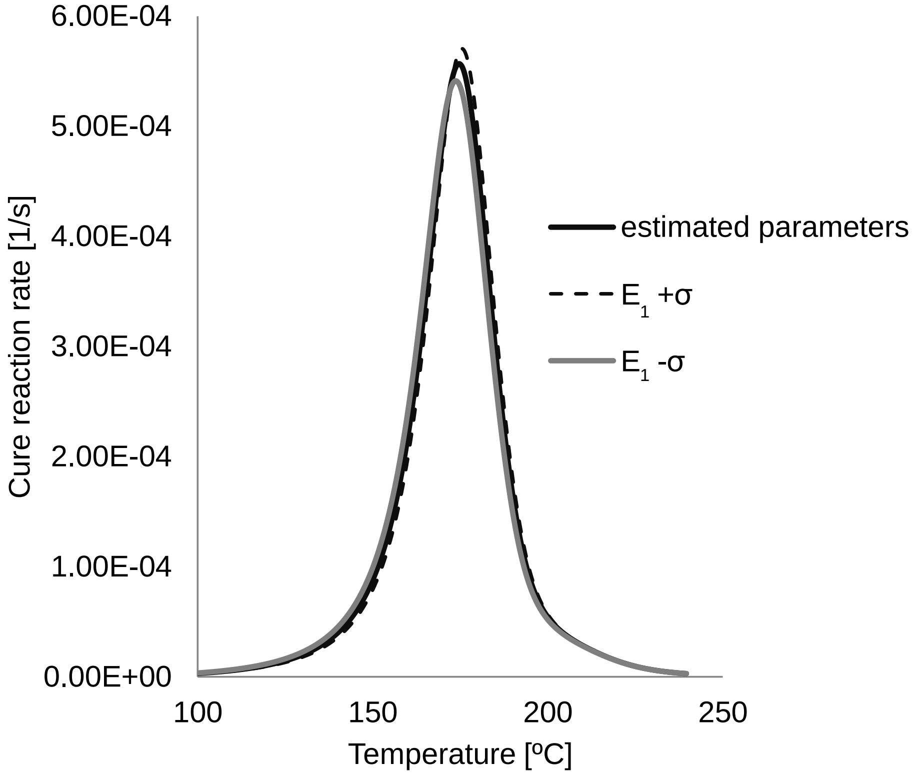

Fig. 6-6 Sensitivity analysis results; reaction energy E_1.

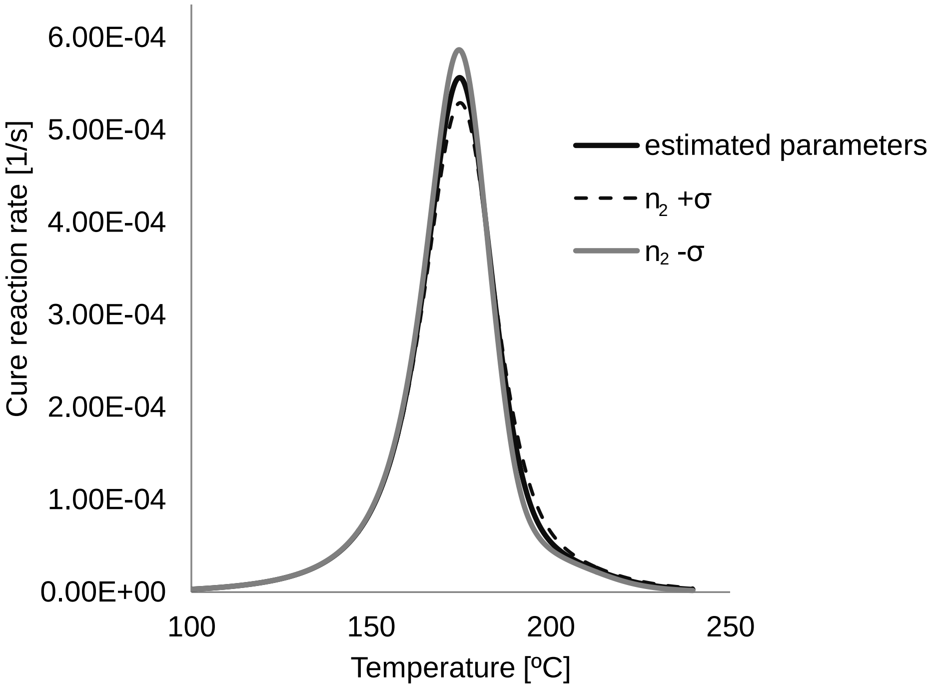

Fig. 6-7 Sensitivity analysis results; reaction order n_2.

6.2.3 Statistical properties of cure kinetics

The basic statistical properties of the three stochastic variables are summarised in Table 6-2. The initial degree of cure presents the highest level of variation among the three stochastic variables. This can be attributed to thermal history variations between the different batches during their storage and transport. The activation energy E_2 and the reaction order m are strongly correlated, whilst a_o and m show moderate correlation (Table 6-3).

Table 6-2 statistical properties of uncertain parameters.

variables	a_o	E_2 [J/mol]	m
μ	0.033	57820	1.29
σ	0.006	600	0.094
μ/σ [%]	18	1	7

Table 6-3 Correlation matrix of kinetics parameters.

variables	a_o	E_2	m
a_o	1	-0.09	0.55
E_2	-0.09	1	-0.84
m	0.55	-0.84	1

The Kolmogorov-Smirnov goodness of fit test was carried out to investigate which statistical distribution is suitable to fit the stochastic variables, due to the limited number of experimental data.

The stochastic variable Ψ, with $\psi_1, \psi_2, \ldots, \psi_N$ values is considered. If $\Phi^*(\psi)$ is the cumulative distribution and $\Phi(\psi)$ the corresponding cumulative function of the statistical distribution for which the goodness of fit test is carried out for values $\leq \psi$, then the maximum absolute difference between the observed and expected cumulative distribution for values $\leq \psi$ is the following [143]:

$$D_N(\psi) = max|\Phi^*(\psi) - \Phi(\psi)| \quad (6\text{-}1)$$

If the value of $D_N(\psi)$ is high, then the hypothesis is rejected and Ψ does not follow the statistical distribution for which the analysis is carried out. In particular, the hypothesis is rejected if $D_N(\psi) \geq D(\psi)$, where $D(\psi)$ is the Kolmogorov-Smirnov critical value for a given level of confidence. Values for $D(\psi)$ can be found in [143]. Table 6-4 illustrates $D_N(\psi)$ for the three stochastic variables for a normal distribution. In the case of eight samples and for 99% level of confidence, $D(\psi)$ is 0.54. Consequently, all variables can be represented by a normal random variable with 99% level of confidence.

Table 6-4 Maximum absolute difference between the observed and expected cumulative distribution; Kolmogorov-Smirnov goodness of fit.

variable	a_o	E_2	m
$D_N(x)$	0.10	0.17	0.17

6.3 Stochastic cure simulation: cure kinetics only

The cure process of Hexcel RTM6 [101] epoxy resin was simulated by using Eqs. (4-10)- (4-15). The stochastic cure kinetics simulation model was implemented in FORTRAN by coupling the cure kinetics model with MC and PCM (section 5.5.1, Appendix B). The instantaneous cure reaction rate and the degree of cure evolution were computed by integrating Eq. (4-11) numerically. Explicit numerical integration was employed. The applied cure profile is illustrated in Figure 6-8.

In the collocation method implementation, a second order response surface was constructed to represent the cure reaction rate at every increment (Fig. 6-9). A modified regression-based collocation approach was implemented to improve accuracy. The number of collocation points used was larger than the number of the unknown coefficients. In particular, the number of the unknown coefficients for a three dimensional second order polynomial chaos is 10 [9], however, 21 collocation points were used in this study, implying that only 21 deterministic model runs were required. In addition, a crude Monte Carlo simulation was performed to carry out the statistical analysis using the constructed response surface. The second order response surface for the maximum cure reaction rate following this approach was found to be:

$$\frac{\widehat{da}}{dt}_{max} = 3.43\,10^{-4} - 7.18\,10^{-6}\xi_1 - 3.4\,10^{-5}\xi_2 - 3.71\,10^{-6}\xi_3 - 4.93\,10^{-7}(\xi_1^2 - 1) + 1.14\,10^{-8}\xi_1\xi_2 - 2.45\,10^{-6}\xi_1\xi_3 + 2.03\,10^{-6}(\xi_2^2 - 1) - 4.58\,10^{-7}\xi_2\xi_3 - 2.42\,10^{-6}(\xi_3^2 - 1) \qquad (6\text{-}2)$$

The cure reaction rate as a function of time is illustrated in Fig. 6-9. As it can be observed, the maximum cure reaction rate as well as the region before the second ramp exhibit significant variability. This is due to the fact that the three stochastic variables i.e. the initial degree of cure a_o, activation energy E_2 and reaction order m mainly affect the position and the height of the maximum cure reaction rate. It was shown that the maximum cure reaction rate presented a coefficient of variation of about 11%. This can introduce significant variability to the temperature overshoot as well as influence the cure time for different cure cycles. Limited variability was manifested in the remaining regions. Figures 6-10 and 6-11 illustrate the evolution of statistics of the cure reaction rate as a function time, for the two stochastic simulation schemes. Note that the second peak in Figure 6-9 is due to post-cure (second dwell in Figure 6-8). The results suggest that very good agreement is presented between the Monte Carlo scheme and the collocation method, especially for the mean value. Given that the standard deviation converges slower than the mean value, the convergence criteria were based on the convergence of the standard deviation. The convergence behaviour of the statistics of the mean and the standard deviation of the maximum cure reaction rate is presented in Figures 6-12 and 6-13, respectively. Considering a convergence criterion of 5% of coefficient of variation in the standard deviation of maximum cure reaction rate, a quite satisfactory convergence was achieved after 250 Monte Carlo realisations, with the discrepancies between the two methods being negligible. Examination of the probability distribution of the maximum cure reaction rate shown in Fig. 6-14 indicates that the maximum cure reaction rate can be represented by a normally distributed variable. Table 6-5 summarises the cure stochastic simulation results.

The results presented here suggest that cure kinetics variability due to different resin handling/storage conditions can significantly affect the curing process with potential implications in the temperature overshoot and cure time. Moreover, the Probabilistic Collocation Method has clearly demonstrated its capabilities in this context providing an efficient way of simulating this variability.

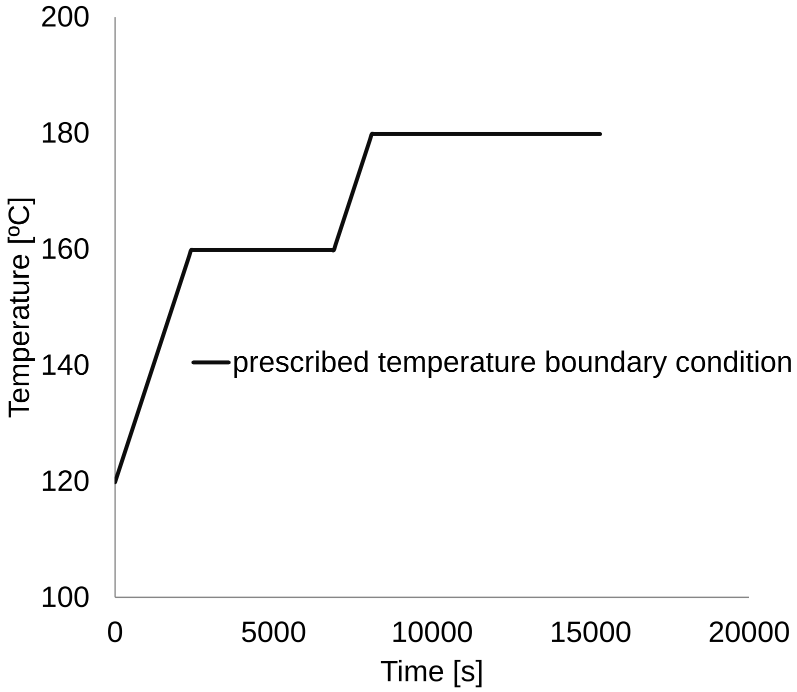

Fig. 6-8 Prescribed temperature boundary condition.

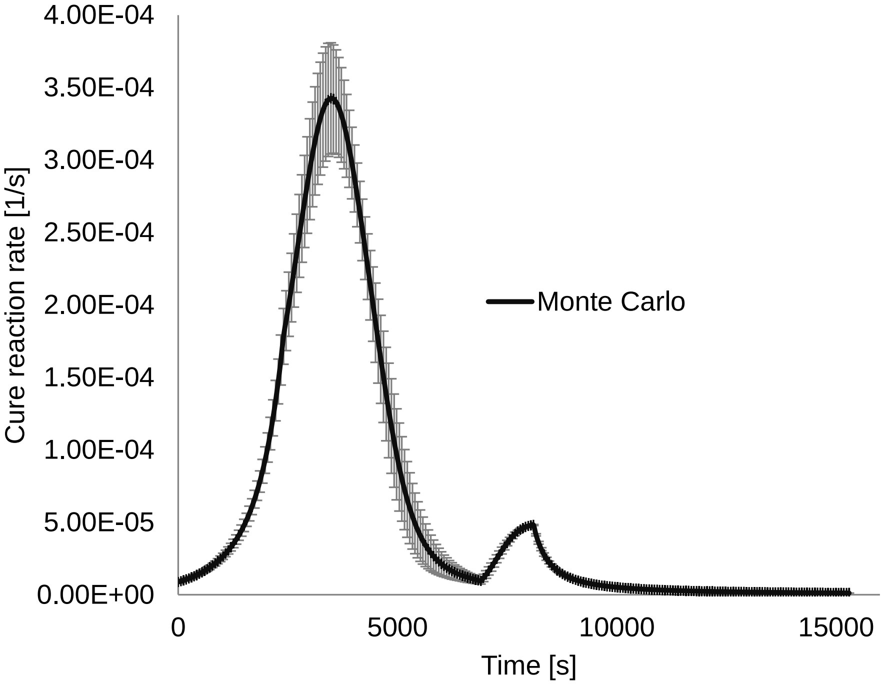

Fig. 6-9 Cure reaction rate vs time.

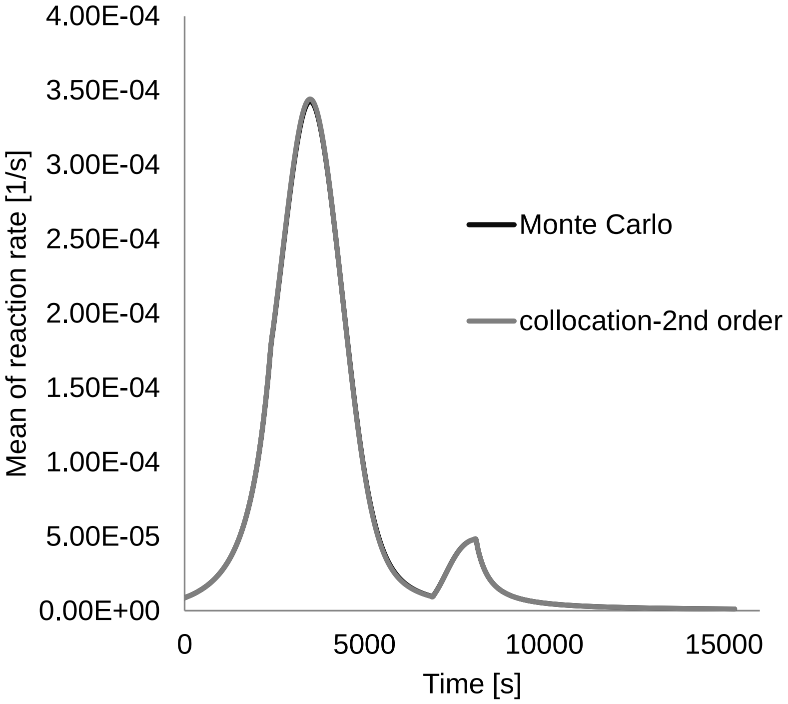

Fig. 6-10 Evolution of mean of cure reaction rate vs time.

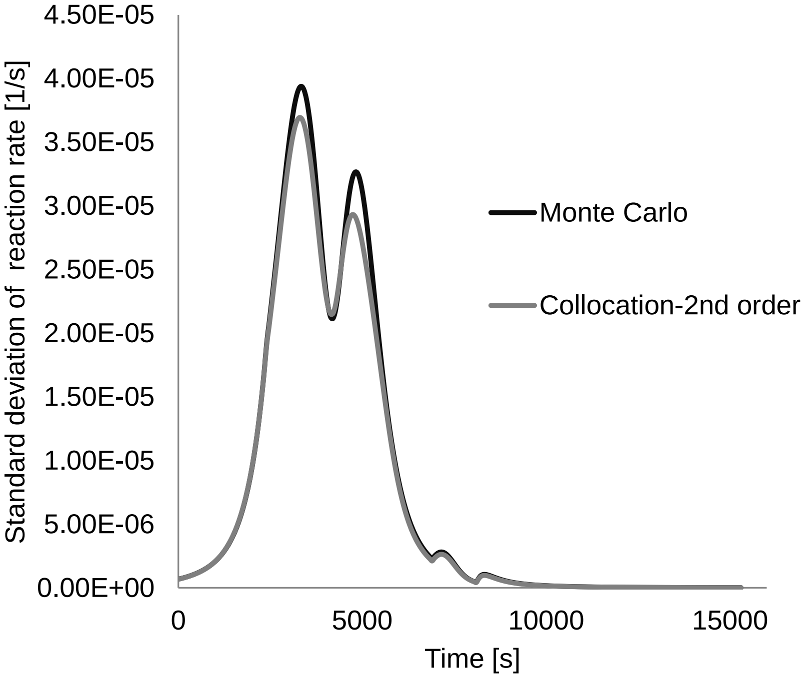

Fig. 6-11 Evolution of standard deviation of cure reaction rate vs time.

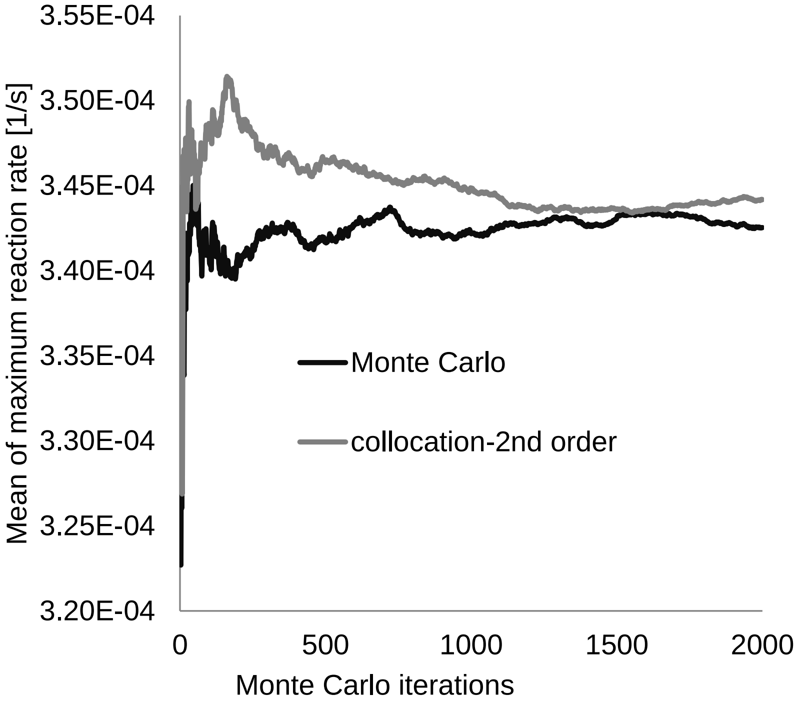

Fig. 6-12 Convergence of statistics of mean of maximum cure reaction rate.

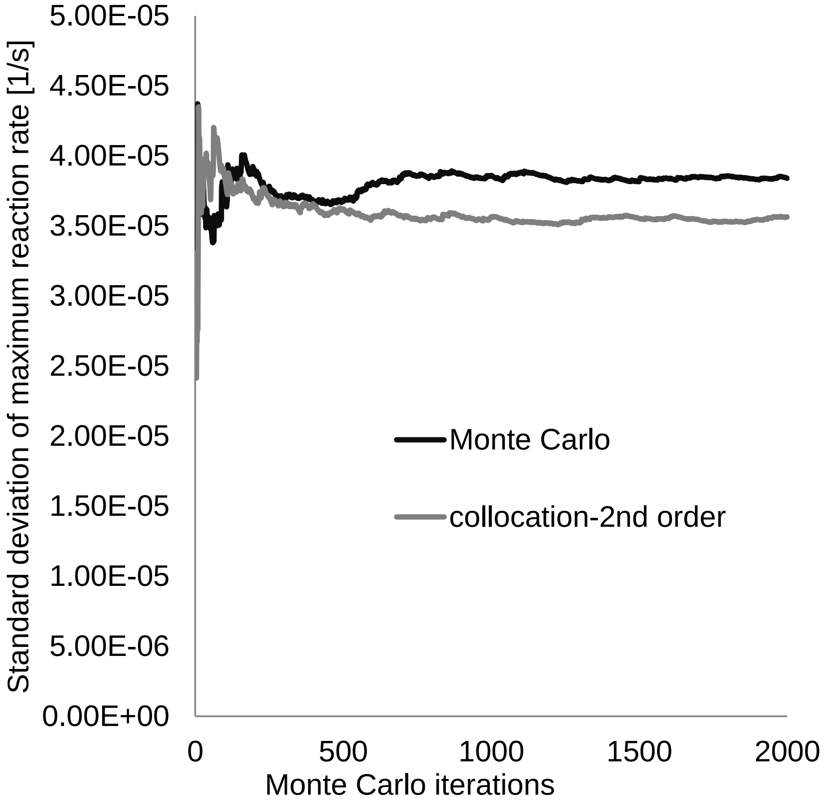

Fig. 6-13 Convergence of statistics of standard deviation of maximum cure reaction rate.

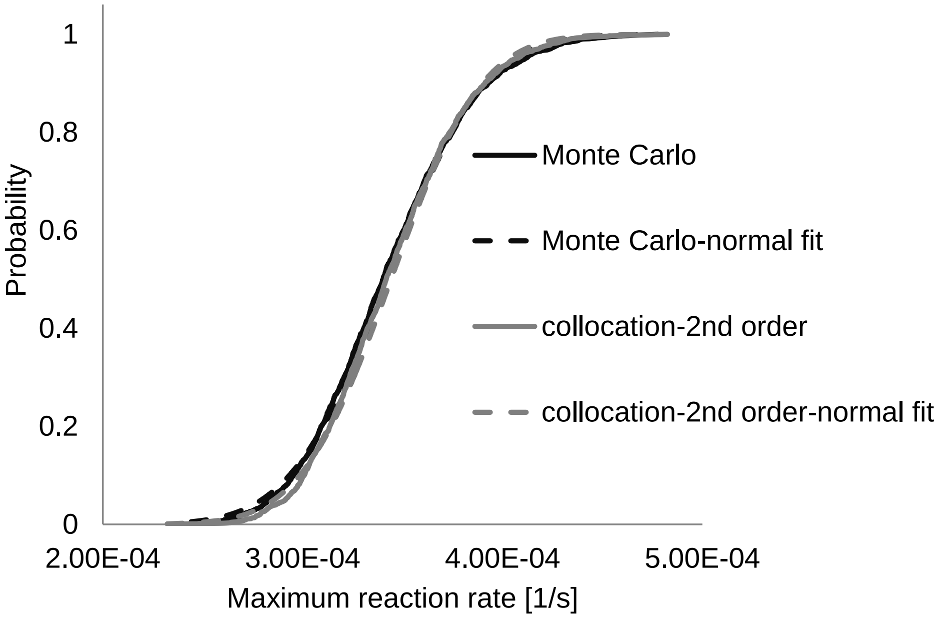

Fig. 6-14 Probability distribution of maximum cure reaction rate.

Table 6-5 Stochastic cure simulation results; maximum cure reaction rate.

Process output	Statistical Moments	Monte Carlo	Collocation
Maximum cure reaction rate	μ [1/s]	3.4 E-04	3.4 E-04
	σ [1/s]	3.7 E-05	3.6 E-05
	σ/μ [%]	11.2	10.4

6.4 Stochastic cure simulation: thick carbon fibre-epoxy laminate

The cure of a 30 mm thick carbon fibre- epoxy laminate fabricated by infusion was modelled by coupling the two stochastic simulation schemes (MC, PCM) with the finite element based cure simulation model (section 5.5.1, Appendix B). The materials involved are described in Chapter 3 and the cure simulation procedures using MSC.Marc in Chapter 4. The applied cure profile is illustrated in Fig. 6-8. The lay-up sequence of the laminate considered was $[0^o/90^o/90^o/0^o]_{25}$. The initial temperature was set at 15 ºC and was applied to all the nodes of the model. A prescribed temperature boundary condition defined by the cure profile was applied to the nodes in contact with the mould, whereas natural air convection with a surface heat transfer coefficient of 5 W/(m^{2}K) was applied on the surface in contact with the vacuum bag. The parameters of investigation were the temperature overshoot and the time at which the temperature overshoot occurs.

In the implementation of the collocation method a second order response surface was constructed for both investigated parameters and 21 collocation points were considered. This was followed by a Monte Carlo simulation using the corresponding response surfaces. The second order response surface for the temperature overshoot was the following:

$$\hat{T}_{ex} = 23.19 - 2.63\xi_1 - 5.01\xi_2 - 3.32\xi_3 + 2.58\ 10^{-2}(\xi_1^2 - 1) + 7.12\ 10^{-2}\xi_1\xi_2 + 1.56\ 10^{-2}\xi_1\xi_3 + 0.33(\xi_2^2 - 1) + 0.29\xi_2\xi_3 - 0.36(\xi_3^2 - 1) \tag{6-3}$$

whilst the surrogate model for the time of temperature overshoot was:

$$\hat{t}_{ex} = 6906.06 + 20.53\xi_1 - 11.22\xi_2 + 75.38\xi_3 - 1.48(\xi_1^2 - 1) - 18.92\xi_1\xi_2 - 10.03\xi_1\xi_3 + 16.29(\xi_2^2 - 1) - 55.6\xi_2\xi_3 - 8.15(\xi_3^2 - 1) \tag{6-4}$$

Figures 6-15- 6-19 present deterministic cure simulation results at three different points across the thickness of the laminate. Point A lies on the prescribed temperature boundary condition; point B is located at the centre of the laminate and point C lies on the natural air convection boundary condition at the top of the laminate. A large out of plane temperature gradient is present due to the low thermal conductivity of the material in the through the thickness direction, as illustrated in Figures 6-15 and 6-16. The temperature at points B and C is initially lower than the prescribed temperature, whereas a temperature overshoot occurs at the beginning of the second dwell due to high exothermic heat. This is followed by a decrease until the end of the cycle. However, the temperature at point C is lower than that of point B throughout the duration of the cycle due to dissipation of heat caused by natural air convection. In addition, heat dissipation introduces higher temperature gradients over time at point C. These phenomena lead to different cure reaction rate and degree of cure evolution through the thickness of the laminate, as shown in Figures 6-17 and 6-18, respectively. As it can be seen the onset of the reaction is shifted from point A to point C with point C presenting the highest maximum cure reaction rate and point B and point A to follow. This is explained by the different temperature gradients over time observed through the laminate thickness (Figure 6-16). As illustrated in Figure 6-18 the degree of cure at point B and C is lower than the nominal value at the initial stage of the process, whilst it increases abruptly at the time of temperature overshoot. Similarly to temperature point C presents lower degree of cure than point B throughout the cycle due to heat dissipation.

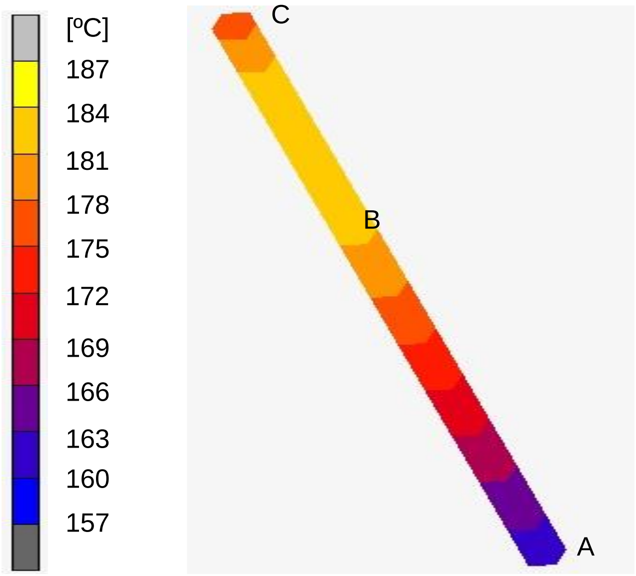

Fig. 6-15 Colour map of laminate temperature; point A prescribed temperature boundary condition, point B centre of the laminate, point C natural air convection boundary condition. Deterministic model results.

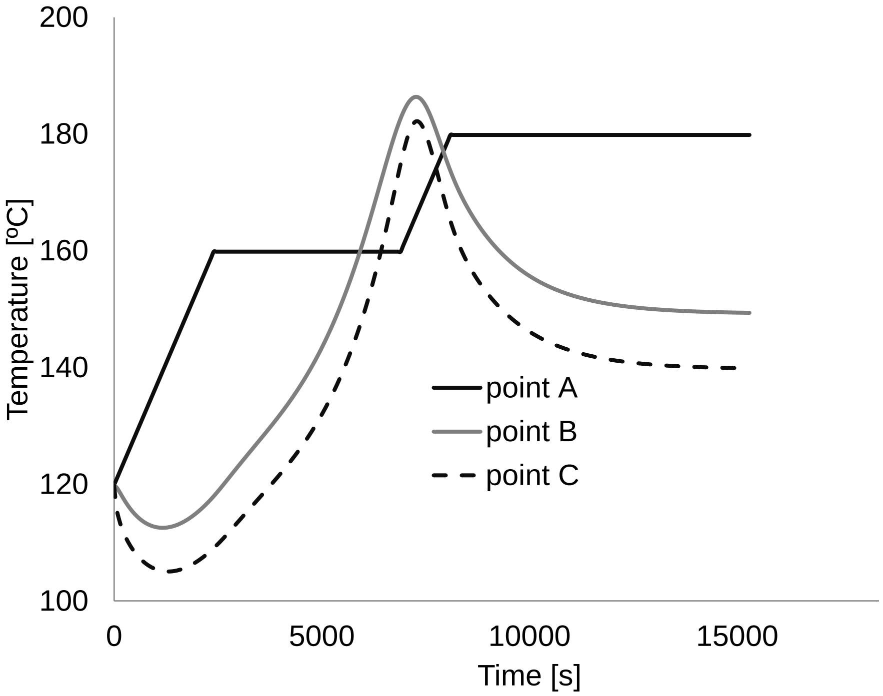

Fig. 6-16 Evolution of laminate temperature; point A prescribed temperature boundary condition, point B centre of the laminate, point C natural air convection boundary condition. Deterministic model results.

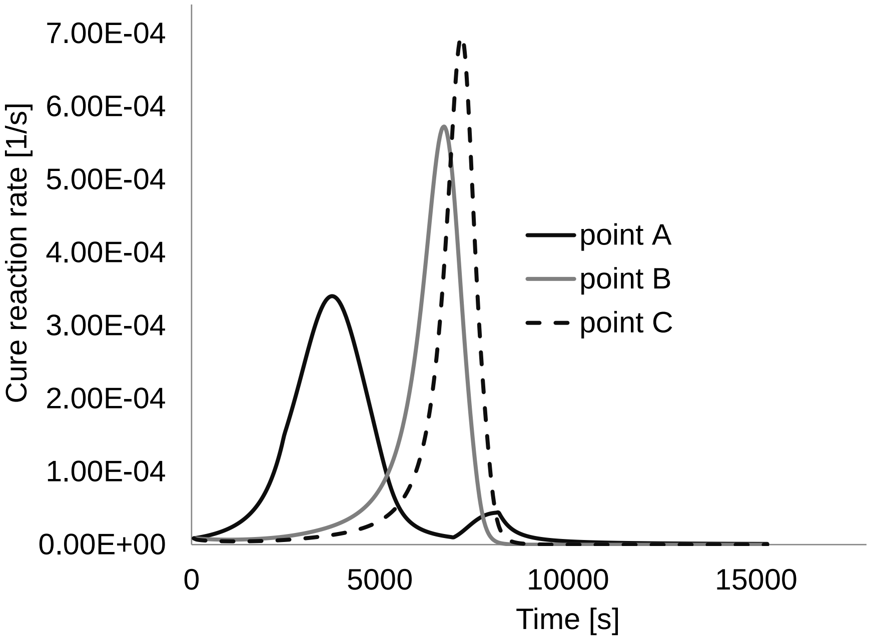

Fig. 6-17 Evolution of cure reaction rate; point A prescribed temperature boundary condition, point B centre of the laminate, point C natural air convection boundary condition. Deterministic model results.

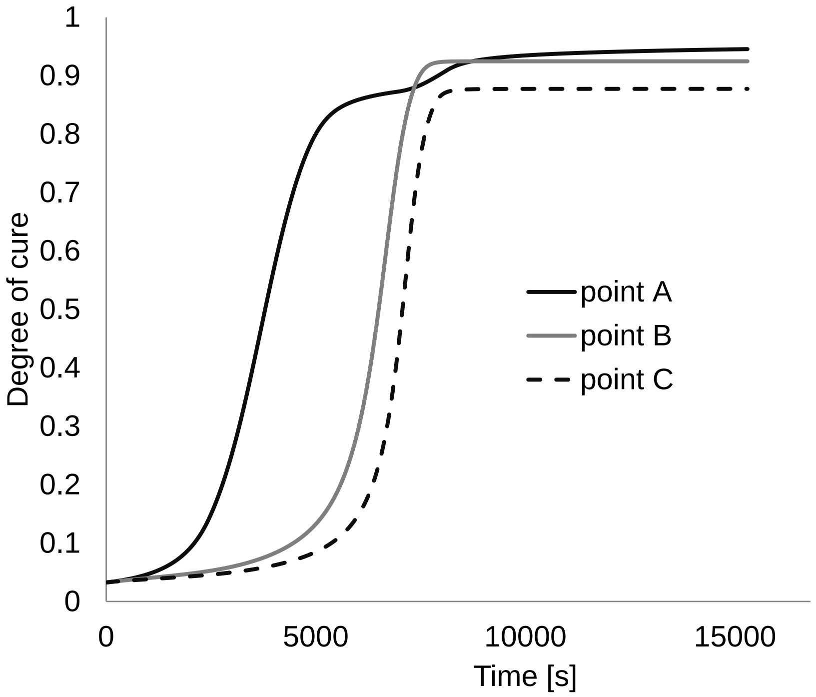

Fig. 6-18 Evolution of laminate degree of cure; point A prescribed temperature boundary condition, point B centre of the laminate, point C natural air convection boundary condition. Deterministic model results.

It was shown that 1000 Monte Carlo iterations were adequate to produce a convergence of less than 5% of coefficient of variation in the standard deviation of temperature overshoot for both stochastic simulation schemes (Figures 6-19 and 6-20). A very good agreement was achieved between MC and the collocation method. The results suggested that temperature overshoot presents a coefficient of variation of 31 %. Examination of the probability distribution of temperature overshoot shown in Figure 6-21 indicates that temperature overshoot can be considered a normally distributed random variable. These findings are of crucial importance especially in the case of more complex geometries or ultra-thick components where temperature overshoots are more pronounced and thus the probability of resin degradation can be higher resulting in large amount of scrap.

Figures 6-22 and 6-23 illustrate the results for the time of temperature overshoot. Similarly to temperature overshoot the simulation converges after 1000 Monte Carlo iterations, with the two stochastic models presenting satisfactory agreement. The time at which temperature overshoot occurs exhibits a coefficient of variation of 1.7 %, and can be represented by a normally distributed variable, as illustrated in Figure 6-24. Note that the sharp shape of the probability distribution of time of temperature overshoot in the case of MC (Figure 6-24) is due to the fact that a fixed number of time increments was used in the FEA solver. Refining the time increments could overcome this issue, however, this would increase the computational cost significantly especially in the context of stochastic simulation.

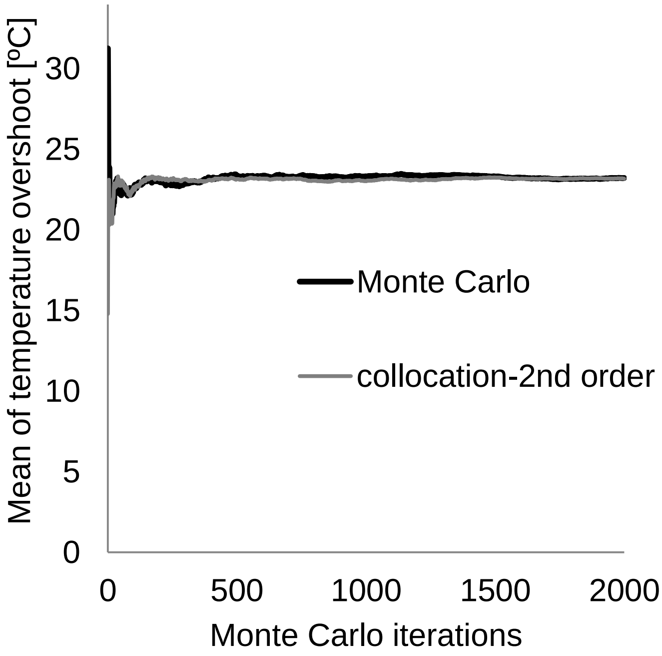

Fig. 6-19 Convergence of statistics of mean of temperature overshoot.

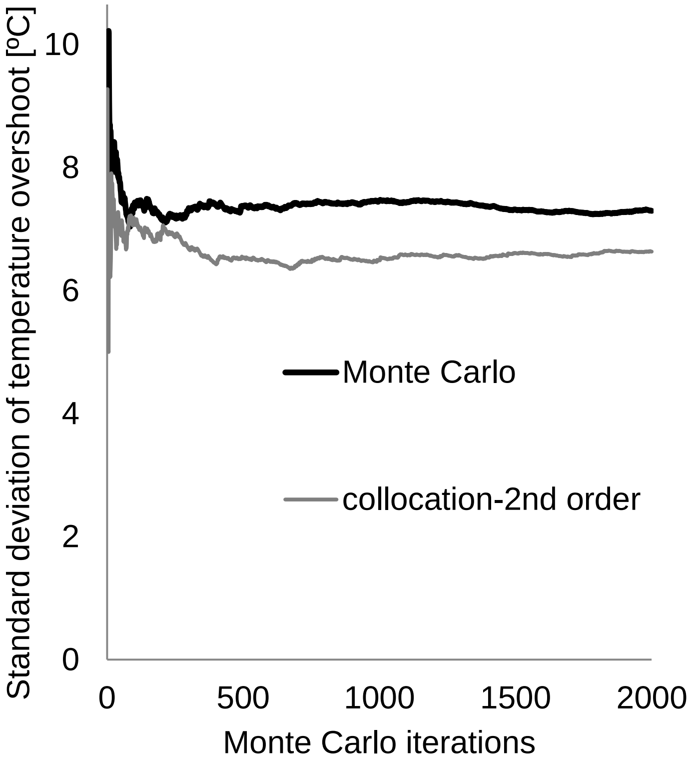

Fig. 6-20 Convergence of statistics of standard deviation of temperature overshoot.

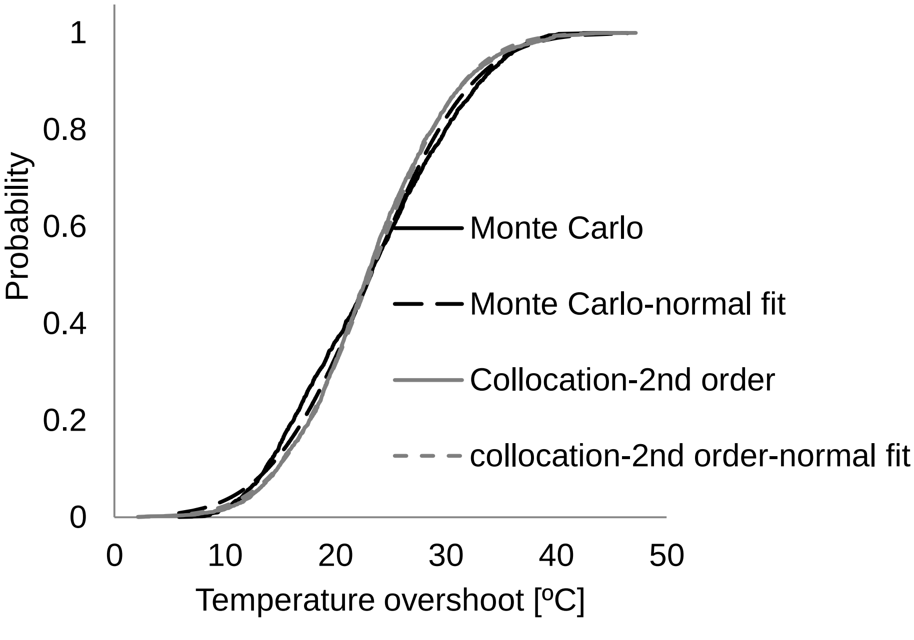

Fig. 6-21 Probability distribution of temperature overshoot.

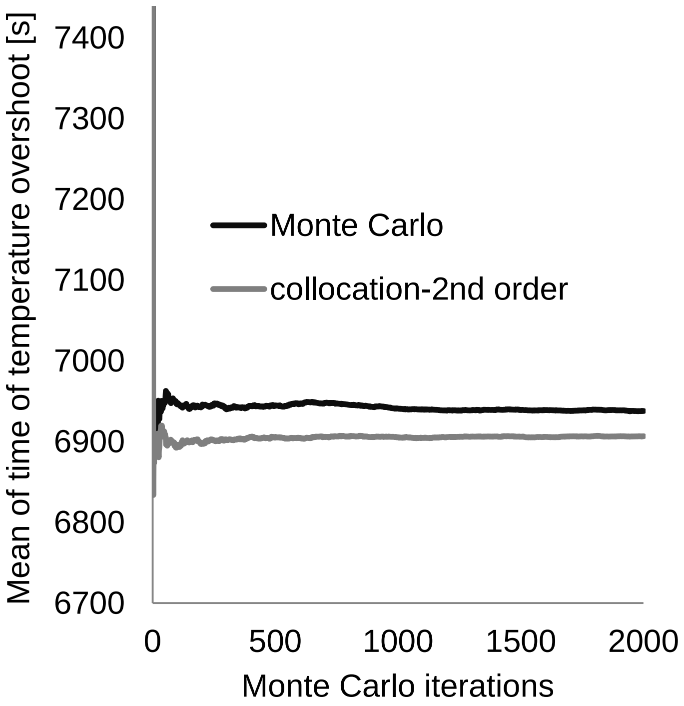

Fig. 6-22 Convergence of statistics of mean of time of temperature overshoot.

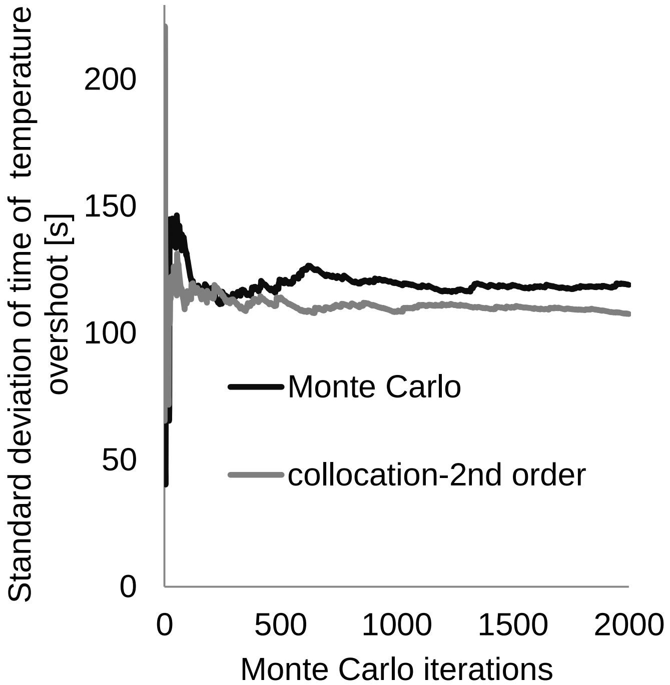

Fig. 6-23 Convergence of standard deviation of time of temperature overshoot.

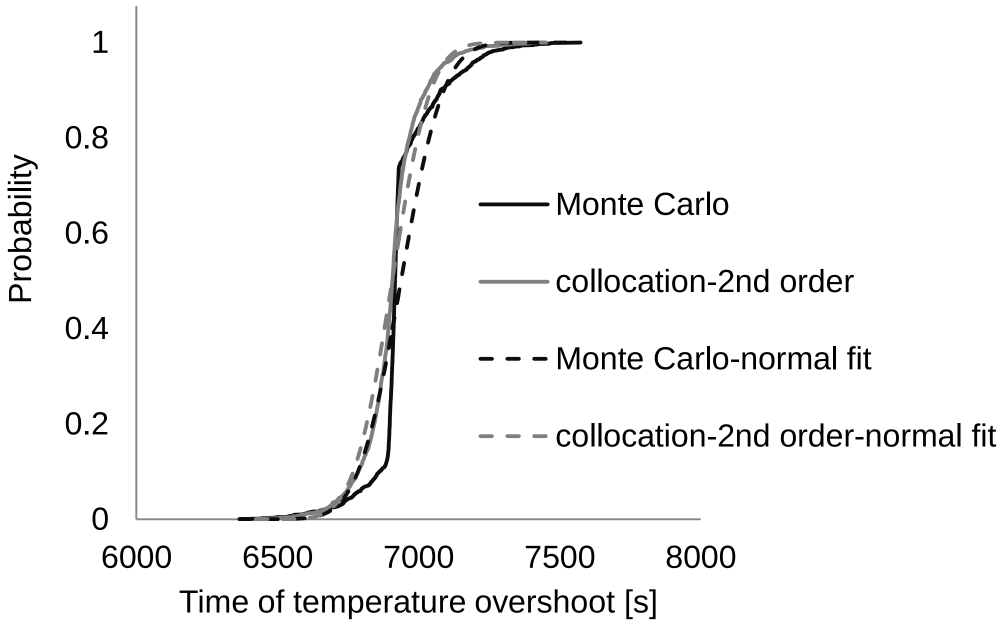

Fig. 6-24 Probability distribution of time of temperature overshoot.

Table 6-6 stochastic cure simulation results; temperature overshoot, time of temperature overshoot.

Process output	Statistical moments	Monte Carlo	collocation
Temperature overshoot	μ [ºC]	23.2	23.2
	σ [ºC]	7.3	6.6
	σ/μ [%]	31.4	28.6
Time of temperature overshoot	μ [s]	6937	6906
	σ [s]	119	107
	σ/μ [%]	1.7	1.6

The stochastic cure simulation results are summarised in Table 6-6. Both MC and PCM have the capability of capturing variability propagation, with the MC presenting a computationally expensive and rich solution and the PCM offering an efficient approximation (e.g. for the given case, the computational cost of the PCM is 2 % of that of the MC), with comparable accuracy. The results presented here show that cure kinetics uncertainty can introduce significant variability in temperature overshoot with considerable cost implications in industrial practice, especially in the case of ultra-thick complex geometry components where exothermic effects can be severe. Consequently, variability effects should be incorporated in cure profile optimisation to minimise the probability of resin degradation due to temperature overshoot variations whilst using a process design as efficient as possible in terms of duration and energy consumption. This can be achieved by integrating the stochastic simulation methodology presented here with an optimisation tool.

6.5 Overview

The methodologies demonstrated here allow the quantification of the influence of variability on the cure process outcome. The experimental results showed that the cure behaviour of high specification thermosets involves uncertainty, which in turn can introduce significant variability to the process outcome. It was found that the main source of uncertainty is caused by variations in the initial degree of cure, activation energy and reaction order. The stochastic simulation results suggested that temperature overshoot can present a coefficient of variation of about 30 %, with potential implications in the amount of scrap during the manufacturing process of composite materials. Furthermore, the time of temperature overshoot showed a coefficient of variation of about 1.7 %. The collocation method has clearly demonstrated its capabilities in this context, inducing tremendous advantages (computational time of the PCM is 2 % of that of the MC) in terms of computational time compared to MC with comparable accuracy.

7. Stochastic simulation of the influence of fibre path variability on residual stress and distortion generated during composites cure

7.1 Introduction

Fibre misalignment is mainly associated with in-plane and out-of-plane tow waviness and can be caused during the manufacturing, transport and storage of dry fabrics and pre-pregs as well as during forming/draping of doubly curved parts where the fabric is subjected to considerable shear deformation, which may intensify the already existing geometrical heterogeneities. Fibre misalignment along with fibre volume fraction variations can potentially affect the mechanical, thermo-mechanical and thermal properties of the material during the curing process. For instance, the compressive strength of the material is the property with the highest sensitivity to local variations in the orientation of the reinforcement [144]. Therefore, fibre architecture plays a crucial role in the structural performance of composite materials governing non-linear phenomena such as failure and damage initiation. Furthermore these effects can effect cure process defects and introduce variability in residual stresses/shape distortion. Residual stresses are of crucial importance since they can initiate delamination, matrix cracks and distortion such as warpage and spring-in affecting the performance and dimensional fidelity of the produced part [145-147]. The influence of geometrical heterogeneity effects on the cure process has received little attention so far in the literature and consequently has not been investigated explicitly. A characterisation and modelling approach that takes these effects into consideration explicitly can be beneficial as it allows quantification of corresponding process outcome variability within a stochastic simulation framework.

In this chapter the methodology developed to characterise and model in plane fibre misalignment in non-crimp fabrics described in chapter 3 and 5 is used to investigate the influence of fibre misalignment on the cure process and its outcome. The image analysis methodology based on fast Fourier Transform (FFT) and correlation analysis presented in section 3.4 was used to measure local fibre angle variability on a ±45^{o} NCF. The autocorrelation structure of the fabric is modelled using a two-dimensional second-order autoregressive process, the Ornstein-Uhlenbeck (OU) sheet described in section 5.2.3. Generation of realisations of the tow orientations of the textile was performed using Cholesky factorisation. The resulting stochastic process is simulated by coupling the coupled thermo-mechanical cure simulation model, described in Chapter 4 with the Monte Carlo (MC) scheme (section 5.5.2, Appendix B). This stochastic simulation approach is applied to the cure process of a bracket carbon fibre-epoxy subcomponent with three different lay-up sequences to study the effect of fibre misalignment on residual stress generation and shape distortion.

7.2 Analysis of fibre misalignment of non-crimp fabrics

A set of digital images were acquired from each side (upper/lower) of the 6k carbon fibre ± 45º NCF HTS Hexcel [102] as detailed in section 3.4. The image analysis results are illustrated as two lines; (i) stitch orientation, set always at 0º, (ii) carbon tow orientation (Figure 7-1).

It was indicated that the analysis results do not depend on the grid size in terms of variance and autocorrelation structure.

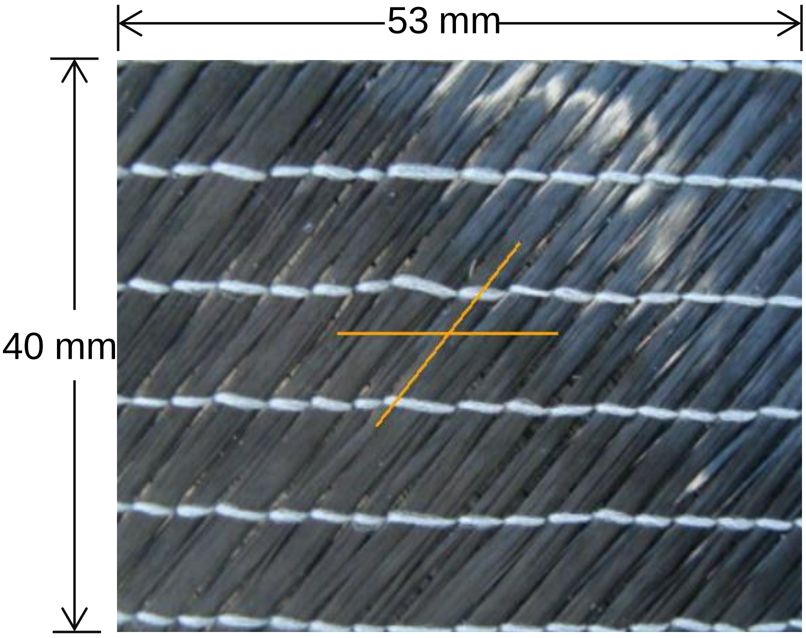

Fig. 7-1 Image analysis of ± 45º NCF.

7.2.1 Statistical properties and spatial autocorrelation

Table 7-1 summarises the basic statistical properties of tow orientation of the 6k carbon fibre ± 45º NCF HTS. The experimental results indicated that both sides present identical statistical behaviour in terms of standard deviation and autocorrelation structure. The probability distributions of the upper and lower side of the ± 45º NCF are depicted in Figures 7-2 and 7-3, respectively. Fibre angles were measured in an anti-clockwise direction relative to the stitch of the fabric (0º) as depicted in Figure 7-1. The statistical properties detailed in Table 7-2, include the average μ and the standard deviation σ of the sample field. The fabric showed variability in tow orientation of about 1.2º. This result should be compared with the standard deviation obtained for the set of images from a single location which was 0.1º, showing that the experimental and signal analysis method introduced negligible variations to the results. The results reported in Table 7-2 show that there is no correlation between tow orientations of the two sides. Examination of Figures 7-2 and 7-3 suggests that tow orientation in both sides can be represented by a normally distributed variable. The discrepancies between the experimental data and corresponding normal fits can be attributed to the fact that only one sample was used to characterise fibre misalignment.

Table 7-1 Statistical properties of tow orientation of carbon fibre ± 45º NCF.

variable	upper side	lower side
μ [º]	45	-45
σ [º]	1.2	1.2

Table 7-2 Correlation matrix of tow orientation of carbon fibre ± 45º NCF.

variable	upper side	lower side
upper side	1	0.014
lower side	0.014	1

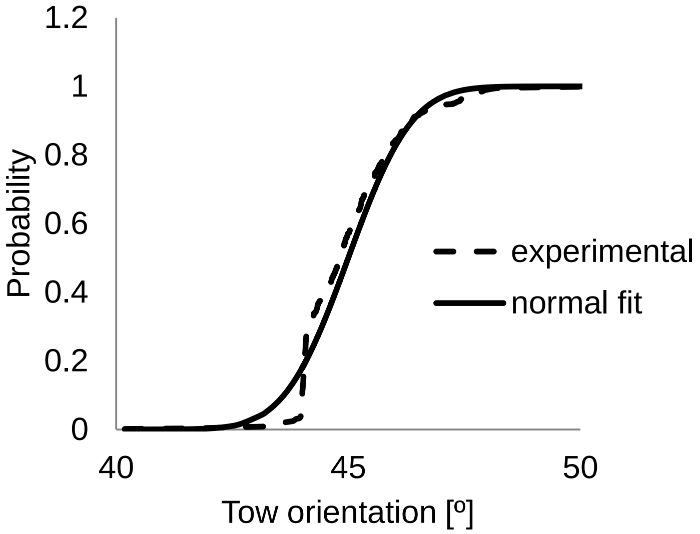

Fig. 7-2 Probability distributions of fibre orientation of carbon fibre ± 45º NCF; upper side.

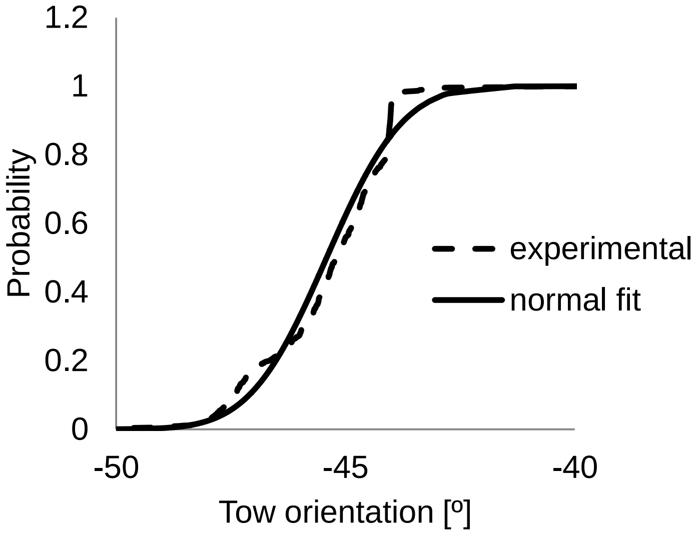

Fig. 7-3 Probability distributions of fibre orientation of carbon fibre ± 45º NCF; lower side.

The autocorrelation structure of the orientation of the tows was investigated in order to estimate the spatial dependence of variability. The method of moments was used to quantify spatial autocorrelation as a function of distance and direction [13]. The correlation between two samples of all pairs of points obtained from the experimental results located at a specific distance and direction was calculated and is reported in Figure 7-4 as a function of distance. It can be observed that fibre misalignment of the ± 45º NCF exhibits high anisotropic spatial autocorrelation with the major direction of autocorrelation coinciding with the direction of the stitch (0º). This would indicate that a major part of the misalignment of non-crimp fabrics is introduced during the stitching process. Autocorrelation in the ±25º directions reaches a value close to zero at about 40 mm, whilst autocorrelation in ±50º and ±75º directions shows a faster decay reaching zero at approximately 25 mm. It can be observed, that the autocorrelation in opposite directions is very similar, suggesting that the autocorrelation structure of this fabric is quadrant symmetric. The fluctuations observed above 50 mm can be attributed to long term trend effects. Spatial cross-correlation between orientation of the tows of the two sides was found to be negligible.

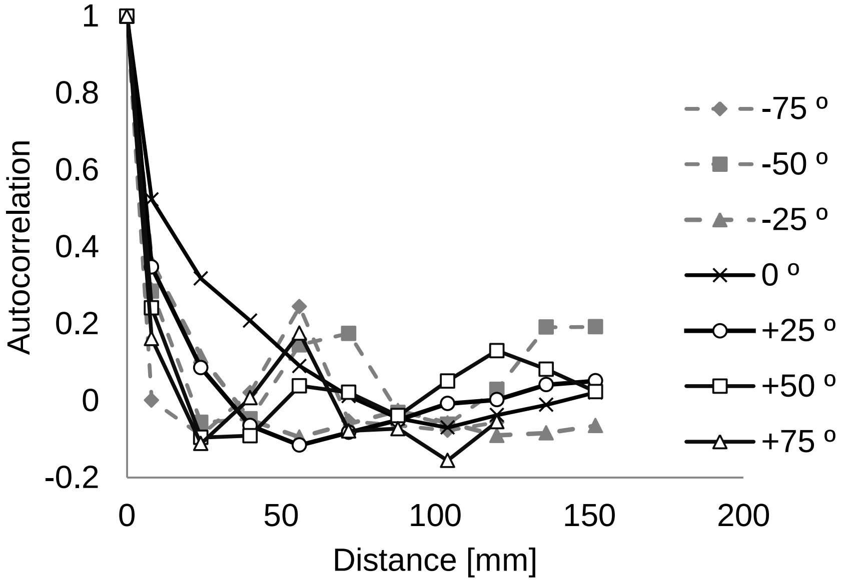

Fig. 7-4 Directional autocorrelation of fibre orientation of carbon fibre ± 45º NCF.

7.2.2 *Stochastic textile simulation*

The random field was modelled using a two-dimensional autoregressive random process, the Ornstein-Uhlenbeck sheet (OU) (section 5.2.2), as shown in Eq. (5-13). Estimation of b_x and b_y in Eq. (5-13) was carried out using least squares and it was performed by the Evolutionary Optimisation method implemented in Microsoft Excel [148]. This approach yielded a value of 20.21 mm for b_x and 4.67 mm for b_y.

Cholesky factorisation, spectral decomposition and the Karhunen–Loève (K–L) expansion as presented in chapter 5 were utilised to simulate fibre misalignment of the 6k carbon fibre ± 45º NCF HTS. The three discretisation techniques were compared in terms of efficiency and accuracy. Figures 7-5 and 7-6 illustrate the autocorrelation of the simulated tow orientation generated on a 68×22 grid with 5mm spacing. The autocorrelation of the sample field generated using the K-L is not presented due to the poor quality of results. This is attributed to the fact that the performance of the K-L is high only in the case of highly correlated stochastic fields [135]. The intervals N_x and N_y (section 5.2.3) were set at 68 and 22, respectively, in order to compare the Cholesky factorisation and the spectral decomposition in terms of accuracy and efficiency. It can be observed that both discretisation techniques can reproduce the stochastic field with very good accuracy, with the discrepancies between the two methods being negligible. In addition, there were some discrepancies between the two techniques and the experimental data at the region of the plateau; however this introduces a negligible error since the autocorrelation is close to zero at this region. Therefore, given the similar computational effort, both techniques are capable of modeling fibre misalignment of the fabric of this study, with quite good accuracy. Consequently, the Cholesky method was considered to be the most appropriate technique to reproduce the stochastic field of this study, due to its simplicity in comparison to spectral decomposition.

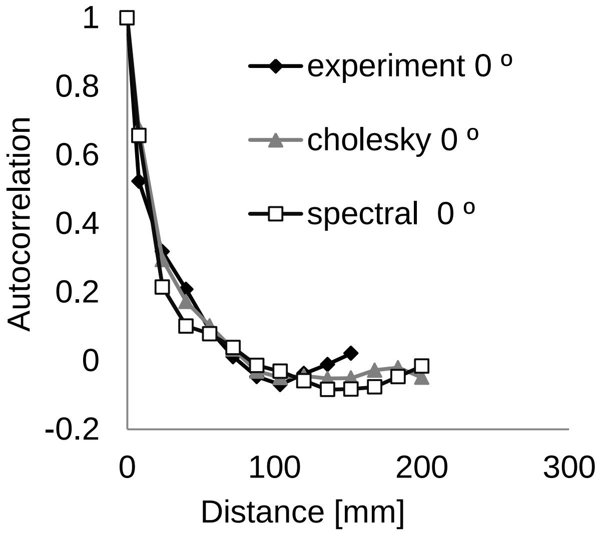

Fig. 7-5 Directional autocorrelation of simulated tows; 0º.

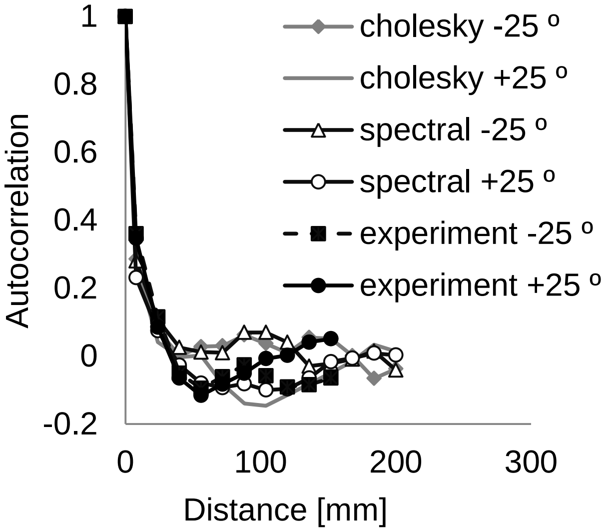

Fig. 7-6 Directional autocorrelation of simulated tows ±25 º.

7.3 Stochastic cure simulation

A coupled thermo-mechanical cure simulation model was implemented in the finite element analysis solver MSC.Marc as described in Chapter 4. The model was three dimensional and transient. The materials considered were HTS carbon fibre [102] and Hexcel RTM6 [101] epoxy resin. The material sub-models of cure kinetics, specific heat capacity, thermal conductivity, moduli, cure shrinkage and thermal expansion were implemented in user defined subroutines UCURE, USPCHT, ANKOND, HOOKLW, USHRINKAGE and ANEXP [111], as described in chapter 4. The parameters required for the cure kinetics material sub-model were those obtained from the DSC tests, as reported in section 6.2.2.

The cure of an angle shape carbon fibre- epoxy subcomponent was modelled by coupling a Monte Carlo scheme with the finite element cure simulation model. The bracket is 2 mm thick, with two arms of 100 mm in length whilst the inner radius is 3 mm (Figure 7-7). The width of the part is 40 mm. The applied cure profile and the nominal evolution of the degree of cure at the boundary are illustrated in Figure 7-8. Three different lay-up sequences were investigated: a cross-ply $[0/90/90/0]_s$, and bias-ply $[45/-45/-45/45]_s$ and a quasi-isotropic (QI) $[0/45/-45/90]_s$ laminate; here all orientations are with respect to the long axis of the component. The initial temperature was set at 15 ºC and was applied to all the nodes of the model. A prescribed temperature boundary condition defined by the cure profile was applied to the nodes in contact with the mould, whereas natural air convection with a surface heat transfer coefficient of 5 W/(m^{2}K) was applied on the surface in contact with the vacuum bag.

Generation of residual stresses/shape distortion is mainly caused by thermal expansion coefficient mismatch between the different layers of the material, resin cure shrinkage and tool-part interactions [149]. The latter was not taken into consideration since the aim of this study was to investigate the influence of inherent material properties variability on the cure process.

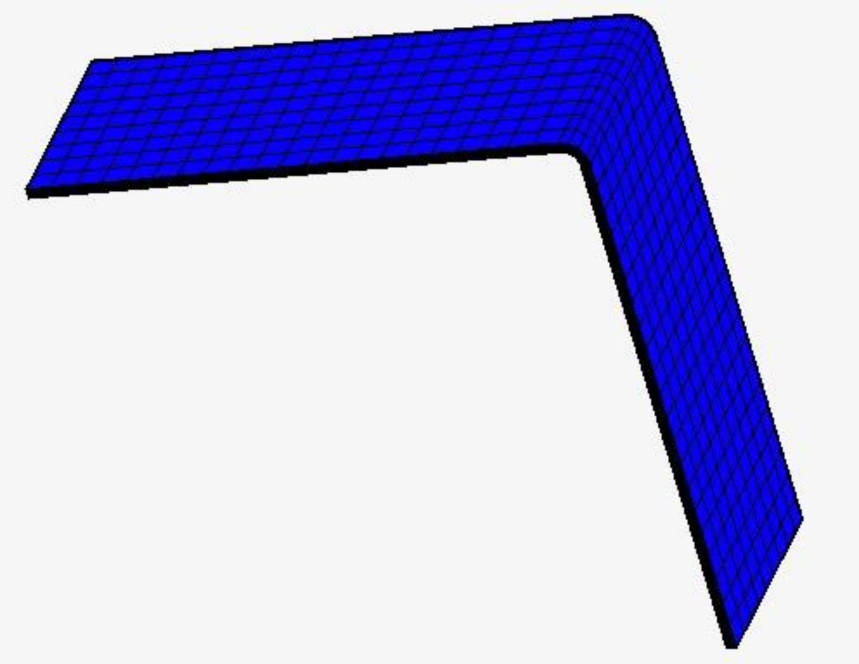

Figure 7-7 Angle shape carbon fibre- epoxy subcomponent.

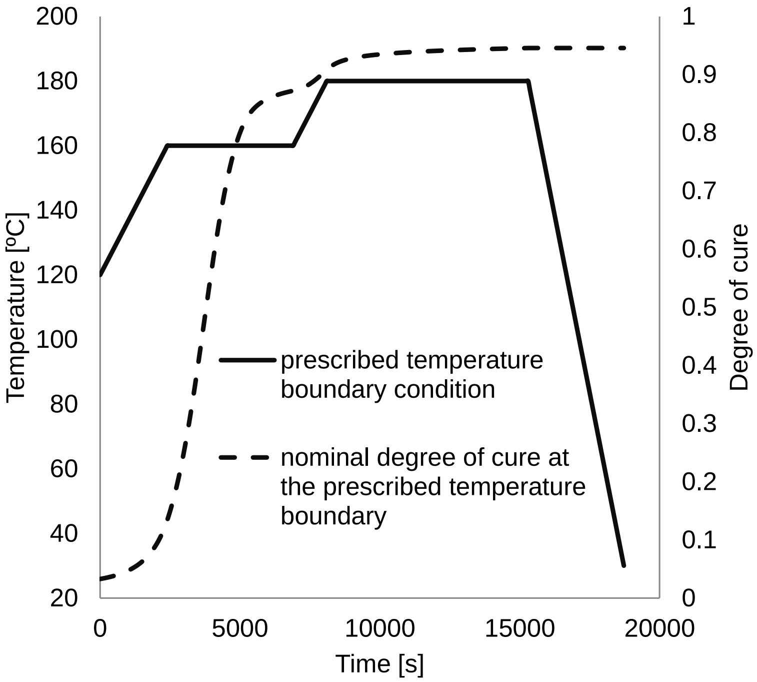

Fig. 7-8 prescribed temperature boundary condition, degree of cure at boundary.

7.3.1 Incorporation of fibre misalignment

Incorporation of local tow waviness was carried out by modifying the thermal conductivity matrix, compliance tensor, cure shrinkage coefficient matrix and thermal expansion coefficient matrix. This was performed by applying the coordinate transformation corresponding to the rotation of the principal axis of the individual plies by the angle corresponding to the local fibre misalignment of each element.

7.3.1.1 Thermal conductivity

The textile used in this study comprised unidirectional layers. The rotation transformation of the components of the conductivity matrix (Eq. 4-45) of a single lamina for an in plane rotation is given by the following relations [120]:

$$K_{11}{}' = K_{11}\cos^2(\theta) + K_{22}\sin^2(\theta) \tag{7-1}$$

$$K_{22}{}' = K_{22}\cos^2(\theta) + K_{11}\sin^2(\theta) \tag{7-2}$$

$$K_{12}{}' = (K_{11} - K_{22})\cos(\theta)\sin(\theta) = K_{21}{}' \tag{7-3}$$

$$K_{33}{}' = K_{33} \tag{7-4}$$

Here K_{11}, K_{22} and K_{33} denote the thermal conductivity in the three principal lamina directions respectively, whilst θ is the angle between the perfect nominal tow orientation and the local fibre misalignment.

7.3.1.2 Mechanical/ thermo-mechanical properties

The rotation transformation of the stress tensor $\boldsymbol{\sigma}$ for an in plane rotation θ can be computed using directional cosines and is given by $\boldsymbol{\sigma}' = \boldsymbol{J_\sigma \sigma}$ [150]:

$$\begin{pmatrix} \sigma_{11}{}' \\ \sigma_{22}{}' \\ \sigma_{33}{}' \\ \sigma_{12}{}' \\ \sigma_{23}{}' \\ \sigma_{31}{}' \end{pmatrix} = \begin{bmatrix} c^2 & s^2 & 0 & 2cs & 0 & 0 \\ s^2 & c^2 & 0 & -2cs & 0 & 0 \\ 0 & 0 & 1 & 0 & 0 & 0 \\ -cs & cs & 0 & c^2 - s^2 & 0 & 0 \\ 0 & 0 & 0 & 0 & c & s \\ 0 & 0 & 0 & 0 & -s & c \end{bmatrix} \begin{pmatrix} \sigma_{11} \\ \sigma_{22} \\ \sigma_{33} \\ \sigma_{12} \\ \sigma_{23} \\ \sigma_{31} \end{pmatrix} \tag{7-5}$$

where $c = \cos\theta$ and $s = \sin\theta$. Similarly, the rotation transformation of the strain tensor is given by $\boldsymbol{\varepsilon}' = \boldsymbol{J_\epsilon \varepsilon}$ [150]:

$$\begin{pmatrix} \varepsilon_{11}{}' \\ \varepsilon_{22}{}' \\ \varepsilon_{33}{}' \\ \gamma_{12}{}' \\ \gamma_{23}{}' \\ \gamma_{31}{}' \end{pmatrix} = \begin{bmatrix} c^2 & s^2 & 0 & cs & 0 & 0 \\ s^2 & c^2 & 0 & -cs & 0 & 0 \\ 0 & 0 & 1 & 0 & 0 & 0 \\ -2cs & 2cs & 0 & c^2 - s^2 & 0 & 0 \\ 0 & 0 & 0 & 0 & c & s \\ 0 & 0 & 0 & 0 & -s & c \end{bmatrix} \begin{pmatrix} \varepsilon_{11} \\ \varepsilon_{22} \\ \varepsilon_{33} \\ \gamma_{12} \\ \gamma_{23} \\ \gamma_{31} \end{pmatrix} \tag{7-6}$$

The rotation transformation for the compliance matrix $\boldsymbol{Q}$ is defined as [151]:

$$\boldsymbol{Q}' = \boldsymbol{J_\epsilon Q J_\sigma}^{-1} \tag{7-7}$$

The cure shrinkage and thermal expansion coefficient matrices are rotated using directional cosines as follows [150]:

$$\begin{pmatrix} {C_{11}}' \\ {C_{22}}' \\ {C_{33}}' \\ {C_{12}}' \\ {C_{23}}' \\ {C_{31}}' \end{pmatrix} = \begin{bmatrix} c^2 & s^2 & 0 & 2cs & 0 & 0 \\ s^2 & c^2 & 0 & -2cs & 0 & 0 \\ 0 & 0 & 1 & 0 & 0 & 0 \\ -cs & cs & 0 & c^2-s^2 & 0 & 0 \\ 0 & 0 & 0 & 0 & c & s \\ 0 & 0 & 0 & 0 & -s & c \end{bmatrix} \begin{pmatrix} C_{11} \\ C_{22} \\ C_{33} \\ C_{12} \\ C_{23} \\ C_{31} \end{pmatrix} \qquad (7\text{-}8)$$

$$\begin{pmatrix} a_{11}^{th'} \\ a_{22}^{th'} \\ a_{33}^{th'} \\ a_{12}^{th'} \\ a_{23}^{th'} \\ a_{31}^{th'} \end{pmatrix} = \begin{bmatrix} c^2 & s^2 & 0 & 2cs & 0 & 0 \\ s^2 & c^2 & 0 & -2cs & 0 & 0 \\ 0 & 0 & 1 & 0 & 0 & 0 \\ -cs & cs & 0 & c^2-s^2 & 0 & 0 \\ 0 & 0 & 0 & 0 & c & s \\ 0 & 0 & 0 & 0 & -s & c \end{bmatrix} \begin{pmatrix} a_{11}^{th} \\ a_{22}^{th} \\ a_{33}^{th} \\ a_{12}^{th} \\ a_{23}^{th} \\ a_{31}^{th} \end{pmatrix} \qquad (7\text{-}9)$$

7.3.2 Stochastic cure simulation results

Figure 7-9 illustrates the final stress state in the fibre direction of the outer layers and the final distortion of the component for the deterministic model and one realisation of the stochastic simulation for each case study. It should be noted that the distortion shown in the deformed shape is multiplied by a factor of 50 to facilitate visualisation. Compressive residual stresses are generated in the longitudinal direction whilst tensile residual stresses are generated in the transverse direction, due to the fact that the response of the ply in the longitudinal direction is dominated by the fibre properties and in the transverse direction by the matrix. Shape distortion in the form of spring-in was observed in the case of both the deterministic models and the models incorporating variability in fibre orientation. This is a result of the difference in thermo-mechanical behaviour between the out-of-plane and the in-plane directions. In addition to this type of distortion, laminates with stochastic fibre orientation present qualitative differences compared to the nominal cases, as shown in Figure 7-9. In the case of the cross-ply and quasi-isotropic laminates a twist is present in the realisations of the stochastic model. The twist tends to be more pronounced in the cross ply than in the quasi-isotropic layup. A similar effect occurs in the bias ply laminate, with the qualitative difference that distortion is manifested mainly as bowing of the flange. These effects are due to deviations from the perfect nominal orientations which induces local asymmetry and imbalance in the layup. The differences in the type and magnitude of distortion are governed by the differences in stiffness in each layup. In the case of the cross ply laminate small variations in fibre angle induced a twisting moment that is not resisted sufficiently by the material, given that no fibres are aligned to the bias direction. As a consequence, twisting becomes the dominant mode of distortion. In contrast, in the case of the bias layup twisting is counteracted by the ±45º layers, whereas any asymmetry induced bending moment is not resisted sufficiently, due to the lack of fibres aligned to the longitudinal direction of the component, resulting in some bowing. The case of the quasi-isotropic laminate is intermediate, with twisting being the main mode of distortion due to the fact that the outer layers are 0º and the overall twisting kept significantly lower than in the case of the cross ply laminate.

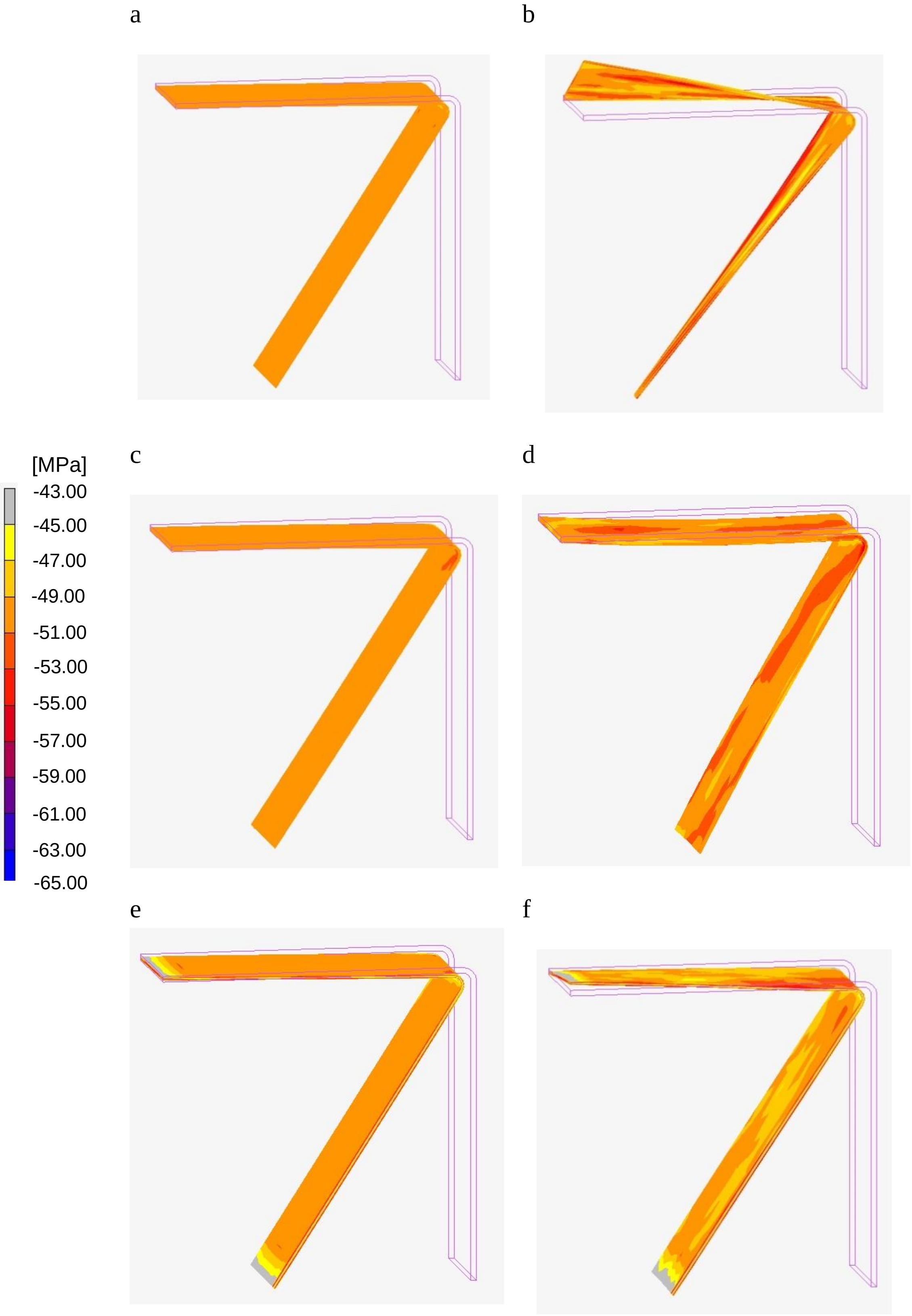

Fig. 7-9 Residual stress of the outer layers in the fibre direction at the end of the process after release from the tool and final distortion multiplied by a factor of 50: (a) cross ply-deterministic model; (b) cross ply-stochastic model; (c) bias ply-deterministic model; (d) bias ply-stochastic model; (e) quasi-isotropic-deterministic model; (f) quasi-isotropic-stochastic model.

Here, the convergence criterion was based on the convergence of the standard deviation; 5% of coefficient of variation in standard deviation of the output parameters. Satisfactory convergence was obtained in the Monte Carlo simulation for the first and second statistical moments of maximum longitudinal residual stress of all layers in the fibre direction after 200 iterations as shown in Figures 7-10 and 7-11. The results suggest that maximum longitudinal residual stress have a coefficient of variation of 2.3, 1.4 and 1.2 % (standard deviation of 1.29, 0.76 and 0.75 MPa), for the cross ply, bias ply and quasi-isotropic laminate respectively. Examination of the probability distributions shown in Figure 7-12 indicates that maximum stress can be considered a normally distributed random variable for all three lay-ups. The mean value of stress is higher than the corresponding nominal value resulting from the deterministic simulation in all three case studies, as shown in Figure 7-12. This is due to the fact that the distribution of residual stresses over the laminate depends on the local properties of the laminate and deviations of the nominal fibre orientation at a local level generate higher levels of stresses locally.

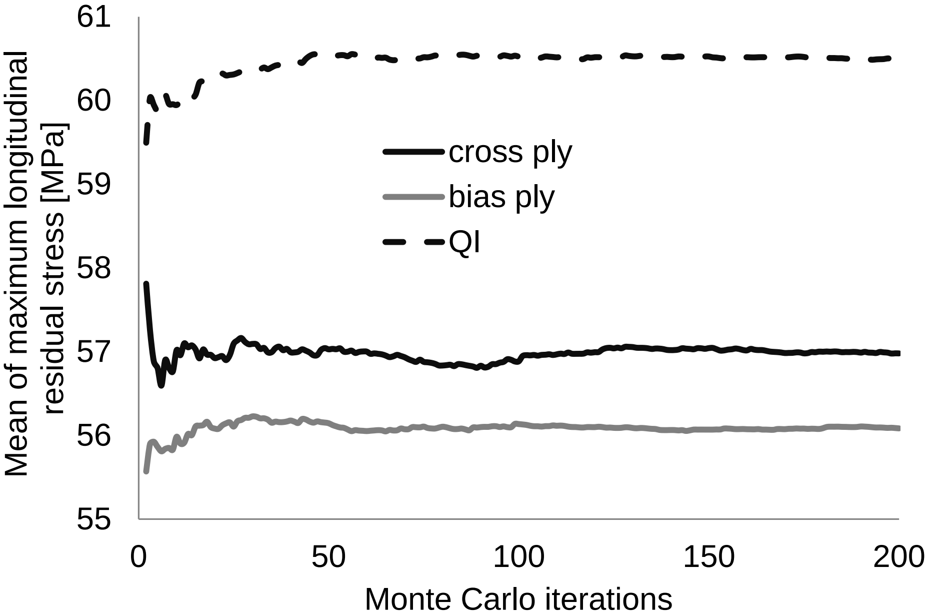

Fig. 7-10 Convergence of Monte Carlo simulation: mean of maximum longitudinal residual stress.

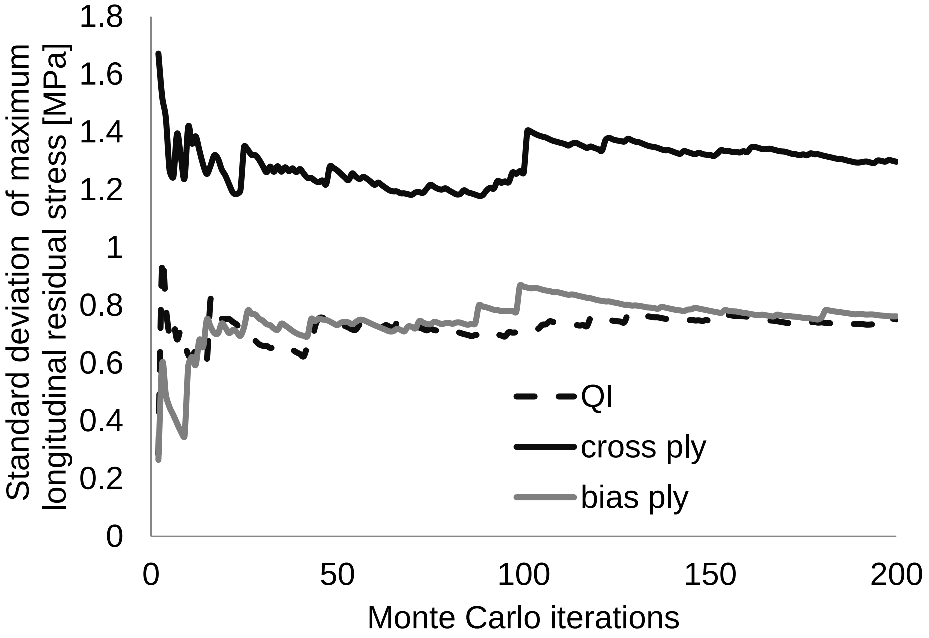

Fig. 7-11 Convergence of Monte Carlo simulation: standard deviation of maximum longitudinal residual stress.

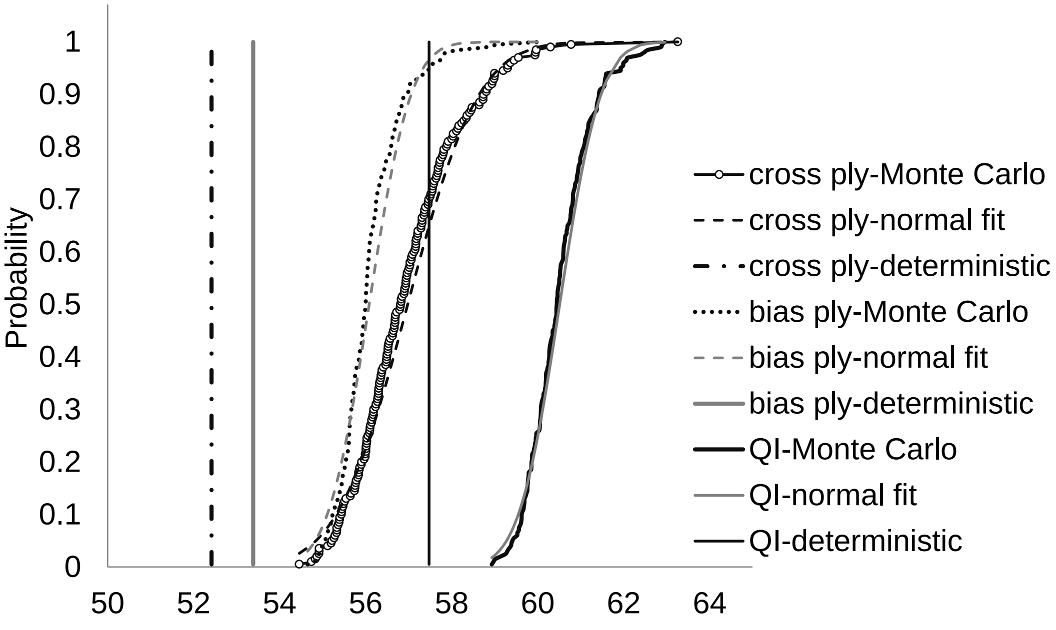

Fig. 7-12 Probability distribution of maximum longitudinal residual stress.

Figures 7-13 and 7-14 depict the convergence of the mean and standard deviation of corner distortion of the lower flange, respectively. The corner distortion refers to the angle observed at the edge of the lower flange 100 mm distance from the corner and it is a combination of spring-in and bowing effects. As it can be observed, satisfactory convergence was obtained for the mean and standard deviation of the corner angle for all three cases. The distortion angle exhibits small variation with a standard deviation not higher than 0.05 º for all lay-ups and can be represented by a normally distributed variable as shown in Figure 7-15. In addition, small differences exist between the mean values of distortion angle for the different lay-ups. Given that the effective in-plane CTE is the same for the three lay-ups, this can be attributed to the presence of twist and bowing effects. Examination of Figures 7-16 and 7-17 indicates that a quite satisfactory convergence was obtained after 200 Monte Carlo iterations for both the statistical moments of the twist angle. It should be noted that twist refers to the angle observed at the edge of the upper flange 100 mm distance from the corner. Figure 7-18 shows that twist angle can be represented as a normal random variable for the three lay-up sequences studied.

The mean values of both distortion angle and twist converge to values close to the corresponding results from the deterministic simulation for all three lay-ups. Examination of the deterministic model results illustrated in Figure 7-18 suggest that the quasi-isotropic laminate presents a small but finite twist, with the bias-ply and cross-ply laminate showing negligible twist. In the case of the deterministic model the perfect cross ply laminate presents no twist due to the fact that no twisting moment is generated. In the case of the perfect bias-ply lay-up twisting is counteracted by the ±45º layers, whereas in the case of the perfect quasi-isotropic lay-up the twisting moment is not resisted sufficiently at the bias direction showing the highest levels of twist. This explains the deterministic model results for the maximum longitudinal stress shown in Figure 7-12; higher levels of distortion correspond to higher stress levels. The results suggest that the twist presents a standard deviation of 0.4º, 0.01º and 0.08º, for the cross ply, bias ply and quasi-isotropic laminate respectively. This is attributed to the differences in stiffness in the bias direction in each lay-up. Therefore, the cross ply laminate is the most susceptible in local deviations from the perfect nominal orientations, presenting the highest variability in twist given that no fibres are aligned in the ±45º. In addition, the different levels of variability in twist can explain the differences in standard deviation of maximum stress between the three lay-ups as shown in Figure 7-11. Although for small levels of misalignment the bias ply laminate is expected to show the highest variability in the effective in plane CTE, the quasi-isotropic laminate exhibits the lowest variation in corner angle, whilst the other two lay-ups show higher and similar levels of variability. This is due to the fact that the cross ply and bias ply laminates have high levels of variability in twist and bowing, resulting to higher levels of variability in corner angle, given that the variations are a combination of spring-in, twist and bowing. In the case of the quasi-isotropic laminate the low levels of variability in twist and bowing lead to small variability in corner angle. Table 7-3 summarises the deterministic and stochastic cure simulation results for the three case studies.

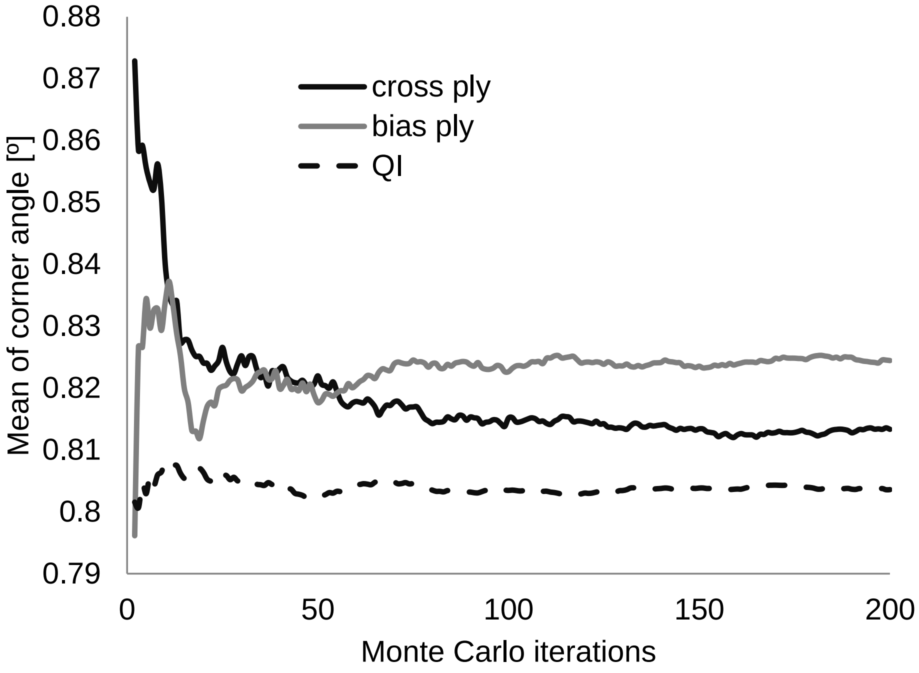

Fig. 7-13 Convergence of Monte Carlo simulation: mean of corner angle of the lower flange.

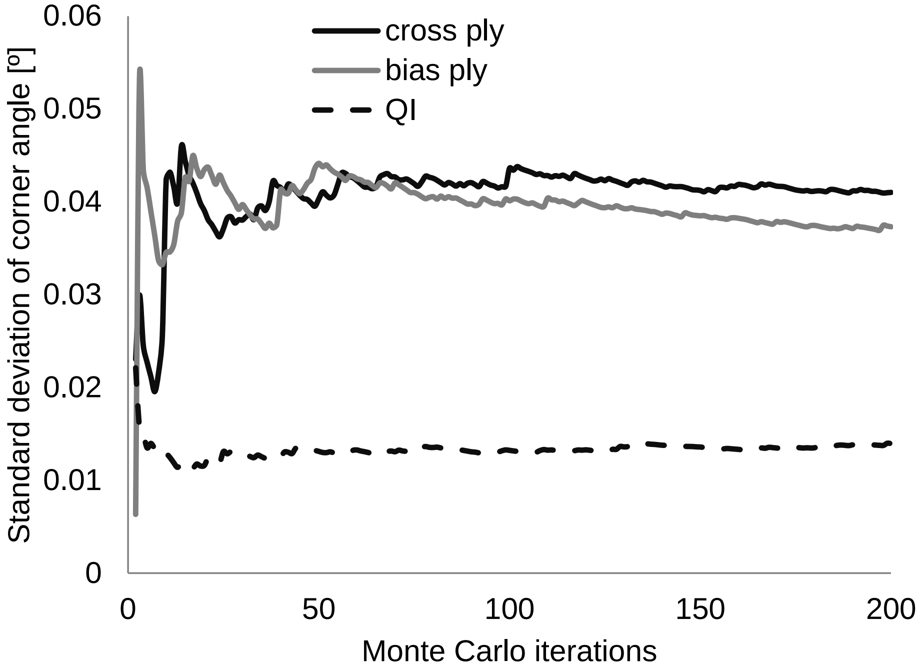

Fig. 7-14 Convergence of Monte Carlo simulation: standard deviation of corner angle of the lower flange.

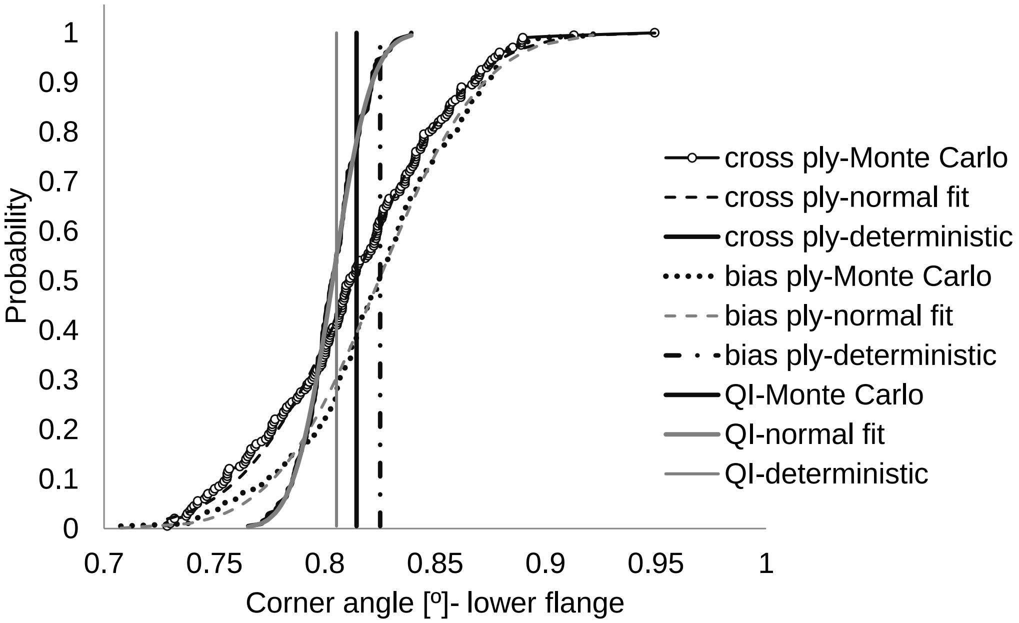

Fig. 7-15 Probability distribution of corner angle.

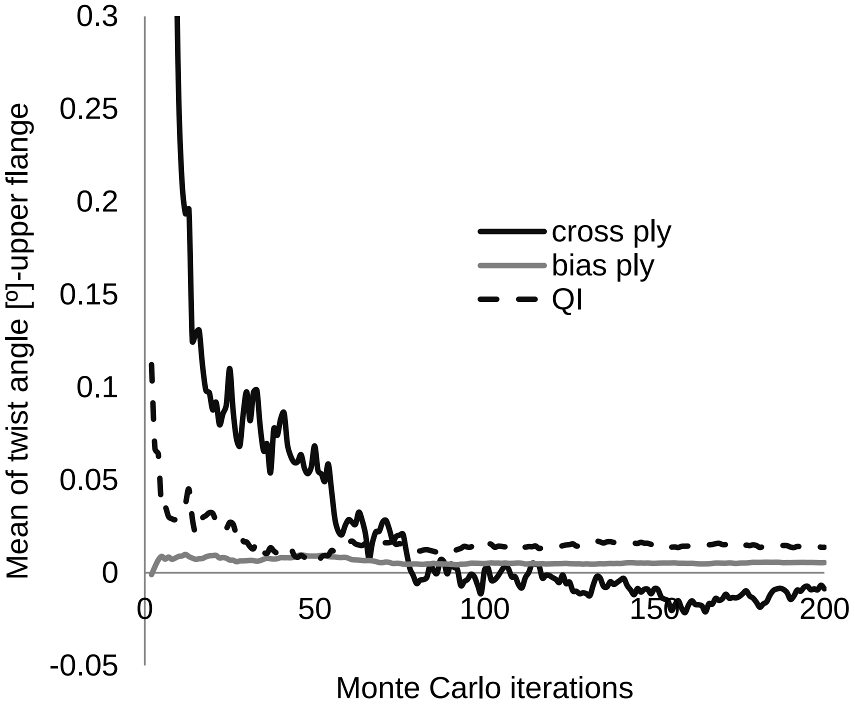

Fig. 7-16 Convergence of Monte Carlo simulation: mean of twist angle of the upper flange.

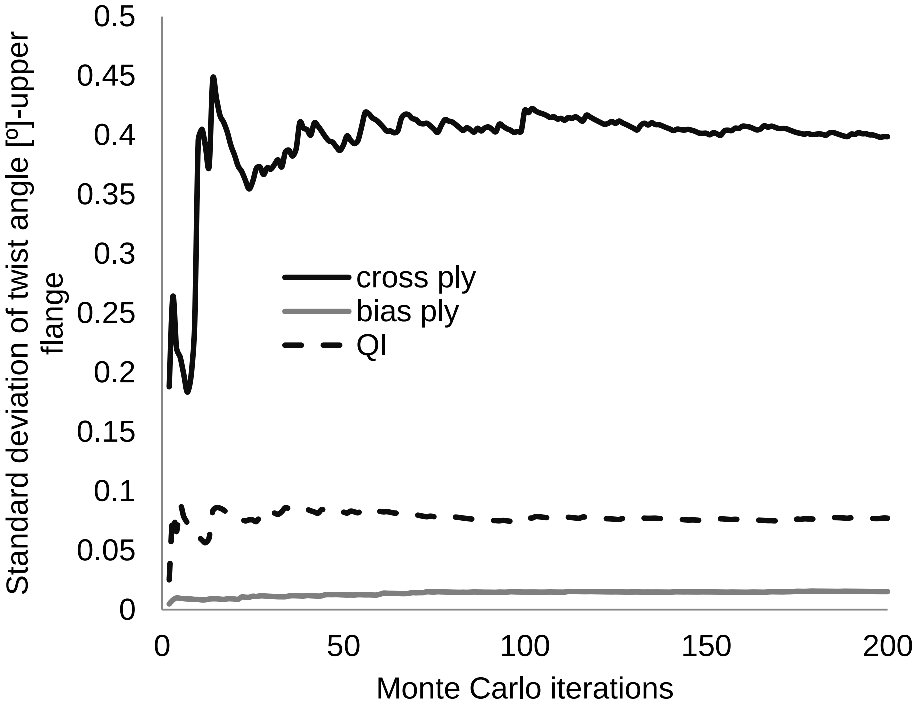

Fig. 7-17 Convergence of Monte Carlo simulation: standard deviation of twist angle of the upper flange.

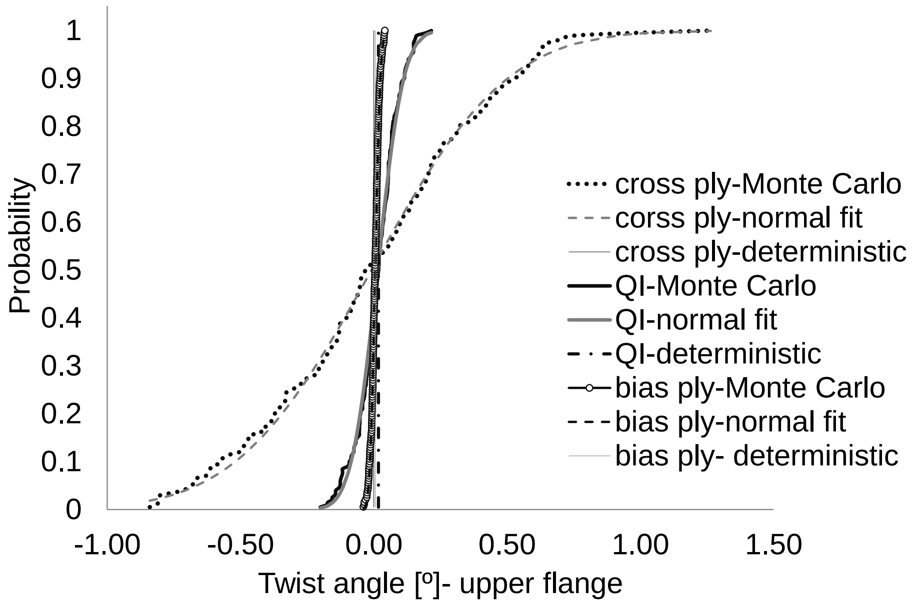

Fig. 7-18 Probability distribution of twist angle of upper flange.

Table 7-3 Deterministic model and stochastic simulation results: maximum longitudinal residual stress, corner angle and twist angle of the upper flange.

Parameter	Results	Cross-ply	Bias-ply	QI
Maximum longitudinal residual stress	Deterministic [MPa]	52.4	53.4	57.5
	μ [MPa]	56.9	56.1	60.5
	σ [MPa]	1.29	0.76	0.75
Corner angle	Deterministic [º]	0.81	0.82	0.8
	μ [º]	0.81	0.82	0.8
	σ [º]	0.04	0.04	0.01
Twist angle-upper flange	Deterministic [º]	0	0.005	0.013
	μ [º]	-0.008	0.005	0.017
	σ [º]	0.4	0.001	0.08

The results presented here indicate that fibre misalignment in the order of 1° can introduce significant variability in residual stresses, implying that in the case of higher levels of variability phenomena such as matrix pre-cracking may be affected at a local level. In addition, it is shown that fibre misalignment can considerably alter the final shape of the formed part depending on the lay-up sequence.

A sensitivity analysis was carried out to investigate the effect of different levels of variance and autocorrelation on the process outcome in the case of the cross ply laminate. In particular, three different case scenarios were investigated to study the effect of different levels of variance by setting a standard deviation of 2.5°, 5° and 7.5°, whilst the experimental values of correlation lengths were used in all three cases. In addition, four different case scenarios were studied to investigate the effect of different autocorrelation structure by setting zero correlation lengths, correlation lengths half, double and quadruple the corresponding experimental values, whilst the experimental value of standard deviation was used in all four cases. These results were used alongside the results of the deterministic model and the results of the variability corresponding to the experimental results. All the cases considered are summarised in Table 7-4.

Table 7-4 Sensitivity analysis case scenarios.

Cases	σ [°]	b_x [mm]	b_y [mm]
Case 1	2.5	20.21	4.67
Case 2	5	20.21	4.67
Case 3	7.5	20.21	4.67
Case 4	1.2	0	0
Case 5	1.2	10.11	2.34
Case 6	1.2	40.42	9.34
Case 7	1.2	80.84	18.68

The dependence of output variability on standard deviation of the fibre misalignment is illustrated in Figure 7-19. As it can be observed in Figure 7-19a both the maximum longitudinal stress average and standard deviation increase with increasing the standard deviation. The mean of maximum residual stress increases due the fact that twist is more pronounced due to higher levels of variability; higher levels of distortion result in higher stresses. The increase of the maximum stress average is non-linear and convex, i.e. the sensitivity of maximum stress on standard deviation of fibre misalignment increases with increasing input variability. This can be explained by the local character of the generation of residual stress which results in higher maximum stress over the whole component as the probability of extreme local variability increases. The trend of maximum residual stress standard deviation is linear as a function of the standard deviation of tow orientation (Figure 7-19a), with a sensitivity of about 1 MPa per 1° of misalignment. This behaviour points to a generic behaviour of a strong dependence of maximum stress and of the likelihood of potential damage on increased variability with the effect being accentuated as variability reaches higher levels. This is combined with a slow decrease in coefficient of variation of the maximum residual stress, indicating that the certainty of the highly non-desirable possibility of damage due to the residual stress increases with increasing variability.

Similarly to residual stresses, increasing the standard deviation in local tow orientation induces an increase of the standard deviation in both corner and twist angle (Figure 7-19b). This effect is non-linear following a concave dependence, i.e. the positive sensitivity of both corner and twist angle on the standard deviation of fibre misalignment decreases with increasing variability. This can be explained by the stronger random character of variability as standard deviation increases at the same level of autocorrelation length. Since macroscopic manifestations of variability, such as the twist and corner angle, are affected by the misalignment over an area of the component the increase in random misalignment, whilst global imbalance of the layup is kept at the same level, results in a lower sensitivity at higher levels of variability.

a

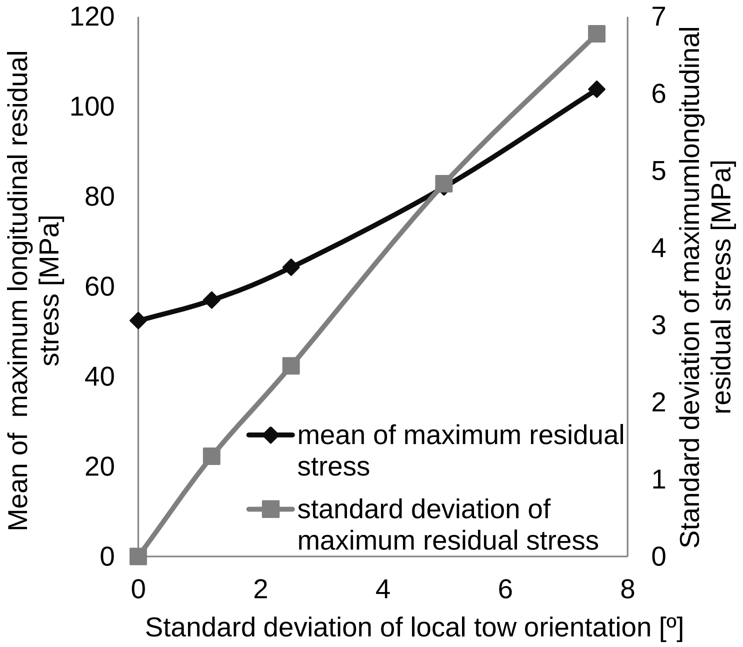

b

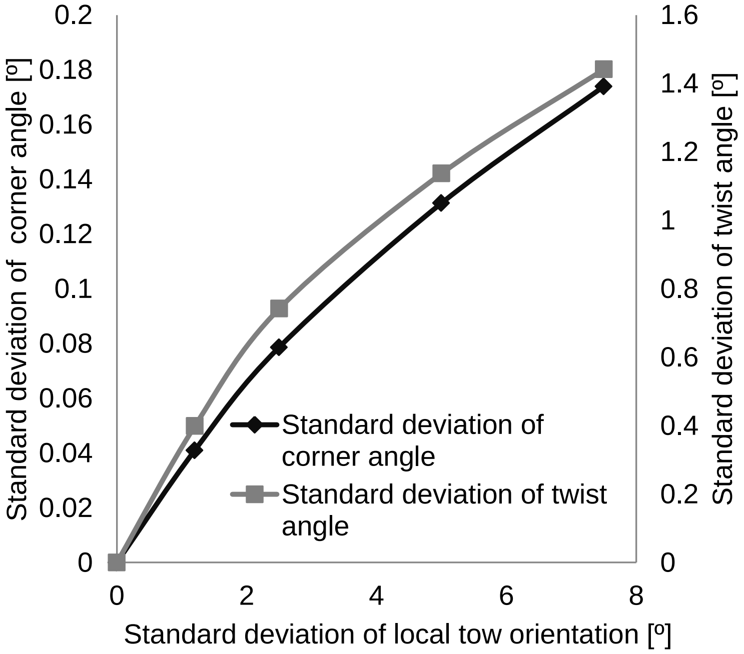

Figure 7-19 Sensitivity analysis results, standard deviation: (a) maximum longitudinal stress; (b) shape distortion.

Figure 7-20 illustrates the effect of correlation lengths. It can be observed that the influence on the mean of maximum residual stress is negligible, whilst the standard deviation of maximum residual stress presents a slight increase as the correlation length increase from zero to the nominal values with a plateau occurring at higher values of correlation lengths (Figure 7-20a). This can be attributed to the fact that formation of residual stresses is a local phenomenon; therefore it is governed by local tow orientation rather than the dependence of fibre misalignment over the space domain. The slight initial increase in standard deviation of maximum residual stress is due to the fact that tail events are reinforced due to the increased correlation; this influences the standard deviation but not the maximum as the effect is symmetric. The effect on standard deviation becomes weaker at high correlation lengths (over 20 mm in the x direction) as the characteristic patches of variability reach a size similar to the width of the component (40 mm).

The standard deviation of both corner and twist angles increases as correlation lengths increase. This is attributed to the fact that shape distortion is a macroscopic phenomenon and it increases as the imbalances in layup introduced by variability increases in size. The dependence is non-linear with a convex curvature at low autocorrelation lengths and a concave curvature at high lengths. The initial increase in sensitivity is due to the stronger effect of macroscopic balances. The sensitivity dependence reverses over 20 mm in the x direction as the size of misaligned areas reached the size of the component. Table 7-5 summarises the sensitivity analysis results for the seven case scenarios.

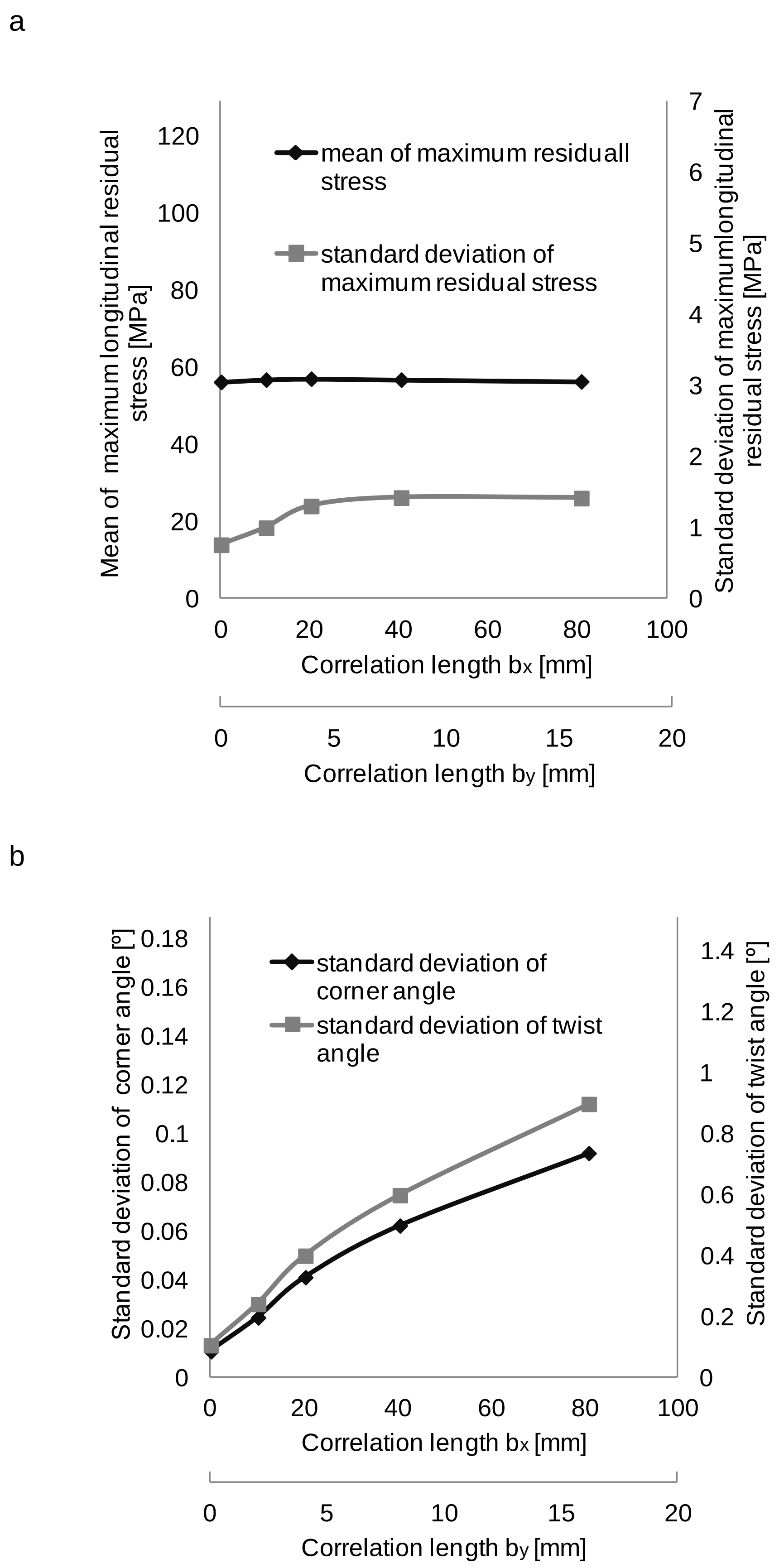

Figure 7-20 Sensitivity analysis results, autocorrelation: (a) maximum longitudinal stress; (b) shape distortion.

Table 7-5 Sensitivity analysis results.

Parameter	Results	Case 1	Case 2	Case 3	Case 4	Case 5	Case 6	Case 7
Maximum longitudinal residual stress	μ [MPa]	64.3	82.1	103.8	56.16	56.75	56.74	56.27
	σ [MPa]	2.5	4.8	6.8	0.75	1	1.4	1.4
Corner angle	σ [º]	0.08	0.13	0.17	0.01	0.024	0.06	0.09
Twist angle	σ [º]	0.74	1.14	1.44	0.1	0.24	0.6	0.9

7.4 Overview

The methodologies demonstrated in this chapter allow the quantification of the influence of variability in fibre orientation on the cure process outcome. The experimental results showed that high specification fabrics can involve considerable geometrical variability, which in turn can introduce significant variation to the process outcome. It was found that tow orientation of high specification carbon NCFs can vary with a standard deviation of 1.2º, showing high anisotropic autocorrelation with the major direction of autocorrelation coinciding with the direction of the non-structural stitching of the fabric. Furthermore, it was shown that the Cholesky factorisation and spectral decomposition are capable of representing the spatial field accurately with the same accuracy and efficiency. On the contrary, the Karhunen-Loève expansion yielded poor results for the given study. The Cholesky method was deemed to be the most appropriate technique to reproduce the stochastic field of this study due to its simplicity in comparison to the spectral decomposition.

The stochastic simulation results suggested that maximum residual stress can present a coefficient of variation up to about 2%, whilst the average level of stress is higher than that for the nominal fibre orientations, with potential implications in the performance of manufactured parts. Although the variability in distortion angle is small in absolute terms, considerable qualitative variations in shape can be induced by the presence of fibre geometrical variability. Moreover, the way shape distortion due to fibre misalignment is manifested is sensitive to the lay-up, with fibre misalignment having a stronger effect in modes of distortion manifested in the most compliant direction of the component. These findings are of crucial importance since shape variations lead to considerable part quality and assembly issues, especially in the case of large components.

8. Stochastic simulation of the influence of boundary conditions and cure kinetics uncertainty on cure time in composites cure

8.1 Introduction

In this chapter the influence of variability on heat transfer effects occurring during the cure process is presented. Boundary condition uncertainty is quantified experimentally as detailed in section 3.5 and appropriate stochastic processes are developed to represent variability in tool/air temperature and surface heat transfer coefficient. This information is combined with the models of cure kinetics variability presented in chapter 6 and the overall stochastic simulation problem is addressed by coupling the finite element based cure simulation model (Chapter 4) with the Monte Carlo scheme (MC) and an implementation of the Probabilistic Collocation Method (PCM) presented in Chapter 5. The methodology is demonstrated in the case of thin carbon fibre-epoxy laminates.

8.2 Stochastic process development

The procedure for selecting and developing the boundary condition stochastic models uncertainty is illustrated in Figure 8-1. The first step is to estimate the autocorrelation structure of the raw data for each variable in order to investigate the dependence of variability on time. In the case of a stationary process no trend is present in the data and the autocorrelation decays close to the zero value within several time increments. If the autocorrelation is close to zero on average, the time series is considered a random sequence of observations that are independent and therefore can be modelled as a random variable. If the autocorrelation does not decay towards a negligible plateau in the long term, i.e. the population shows strong autocorrelation with time (the population presents a trend over time) then the process is considered non-stationary and de-trending needs to be applied in order to generate a stationary stochastic process (Figure 8-1). After removing the trends, the residual variability is modelled using a stationary stochastic process. This procedure is repeated for every experimental curve of the three parameters to model variability across the different experimental runs.

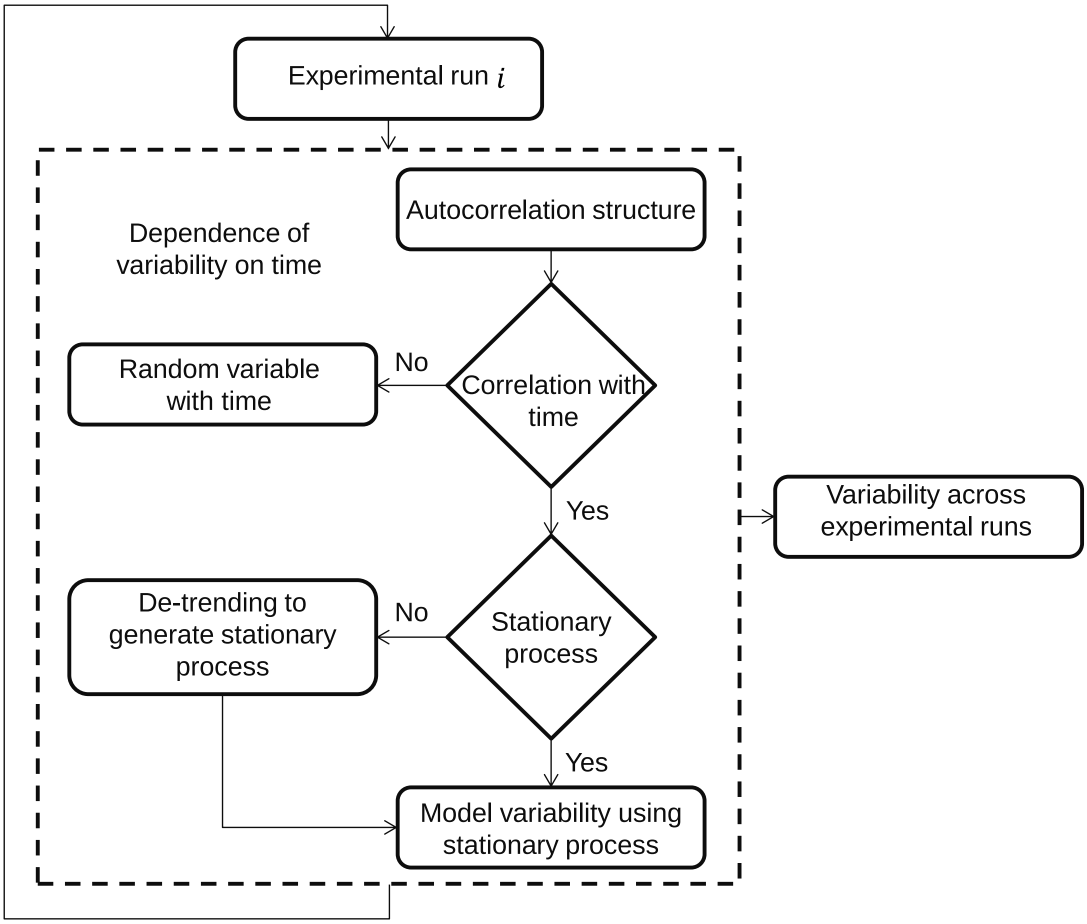

Fig. 8-1 Schematic representation of methodology for modelling of boundary conditions uncertainty.

8.3 Boundary conditions uncertainty

8.3.1 Experimental results

Figures 8-2, 8-3 and 8-4 summarise the experimental results of tool temperature, ambient temperature and surface heat transfer coefficient evolution for the ten tests carried out using the experimental set-up illustrated in Figure 3-4. A variable level across the different experimental runs is observed for all three parameters. This implies that in addition to time variations there is a dependence of the underlying level of each parameter across the different runs.

In terms of time dependence the tool temperature presented a periodic trend and short term variability as shown in Figure 8-2. The periodic trend is more pronounced and is governed by the temperature controller, whilst short term variability is due to random variations. The periodic features presented here correspond to the tooling set up of this study. It is expected that in the case of larger components and more complex geometries deviations from the nominal set point can be higher, resulting in a periodic trend of higher amplitude. The ambient temperature measurements exhibit a non-periodic long term trend and short term variability (Figure 8-3). This behaviour is attributed to several factors including the local temperature conditions, humidity, the use of heating or cooling systems and the quality of the insulation of the laboratory.

The differences between the results obtained by the two heat flux sensors placed at different location on the vacuum bags are negligible implying that there is no spatial dependence of the surface heat transfer variability. The surface heat transfer coefficient shows short term variability and a variable level. This type of variability can be attributed to the fact that natural air convection is driven by buoyancy forces caused by density differences due to temperature variations in air. As temperature increases the density of the fluid in the boundary layer decreases which causes the fluid to rise and be replaced by cooler fluid that also will heat and rise. Consequently, natural air convection is strongly influenced by the motion of air streams at a local level. No correlation is observed between the three variables implying that variability is generated independently between the three variables.

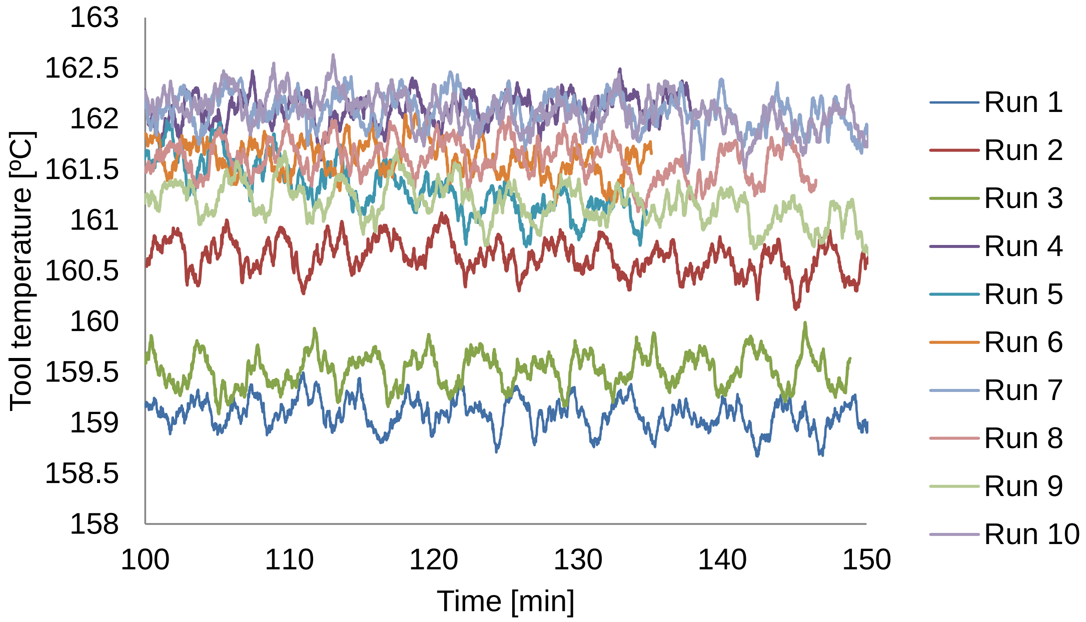

Fig. 8-2 Tool temperature as a function of time.

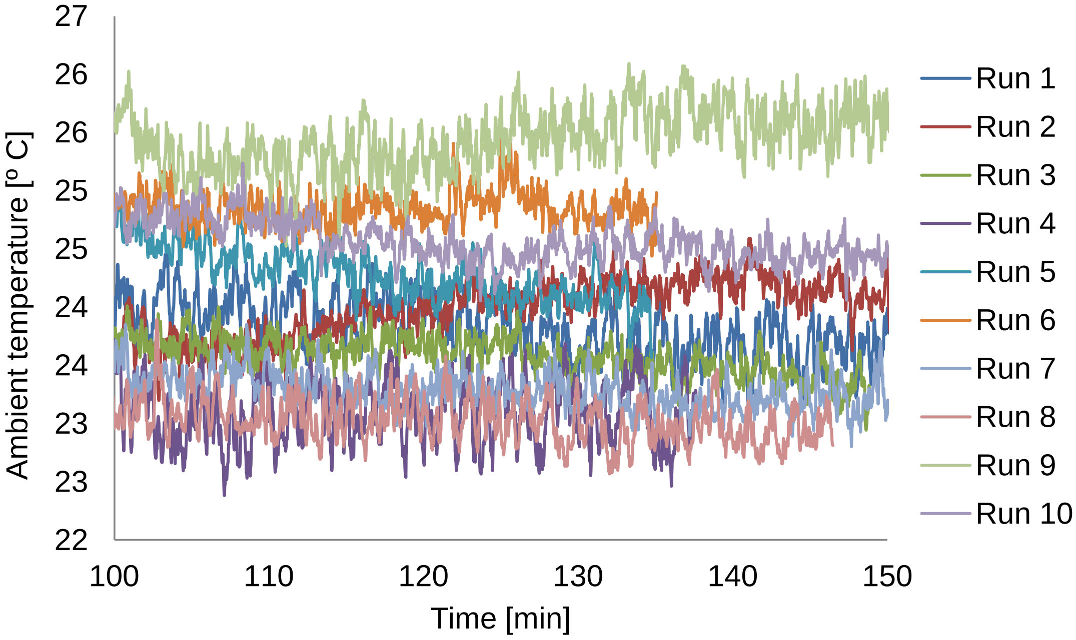

Fig. 8-3 Ambient temperature as a function of time.

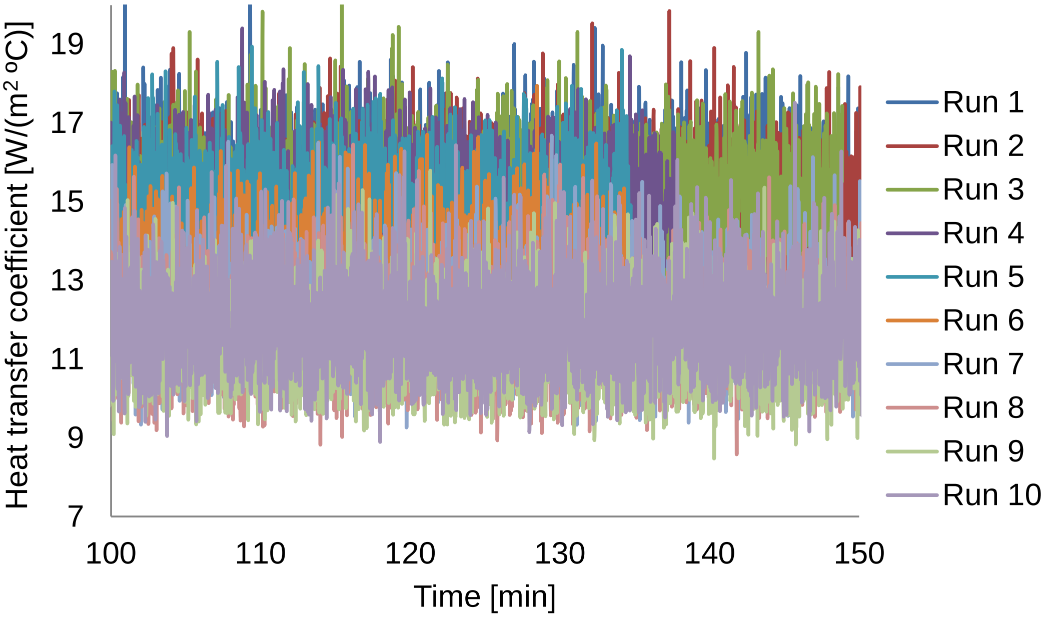

Fig. 8-4 Surface heat transfer coefficient as a function of time.

8.3.2 Stochastic processes

Figures 8-5, 8-6 and 8-7 illustrate the autocorrelation structure for one experiment (Run 1) for the three variables. Each variable had identical autocorrelation structure across different runs. Both tool temperature and ambient temperature present long term strong autocorrelation (Figures 8-5 and 8-6), implying non-stationary processes. Autocorrelation measures the extent to which variation of a variable behaves similarly for specific time lags. A periodic and a constant autocorrelation structure are observed in the case of tool temperature and ambient temperature, reflecting the periodic trend (Figure 8-2) and linear trend (Figure 8-3) in the experimental data, respectively. Consequently, de-trending needs to be applied to generate stationary stochastic processes for these two variables. The stationary stochastic process adopted to represent the ambient and tool temperature residuals after de-trending is the Ornstein-Uhlenbeck process (OU) described in detail in section 5.2.2.

In the case of surface heat transfer coefficient the autocorrelation structure shows very fast decay reaching a value close to zero after the first lag of time, implying that heat transfer coefficient shows no serial correlation over time (Figure 8-7). Therefore, the surface heat transfer coefficient can be treated as a random series of observations over time (section 5.2.1) and modelled as follows:

$$h = A_h + B_h y \tag{8-1}$$

where A_h expresses the level and is the mean value and B_h the volatility of the process for each experimental run, whilst y is a standard normal variable.

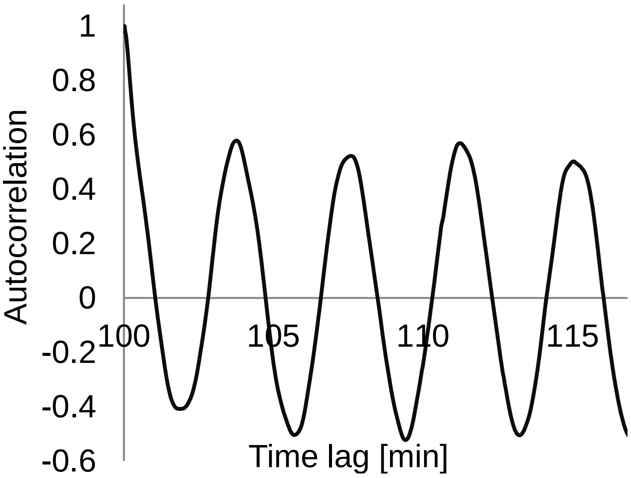

Fig. 8-5 Autocorrelation as a function of time lag- Run 1; tool temperature.

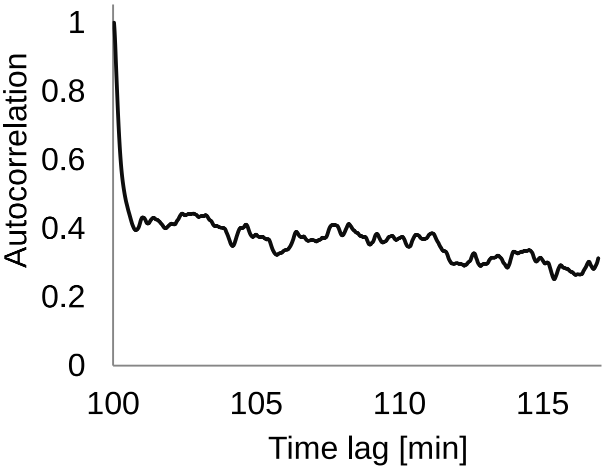

Fig. 8-6 Autocorrelation as a function of time lag- Run 1; ambient temperature.

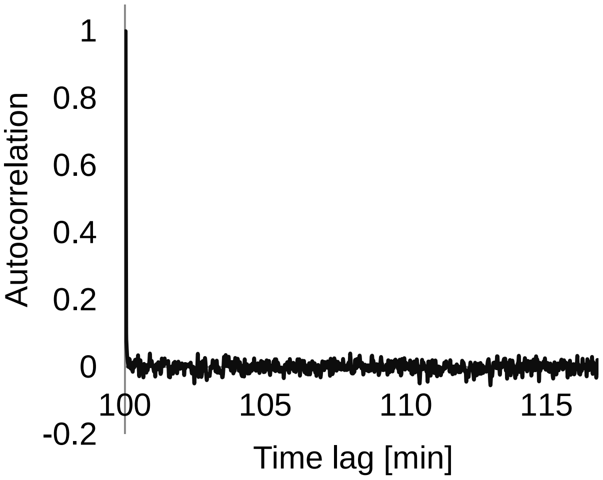

Fig. 8-7 Autocorrelation as a function of time lag- Run 1; surface heat transfer coefficient.

Figure 8-8 illustrates the results obtained in the different steps of the analysis of tool temperature variability. Fast Fourier transform (FFT) implemented in MATLAB was used to estimate the frequency of the periodic component of the process shown in Figure 8-2. A cosinusoidal fit (Figure 8-8a) was performed using the generalised reduced gradient non-linear optimisation method implemented in Microsoft Excel [148] to obtain an estimate of the amplitude of the periodic component. The residuals from the cosinusoidal fit present strong autocorrelation; therefore linear regression was applied to the residuals to remove the remaining trend as shown in Figure 8-8b. The residuals from the linear fit are modelled using Eq. (5-3). Figure 8-8d illustrates the autocorrelation of simulated residuals of tool temperature generated using a time increment of 1.25 s. It can be observed that the OU process reproduces the decay of the autocorrelation structure successfully. There are some discrepancies in the region of the plateau; however, this introduces a negligible error since the autocorrelation is close to zero at this region.

This procedure was iterated for every experimental run and yielded the following stochastic equation:

$$T_T = A_T + B_T t + C_T \cos(\omega_T t) + S_T \tag{8-2}$$

The first two terms express the linear fit and represent the level and slope of each experimental curve, whilst C_T and ω_T are the amplitude and the frequency of the cosinusoidal fit, respectively. In addition, S_T expresses the mean reverting stationary stochastic process (OU).

Figure 8-9 illustrates the analysis steps in the case of ambient temperature variability. As shown in Figure 8-9a, a linear fit was carried out to remove the long term trend in ambient temperature over time. The residuals resulting from the linear fit present strong autoregression (Figure 8-9b) and are modelled using Eq. (5-3). Figure 8-9c illustrates the autocorrelation of simulated residuals of ambient temperature generated using a time increment of 1.25 s. Similarly to tool temperature, the OU process is capable of capturing the decay of the autocorrelation structure successfully.

Ambient temperature variability is modelled using the following stochastic relation:

$$T_A = A_A + B_A t + S_A \tag{8-3}$$

where A_A and B_A are the constants of the linear fit and represent the level and slope of each experimental curve, and S_A is a mean reverting stochastic process expressed by Eq. (5-3).

All terms in Eqs. (8-1), (8-2) and (8-3) were estimated for each experimental curve for the three parameters and were considered normal random variables across different runs constant with time. Table 8-1 summarises their statistical properties. Examination of Table 8-1 suggests that all three variables (tool/ambient temperature, heat transfer coefficient) present a significant variation in level (A_h, A_T, A_A) across the different runs with the surface heat transfer coefficient showing the highest variability. The mean value of λ_A is considerably higher than that of λ_T, implying that ambient temperature shows stronger autoregression than tool temperature.

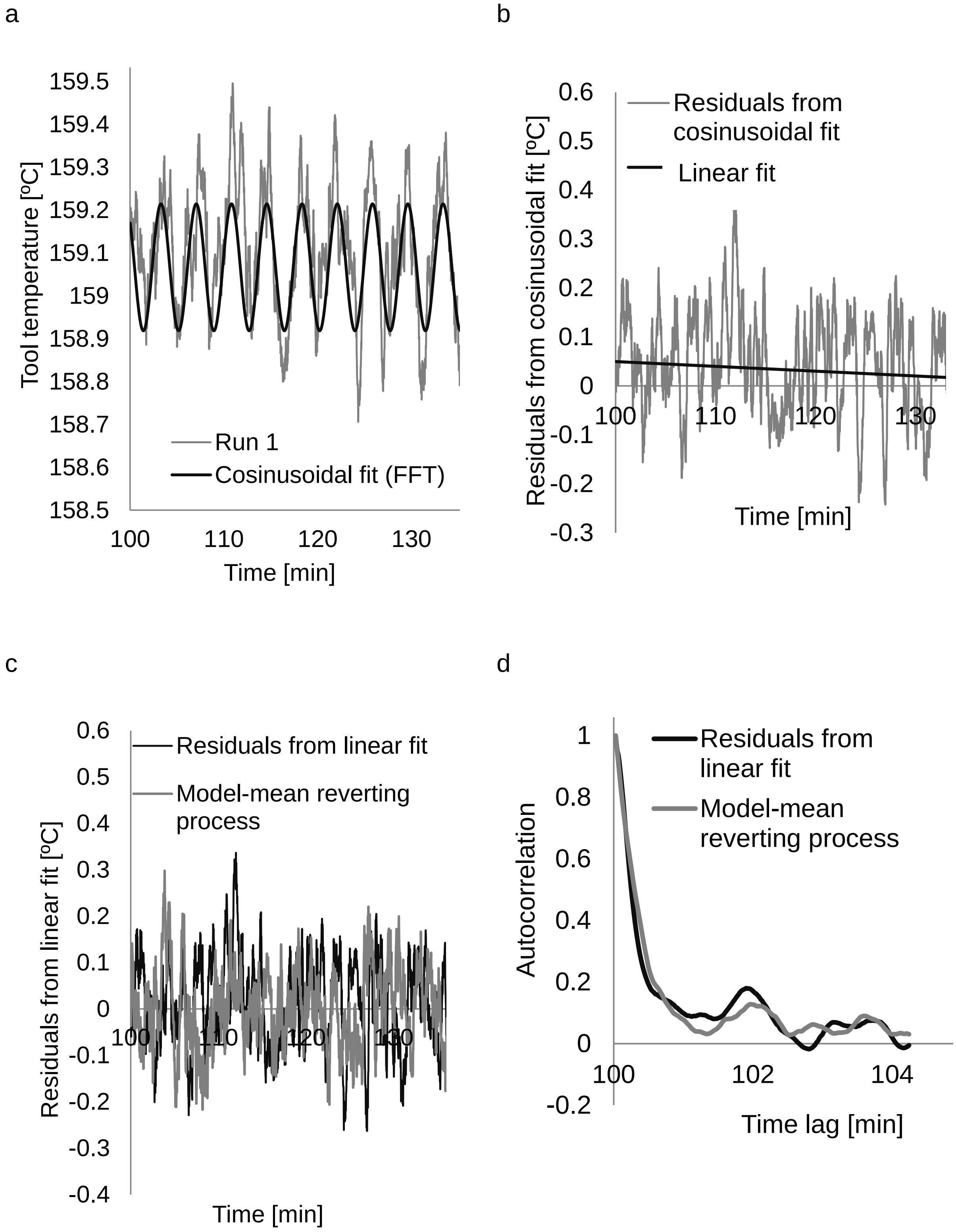

Fig. 8-8 Procedure of modelling of tool temperature uncertainty (a) cosinusoidal fit, (b) linear fit, (c) modelling of stationary process, (d) autocorrelation of simulated residuals over time.

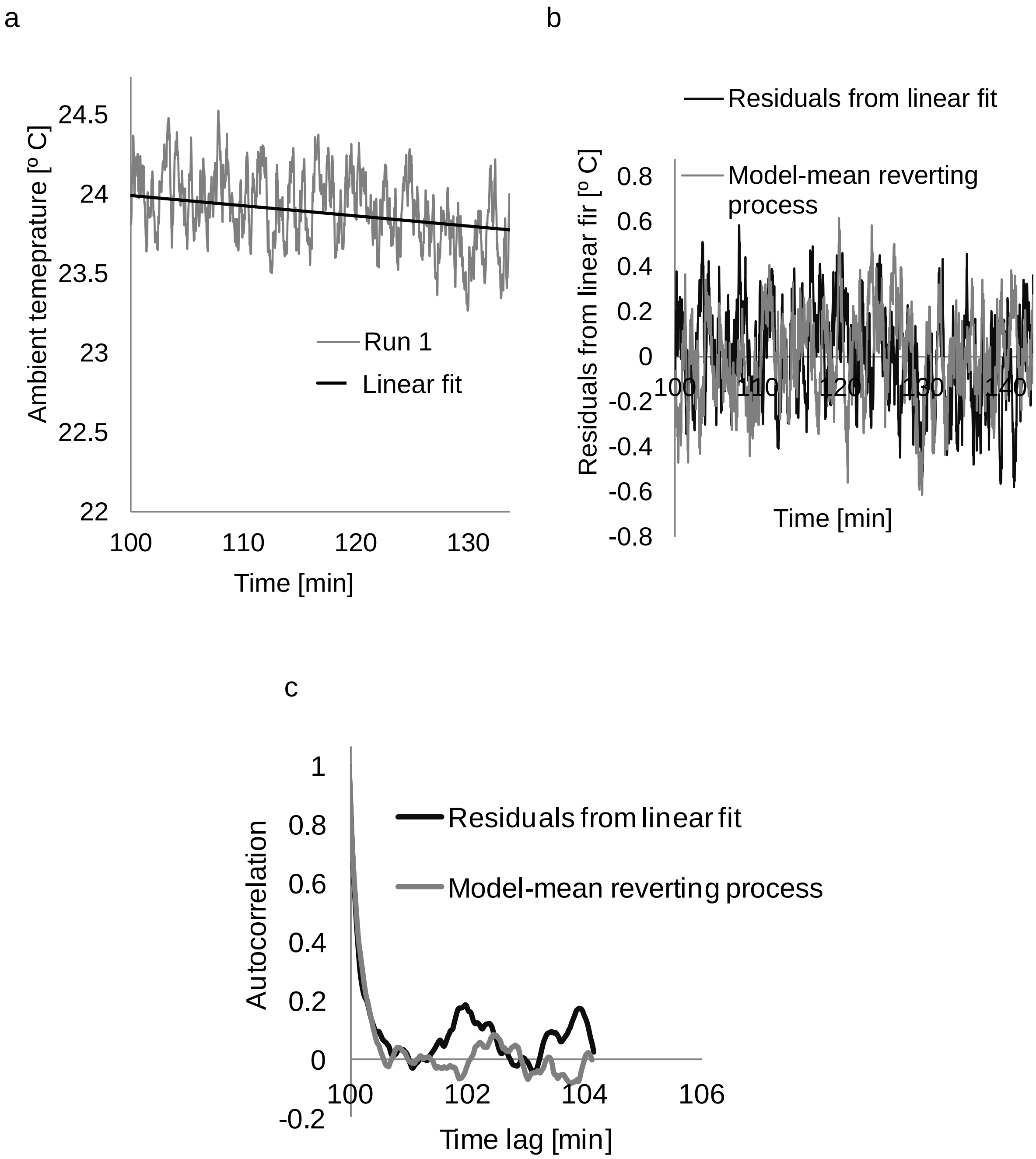

Fig. 8-9 Procedure of modelling of ambient temperature uncertainty (a) linear fit, (b) modelling of stationary process, (c) autocorrelation of simulated residuals over time.

Table 8-1 Statistical properties of boundary conditions uncertainty across different experimental runs.

Boundary conditions	Stochastic model parameter	Mean	Standard deviation
h [W/m^2/^{o}C]	A_h	13.47	1.65
	B_h	1.16	0.04
T_T [^{o}C]	A_T	161.59	1.39
	B_T	0.004	0.0006
	C_T	0.16	0.02
	ω_T	0.004	0.00006
	λ_T	1.95	0.4
	μ_T	-0.00006	0.004
	σ_T	0.21	0.004
T_A [^{o}C]	A_A	24.5	1.2
	B_A	-0.011	0.007
	λ_A	3.13	1.14
	μ_A	-0.055	0.18
	σ_A	0.43	0.085

8.4 Stochastic cure simulation

The cure of a 3.6 mm thick carbon fibre- epoxy laminate fabricated by infusion was modelled using the stochastic simulation approach developed in this study. The lay-up sequence of the laminate is [0^o/90^o/90^o/0^o]$_3$. The initial temperature is 15 ^{o}C and is applied to all the nodes of the model. A prescribed temperature boundary condition defined by the cure profile is applied to the nodes in contact with the mould, whereas a natural air convection boundary condition is applied on the surface in contact with the vacuum bag. The standard cure profile for the epoxy system of this study (Hexcel RTM6) is used comprising two dwells at two different temperatures linked by two standard ramps of 1 ºC/min. The temperature of the first dwell T_1 as well as the post cure temperature T_2 are considered stochastic following Eq. (8-2). In the case of T_2 the mean value of A_T is 180 ºC.

A time increment of 1 min is used in the cure simulation and the three parameters are set at the mean values of A_h, A_T and A_A, respectively. Figure 8-10 presents deterministic cure simulation results at three different points across the thickness of the laminate. The three points are located at the lower boundary (prescribed temperature boundary condition), middle and top (natural air convection boundary condition) of the laminate. An out of plane degree of cure gradient is present, due to heat dissipation caused by natural air convection at the top of the laminate. This leads to different degree of cure and cure reaction rate evolution through the thickness of the laminate, as shown in Figure 8-10. The onset of the reaction is shifted towards higher times from the lower side to the top of the laminate. This is explained by the presence of a temperature gradient through the thickness of the laminate; the temperature at the top of the laminate is lower than the control temperature throughout the cycle resulting in a lag in reaction progress. Similarly, the degree of cure at the end of the cycle is maximised on the lower face with a value of 0.95, in contrast to a final value of 0.91 at the upper face of the curing component (Figure 8-10).

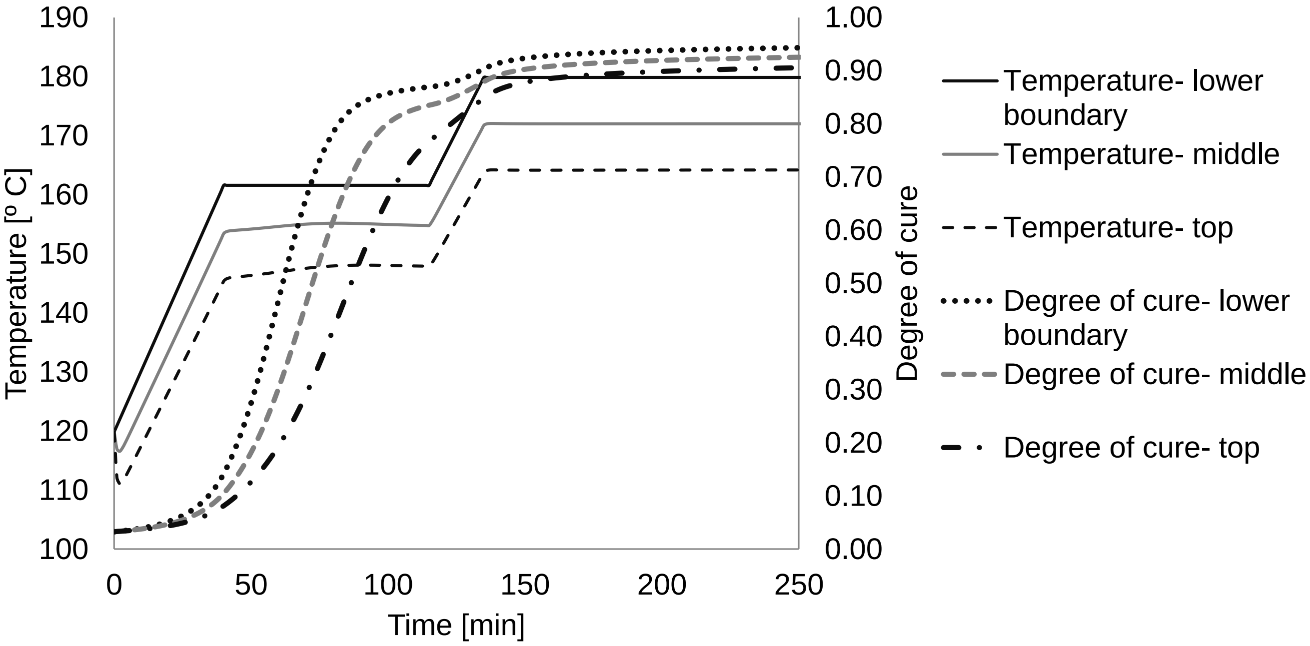

Fig. 8-10 Evolution of laminate degree of cure and temperature through the thickness of the laminate. Deterministic model results.

8.4.1 Short term variability

The effect of variability over time for the three parameters is investigated to study the influence of short term variability on the process outcome. This was carried using Eqs. (8-1), (8-2) and (8-3) assuming constant values for A_h, A_T and A_A equal to the corresponding means. Three cases are considered; surface heat transfer coefficient uncertainty over time only, tool temperature variability over time only and ambient temperature variability over time only. A time increment of 1.25 s is used in all three cases in order to reproduce the dependence of variability on time for these parameters accurately, increasing significantly the computational cost.

Table 8-2 summarises the stochastic simulation results for the three cases. Figures 8-11, 8-12 and 8-13 present the evolution of temperature and degree of cure for the three cases respectively. In the case of surface heat transfer coefficient variability over time (Figure 8-11), the temperature at the natural air convection boundary condition presents strong variations, governed by variations in surface heat transfer coefficient with time. The temperature at the middle of the laminate shows considerably weaker variation with lower volatility, whilst the evolution of degree of cure through the thickness of the laminate is not affected, implying that time variations in surface heat transfer coefficient uncertainty introduces negligible variability on the cure process outcome. In particular, the absolute differences in the degree of cure between this case and the deterministic model vary from 9×10^{-8} to 5×10^{-5}.

In the case of tool temperature variability over time, the temperature at the temperature boundary condition shows a periodic trend reflecting the periodic trend of tool temperature (Figure 8-12). Similar behaviour is observed through the thickness of the laminate, implying that tool temperature variations propagates evenly through the thickness of the laminate; however, the evolution of degree of cure through the thickness of the laminate is not influenced with the absolute differences in the degree of cure between this case and the deterministic model varying from 8×10^{-8} to 7×10^{-5}.

Time variations of ambient temperature uncertainty introduce negligible variability in the temperature field and consequently in the degree of cure of the laminate (Figure 8-13), due to the fact that ambient temperature plays a less important role in heat dissipation caused by natural air convection. The absolute differences between this case and the deterministic model varied from 9×10^{-8} to 5.5×10^{-5}.

These results show that time variability has a negligible influence on the outcome of the process. This is due to the fact that for the given spread of values, the autoregressive nature of the stochastic parameters compensates their instantaneous variations over time introducing negligible variability to the cure process outcome. The stochastic simulation results indicate that variability over time introduces negligible variations in cure time, with a coefficient of variation of 0.9 %, 0.01% and 0.007% for the surface heat transfer coefficient, tool temperature and ambient temperature, respectively. In addition, the mean value of cure time converges to the corresponding nominal value resulting from the deterministic simulation in all three case studies, implying that the response of the model is not biased by short term variability. Therefore, stochastic simulation using the three levels as the only stochastic parameters and a time increment of 1 min in the simulations is sufficient to capture variability propagation accurately.

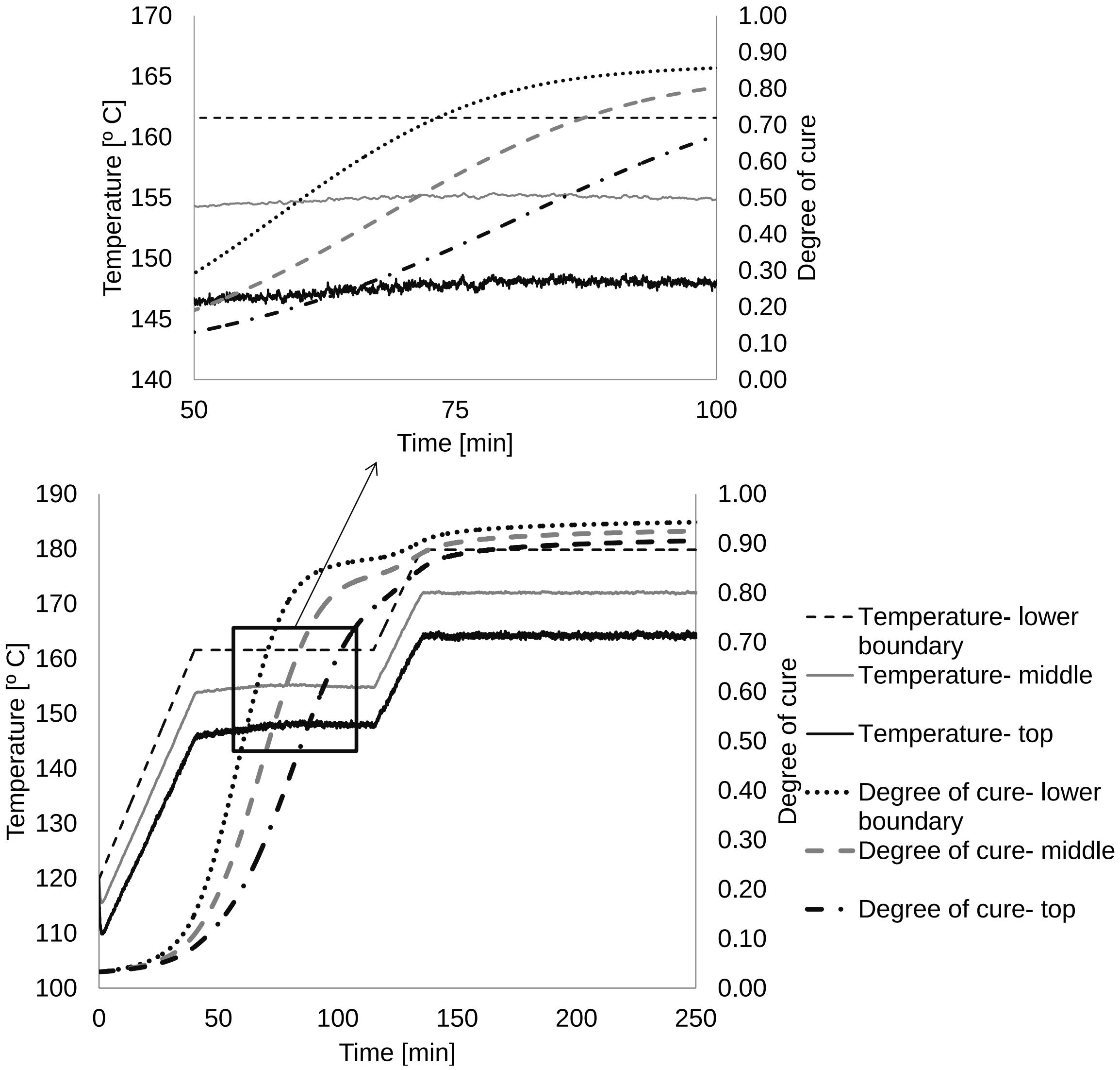

Fig. 8-11 Surface heat transfer coefficient variability over time; evolution of laminate degree of cure and temperature through the thickness of the laminate. Inset: detail during the first dwell.

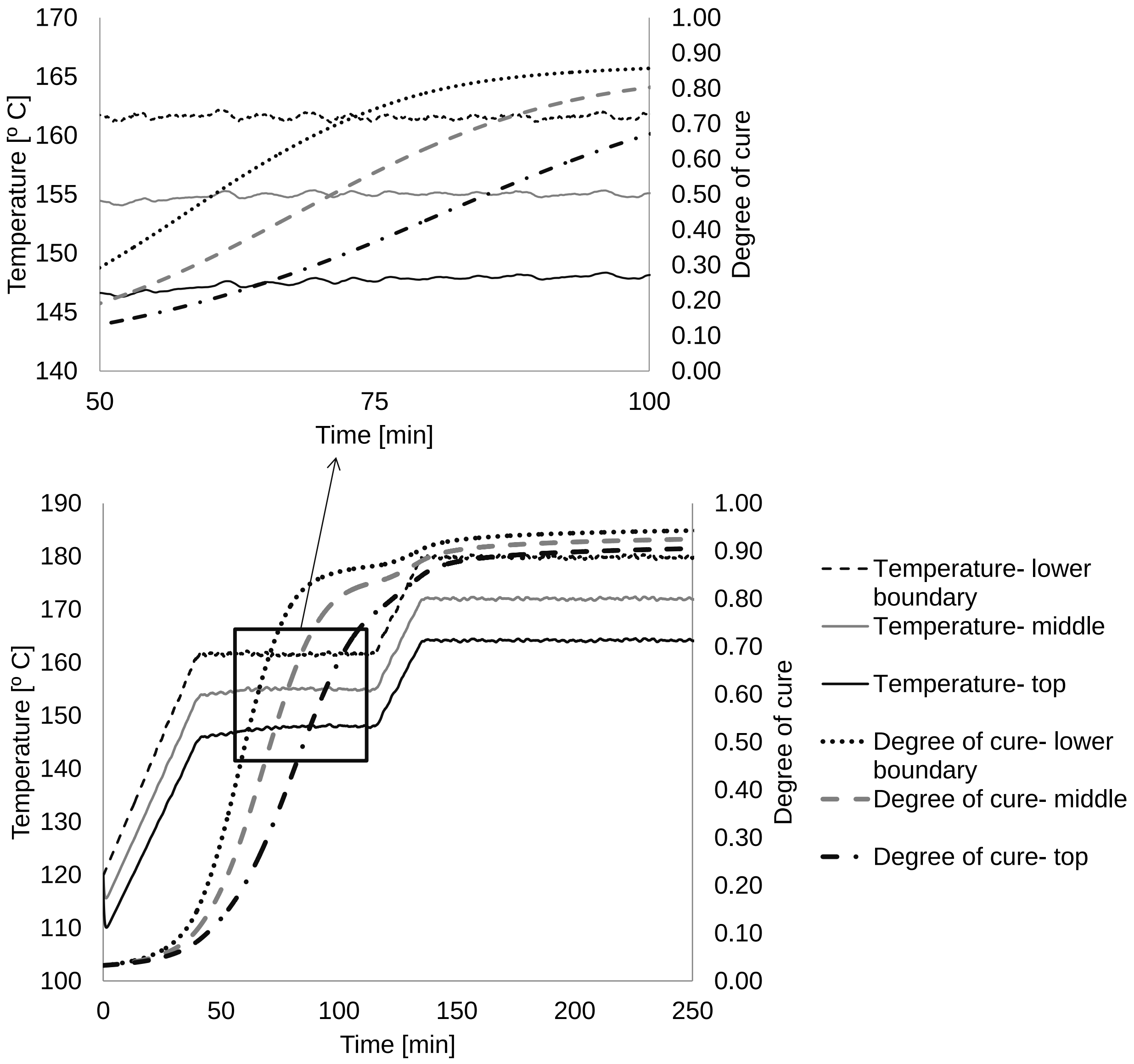

Fig. 8-12 Tool temperature variability over time; evolution of laminate degree of cure and temperature through the thickness of the laminate. Inset: detail during the first dwell.

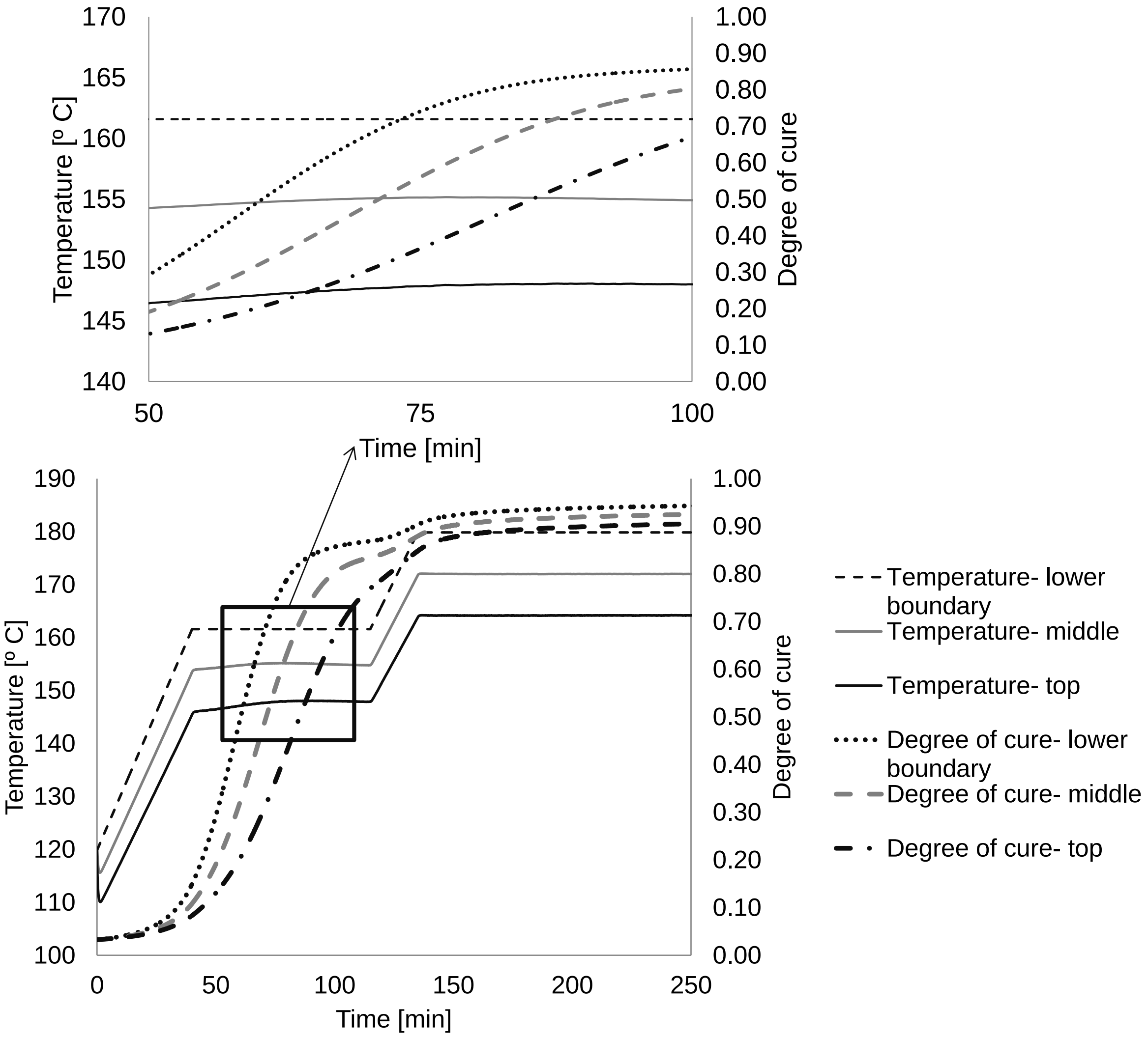

Fig. 8-13 Ambient temperature variability over time; evolution of laminate degree of cure and temperature through the thickness of the laminate. Inset: detail during the first dwell.

Table 8-2 Stochastic simulation results; effect of variability over time on cure time.

Case	Mean [min]	Standard deviation [min]
Deterministic	207.69	-
h	207.62	0.19
T_T	207.68	0.021
T_A	207.69	0.016

8.4.2 Effect of level variability across different runs

Following from the results of the previous section the overall simulation can be carried out considering the variability of the level of surface heat transfer coefficient and tool and air temperature. Thus Eqs. (8-1), (8-2) and (8-3) can be truncated to:

$$h = A_h \tag{8-4}$$

$$T_T = A_T \tag{8-5}$$

$$T_A = A_A \tag{8-6}$$

In addition to boundary conditions variability the effect of cure kinetics uncertainty is considered using the uncertainty model detailed in Chapter 6.

Five different cases are investigated using Monte Carlo taking into account: (i) cure kinetics and boundary conditions uncertainty, (ii) cure kinetics uncertainty only, (iii) ambient temperature variability, (iv) tool temperature variability and (v) surface heat transfer coefficient variability. The stochastic simulation results for the five cases are summarised in Table 8-3. Considering a convergence criterion of 5% of coefficient of variation in the standard deviation of cure time, satisfactory convergence is obtained in the Monte Carlo simulation after 1000 iterations for the first and last cases, whilst 500 iterations are required for the rest. Figures 8-14 to 8-18 illustrate the probability distribution of cure time for the five cases. The results suggest that cure time presents a coefficient of variation of 21.8 %, 1.2%, 1.1%, 12% and 17.4% (standard deviation of 47.4, 2.6, 2.3, 25.7 and 37.4 min) for the five cases. Examination of the probability distribution for the different cases shown in Figures 8-14 to 8-18 indicates that cure time can be considered a normally distributed random variable. These findings show that the surface heat transfer coefficient and tool temperature dominates cure time variability. Cure kinetics (Figure 8-15) and ambient temperature (Figure 8-16) uncertainty affect cure time variability; however, their influence is weak compared to variations in surface heat transfer coefficient and tool temperature as shown in Figures 8-14, 8-17 and 8-18. Furthermore, the mean value of cure time converges to the corresponding nominal value resulting from the deterministic simulation in the second and third cases, whilst it is slightly higher for the rest. This implies that there is a non-linear relation between cure time and surface heat transfer and tool temperature.

Table 8-3 Stochastic cure simulation results; effect of level variability on cure time.

Case	Mean [min]	Standard deviation [min]
kinetics, h, T_T, T_A	217.97 (MC)	47.41 (MC)
h	215 (MC)	37.4 (MC)
T_T	212.6 (MC)	25.7 (MC)
T_A	207.7 (MC)	2.31 (MC)
kinetics	208.3 (MC)	2.63 (MC)
h, T_T	219.7 (MC), 218.6 (PCM)	49.5 (MC), 47.8 (PCM)

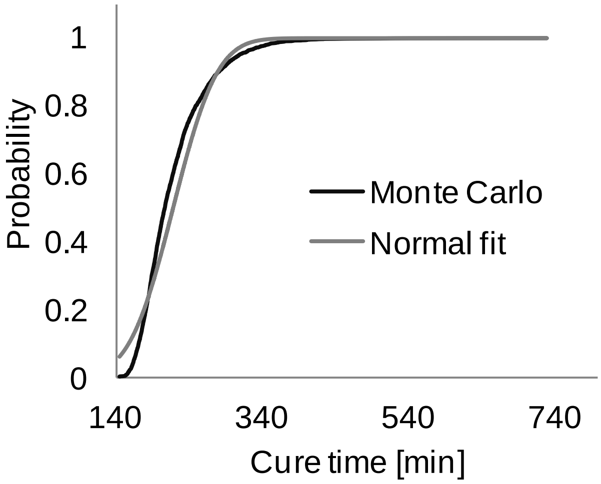

8-14 Probability distribution of cure time for boundary conditions and cure kinetics uncertainty.

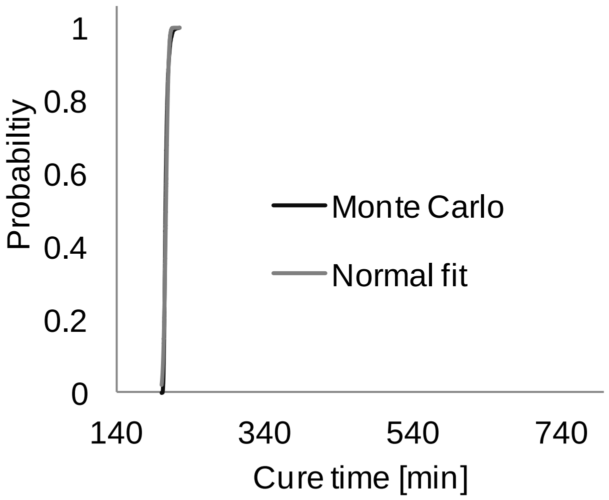

8-15 Probability distribution of cure time for cure kinetics uncertainty only.

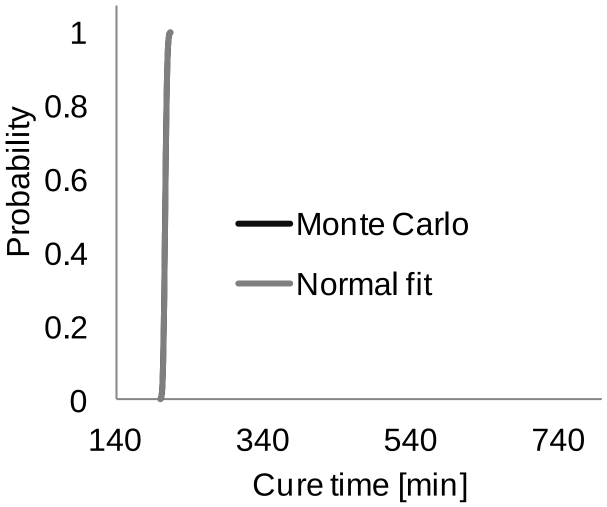

8-16 Probability distribution of cure time for ambient temperature uncertainty only.

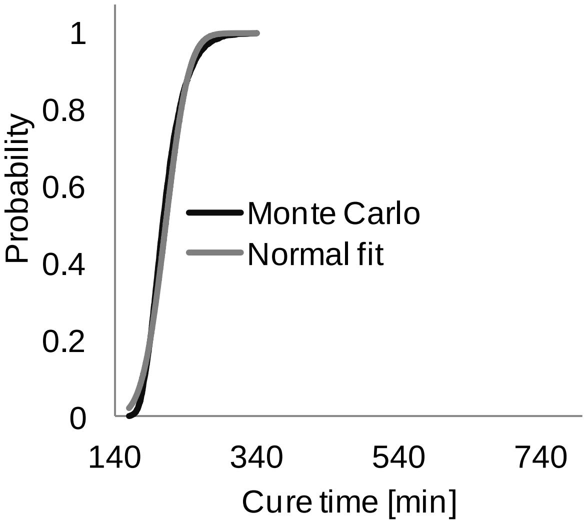

8-17 Probability distribution of cure time for tool temperature uncertainty only.

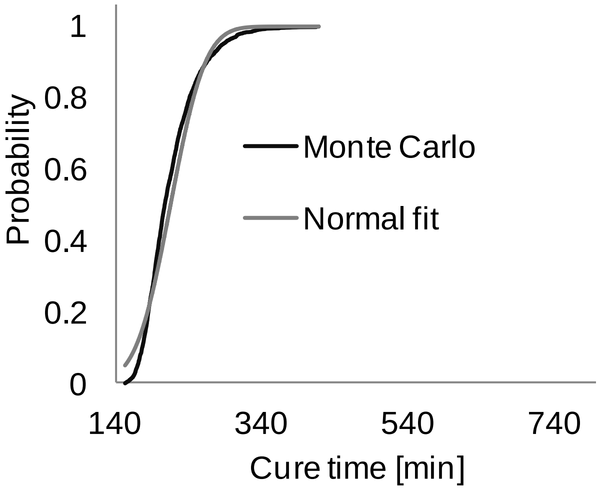

8-18 Probability distribution of cure time for heat transfer coefficient uncertainty only.

The propagation of variability can be explained considering the heat transfer mechanisms and kinetics followed during the cure. When surface heat transfer coefficient is higher, the cure time increases due to heat dissipation on the top of the laminate. In the case of tool temperature variability, higher values of tool temperature result in higher reaction rate which in turn lead to lower cure times. The same behaviour can be observed with ambient temperature due to the fact that higher values of ambient temperature lead to lower natural air convection resulting in lower cure times. In the case of cure kinetics uncertainty low initial degree of cure and low activation energy result in a shift to the peak of reaction to lower times leading to lower cure times.

Figure 8-19 illustrates the evolution of cure reaction rate with time for two realisations of the stochastic simulation model considering the combined effect of boundary conditions and cure kinetics uncertainty and for the deterministic model. The two stochastic cases reported represent the extremes of maximum and minimum cure time. Table 8-4 reports the values of the stochastic parameters for the two realisations. In realisation 1 (maximum cure time) the cure reaction rate has lower peak values throughout the thickness of the laminate, with the peak of reaction at the top of the laminate shifted considerably towards higher times leading to longer cure time. This is due to the high surface heat transfer coefficient, low tool temperature and low initial degree of cure values corresponding to this realisation. In contrast, in the case of realisation 2 (minimum cure time), the reaction starts considerably earlier and the peak is higher than the other two cases. Furthermore, the time lag of the onset of reaction between the lower side and the top of the laminate is significantly lower for minimum cure time case (realisation 2). This behaviour can be explained by the low surface heat transfer coefficient, high tool temperature and high initial degree of cure of this realisation (Table 8-4).

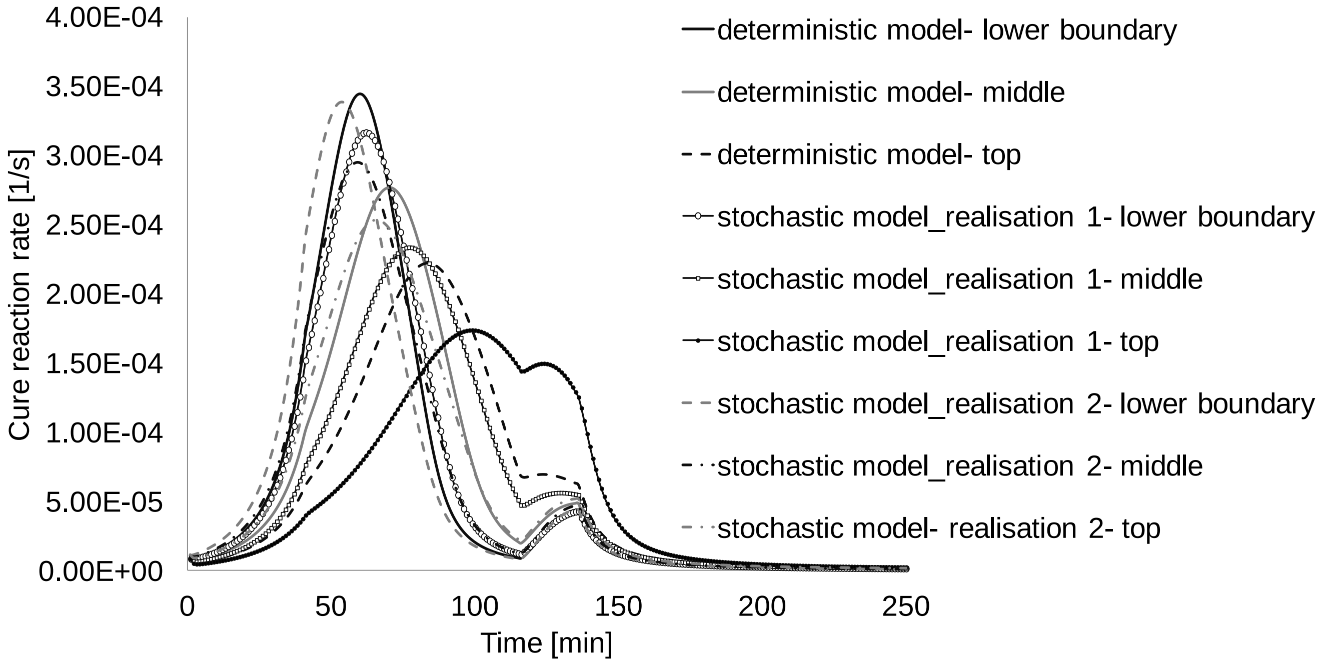

8-19 Evolution of cure reaction rate as a function of time through the thickness of the laminate.

Table 8-4 Values of stochastic parameters for two realisations of stochastic model.

Values	Realisation 1	Realisation 2
a_o	0.025	0.039
E_2 [J/mol]	58045	58589
m	1.2	1.16
h [W/m^2/^{o}C]	18.6	8.75
T_A [^{o}C]	24.1	25.1
T_1 [^{o}C]	159.9	163.4
T_2 [^{o}C]	177.2	183.2

Surface heat transfer coefficient and tool temperature uncertainty dominate cure time variability explaining more than 90% of the overall variability. Therefore, for carbon/epoxy composites stochastic simulation can be limited to these two factors, when efficiency is important, e.g. in iterative use. In addition, utilisation of a surrogate model based on PCM can reduce execution times further. This scenario is tested here, with the simulation of surface heat transfer and tool temperature variability propagation using both MC and PCM. In the implementation of the collocation method in this study a third order response surface was constructed to represent cure time as a function of the stochastic parameters. The number of the unknown coefficients for a three dimensional third order polynomial is 20 [9] and 39 collocation points were used to improve accuracy. Therefore, the final Monte Carlo simulation using the surrogate model based on the PCM representation required only 39 evaluations of the cure model. The third order response surface expressing the cure time as a function of three standard normal variables ξ_1, ξ_2 and ξ_3 which represent the three stochastic parameters (h, T_1, T_2) is reported in Table 8-5.

Table 8-5 Third order response surface of cure time.

Polynomial coefficients	Uncertain parameters
13168	-
2241.7	ξ_1
-64.9	ξ_2
-1665.2	ξ_3
457.9	$\xi_1^2 - 1$
-10.4	$\xi_1\xi_2$
-659	$\xi_1\xi_3$
3.4	$\xi_2^2 - 1$
5.9	$\xi_2\xi_3$
292.9	$\xi_3^2 - 1$
64.4	$\xi_1^3 - 3\xi_1$
1.7	$\xi_1^2\xi_2 - \xi_2$
-181.8	$\xi_1^2\xi_3 - \xi_3$
-3.9	$\xi_2^2\xi_1 - \xi_1$
4.4	$\xi_1\xi_2\xi_3$
114.4	$\xi_3^2\xi_1 - \xi_1$
-0.4	$\xi_2^3 - 3\xi_2$
-3.4	$\xi_2^2\xi_3 - \xi_3$
0.65	$\xi_3^2\xi_2 - \xi_2$
-34.5	$\xi_3^3 - 3\xi_3$

The stochastic simulation results are reported in Table 8-3. Figure 8-20 illustrates the probability distribution of cure time and Figures 8-21 and 8-22 present the convergence of the mean and standard deviation of cure time for the two stochastic simulation schemes. Satisfactory convergence is obtained for the first and second statistical moments of cure time after 1000 Monte Carlo iterations for both stochastic simulation schemes. A very good agreement is achieved between Monte Carlo and the collocation method for the first two statistical moments of cure time. Both stochastic simulation schemes are able to capture the combined effect of surface heat transfer coefficient and tool temperature variability on cure time accurately. The Monte Carlo is a computationally expensive and rich solution, whereas the PCM offers an efficient approximation with significant benefits in terms of computational cost (for the given case, the computational cost of the PCM is 3.9 % of that of the MC), and comparable results.

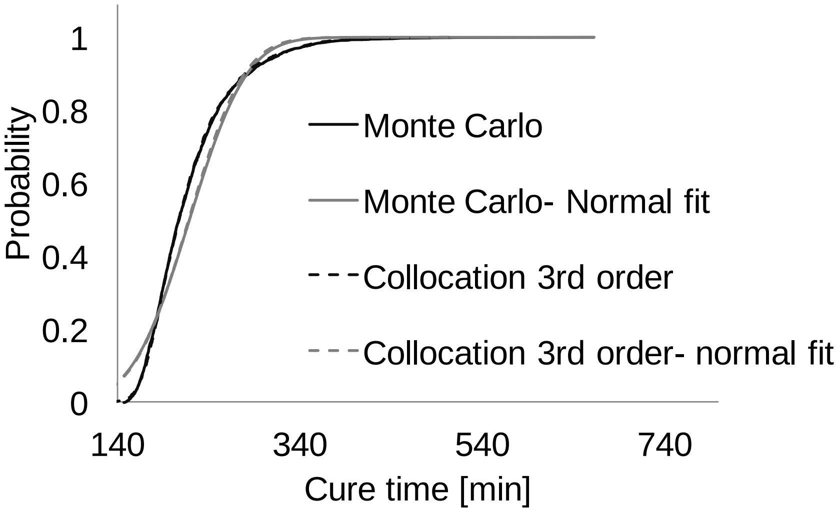

Fig. 8-20 Probability distribution for cure time; surface heat transfer coefficient and tool temperature uncertainty.

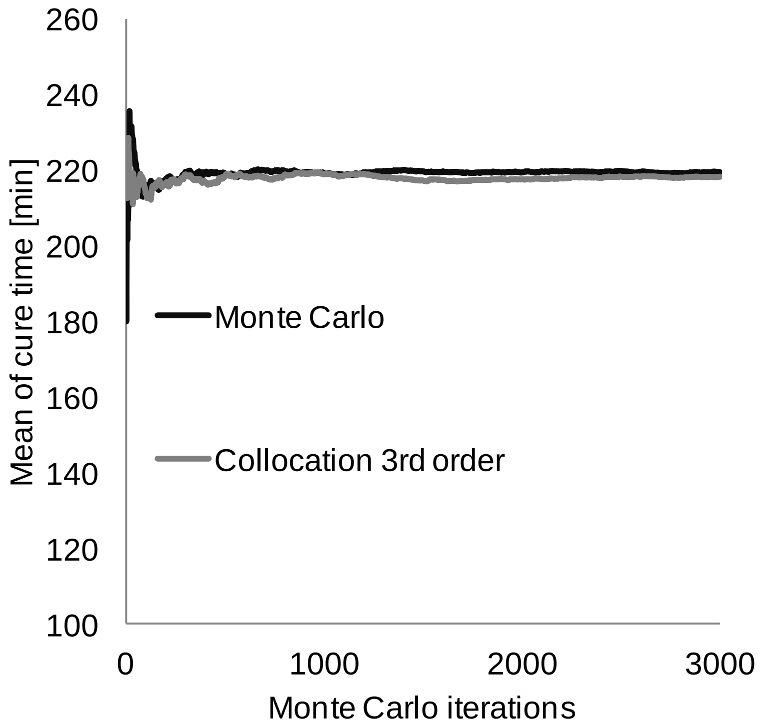

Fig. 8-21 Convergence of mean of cure time; surface heat transfer coefficient and tool temperature uncertainty.

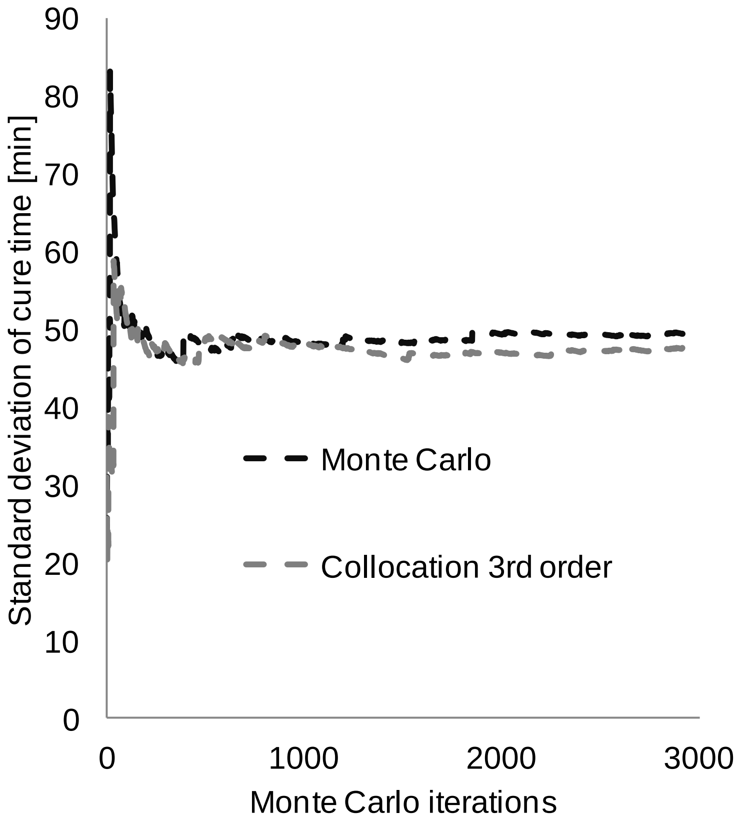

Fig. 8-22 Convergence of standard deviation of cure time; surface heat transfer coefficient and tool temperature uncertainty.

8.5 Overview

The methodologies developed in this chapter allow the quantification of the influence of boundary conditions variability, cure kinetics uncertainty and their combined effect on the cure process outcome. The experimental results showed that boundary conditions have considerable variability, which in turn can introduce significant variation to the process outcome. It was found that the main source of uncertainty in boundary conditions is the variation in level across different runs. The stochastic cure simulation results taking into account level variability suggest that surface heat transfer coefficient and tool temperature dominate cure time variability, introducing a coefficient of variation of about 22%, with considerable implications in cost associated with process duration and part quality. Cure kinetics and ambient temperature variations introduce negligible variability in cure time in the case of thin epoxy carbon fibre composites. Variations over time introduce negligible variability in cure time in this type of application; however, the effect of variability over time could be significant in cases which variations in surface heat transfer coefficient and tool temperature are more pronounced (e.g. wind turbine blade manufacturing). These uncertainty effects can be more pronounced in industrial practice where boundary conditions can show significant variability. Overall, the modelling approaches demonstrated in this study can be implemented to characterise and model boundary conditions uncertainty as well as cure kinetics variability in industrial scale applications and to investigate its influence on heat transfer effects and residual stress formation during the cure process.

9. Overall discussion

This investigation concerned the development and implementation of a stochastic simulation methodology to study the effect of material properties and process parameters variability on the cure process. Up to now stochastic simulation studies in the context of composites manufacturing have predominantly focused on the filling stage of the process investigating the effect of fibre geometrical heterogeneity on permeability variations. The present study constitutes the first comprehensive investigation on variability in the cure stage of advanced composites manufacturing and is focused on the quantification of cure kinetics uncertainty, fibre misalignment and boundary conditions variability related to tool temperature, ambient temperature and surface heat transfer coefficient, and their propagation through the process of cure. So far studies of the influence of cure kinetics uncertainty and boundary conditions variability on the process outcome were based on hypothetical values of variability rather than experimental data. The methodologies presented here move towards the direction of eliminating the gap between real phenomena and process simulation.

A methodology was developed and implemented to characterise cure kinetics uncertainty due to variable resin handling/storage conditions based on dynamic DSC tests. The experimental data were fitted with a cure kinetics model and the variability between the different experimental runs was attributed to certain parameters of cure kinetics. An infusion set-up was used to quantify boundary conditions uncertainty using thermocouples (tool/ambient temperature) and heat flux sensors (heat transfer coefficient). This uncertainty was modelled considering variation in time using a one-dimensional stochastic process as well as variability across different experimental runs. Although fibre misalignment has been investigated in detail in several studies, its influence on the outcome of the curing process has not been investigated so far. In this study, image analysis was used to quantify fibre misalignment and the spatial dependence of variability was modelled using a two-dimensional stochastic field. It was indicated that high specification thermosets and reinforcements can show significant variability in cure kinetics and local tow orientation, respectively. In addition, boundary conditions can show considerable variations related to short term and long term variability.

A finite element based cure simulation model was implemented comprising material sub-models of cure kinetics, specific heat capacity, thermal conductivity, moduli, thermal expansion and cure shrinkage. The material sub-models used in this work can serve as sub-models of a cure simulation in any commercial simulation tool, where they can be implemented directly as user subroutines. Two stochastic simulation approaches were developed based on conventional Monte Carlo (MC) and the Probabilistic Collocation Method (PCM), respectively. The two stochastic simulation models were coupled with the finite element based cure simulation model. In terms of development, MC is considerably simpler than PCM; however, PCM has the potential to decrease the computational cost significantly. Flexibility of the corresponding interfaces allows integration of the two stochastic simulation approaches with different FEA solvers as well as implementation of stochastic simulation in different applications in the context of composites manufacturing.

The Monte Carlo scheme was implemented in all cases presenting a robust but computationally expensive solution, whilst the collocation method was used only in the case of cure kinetics uncertainty, as well as in the case of surface heat transfer coefficient and tool temperature uncertainty showing tremendous benefits in terms of computational cost with quite good accuracy. The Monte Carlo scheme is not limited by the dimensionality of the stochastic problem and therefore is capable to address every stochastic problem in the context of composites manufacturing. On the contrary, the collocation method can offer an efficient alternative to Monte Carlo for a small number of Gaussian stochastic variables, implying that it is limited to addressing specific sub-problems of the manufacturing process (for example cure kinetics uncertainty) and not the full stochastic problem, where several sources of variability are in action. Therefore, the collocation method is not indicated to address stochastic problems involving stochastic fields such as fibre misalignment, due to the fact that in most cases a large number of stochastic variables is required to represent a stochastic field accurately. However, the collocation method has the potential to provide an efficient and accurate solution in the case highly correlated stochastic fields which can be represented with a small number of stochastic variables using the Karhunen–Loève expansion [11].

The implementation of the stochastic simulation approaches allowed quantification of the influence of input parameters variability on the process outcome. It was shown that variability in cure kinetics can introduce significant scatter in temperature overshoot with considerable cost implications related to the amount of scrap. Considering a process tolerance of 30 °C the probability of severe temperature overshoots in the case of a thick carbon fibre epoxy laminate is about 20%, implying that the manufacturing of thick laminates can involve a significant amount of scrap related to defects due to temperature overshoots. Local tow orientation variability can lead to significant variations in residual stress generation, which in the case of higher levels of variability phenomena such as matrix pre-cracking, may be initiated at a local level affecting part quality. Furthermore, fibre misalignment introduces considerable qualitative variations in shape distortion, altering the final shape of the formed part depending on the lay-up sequence. These findings are of crucial importance in the case of curved parts since shape variations can lead to considerable part quality and assembly issues, especially in the case of large components such as c-spars used in aerospace applications. In addition, the dependence of maximum residual stress and shape distortion on different levels of fibre misalignment and autocorrelation highlight the significance of fibre variability in the development of residual stress during the process and final distortion of the component. The potentially damaging maximum residual stress increases non-linearly in an unfavourable manner with increasing variability. Therefore the benefits of controlling closely tow orientation can be significant even in situations where the process involves low quality reinforcement. The influence of autocorrelation lengths on macroscopic distortion metrics is significant at lengths that are small compared to the size of the component, highlighting the importance of controlling the size of variability patches in high end applications. Variations over time in boundary conditions introduce negligible variability in cure time; however, the effect of variability over time can be significant in industrial scale applications in which tool temperature can show considerable variations over time related to the controller. The stochastic cure simulation results, taking into account level variability in boundary conditions, suggest that surface heat transfer coefficient and tool temperature dominates cure time variability introducing a coefficient of variation of about 22%. More specifically, the probability of under cure in the case of a thin laminate using the standard cure profile of RTM6 [101] is about 10% implying that conventional cure profiles should be modified to minimise defect generation due to variability.

These variability effects can be more severe in processes involving higher variability due to lower specification materials and/or higher levels of variability in boundary conditions. For instance, in the case of wind turbine applications [152-154], where lower specification resins and fabrics are used and boundary conditions are subject to limited control compared to the aerospace industry, uncertainty can be considerably more pronounced introducing higher levels of variability on the heat transfer effects and residual stresses/ shape distortion, respectively. In addition, variations in surface heat transfer coefficient can be more pronounced presenting spatial dependence in the case of large components of complex geometries due to formation of wrinkles in the vacuum bags.

The findings presented here brought light to the qualitative and quantitative characteristics of material properties and process parameters variability and uncovered the relationship between this variability and the curing process outcome. This enhances the knowledge of the curing process and brings new awareness in terms of decision making. In addition, this work provided greater insight regarding the sources of variability in composites cure, which in turn can be used in order to eliminate this variability. The methodologies developed in this study can serve as a starting point for incorporation of variability in process design/optimisation to minimise the probability of process induced defects such as resin degradation due to temperature overshoot variations, undercure, matrix cracks due to variations in residual stresses generation and shape distortion while using a process design as efficient as possible in terms of duration and energy consumption. This requires integration of the stochastic simulation schemes presented here with multi-objective optimisation tools [155,156] to address performance robustness trade-offs of the manufacturing process.

The cost of the manufacturing process and the quality of the final part are of crucial importance and are dictated by material properties and process design. A process design procedure that does not take into account variability is not capable of predicting the amount of scrap accurately leading to underestimation of the manufacturing costs. Understanding and quantifying the relationship between process parameters and material properties will allow identification and evaluation of trade-offs between process robustness, part quality and manufacturing costs. The outcome of this work constitutes a powerful tool for designers, which is capable to characterise uncertainty in composites manufacturing and investigate how this variability can affect the manufacturing process. The methodologies presented here can contribute towards the development of a standard procedure for characterisation and quantification of input parameters uncertainty. Implementation of stochastic simulation will provide the designer with important information for evaluation of whether eliminating variability is beneficial in terms of part quality and cost or not. Incorporation of stochastic simulation in industrial practice can result in significant benefits in several aspects. The amount of scrap can be reduced considerably and delivery delays can be minimised. The duration of process cycles can be optimised and the use of extended and conservative cycles can be eliminated. Consequently, manufacturing costs can be reduced significantly. The manufacturing process of composite materials can become a more sustainable and environmentally friendly procedure consuming less energy while minimising the emission of pollutants and the amount of scrap. Overall, incorporation of stochastic simulation in composites manufacturing can contribute towards the optimisation of the process in terms of part quality, time and cost as well as minimise its environmental footprint.

10. Conclusions

The main outcomes of this study can be summarised as follows:

Stochastic simulation

- A stochastic cure simulation methodology based on the conventional Monte Carlo scheme and on the Probabilistic Collocation Method has been developed and implemented.
- The Monte Carlo scheme is capable of predicting uncertainty propagation with high accuracy and it is not limited by the dimension of the stochastic problem; however it is computationally expensive.
- The Probabilistic Collocation Method can offer a considerable reduction in computational costs compared to Monte Carlo, with quite good accuracy; however, this method can produce good quality results only if the dimension of the problem is small i.e. up to four stochastic variables, otherwise it becomes unstable producing poor quality results.
- Both stochastic simulation schemes are able to predict the influence of cure kinetics uncertainty on the heat transfer effects of the cure of a thick carbon fibre epoxy panel, with the computational cost of the collocation method being less than 3 % of that of the Monte Carlo.
- The Probabilistic Collocation Method can also be used to study the effect of surface heat transfer coefficient and tool temperature variability on cure time predicting uncertainty propagation with quite good accuracy, while offering tremendous benefits in terms of computational cost (the computational cost of the collocation method was less than 4 % than that of the Monte Carlo).

Cure kinetics uncertainty

- Cure kinetics uncertainty of a commercial epoxy resin used in aerospace applications was characterised using Differential Scanning Calorimetry and it was shown that high specification thermosets can involve considerable variability in cure behavior.

- Variability in resin kinetics can be attributed to initial degree of cure, activation energy and reaction order uncertainty, showing a coefficient of variation of 19%, 1% and 7%, respectively for the resin system of this study.
- Cure simulation of heat transfer effects of a thick carbon fibre epoxy panel indicated that cure kinetics uncertainty can introduce a significant scatter in the process outcome with a coefficient of variation of about 30% and 1.7% in temperature overshoot and time of temperature overshoot, respectively.
- Stochastic simulation of the cure of a carbon fibre epoxy flat panel within the Monte Carlo scheme showed that cure kinetics uncertainty introduced relatively low variability in cure time showing a coefficient of variation in cure time of about 1%.

Fibre misalignment

- Image analysis was used to characterise tow orientation variability of a ±45º non- crimp fabric and the experimental results showed that tow orientation of high specification carbon NCFs can vary with a standard deviation of 1.2º with strong anisotropic spatial autocorrelation and the major direction of autocorrelation coinciding with the direction of the non-structural stich.
- Cure simulation of an angle shape carbon fibre epoxy panel using the Monte Carlo scheme showed that fibre misalignment can introduce considerable variability in process outcome, presenting a coefficient of variation of up to 2% (1MPa standard deviation) in maximum longitudinal residual stresses.
- Local tow orientation variability can introduce qualitative and quantitative scatter in shape distortion with the standard deviation in twist and corner angle reaching values of 0.4º and 0.05º respectively.
- Increasing the standard deviation of fibre misalignment induces an increase of standard deviation in maximum residual stress in a linear fashion, whilst the standard deviation of both corner and twist angle increases following a concave dependence.
- Increasing the correlation lengths induces a slight increase to the standard deviation of maximum residual at low values of correlation lengths with a plateau occurring at higher values of correlation lengths, whilst the standard

deviation of both corner and twist angle increases presenting a convex dependence.

Boundary conditions uncertainty

- An infusion set-up was used to characterise tool temperature, ambient temperature and surface heat transfer coefficient variability, and it was shown that boundary conditions can involve considerable uncertainty presenting variation over time as well as variability across different experimental runs.
- Tool temperature showed a periodic trend and short term variability over time and was modelled using a cosinusoidal trend and a second order stationary stochastic process, the Ornstein-Uhlenbeck process.
- Ambient temperature presented long term trend and short term variability over time and was modelled using a linear trend and the Ornstein-Uhlenbeck process.
- Surface heat transfer coefficient presented no serial correlation over time and was modelled as a random series of observations.
- Stochastic cure simulation of a thin carbon fibre epoxy flat panel using the Monte Carlo scheme showed that variability over time introduces negligible variability in cure time.
- Investigation of the effect of level variability across different runs showed that surface heat transfer coefficient and tool temperature uncertainty dominates cure time variability, introducing a coefficient of variation of about 22% in cure time, whilst ambient temperature introduced variability in the order of 0.5%.

11. Suggestions for further investigations

The stochastic simulation methodology developed here can be coupled with optimisation tools, such as Genetic Algorithms to enhance optimisation stability and address the process performance-robustness trade-off. This would require the development of an interface between the stochastic simulation model and an optimisation tool. Optimisation can result in unstable solutions, implying that small variations in the input parameters can introduce considerable changes in the objective solution. Solutions of this type can be theoretically acceptable but not appropriate in real world applications. Process robustness in terms of minimum output variations, process performance in terms of time, and part quality expressed as minimum shape distortion and even temperature distribution are the primary objectives in every cure process. Consequently, integration of the stochastic simulation methodology presented here with optimisation tools will contribute towards the creation of a trade-off map quantifying the relationship between these competing parameters. This will add important information on process design and decision making in composite manufacturing.

The modelling approaches demonstrated in this study can be extended to characterise and model out of plane fibre misalignment and investigate its influence on heat transfer effects and residual stress formation during the cure process. This could be achieved using X-ray micro- tomography (X-ray micro CT). In addition, the effect of in plane and out of plane fibre misalignment on the structural behavior of composites can be investigated. Tool temperature variations can be further investigated using industrial scale equipment, where tool temperature can show considerable variability. In addition, the spatial dependence of surface heat transfer coefficient requires further investigation, as wrinkles in vacuum bags and nesting between flexible layers of ancillary materials and reinforcement may affect the heat transfer mechanisms, especially in the case of complex geometries, introducing considerable variations in surface heat transfer coefficient. The combined effect of fibre misalignment, cure kinetics uncertainty and boundary conditions uncertainty, as well as their relative importance on the heat transfer and process stress effects can be investigated within an integrated framework.

A defect map can be generated providing information regarding the importance and the type of defects that can arise from variability. Defects can be categorised depending on the source of variability and the type of components that are more likely occur in. This can provide guidelines for decision making towards potential routes of the manufacturing process that eliminate variability and consequently the defects that are associated to this variability.

The methodologies presented here can be used to investigate the effect of variability in other manufacturing steps such as forming and impregnation. This would require the integration of constitutive material models related to forming and impregnation as well as the development of an interface between the stochastic simulation model and the corresponding constitutive models. In addition, an integrated framework can be developed and implemented to investigate variability propagation through all the manufacturing steps. This will provide qualitative and quantitative information regarding the interdependencies between the different manufacturing steps and provide a greater insight into the manufacturing process of composites.

Real time monitoring can be integrated with the methodologies developed in this study to improve both robustness and quality of the manufacturing process. Variability related to material properties and process parameters uncertainty can be reduced in every step of the manufacturing process using on line monitoring.. A stochastic simulation scheme can be used to model this variability in real time in order to adapt the process parameters based on the data obtained gradually during the manufacturing process.

Overall, stochastic simulation can be incorporated into existing commercial simulation tools to address variability in composites manufacturing. This would require a user friendly interface where the user could choose a stochastic simulation method, the stochastic variables and the output parameters. This would have considerable benefits as stochastic simulation would become accessible to process engineers and incorporation of variability in industrial practice would be easier.

References

[1] Mouritz A. (2012), Introduction to aerospace materials, Elsevier Pubns.

[2] Deo R. B., Starnes J. H. and Holzwarth R. C. (2001), Low-cost composite materials and structures for aircraft applications, NATO RTO AVT Panel spring symposium and specialists' meeting Loen, Norway.

[3] Marsh G. (2010), Airbus A350 XWB update, Reinforced Plastics, vol. 54, no. 6, pp. 20-24.

[4] Endruweit A. and Long A. C. (2006), Influence of stochastic variations in the fibre spacing on the permeability of bi-directional textile fabrics, Composites Part A: Applied Science and Manufacturing, vol. 37, no. 5, pp. 679-694.

[5] Endruweit A. Long, A. C., Robitaille F. and Rudd, C. D. (2006), Influence of stochastic fibre angle variations on the permeability of bi-directional textile fabrics, Composites Part A: Applied Science and Manufacturing, vol. 37, no. 1, pp. 122-132.

[6] Long A., Wiggers J. and Harrison P. (2004), Modelling the Effects of Blank-Holder Pressure and Material Variability on Forming of Textile Preforms, In: Proceedings of the 8th international ESAFORM conference on materials forming, Cluj-Napoca, Romania.

[7] Padmanabhan S. K. and Pitchumani R. (1999), Stochastic analysis of isothermal cure of resin systems, Polymer Composites, vol. 20, no. 1, pp. 72-85.

[8] Padmanabhan S. K. and Pitchumani R. (1999), Stochastic modeling of nonisothermal flow during resin transfer molding, International Journal of Heat and Mass Transfer, vol. 42, no. 16, pp. 3057-3070.

[9] Huang S., Mahadevan S. and Rebba R. (2007), Collocation-based stochastic finite element analysis for random field problems, Probabilistic Engineering Mechanics, vol. 22, no. 2, pp. 194-205.

[10] Ghanem R. G. and Spanos P. D. (2003), Stochastic finite elements: a spectral approach, Dover Pubns.

[11] Zhang F., Cosson B., Comas-Cardona S. and Binetruy C. (2011), Efficient stochastic simulation approach for RTM process with random fibrous permeability, Composites Science and Technology, vol. 71, no. 12, pp. 1478-1485.

[12] Potter K. (2009), Understanding the origin of defects and variability in composites manufacture. In: Proceedings of the 17th international conference on composite materials, Edinburgh, UK.

[13] Skordos A. A. and Sutcliffe M. P. F. (2008), Stochastic simulation of woven composites forming, Composites Science and Technology, vol. 68, no. 1, pp. 283-296.

[14] Verleye B., Lomov S. V., Long A., Verpoest I. and Roose D. (2010), Permeability prediction for the meso–macro coupling in the simulation of the impregnation stage of Resin Transfer Moulding, Composites Part A: Applied Science and Manufacturing, vol. 41, no. 1, pp. 29-35.

[15] Potter K., Khan B., Wisnom M., Bell T. and Stevens J. (2008), Variability, fibre waviness and misalignment in the determination of the properties of composite materials and structures, Composites Part A: Applied Science and Manufacturing, vol. 39, no. 9, pp. 1343-1354.

[16] Abdiwi F., Harrison P., Koyama I., Yu W., Long A., Corriea N. and Guo Z. (2012), Characterising and modelling variability of tow orientation in engineering fabrics and textile composites, Composites Science and Technology, vol. 72, no. 9, pp. 1034-1041.

[17] Endruweit A., McGregor P. Long A. C. and Johnson M. S. (2006), Influence of the fabric architecture on the variations in experimentally determined in-plane permeability values, Composites Science and Technology, vol. 66, no. 11–12, pp. 1778-1792.

[18] Pan R., Liang Z., Zhang C. and Wang B. (2000), Statistical characterization of fiber permeability for composite manufacturing, Polymer composites, vol. 21, no. 6, pp. 996-1006.

[19] Hoes K., Dinesku D., Vanhuele M., Sol H., Parnas R., Belov E. and Lomov S. V. (2002), Statistical distribution of permeability values of different porous materials,

Statistical distribution of permeability values of different porous materials, In: Proceedings of the 10th European conference on composite materials, Brugge.

[20] Endruweit A., Long, A., Robitaille F. and Rudd, C. (2004), Dependence of permeability variations on the textile structure, Proceedings of ECCM, Vol. 11.

[21] Vanaerschot A., Cox, B. N., Lomov S. V. and Vandepitte D. (2013), Stochastic framework for quantifying the geometrical variability of laminated textile composites using micro-computed tomography, Composites Part A: Applied Science and Manufacturing, vol. 44, pp. 122-131.

[22] Vanaerschot A., Cox B. N., Lomov S. V. and Vandepitte D. (2013), Stochastic multi-scale modelling of textile composites based on internal geometry variability, Computers & Structures, vol. 122, pp. 55-64.

[23] Desplentere F., Lomov S. V., Woerdeman D. L., Verpoest I., Wevers M. and Bogdanovich, A. (2005), Micro-CT characterization of variability in 3D textile architecture, Composites Science and Technology, vol. 65, no. 13, pp. 1920-1930.

[24] Karahan M., Lomov S. V., Bogdanovich A. E., Mungalov D. and Verpoest I. (2010), Internal geometry evaluation of non-crimp 3D orthogonal woven carbon fabric composite, Composites Part A: Applied Science and Manufacturing, vol. 41, no. 9, pp. 1301-1311.

[25] Cao J., Akkerman R., Boisse P., Chen, J., Cheng H., De Graaf E., Gorczyca J., Harrison P., Hivet G. and Launay J. (2008), Characterization of mechanical behavior of woven fabrics: experimental methods and benchmark results, Composites Part A: Applied Science and Manufacturing, vol. 39, no. 6, pp. 1037-1053.

[26] Sidhu R. M. J. S., Averill R. C., Riaz M. and Pourboghrat F. (2001), Finite element analysis of textile composite preform stamping, Composite Structures, vol. 52, no. 3–4, pp. 483-497.

[27] Bickerton S., Šimáček P., Guglielmi S. E. and Advani S. G. (1997), Investigation of draping and its effects on the mold filling process during manufacturing of a compound curved composite part, Composites Part A: Applied Science and Manufacturing, vol. 28, no. 9–10, pp. 801-816.

[28] Duhovic M., Mitschang P. and Bhattacharyya D. (2011), Modelling approach for the prediction of stitch influence during woven fabric draping, Composites Part A: Applied Science and Manufacturing, vol. 42, no. 8, pp. 968-978.

[29] Yu W., Harrison P. and Long A. Finite Element Forming Simulation of NCF Considering Natural Variability of Fiber Direction, In: Proceedings of the 8th international ESAFORM conference on materials forming, Cluj-Napoca, Romania .

[30] Skordos A. A., Monroy Aceves C. and Sutcliffe M. P. F. (2007), A simplified rate dependent model of forming and wrinkling of pre-impregnated woven composites, Composites Part A: Applied Science and Manufacturing, vol. 38, no. 5, pp. 1318-1330.

[31] Belov E. B., Lomov S. V., Verpoest I., Peters T., Roose D., Parnas R. S., Hoes, K. and Sol, H. (2004), Modelling of permeability of textile reinforcements: lattice Boltzmann method, Composites Science and Technology, vol. 64, no. 7–8, pp. 1069-1080.

[32] Hoes K., Dinescu D., Sol H., Vanheule M., Parnas R. S., Luo Y. and Verpoest I. (2002), New set-up for measurement of permeability properties of fibrous reinforcements for RTM, Composites Part A: Applied Science and Manufacturing, vol. 33, no. 7, pp. 959-969.

[33] Hoes K., Dinescu D., Sol H., Parnas R. S. and Lomov S. (2004), Study of nesting induced scatter of permeability values in layered reinforcement fabrics, Composites Part A: Applied Science and Manufacturing, vol. 35, no. 12, pp. 1407-1418.

[34] Ding L., Shih C., Liang Z., Zhang C. and Wang B. (2003), In situ measurement and monitoring of whole-field permeability profile of fiber preform for liquid composite molding processes, Composites Part A: Applied Science and Manufacturing, vol. 34, no. 8, pp. 779-789.

[35] Opperer J. G., Kim S. K. and Daniel I. M. (2004), Characterization of local preform defects in resin transfer molding by the gas flow method and statistical analysis, Composites Science and Technology, vol. 64, no. 13–14, pp. 1921-1935.

[36] Wong C. and Long A. (2006), Modelling variation of textile fabric permeability at mesoscopic scale, Plastics, rubber and composites, vol. 35, no. 3, pp. 101-111.

[37] Lundström T. S., Stenberg R., Bergström R., Partanen H. and Birkeland P. A. (2000), In-plane permeability measurements: a nordic round-robin study, Composites Part A: Applied Science and Manufacturing, vol. 31, no. 1, pp. 29-43.

[38] Luthy T., Hintermann M., Mosler H., Ziegmann G. and Ermanni P. (1998), Dependence of the 1-D permeability of fibrous media on the fiber volume content: comparison between measurement and simulation, Structures and Materials, vol. 3, pp. 433-442.

[39] Steenkamer D. A., McKnight S., Wilkins D. and Karbhari V. (1995), Experimental characterization of permeability and fibre wetting for liquid moulding, Journal of Materials Science, vol. 30, no. 12, pp. 3207-3215.

[40] Chick J. P., Rudd, C., Van Leeuwen P. and Frenay T. (1996), Material characterization for flow modeling in structural reaction injection molding, Polymer composites, vol. 17, no. 1, pp. 124-135.

[41] Hammond V. and Loos A. (1997), The effects of fluid type and viscosity on the steady-state and advancing front permeability behavior of textile preforms, Journal of Reinforced Plastics and Composites, vol. 16, no. 1, pp. 50-72.

[42] Dunkers J. P., Phelan F. R., Zimba C. G., Flynn K. M., Sanders D. P., Peterson R. C., Parnas R. S., Li X. and Fujimoto J. G. (2001), The prediction of permeability for an epoxy/E-glass composite using optical coherence tomographic images, Polymer composites, vol. 22, no. 6, pp. 803-814.

[43] Liu Q., Parnas R. S. and Giffard H. S. (2007), New set-up for in-plane permeability measurement, Composites Part A: Applied Science and Manufacturing, vol. 38, no. 3, pp. 954-962.

[44] Chen X. and Papathanasiou T. D. (2008), The transverse permeability of disordered fiber arrays: a statistical correlation in terms of the mean nearest interfiber spacing, Transport in Porous Media, vol. 71, no. 2, pp. 233-251.

[45] Bechtold G. and Ye L. (2003), Influence of fibre distribution on the transverse flow permeability in fibre bundles, Composites Science and Technology, vol. 63, no. 14, pp. 2069-2079.

[46] Endruweit A., Gommer F. and Long, A. (2013), Stochastic analysis of fibre volume fraction and permeability in fibre bundles with random filament arrangement, Composites Part A: Applied Science and Manufacturing, vol. 49, pp. 109-118.

[47] Zhang F., Comas-Cardona S. and Binetruy C. (2012), Statistical modeling of in-plane permeability of non-woven random fibrous reinforcement, Composites Science and Technology, vol. 72, no. 12, pp. 1368-1379.

[48] Endruweit A. and Ermanni P. (2004),The in-plane permeability of sheared textiles. Experimental observations and a predictive conversion model, Composites Part A: Applied Science and Manufacturing, vol. 35, no. 4, pp. 439-451.

[49] Loix F., Badel P., Orgéas L., Geindreau C. and Boisse P. (2008), Woven fabric permeability: From textile deformation to fluid flow mesoscale simulations, Composites Science and Technology, vol. 68, no. 7–8, pp. 1624-1630.

[50] De Parseval Y., Roy R. V. and Advani S. (1995), Effect of local variations of preform permeability on the average permeability during resin transfer molding of composites, ANTEC'95., vol. 2, pp. 3040-3044.

[51] Chen B., Lang E. J. and Chou T. (2001), Experimental and theoretical studies of fabric compaction behavior in resin transfer molding, Materials Science and Engineering: A, vol. 317, no. 1–2, pp. 188-196.

[52] Chen B. and Chou T. (2000), Compaction of woven-fabric preforms: nesting and multi-layer deformation, Composites Science and Technology, vol. 60, no. 12, pp. 2223-2231.

[53] Saunders R., Lekakou C. and Bader M. (1998), Compression and microstructure of fibre plain woven cloths in the processing of polymer composites, Composites Part A: Applied Science and Manufacturing, vol. 29, no. 4, pp. 443-454.

[54] Saunders R. A., Lekakou C. and Bader M. G. (1999), Compression in the processing of polymer composites 1. A mechanical and microstructural study for

different glass fabrics and resins, Composites Science and Technology, vol. 59, no. 7, pp. 983-993.

[55] Lomov S. V. and Verpoest I. (2000), Compression of woven reinforcements: a mathematical model, Journal of Reinforced Plastics and Composites, vol. 19, no. 16, pp. 1329-1350.

[56] Luo Y. and Verpoest I. (1999), Compressibility and relaxation of a new sandwich textile preform for liquid composite molding, Polymer composites, vol. 20, no. 2, pp. 179-191.

[57] Pearce N. and Summerscales J. (1995), The compressibility of a reinforcement fabric, Composites Manufacturing, vol. 6, no. 1, pp. 15-21.

[58] Dungan F., Senoguz M., Sastry A. and Faillaci D. (2001), Simulations and Experiments on Low-Pressure Permeation of Fabrics: Part I—3D Modeling of Unbalanced Fabric, Journal of Composite Materials, vol. 35, no. 14, pp. 1250-1284.

[59] Senoguz M., Dungan F., Sastry A. and Klamo J. (2001), Simulations and Experiments on Low-Pressure Permeation of Fabrics: Part II—The Variable Gap Model and Prediction of Permeability, Journal of Composite Materials, vol. 35, no. 14, pp. 1285-1322.

[60] Delerue J. F., Lomov S. V., Parnas R., Verpoest I. and Wevers M. (2003), Pore network modeling of permeability for textile reinforcements, Polymer composites, vol. 24, no. 3, pp. 344-357.

[61] Lomov S. V., Verpoest I., Peeters T., Roose D. and Zako M. (2003), Nesting in textile laminates: geometrical modelling of the laminate, Composites Science and Technology, vol. 63, no. 7, pp. 993-1007.

[62] Dong C. (2011), Model development for the formation of resin-rich zones in composites processing, Composites Part A: Applied Science and Manufacturing, vol. 42, no. 4, pp. 419-424.

[63] Parnas R. S., Flynn K. M. and Dal-Favero M. E. (1997), A permeability database for composites manufacturing, Polymer Composites, vol. 18, no. 5, pp. 623-633.

[64] Li J., Zhang C., Liang R. and Wang B. (2005), Statistical characterization and robust design of RTM processes, Composites Part A: Applied Science and Manufacturing, vol. 36, no. 5, pp. 564-580.

[65] Lawrence J. M., Fried P. and Advani S. G. (2005), Automated manufacturing environment to address bulk permeability variations and race tracking in resin transfer molding by redirecting flow with auxiliary gates, Composites Part A: Applied Science and Manufacturing, vol. 36, no. 8, pp. 1128-1141.

[66] Lawrence J. M., Barr J., Karmakar R. and Advani S. G. (2004), Characterization of preform permeability in the presence of race tracking, Composites Part A: Applied Science and Manufacturing, vol. 35, no. 12, pp. 1393-1405.

[67] Li J., Zhang, C., Liang Z. and Wang B. (2006), Stochastic simulation based approach for statistical analysis and characterization of composites manufacturing processes, Journal of Manufacturing Systems, vol. 25, no. 2, pp. 108-121.

[68] Judd N. C. W. and Wright W. (1978), Voids and their effects on the mechanical properties of composites- an appraisal, SAMPE Journal, vol. 14, pp. 10-14.

[69] Ghiorse S. (1993), Effect of void content on the mechanical properties of carbon/epoxy laminates, SAMPE quarterly, vol. 24, no. 2, pp. 54-59.

[70] Bowles K. J. and Frimpong S. (1992), Void effects on the interlaminar shear strength of unidirectional graphite-fiber-reinforced composites, Journal of Composite Materials, vol. 26, no. 10, pp. 1487-1509.

[71] Hamidi Y. K., Aktas L. and Altan M. C. (2004), Formation of microscopic voids in resin transfer molded composites, Journal of engineering materials and technology, vol. 126, pp. 420.

[72] Avila A. F. and Morais D. T. S. (2005), A multiscale investigation based on variance analysis for hand lay-up composite manufacturing, Composites Science and Technology, vol. 65, no. 6, pp. 827-838.

[73] Park C. H., Lebel A., Saouab A., Bréard J. and Lee W. I. (2011), Modeling and simulation of voids and saturation in liquid composite molding processes, Composites Part A: Applied Science and Manufacturing, vol. 42, no. 6, pp. 658-668.

[74] Hamidi Y. K., Dharmavaram S., Aktas L. and Altan M. C. (2009), Effect of Fiber Content on Void Morphology in Resin Transfer Molded E-Glass/Epoxy Composites, Journal of Engineering Materials and Technology, vol. 131, pp. 021014.

[75] Markicevic B., Heider D., Advani S. G. and Walsh S. (2005), Stochastic modeling of preform heterogeneity to address dry spots formation in the VARTM Process, Composites Part A: Applied Science and Manufacturing, vol. 36, no. 6, pp. 851-858.

[76] Guo Z., Du S. and Zhang B. (2005), Temperature field of thick thermoset composite laminates during cure process, Composites Science and Technology, vol. 65, no. 3–4, pp. 517-523.

[77] Hsiao K., Little R., Restrepo O. and Minaie B. (2006), A study of direct cure kinetics characterization during liquid composite molding, Composites Part A: Applied Science and Manufacturing, vol. 37, no. 6, pp. 925-933.

[78] Kessler M. R. and White S. R. (2002), Cure kinetics of the ring-opening metathesis polymerization of dicyclopentadiene, Journal of Polymer Science Part A: Polymer Chemistry, vol. 40, no. 14, pp. 2373-2383.

[79] Liaw D., Singhal S., Murthy P. and Chamis C. C. (1993), Quantification of uncertainties in composites, 34th AIAA/ASME/ASCE/AHS/ASC Structures, Structural Dynamics, and Materials Conference, pp. 1163.

[80] Chamis C. C. (1998), Probabilistic composite mechanics assurance for better-cheaper-faster products, AIAA/ASME/ASCE/AHS/ASC Structures, Structural Dynamics, and Materials Conference and Exhibit, 39 th, and AIAA/ASME/AHS Adaptive Structures Forum, Long Beach, CA, pp. 1940.

[81] Elseifi, M. (2001), Probabilistic analysis of thick composite plates with manufacturing and material uncertainties, AIAA/ASME/ASCE/AHS/ASC Structures, Structural Dynamics, and Materials Conference and Exhibit, 42nd , Seattle, WA, .

[82] Telikicherla M. K., Altan M. C. and Lai F. C. (1994), Autoclave curing of thermosetting composites: Process modeling for the cure assembly, International Communications in Heat and Mass Transfer, vol. 21, no. 6, pp. 785-797.

[83] Li H., Foschi R., Vaziri R., Fernlund G. and Poursartip A. (2002), Probability-based modelling of composites manufacturing and its application to optimal process design, Journal of Composite Materials, vol. 36, no. 16, pp. 1967-1991.

[84] Hilton H. H. and Yi S. (1999), Stochastic delamination simulations of nonlinear viscoelastic composites during cure, Journal of Sandwich Structures and Materials, vol. 1, no. 2, pp. 111-127.

[85] Hsiao K. T. (2007), Uncertainty modeling of residual stress development in polymeric composites manufactured with resin transfer molding process, In: Proceedings of ASME international mechanical engineering congress and exposition, Seattle, Washington, USA.

[86] Hubert P., Pipes R. B. and Grimsley B. W. (2002), Variability analysis in vacuum assisted resin transfer molding, Society for the Advancement of Material and Process Engineering. International SAMPE Europe conference, pp. 415.

[87] Antonucci V., Cusano A., Giordano M., Nasser J. and Nicolais L. (2006), Cure-induced residual strain build-up in a thermoset resin, Composites Part A: Applied Science and Manufacturing, vol. 37, no. 4, pp. 592-601.

[88] Arbter R., Beraud J., Binetruy C., Bizet L., Bréard J., Comas-Cardona S., Demaria C., Endruweit A., Ermanni P. and Gommer F. (2011), Experimental determination of the permeability of textiles: a benchmark exercise, Composites Part A: Applied Science and Manufacturing, vol. 42, no. 9, pp. 1157-1168.

[89] Parnas R. S. and Salem A. J. (1993), A comparison of the unidirectional and radial in-plane flow of fluids through woven composite reinforcements, Polymer Composites, vol. 14, no. 5, pp. 383-394.

[90] Gebart B. R. and Lidström P. (1996), Measurement of in-plane permeability of anisotropic fiber reinforcements, Polymer Composites, vol. 17, no. 1, pp. 43-51.

[91] Parnas R. S., Howard J. G., Luce, T. L. and Advani S. G. (1995), Permeability characterization. Part 1: A proposed standard reference fabric for permeability, Polymer Composites, vol. 16, no. 6, pp. 429-445.

[92] Ahn S. H., Lee W. I. and Springer G. S. (1995), Measurement of the three-dimensional permeability of fiber preforms using embedded fiber optic sensors, Journal of Composite Materials, vol. 29, no. 6, pp. 714-733.

[93] Lekakou C., Johari M. A. K., Norman D. and Bader M. G. (1996), Measurement techniques and effects on in-plane permeability of woven cloths in resin transfer moulding, Composites Part A: Applied Science and Manufacturing, vol. 27, no. 5, pp. 401-408.

[94] Bickerton S., Advani S., Mohan R. and Shires D. (2000), Experimental analysis and numerical modeling of flow channel effects in resin transfer molding, Polymer composites, vol. 21, no. 1, pp. 134-153.

[95] James W., Wu C. and James L. (1994), In-plane permeability measurement and analysis in liquid composite molding, Polymer composites, vol. 15, no. 4, pp. 278-288.

[96] Pillai K. M. (2004), Modeling the unsaturated flow in liquid composite molding processes: a review and some thoughts, Journal of Composite Materials, vol. 38, no. 23, pp. 2097-2118.

[97] Dykeman D. (2008), Minimizing uncertainty in cure modeling for composites manufacturing, PhD thesis. The University of British Columbia, Vancouver.

[98] Vernet N., Ruiz, E., Advani S., Alms J., Aubert M., Barburski M., Barari B., Beraud J., Berg D. and Correia N. (2014), Experimental determination of the permeability of engineering textiles: Benchmark II, Composites Part A: Applied Science and Manufacturing, vol. 61, pp. 172-184.

[99] Bang K. G., Kwon J. W., Lee D. G. and Lee J. W. (2001), Measurement of the degree of cure of glass fiber–epoxy composites using dielectrometry, Journal of Materials Processing Technology, vol. 113, no. 1, pp. 209-214.

[100] Mulligan D., Gnaniah S. and Sims G. (2000), Thermal analysis techniques for composites and adhesives, National Physical Laboratory.

[101] Hexcel® (2009), RTM 6 180°C epoxy system for Resin Transfer Moulding monocomponent system Product Data, www.hexcel.com.

[102] Hexcel® (2013), US Technical Fabrics Handbook , www.hexcel.com.

[103] HexTow® (2010), AS7 carbon fiber, www.hexcel.com.

[104] Skordos A. and Partridge I. (2001), Cure kinetics modeling of epoxy resins using a non-parametric numerical procedure, Polymer Engineering & Science, vol. 41, no. 5, pp. 793-805.

[105] Bandara U. (1986), A systematic solution to the problem of sample background correction in DSC curves, Journal of Thermal Analysis and Calorimetry, vol. 31, no. 5, pp. 1063-1071.

[106] Karkanas P. I. and Partridge I. K. (2000), Cure modeling and monitoring of epoxy/amine resin systems. I. Cure kinetics modeling, Journal of Applied Polymer Science, vol. 77, no. 7, pp. 1419-1431.

[107] Millán M. S. and Escofet J. (1996), Fourier-domain-based angular correlation for quasiperiodic pattern recognition. Applications to web inspection, Applied Optics, vol. 35, no. 31, pp. 6253-6260.

[108] RdF®. Heat flux sensors. http://www.rdfcorp.com/products/hflux/hfs-a_01.shtml (assessed 10th July, 2014).

[109] Marc® (2011), Volume A: Theory and user information, www.mscsoftware.com.

[110] Marc® (2011), Volume B: Elements library, www.mscsoftware.com.

[111] Marc® (2011), Volume D: User subroutine and special routines, www.mscsoftware.com.

[112] Shojaei A., Reza Ghaffarian S. and Mohammad Hossei Karimian S. (2004), Three-dimensional process cycle simulation of composite parts manufactured by resin transfer molding, Composite Structures, vol. 65, no. 3, pp. 381-390.

[113] Yue G., Zhang B., Dai F. and Du S. (2010), Three-dimensional Cure Simulation of Stiffened Thermosetting Composite Panels, Journal of materials science & technology, vol. 26, no. 5, pp. 467-471.

[114] HexForce® (2013), G1157 D1300 INJ 2F Carbon fabric, www.hexcel.com.

[115] Pascault J. and Williams R. (1990), Relationships between glass transition temperature and conversion, Polymer Bulletin, vol. 24, no. 1, pp. 115-121.

[116] Karkanas P. I., Partridge I. K. and Attwood D. (1996), Modelling the cure of a commercial epoxy resin for applications in resin transfer moulding, Polymer International, vol. 41, no. 2, pp. 183-191.

[117] Karkanas P. I. and Partridge I. K. (2000), Cure modeling and monitoring of epoxy/amine resin systems. II. Network formation and chemoviscosity modeling, Journal of Applied Polymer Science, vol. 77, no. 10, pp. 2178-2188.

[118] Simon S. L. and Gillham J. (1993), Cure kinetics of a thermosetting liquid dicyanate ester monomer/high-Tg polycyanurate material, Journal of Applied Polymer Science, vol. 47, no. 3, pp. 461-485.

[119] Skordos A. A. and Partridge I. K. (2004), Inverse heat transfer for optimization and on-line thermal properties estimation in composites curing, Inverse Problems in Science and Engineering, vol. 12, no. 2, pp. 157-172.

[120] Farmer J. and Covert E. (1996), Thermal conductivity of a thermosetting advanced composite during its cure, Journal of Thermophysics and Heat Transfer(USA), vol. 10, no. 3, pp. 467-475.

[121] Yamane T., Katayama S., Todoki M. and Hatta I. (2000), The measurements of thermal conductivity of carbon fibers, Journal of Wide Bandgap Materials, vol. 7, no. 4, pp. 294-305.

[122] Chamis C. (1989), Mechanics of composite materials- Past, present and future, Journal of Composites Technology and Research, vol. 11, pp. 3-14.

[123] Vaughan T. and McCarthy C. (2011), Micromechanical modelling of the transverse damage behaviour in fibre reinforced composites, Composites Science and Technology, vol. 71, no. 3, pp. 388-396.

[124] Pansart S., Sinapius M. and Gabbert U. (2009), A comprehensive explanation of compression strength differences between various CFRP materials: Micro-meso model, predictions, parameter studies, Composites Part A: Applied Science and Manufacturing, vol. 40, no. 4, pp. 376-387.

[125] Svanberg J., Altkvist C. and Nyman T. (2005), Prediction of shape distortions for a curved composite C-spar, Journal of Reinforced Plastics and Composites, vol. 24, no. 3, pp. 323-339.

[126] Zimmermann K. and Van Den Broucke B. (2012), Assessment of process-induced deformations and stresses in ultra thick laminates using isoparametric 3D elements, Journal of Reinforced Plastics and Composites, vol. 31, no. 3, pp. 163-178.

[127] Pradere C. and Sauder C. (2008), Transverse and longitudinal coefficient of thermal expansion of carbon fibers at high temperatures (300-2500 K), Carbon, vol. 46, no. 14, pp. 1874-1884.

[128] Smith W. (2010), On the simulation and estimation of the mean-reverting ornstein-uhlenbeck process, Commodities Markets and Modelling, .

[129] Terdik G. and Woyczynski W. A. (2005), Notes on fractional Ornstein-Uhlenbeck random sheets, Publ.Math.Debrecen, vol. 66, no. 1.

[130] Arató M., Pap G. and Van Zuijlen M. C. (2001), Asymptotic inference for spatial autoregression and orthogonality of Ornstein-Uhlenbeck sheets, Computers & Mathematics with Applications, vol. 42, no. 1, pp. 219-229.

[131] Shinozuka M. and Deodatis G. (1996), Simulation of multi-dimensional Gaussian stochastic fields by spectral representation, Applied Mechanics Reviews, vol. 49, pp. 29-53.

[132] Stefanou G. and Papadrakakis M. (2007), Assessment of spectral representation and Karhunen–Loève expansion methods for the simulation of Gaussian stochastic fields, Computer Methods in Applied Mechanics and Engineering, vol. 196, no. 21, pp. 2465-2477.

[133] Grigoriu M. (1993), On the spectral representation method in simulation, Probabilistic Engineering Mechanics, vol. 8, no. 2, pp. 75-90.

[134] Stefanou G. (2009), The stochastic finite element method: past, present and future, Computer Methods in Applied Mechanics and Engineering, vol. 198, no. 9, pp. 1031-1051.

[135] Huang S., Quek S. and Phoon K. (2001), Convergence study of the truncated Karhunen–Loeve expansion for simulation of stochastic processes, International Journal for Numerical Methods in Engineering, vol. 52, no. 9, pp. 1029-1043.

[136] Phoon K., Huang H. and Quek S. (2004), Comparison between Karhunen–Loeve and wavelet expansions for simulation of Gaussian processes, Computers & Structures, vol. 82, no. 13, pp. 985-991.

[137] Courant R. and Hilbert D. (1966), Methods of mathematical physics. vol. 1. CUP Archive.

[138] Tatang M. and McRae G. (1994), Direct treatment of uncertainty in models of reaction and transport, Tech. Rep., MIT Technical Report.

[139] Webster M. D., Tatang M. A. and McRae G. J. (1996), Application of the probabilistic collocation method for an uncertainty analysis of a simple ocean model, MIT Joint Program on the Science and Policy of Global Change.

[140] Isukapalli S., Roy A. and Georgopoulos P. (1998), Stochastic response surface methods (SRSMs) for uncertainty propagation: application to environmental and biological systems, Risk analysis, vol. 18, no. 3, pp. 351-363.

[141] Acquah C., Datskov I., Mawardi A., Zhang, F., Achenie L. E. K., Pitchumani R. and Santos, E. (2006), Optimization under uncertainty of a composite fabrication process using a deterministic one-stage approach, Computers & Chemical Engineering, vol. 30, no. 6–7, pp. 947-960.

[142] Barati R. (2013), Application of Excel Solver for parameter estimation of the nonlinear Muskingum models, KSCE Journal of Civil Engineering, vol. 17, no. 5, pp. 1139-1148.

[143] O'Connor P. and Kleyner A. (2011), Practical reliability engineering, John Wiley & Sons Pubns.

[144] Liu D., Fleck N. and Sutcliffe M. (2004), Compressive strength of fibre composites with random fibre waviness, Journal of the Mechanics and Physics of Solids, vol. 52, no. 7, pp. 1481-1505.

[145] Bogetti T. A. and Gillespie J. W. (1992), Process-induced stress and deformation in thick-section thermoset composite laminates, Journal of Composite Materials, vol. 26, no. 5, pp. 626-660.

[146] Ersoy N., Garstka T., Potter K., Wisnom M. R., Porter D. and Stringer G. (2010), Modelling of the spring-in phenomenon in curved parts made of a thermosetting composite, Composites Part A: Applied Science and Manufacturing, vol. 41, no. 3, pp. 410-418.

[147] Ersoy N., Potter K., Wisnom M. R. and Clegg M. J. (2005), Development of spring-in angle during cure of a thermosetting composite, Composites Part A: Applied Science and Manufacturing, vol. 36, no. 12, pp. 1700-1706.

[148] Fylstra D., Lasdon L., Watson J. and Waren A. (1998), Design and use of the Microsoft Excel Solver, Interfaces, vol. 28, no. 5, pp. 29-55.

[149] Wisnom M., Gigliotti M., Ersoy N., Campbell, M. and Potter K. (2006), Mechanisms generating residual stresses and distortion during manufacture of polymer–matrix composite structures, Composites Part A: Applied Science and Manufacturing, vol. 37, no. 4, pp. 522-529.

[150] Jaeger L. G. (1966), Cartesian tensors in engineering science, Pergamon Pubns.

[151] Daniel I. M., Ishai O., Daniel I. M. and Daniel I. (1994), Engineering mechanics of composite materials, Oxford university press New York.

[152] Brøndsted P., Lilholt H. and Lystrup A. (2005), Composite materials for wind power turbine blades, Annu. Rev. Mater. Res., vol. 35, pp. 505-538.

[153] Hayman B., Wedel-Heinen J. and Brøndsted P. (2008), Materials challenges in present and future wind energy, MRS Bulletin, vol. 33, no. 04, pp. 343-353.

[154] Brouwer W., Van Herpt E. and Labordus M. (2003), Vacuum injection moulding for large structural applications, Composites Part A: Applied Science and Manufacturing, vol. 34, no. 6, pp. 551-558.

[155] Struzziero G. and Skordos A. Multi-objective optimisation of composites cure using Genetic Algorithms, In: Proceedings of the 15th European Conference on Composites Materials (ECCM), 24 - 28 June 2012, Venice, Italy.

[156] Chao L. (1996), Multiobjective optimization design methodology for incorporating manufacturing uncertainties in advanced composite structures, Engineering Optimization, vol. 25, no. 4, pp. 309-323.

Appendices

Appendix A Cure simulation model user subroutines

Examples of the user subroutines used to incorporate the respective material sub-models described in Chapter 4 to the main code are presented in this section. These user subroutines can be used with any MSC.Marc cure simulation model. Listing A-1 presents the UCURE subroutine used to implement the cure kinetics model described in section 4.2.2.

```
  subroutine ucure(m,n,nn,kcus,matus,dt,ak,density,volumi,curedat,
1   tempbeg,tempend,deltime,time,curerate)
    include 'concom'
    include 'creeps'
    dimension curedat(*),matus(2)
    real*8 ak, curedat, curerate, deltime, density, dt
    integer kcus, m, matus, n, nn
    real*8 tempbeg, tempend, time, volumi
    real*8 K1,K2,K1c,K2c,Kd,A1
    real*8 A2,Ad,n1,n2,mi,E1,E2
    real*8 Ed, H, R, vf, l, ba
    real*8 Tginf, Tgo, g, f,w,ako,Tg
    vf=0.6d0
    ako=0.032661094
    A1=19006.41379
    A2=22082.69835
    Ad=6.7557E+18
      E1=72892.53275
      E2=57827.01505
    Ed=137561.5952
    n1=1.965580509
      n2=1.525367094
    mi=1.288659069
    l=0.435d0
    ba=0.452381424
    Tginf=206d0
    Tgo=-11d0
    H=465000.0
    R=8.3144
    g=0.029212404
    w=0.000466142
  Tg=Tgo-(Tginf-Tgo)*l*dt/(1-(1-l)*dt)
  f=w*(tempbeg-273.15-Tg)+g
    K1c=A1*exp(-E1/(R*tempbeg))
    K2c=A2*exp(-E2/(R*tempbeg))
    Kd=Ad*exp(-Ed/(R*tempbeg))*exp(-ba/f)
    K1=1/(1/Kd+1/K1c)
    K2=1/(1/Kd+1/K2c)
    curerate=K1*(1-dt)**n1+K2*dt**mi*(1-dt)**n2
    curedat(9)=H*(1-vf)
    volumi=1.0
    ak=dt+deltime*curerate
    if (ak>0.999) then
            curerate=0.0
            ak=1.0
     end if
  return
  end
```

Listing A-1 Implementation of UCURE subroutine for RTM6 epoxy resin.

Listings A-2, A-3 and A-4 show the ANKOND, HOOKLW and ANEXP subroutines used for the implementation of the thermal conductivity, mechanical properties and thermal expansion material sub-models, respectively.

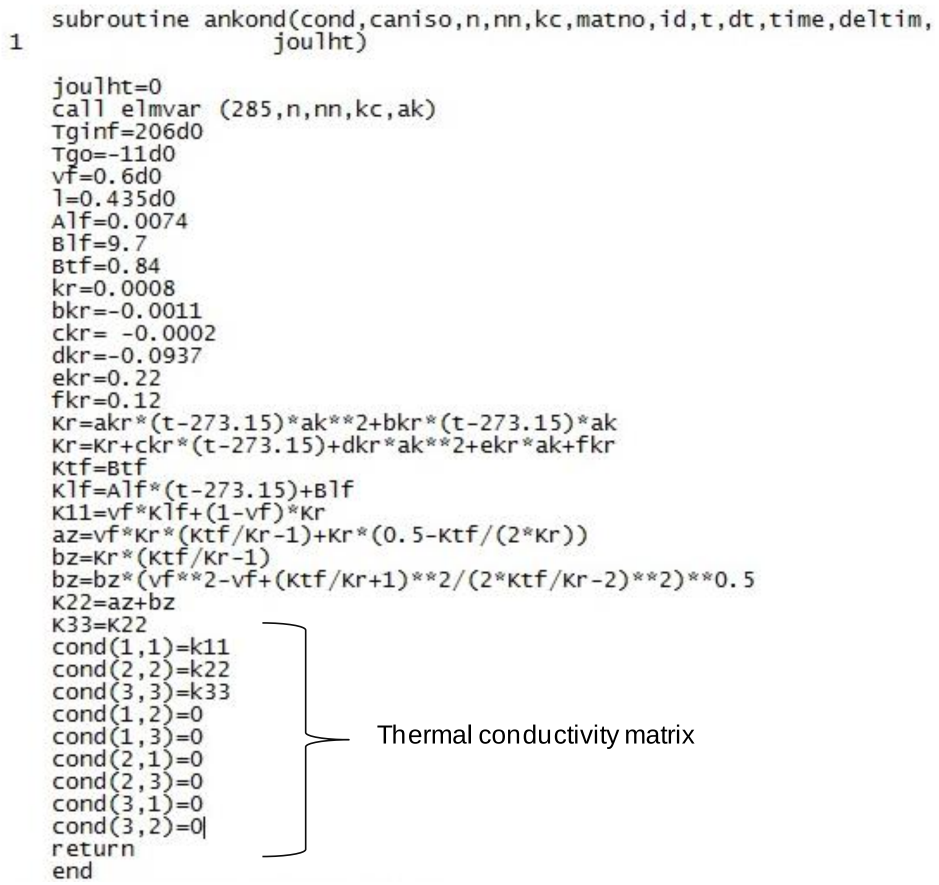

```
      subroutine ankond(cond,caniso,n,nn,kc,matno,id,t,dt,time,deltim,
     1                  joulht)

      joulht=0
      call elmvar (285,n,nn,kc,ak)
      Tginf=206d0
      Tgo=-11d0
      vf=0.6d0
      l=0.435d0
      Alf=0.0074
      Blf=9.7
      Btf=0.84
      kr=0.0008
      bkr=-0.0011
      ckr= -0.0002
      dkr=-0.0937
      ekr=0.22
      fkr=0.12
      Kr=akr*(t-273.15)*ak**2+bkr*(t-273.15)*ak
      Kr=Kr+ckr*(t-273.15)+dkr*ak**2+ekr*ak+fkr
      Ktf=Btf
      Klf=Alf*(t-273.15)+Blf
      K11=vf*Klf+(1-vf)*Kr
      az=vf*Kr*(Ktf/Kr-1)+Kr*(0.5-Ktf/(2*Kr))
      bz=Kr*(Ktf/Kr-1)
      bz=bz*(vf**2-vf+(Ktf/Kr+1)**2/(2*Ktf/Kr-2)**2)**0.5
      K22=az+bz
      K33=K22
      cond(1,1)=k11
      cond(2,2)=k22
      cond(3,3)=k33
      cond(1,2)=0
      cond(1,3)=0
      cond(2,1)=0
      cond(2,3)=0
      cond(3,1)=0
      cond(3,2)=0
      return
      end
```

Listing A-2 Implementation of ANKOND subroutine for RTM6 epoxy resin and G1157 pseudo unidirectional carbon fibre reinforcement.

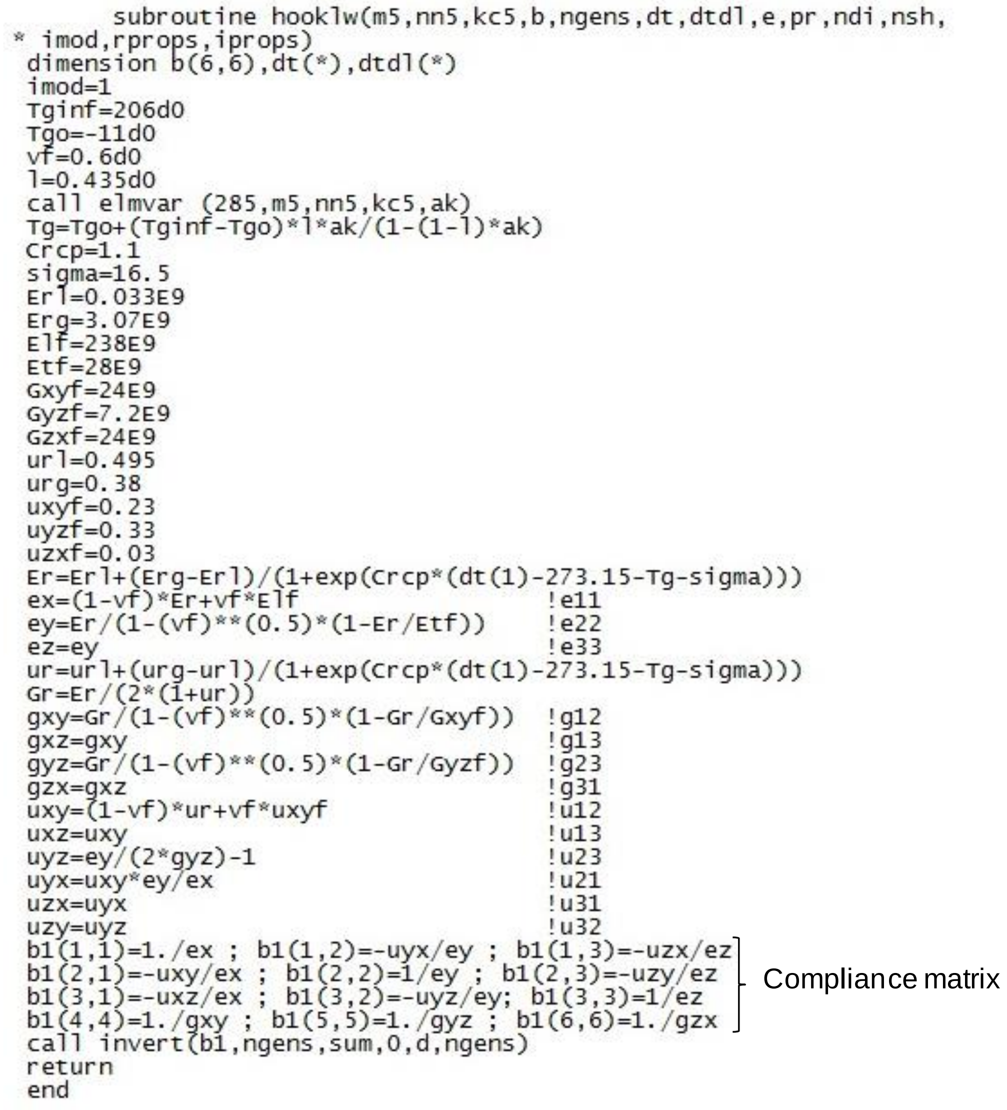

```
       subroutine hooklw(m5,nn5,kc5,b,ngens,dt,dtdl,e,pr,ndi,nsh,
* imod,rprops,iprops)
 dimension b(6,6),dt(*),dtdl(*)
 imod=1
 Tginf=206d0
 Tgo=-11d0
 vf=0.6d0
 l=0.435d0
 call elmvar (285,m5,nn5,kc5,ak)
 Tg=Tgo+(Tginf-Tgo)*l*ak/(1-(1-l)*ak)
 Crcp=1.1
 sigma=16.5
 Erl=0.033E9
 Erg=3.07E9
 Elf=238E9
 Etf=28E9
 Gxyf=24E9
 Gyzf=7.2E9
 Gzxf=24E9
 url=0.495
 urg=0.38
 uxyf=0.23
 uyzf=0.33
 uzxf=0.03
 Er=Erl+(Erg-Erl)/(1+exp(Crcp*(dt(1)-273.15-Tg-sigma)))
 ex=(1-vf)*Er+vf*Elf                  !e11
 ey=Er/(1-(vf)**(0.5)*(1-Er/Etf))     !e22
 ez=ey                                !e33
 ur=url+(urg-url)/(1+exp(Crcp*(dt(1)-273.15-Tg-sigma)))
 Gr=Er/(2*(1+ur))
 gxy=Gr/(1-(vf)**(0.5)*(1-Gr/Gxyf))   !g12
 gxz=gxy                              !g13
 gyz=Gr/(1-(vf)**(0.5)*(1-Gr/Gyzf))   !g23
 gzx=gxz                              !g31
 uxy=(1-vf)*ur+vf*uxyf                !u12
 uxz=uxy                              !u13
 uyz=ey/(2*gyz)-1                     !u23
 uyx=uxy*ey/ex                        !u21
 uzx=uyx                              !u31
 uzy=uyz                              !u32
 b1(1,1)=1./ex ; b1(1,2)=-uyx/ey ; b1(1,3)=-uzx/ez
 b1(2,1)=-uxy/ex ; b1(2,2)=1/ey ; b1(2,3)=-uzy/ez
 b1(3,1)=-uxz/ex ; b1(3,2)=-uyz/ey; b1(3,3)=1/ez
 b1(4,4)=1./gxy ; b1(5,5)=1./gyz ; b1(6,6)=1./gzx
 call invert(b1,ngens,sum,0,d,ngens)
 return
 end
```

Listing A-3 Implementation of HOOKLW subroutine for RTM6 epoxy resin and G1157 pseudo unidirectional carbon fibre reinforcement.

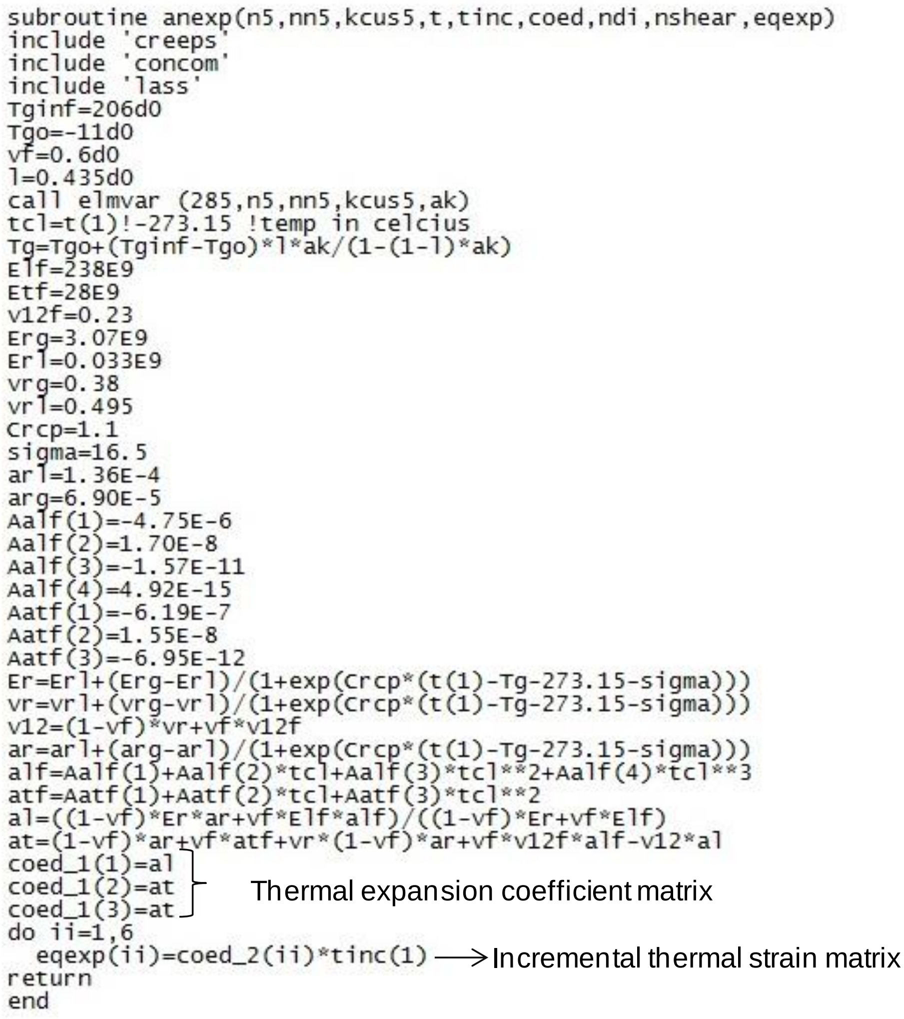

```
subroutine anexp(n5,nn5,kcus5,t,tinc,coed,ndi,nshear,eqexp)
include 'creeps'
include 'concom'
include 'lass'
Tginf=206d0
Tgo=-11d0
vf=0.6d0
l=0.435d0
call elmvar (285,n5,nn5,kcus5,ak)
tcl=t(1)!-273.15 !temp in celcius
Tg=Tgo+(Tginf-Tgo)*l*ak/(1-(1-l)*ak)
Elf=238E9
Etf=28E9
v12f=0.23
Erg=3.07E9
Erl=0.033E9
vrg=0.38
vrl=0.495
Crcp=1.1
sigma=16.5
arl=1.36E-4
arg=6.90E-5
Aalf(1)=-4.75E-6
Aalf(2)=1.70E-8
Aalf(3)=-1.57E-11
Aalf(4)=4.92E-15
Aatf(1)=-6.19E-7
Aatf(2)=1.55E-8
Aatf(3)=-6.95E-12
Er=Erl+(Erg-Erl)/(1+exp(Crcp*(t(1)-Tg-273.15-sigma)))
vr=vrl+(vrg-vrl)/(1+exp(Crcp*(t(1)-Tg-273.15-sigma)))
v12=(1-vf)*vr+vf*v12f
ar=arl+(arg-arl)/(1+exp(Crcp*(t(1)-Tg-273.15-sigma)))
alf=Aalf(1)+Aalf(2)*tcl+Aalf(3)*tcl**2+Aalf(4)*tcl**3
atf=Aatf(1)+Aatf(2)*tcl+Aatf(3)*tcl**2
al=((1-vf)*Er*ar+vf*Elf*alf)/((1-vf)*Er+vf*Elf)
at=(1-vf)*ar+vf*atf+vr*(1-vf)*ar+vf*v12f*alf-v12*al
coed_1(1)=al
coed_1(2)=at
coed_1(3)=at
do ii=1,6
  eqexp(ii)=coed_2(ii)*tinc(1)
return
end
```

Thermal expansion coefficient matrix

Incremental thermal strain matrix

Listing A-4 Implementation of ANEXP subroutine for RTM6 epoxy resin and G1157 pseudo unidirectional carbon fibre reinforcement.

Appendix B Interfaces between stochastic model and FEA solver

Examples of the interfaces developed to link the stochastic simulation models described in Chapter 5 with the finite element based cure simulation model presented in Chapter 4 are presented in this section.

Appendix B.1 cure kinetics uncertainty/ boundary conditions uncertainty

Listing B-1 shows the part of the interface developed to identify the location of the stochastic parameters in the MSC.Marc user defined subroutine and write a new user subroutine using the realisations generated for each of the stochastic variables. This was used in both the Monte Carlo and collocation method.

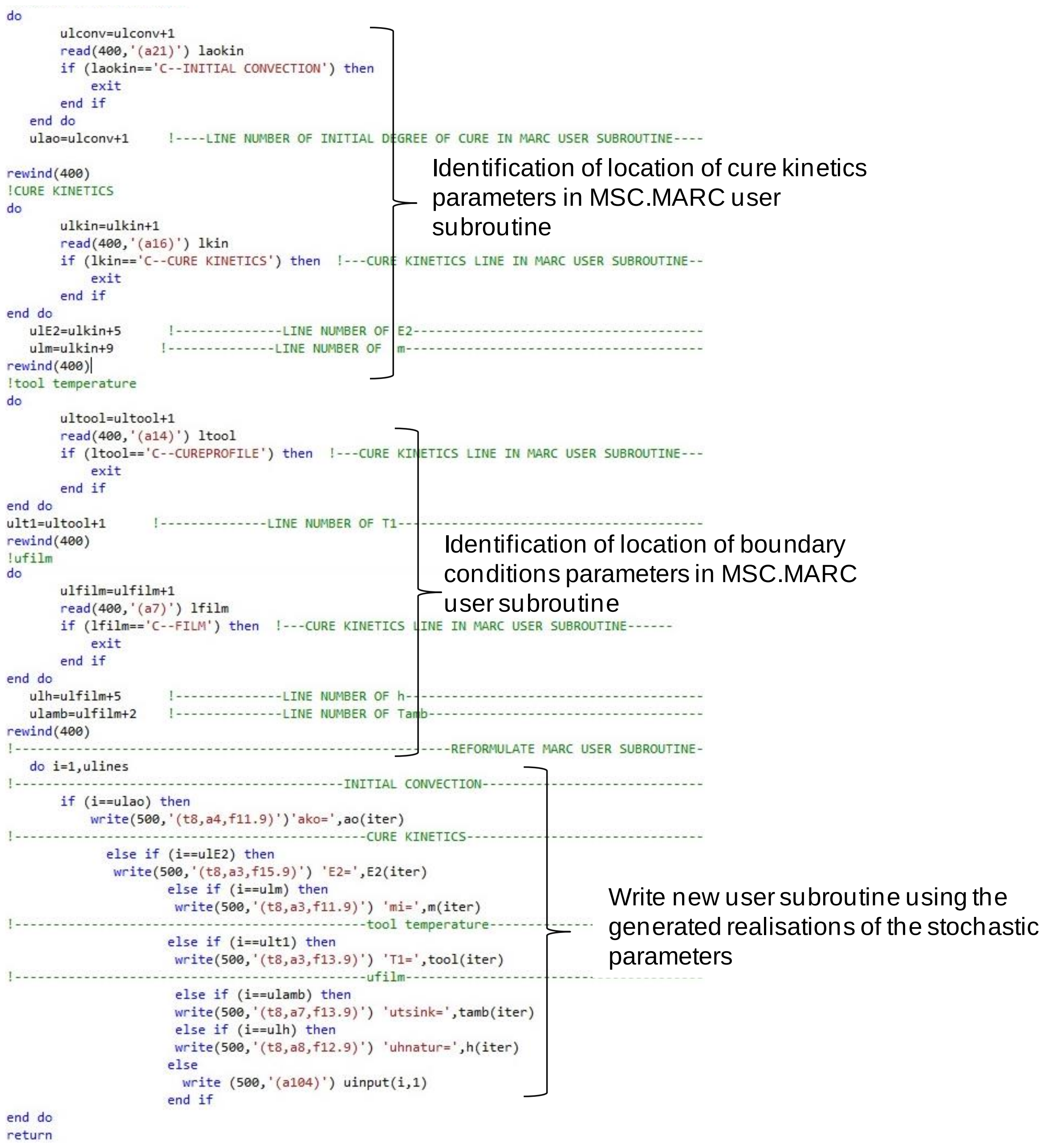

```
do
       ulconv=ulconv+1
       read(400,'(a21)') laokin
       if (laokin=='C--INITIAL CONVECTION') then
           exit
       end if
   end do
   ulao=ulconv+1     !----LINE NUMBER OF INITIAL DEGREE OF CURE IN MARC USER SUBROUTINE----

rewind(400)
!CURE KINETICS
do
       ulkin=ulkin+1
       read(400,'(a16)') lkin
       if (lkin=='C--CURE KINETICS') then  !---CURE KINETICS LINE IN MARC USER SUBROUTINE--
           exit
       end if
end do
   ulE2=ulkin+5      !--------------LINE NUMBER OF E2--------------------------------------
   ulm=ulkin+9      !--------------LINE NUMBER OF  m---------------------------------------
rewind(400)
!tool temperature
do
       ultool=ultool+1
       read(400,'(a14)') ltool
       if (ltool=='C--CUREPROFILE') then  !---CURE KINETICS LINE IN MARC USER SUBROUTINE---
           exit
       end if
end do
ult1=ultool+1      !--------------LINE NUMBER OF T1----------------------------------------
rewind(400)
!ufilm
do
       ulfilm=ulfilm+1
       read(400,'(a7)') lfilm
       if (lfilm=='C--FILM') then  !---CURE KINETICS LINE IN MARC USER SUBROUTINE------
           exit
       end if
end do
   ulh=ulfilm+5      !--------------LINE NUMBER OF h--------------------------------------
   ulamb=ulfilm+2    !--------------LINE NUMBER OF Tamb-----------------------------------
rewind(400)
!---------------------------------------------------------REFORMULATE MARC USER SUBROUTINE-
   do i=1,ulines
!-------------------------------------------INITIAL CONVECTION-----------------------------
       if (i==ulao) then
           write(500,'(t8,a4,f11.9)')'ako=',ao(iter)
!----------------------------------------------CURE KINETICS-------------------------------
             else if (i==ulE2) then
              write(500,'(t8,a3,f15.9)') 'E2=',E2(iter)
                     else if (i==ulm) then
                      write(500,'(t8,a3,f11.9)') 'mi=',m(iter)
!----------------------------------------------tool temperature----------------------------
                     else if (i==ult1) then
                      write(500,'(t8,a3,f13.9)') 'T1=',tool(iter)
!----------------------------------------------ufilm---------------------------------------
                      else if (i==ulamb) then
                      write(500,'(t8,a7,f13.9)') 'utsink=',tamb(iter)
                      else if (i==ulh) then
                      write(500,'(t8,a8,f12.9)') 'uhnatur=',h(iter)
                     else
                       write (500,'(a104)') uinput(i,1)
                     end if
end do
return
```

Identification of location of cure kinetics parameters in MSC.MARC user subroutine

Identification of location of boundary conditions parameters in MSC.MARC user subroutine

Write new user subroutine using the generated realisations of the stochastic parameters

Listing B-1 Identification of location of stochastic variables in user subroutine, writing new user subroutine. Cure kinetics uncertainty/ boundary conditions uncertainty stochastic cure simulation interface.

The temperature overshoot and the time of temperature overshoot are identified by using the UPSTNO subroutine as shown in Listing B-2. The difference between the nodes temperature (*Tcurrent*) and the one at the boundary (*Tbound*) is computed for each node of the model and is stored in *Tmax* if its value is higher than the former. The corresponding time is stored in *t_tmax*.

```
 subroutine upstno(nqcode,nodeid,valno,nqncomp,nqtype,
*           nqaver,nqcomptype,nqdatatype,nqcompname)
 implicit real*8 (a-h,o-z)
 common /Tbound/Tbound
 call nodvar(14,nodeid,Tcurrent,nqncomp,nqdatatype)
 valno(1)=Tcurrent !current temp at each node
 !-----MAXIMUM TEMPERATURE-------
 if (inc>0) then
 DTcurrent=Tcurrent-Tbound
 end if
 if (DTcurrent>DTmax) then
     DTmax=DTcurrent
     Tmax=DTmax!+Tbound
     maxbound=Tbound
     t_tmax=cptim
     maxinc=inc
     maxDT=DTmax
 end if
 if (cptim==15300) then
 open(unit=90,file="z:\res\utmax.txt",status="replace")
 write(unit=90,fmt=*),Tmax
 close (unit=90)
 open(unit=80,file="z:\res\ut_tmax.txt",status="replace")
 write(unit=80,fmt=*),t_tmax
 close (unit=80)
 end if

 return
 end
```

Listing B-2 Computation of temperature overshoot and time of temperature overshoot using UPSTNO user subroutine. Cure kinetics uncertainty stochastic cure simulation interface.

Computation of the cure time is carried out using the UEDINC user subroutine as reported in Listing B-3. The minimum degree of cure stored in *amin* is compared with a predefined limit of 0.90 and the time that *amin* is equal or higher than this limit is considered as the cure time and it is stored in *tcure*.

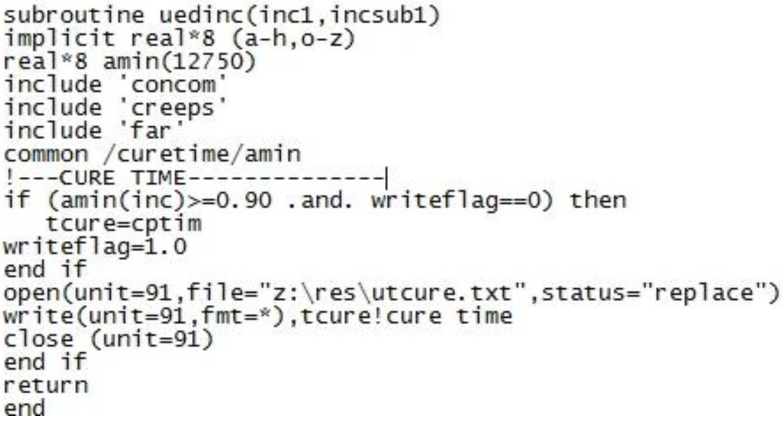

```
subroutine uedinc(inc1,incsub1)
implicit real*8 (a-h,o-z)
real*8 amin(12750)
include 'concom'
include 'creeps'
include 'far'
common /curetime/amin
!---CURE TIME--------------
if (amin(inc)>=0.90 .and. writeflag==0) then
   tcure=cptim
writeflag=1.0
end if
open(unit=91,file="z:\res\utcure.txt",status="replace")
write(unit=91,fmt=*),tcure!cure time
close (unit=91)
end if
return
end
```

Listing B-3 Computation of cure time using UEDINC user subroutine. Cure kinetics uncertainty stochastic cure simulation interface.

Appendix B.2 Fibre misalignment

Listing B-4 reports part of the interface developed to read realisations of local tow orientation and incorporate local tow orientation to each integration point of the model according to the position. This is followed by the rotation transformation of the thermal conductivity matrix, compliance tensor, cure shrinkage coefficient matrix and thermal expansion coefficient matrix. as presented in section 7.3.1.

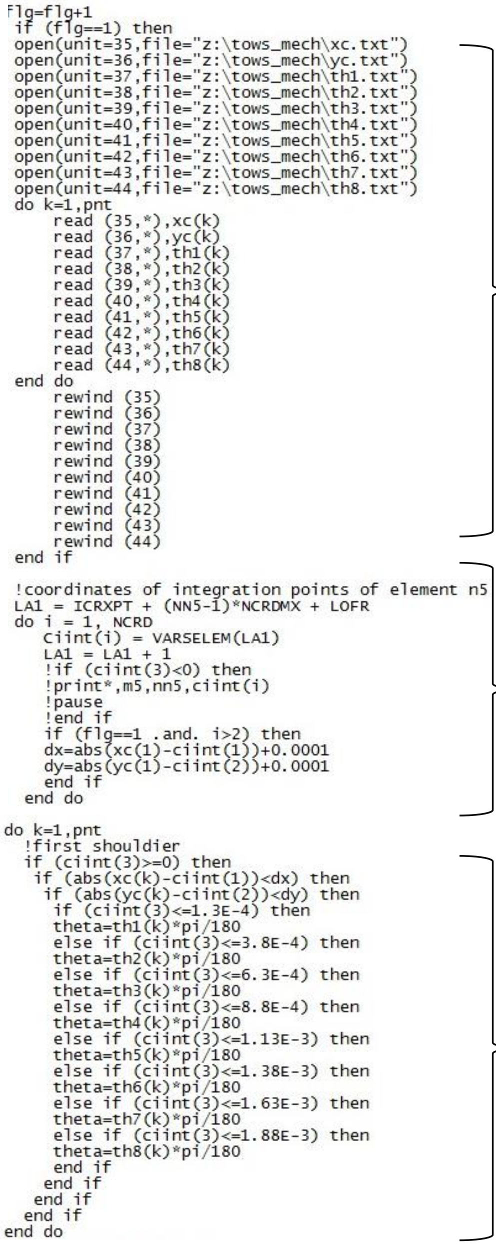

```
Flg=flg+1
 if (flg==1) then
 open(unit=35,file="z:\tows_mech\xc.txt")
 open(unit=36,file="z:\tows_mech\yc.txt")
 open(unit=37,file="z:\tows_mech\th1.txt")
 open(unit=38,file="z:\tows_mech\th2.txt")
 open(unit=39,file="z:\tows_mech\th3.txt")
 open(unit=40,file="z:\tows_mech\th4.txt")
 open(unit=41,file="z:\tows_mech\th5.txt")
 open(unit=42,file="z:\tows_mech\th6.txt")
 open(unit=43,file="z:\tows_mech\th7.txt")
 open(unit=44,file="z:\tows_mech\th8.txt")
 do k=1,pnt
     read (35,*),xc(k)
     read (36,*),yc(k)
     read (37,*),th1(k)
     read (38,*),th2(k)
     read (39,*),th3(k)
     read (40,*),th4(k)
     read (41,*),th5(k)
     read (42,*),th6(k)
     read (43,*),th7(k)
     read (44,*),th8(k)
 end do
     rewind (35)
     rewind (36)
     rewind (37)
     rewind (38)
     rewind (39)
     rewind (40)
     rewind (41)
     rewind (42)
     rewind (43)
     rewind (44)
 end if

 !coordinates of integration points of element n5
 LA1 = ICRXPT + (NN5-1)*NCRDMX + LOFR
 do i = 1, NCRD
    Ciint(i) = VARSELEM(LA1)
    LA1 = LA1 + 1
    !if (ciint(3)<0) then
    !print*,m5,nn5,ciint(i)
    !pause
    !end if
    if (flg==1 .and. i>2) then
    dx=abs(xc(1)-ciint(1))+0.0001
    dy=abs(yc(1)-ciint(2))+0.0001
    end if
  end do

do k=1,pnt
  !first shouldier
  if (ciint(3)>=0) then
   if (abs(xc(k)-ciint(1))<dx) then
    if (abs(yc(k)-ciint(2))<dy) then
     if (ciint(3)<=1.3E-4) then
     theta=th1(k)*pi/180
     else if (ciint(3)<=3.8E-4) then
     theta=th2(k)*pi/180
     else if (ciint(3)<=6.3E-4) then
     theta=th3(k)*pi/180
     else if (ciint(3)<=8.8E-4) then
     theta=th4(k)*pi/180
     else if (ciint(3)<=1.13E-3) then
     theta=th5(k)*pi/180
     else if (ciint(3)<=1.38E-3) then
     theta=th6(k)*pi/180
     else if (ciint(3)<=1.63E-3) then
     theta=th7(k)*pi/180
     else if (ciint(3)<=1.88E-3) then
     theta=th8(k)*pi/180
     end if
    end if
   end if
  end if
end do
```

Read realisations of local tow orientation

Identification of coordinates of each integration point

Incorporation of local tow orientation according to position.

Listing B-4 Read realisations of local tow orientation, Incorporation of local tow orientation to integration points. Fibre misalignment stochastic cure simulation interface.

Computation of the maximum longitudinal residual stress, corner angle and twist angle is carried out using the PLOTV user subroutine as illustrated in Listing B-5. The maximum residual stress is stored in *maxstress* whilst corner angle and twist angle are stored in *disp(1)* and *disp(2)*, respectively.

```
 subroutine plotv (v,s,sp,etot,eplas,ecreep,t,m,nn,kcus,ndi,
*                 nshear,jpltcd)
 include 'concom'
 include 'creeps'
 !--------AMIN AT EVERY INCREMENT-------------------
 if (inc==0 .and. zeroflag==0) then
        DTmax=-8065014
        amin=8065014
        minresd=5E9
           zeroflag=1
 end if
 !displacement
 call nodvar(1,8866,disp,nqncomp,nqdatatype)
 !-----MAXSTRESS-311---------------
 if (cptim==18660) then
 k=k+1
 call elmvar (111,m,nn,kc,vmst_1)
 if (abs(vmst_1)>maxstress) then
     maxstress=abs(vmst_1)
 end if
 if (k==ipnt) then
 open(unit=90,file="z:\ser\max311.txt",status="replace")
   write(unit=90,fmt=*),maxstress !maximum stress 311
 close (unit=90)
 end if
 end if
 if (cptim==18720) then
 call elmvar (111,m,nn,kc,vmst)
 i=i+1
 stresses(i)=abs(vmst)
 !print*,stresses(i)
 !pause
 !------MAXSTRESS-----------
 if (cptim==18720 .and. i==ipnt) then
     max=maxval(stresses)
 open(unit=94,file="z:\ser\max.txt",status="replace")
   write(unit=94,fmt=*),max !maximum stress
 close (unit=94)
 end if
 if (cptim==18720 .and. i==ipnt) then
 call nodvar(1,9205,disp1,nqncomp,nqdatatype)
 call nodvar(1,9646,disp2,nqncomp,nqdatatype)
 open(unit=93,file="z:\ser\9205.txt",status="replace")
  write(unit=93,fmt=*),disp1(1),disp1(2)
 close (unit=93)
 end if
 end if
 return
```

Listing B-5 Computation of maximum longitudinal residual stress, corner angle and twist angle using PLOTV subroutine. Fibre misalignment stochastic cure simulation interface.

Appendix C List of publications

Journal publications:

1. Mesogitis TS, Skordos AA, Long AC. Uncertainty in the manufacturing of fibrous thermosetting composites: a review. Composites Part A. Applied Science and Manufacturing, 2014;57:67–75.
2. Mesogitis TS, Skordos AA, Long AC. Stochastic simulation of the influence of cure kinetics uncertainty on composites cure. Composites Science and Technology, In publication.
3. Mesogitis TS, Skordos AA, Long AC. Stochastic simulation of the influence of fibre path variability on composites cure. Composites Part A. Applied Science and Manufacturing Submitted (2014).
4. Mesogitis TS, Skordos AA, Long AC. Stochastic heat transfer simulation of the cure of advanced composites. Journal of Composites Materials, In preparation (2015).

Conference publications:

1. Mesogitis TS, Skordos AA, Long AC. Stochastic simulation of composites cure. In: Proceedings of the 19th International Conference on Composites Materials (ICCM), 28 July- 2 August 2013, Montreal, Canada.
2. Mesogitis TS, Skordos AA, Long AC. Non-crimp fabrics geometrical variability and its influence on composites cure. In: Proceedings of the 16th European Conference on Composites Materials (ECCM), 22 - 26 June 2014, Seville, Spain.
3. Mesogitis TS, Skordos AA, Long AC. Stochastic simulation of the cure of advanced composites. Abstract submitted to the 20th International Conference on Composites Materials (ICCM), 19- 24 July 2015, Copenhagen, Denmark.
4. Struzziero G, Mesogitis TS, Skordos AA. Robust optimisation of stochastic process for composite materials. Abstract submitted to the 10th International Conference on Manufacturing of Advanced Composites (ICMAC), 24- 25 June 2015, Bristol, United Kingdom.